Advances in Experimental Methods to Probe Surface Relief Grating Formation Mechanism in Photosensitive Materials

Dissertation

zur Erlangung des akademischen Grades
"doctor rerum naturalium"
(Dr. rer. nat.)
in der Wissenschaftsdisziplin Experimentalphysik

eingereicht an der
Mathematisch-Naturwissenschaftlichen Fakultät
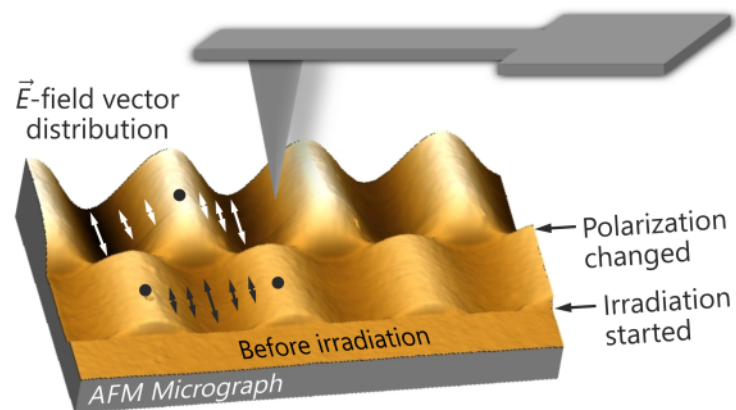**Institut für Physik und Astronomie**
der Universität Potsdam

von

Nataraja Sekhar Yadavalli

Potsdam, April 2014

Advances in Experimental Methods to Probe Surface Relief Grating Formation Mechanism in Photosensitive Materials

$\vec{E}$-field vector distribution

Polarization changed

Irradiation started

Before irradiation

AFM Micrograph

Dissertation

**in partial fulfilment of the requirements
for the degree of
doctor rerum naturalium (Dr. rer. nat.)
in Physics**

**Submitted to the
Faculty of Mathematics and Natural Sciences
Institute of Physics and Astronomy
of the University of Potsdam**

by
Nataraja Sekhar Yadavalli

Potsdam, April 2014

Declaration

I hereby certify that the work presented in this thesis has not been submitted to any other university or higher education institute and that this work is my own and that all sources and aids used are listed with in. Any results not of my own creation are clearly indicated as such.

Potsdam, 17th April 2014

Place, Date

(Nataraja Sekhar Yadavalli)

This page is intentionally left blank

Acknowledgements

I am also thankful to Dr. Leonid. M. Goldenberg, University of Applied Sciences Wildau, for helping with photosensitive materials.

In our lab I have to thank Mr. Felix Linde and Mr. Thomas Papke for their assistance and active discussions.

Not least my gratitude goes to all members of Experimental Physics group for the great time, many discussions, and all fun.

List of Publications in Peer–Reviewed Journals

1. **Probing opto-mechanical stresses within azobenzene containing photosensitive polymer films by a thin metal film placed above**
   N. S. Yadavalli, D. Korolkov, J-F Moulin, M. Krutyeva, and S. Santer
   ACS Appl. Mater. Interfaces (2014) – DOI: 10.1021/am501870t

2. **Confocal Raman microscopy and AFM study of the interface between the photosensitive polymer layer and multilayer graphene**
   G. Di Florio, E. Bründermann, N. S. Yadavalli, S. Santer, and M. Havenith
   Soft Materials (2014) – *In press*

3. Cover page (*1ˢᵗ Aug 2014 issue*) **Photosensitive response of azobenzene containing polymer films towards pure intensity or polarization interference patterns**
   N. S. Yadavalli, M. Saphiannikova, and S. Santer
   Appl. Phys. Lett. **105**, (2014) – *In press*

4. **Polarized 3D Raman and nanoscale near-field optical microscopy of optically inscribed surface relief gratings: chromophore orientation in azo-doped polymer films**
   G. Di Florio, E. Bründermann, N. S. Yadavalli, S. Santer, and M. Havenith
   Soft Matter **10**, 1544–1554 (2014) – DOI: 10.1039/C3SM51787J

5. **Neutron reflectivity characterization of the diffuse layer at metal-polymer interface**
   N. S. Yadavalli, J.-F. Moulin, D. Korolkov, M. Krutyeva and S. Santer
   MLZ Annual report: Soft matter, 54 (2013) – *Scientific Highlight*

6. **Conductivity behaviour of very thin gold films ruptured by mass transport in photosensitive polymer film**
   F. Linde, N. S. Yadavalli, and S. Santer
   Appl. Phys. Lett. **103**, 253101 (2013) – DOI: 10.1063/1.4850595

7. **Structuring of photosensitive material below diffraction limit using far field irradiation**
   N. S. Yadavalli, M. Saphiannikova, N. Lomadze, L. M. Goldenberg, and S. Santer
   Appl. Phys. A **113**, 263–272 (2013) – DOI: 10.1007/s00339-013-7945-3

8. **Soft matter beats hard matter: rupturing of thin metallic films induced by mass transport in photosensitive polymer films**
   <u>N. S. Yadavalli</u>, F. Linde, A. Kopyshev and S. Santer
   ACS Appl. Mater. Interfaces **5**, 7743–7747 (2013) – DOI: 10.1021/am400682w

9. ***In-situ* atomic force microscopy study of the mechanism of surface relief grating formation in photosensitive polymer films**
   <u>N. S. Yadavalli</u> and S. Santer
   J. Appl. Phys. **113**, 224304 (2013) – DOI: 10.1063/1.4809640

10. **Rupturing of thin metallic films – A method to probe the nanoscale molecular forces induced by mass transport in photosensitive polymer films**
    <u>N. S. Yadavalli</u> and S. Santer
    ACS Division of Polymeric Materials: Science & Engineering, **107**, 213 (2012)
    – ISBN: 9781622762071

Submitted for Publication

11. **Graphene as nano-sized optical strain gauge for polymer surface relief gratings**
    G. Di Florio, E. Bründermann, <u>N. S. Yadavalli</u>, S. Santer, and M. Havenith

Manuscripts in preparation

12. **Controlled opto-mechanical stresses in metallised photosensitive polymer films using ±45º interference pattern**
    <u>N. S. Yadavalli</u> and S. Santer

Poster Presentations

6 posters are presented in various international conferences

Abstract

When azobenzene-modified photosensitive polymer films are irradiated with light interference patterns, topographic variations in the film develop that follow the $\vec{E}$-field vector distribution resulting in the formation of surface relief grating (SRG). The exact correspondence of the $\vec{E}$-field vector orientation in interference pattern in relation to the presence of local topographic minima or maxima of SRG is in general difficult to determine. In my thesis, we have established a systematic procedure to accomplish the correlation between different interference patterns and the topography of SRG. For this, we devise a new setup combining an atomic force microscope and a two-beam interferometer (IIAFM). With this set-up, it is possible to track the topography change *in-situ*, while at the same time changing polarization and phase of the impinging interference pattern. To validate our results, we have compared two photosensitive materials named in short as PAZO and trimer. This is the first time that an absolute correspondence between the local distribution of $\vec{E}$-field vectors of interference pattern and the local topography of the relief grating could be established exhaustively. In addition, using our IIAFM we found that for a certain polarization combination of two orthogonally polarized interfering beams namely SP ($\updownarrow$, $\leftrightarrow$) interference pattern, the topography forms SRG with only half the period of the interference patterns. Exploiting this phenomenon we are able to fabricate surface relief structures below diffraction limit with characteristic features measuring only 140 nm, by using far field optics with a wavelength of 491 nm.

We have also probed for the stresses induced during the polymer mass transport by placing an ultra-thin gold film on top (5–30 nm). During irradiation, the metal film not only deforms along with the SRG formation, but ruptures in regular and complex manner. The morphology of the cracks differs strongly depending on the $\vec{E}$-field distribution in the interference pattern even when the magnitude and the kinetic of the strain are kept constant. This implies a complex local distribution of the opto-mechanical stress along the topography grating. The neutron reflectivity measurements of the metal/polymer interface indicate the penetration of metal layer within the polymer resulting in the formation of bonding layer that confirms the transduction of light induced stresses in the polymer layer to a metal film.

This page is intentionally left blank

Zusammenfassung

Azobenzolhaltige Polymere gehören zu einer Klasse funktionaler Materialien, bei denen durch ein äußeres Strahlungsfeld eine starke mechanische Reaktion ausgelöst werden kann. Durch die Bindung an das Polymerrückgrat können die Azobenzole, die unter UV-Belichtung eine Photoisomerisierung ausführen, was zum Teil drastische Effekte zur Folge hat. Unter Belichtung mit Intensitätsmustern, d.h. mit räumlich variierender Verteilung der Polarisation oder der Intensität des einfallenden Lichts verändert sich die Topographie der azobenzolhaltigen Filme, was zur Bildung von Oberflächengittern (engl. Surface Relief Gratings, SRG) führt.

In dieser Arbeit wurde eine neue Methode vorgeschlagen, bei der das Verhalten elastischer/morphologischer Eigenschaften unter verschiedenen Belichtungsbedingungen, d.h. mit unterschiedlicher Verteilung der Polarisation und der Intensität in situ lokal als Funktion der Position entlang der SRG aufgenommen werden kann. Außerdem wurde hier vorgeschlagen, opto-mechanische Spannungen, die innerhalb der photosensitiven Polymerfilme während der Belichtung entstehen, mit Hilfe dünner aufgebrachter metallischen Schichten abzubilden und zu analysieren.

This page is intentionally left blank

Table of Contents

Abbreviations and Symbols

SRG   – Surface Relief Grating

IP   – Interference pattern

IIP   – Intensity interference pattern

PIP   – Polarization interference pattern

I – Intensity

z – Film thickness

D   – Periodicity of interference pattern

d   – Polymer grating periodicity

h   – SRG height (the vertical distance between grating maxima to minima)

SS   – IP with two vertical linearly polarized beams (↕, ↕)

PP   – IP with two horizontal linearly polarized beams (↔, ↔)

‡45° – IP with two +45° linearly polarized beams (↗, ↗)

±45° – IP with two orthogonal 45° linearly polarized beams (↗, ↘)

SP   – IP with two orthogonal linearly polarized beams (↕, ↔)

LL   – IP with two left circularly polarized beams (↺↺)

RR   – IP with two left circularly polarized beams (↻↻)

RL   – IP with two left orthogonal circularly polarized beams (↻↺)

PAZO –   (poly{1-[4-(3-carboxy-4-hydroxyphenylazo)benzenesulfonamido]-1,2-ethanediyl,sodiumsalt})

Trimer– molecular glass consisting of three connected azobenzene units to core benzene ring

IIAFM – *In-situ* Interferometric Atomic Force Microscopy

This page is intentionally left blank

1

Introduction

Azobenzene containing photosensitive polymers are among the most widely studied photochromic materials in the past few decades due to their low cost in synthesis, functional design, and demanding applications in optoelectronics industry, mainly for reversible data storage.[1,2] In addition, the photo-controllability of azobenzene chromophores are being researched intensely for applications in various other disciplines such as micro- and nanofabrication technologies,[3] photonic crystals,[4] plasmonics,[5,6] and biology. Here, we present a brief account on how the azobenzene containing materials are being applied in some of these disciplines to harness their unique photo-response, *viz.* photomechanical effects, photoinduced chirality, photoinduced self-organization, and relief formation.

1.1.   Azobenzene polymers as photo-actuators and photo-manipulators

In azobenzene containing materials, especially thin films, the macroscopic photoinduced deformations takes place due to the microscopic change in the molecular level confirmations. These microscopic changes involve the transduction of optical energy into a mechanical deformation in photosensitive materials, also known as photomechanical effects. Recently, Akira Emoto *et al* (2012) published an up to date review on the advances in various research fields utilizing the photomechanical effects of azobenzene chromophores.[7] In their report, two kinds of phenomena are detailed namely photo-actuation and photo-manipulation.

The photo-actuation phenomenon demonstrates a controlled photoinduced expansion, contraction and bending of an azobenzene containing elastomer. The direction of bending is also proven to be possible in translational and rotational motions.[8] Applications being developed using the photo-actuation phenomena are an artificially driven muscle, optical plastic motor and photo-switchable molecular machines to lift cargo.[9,10]

1

The photo-manipulation phenomenon demonstrates the controlled motion of nanoscopic objects on the reverse configurable azobenzene polymer surface topography. This method is demonstrated by the author of current doctoral thesis in past, utilizing the surface plasmon based reversible nanostructuring of azobenzene containing polymer film topography to displace the nano-objects.[11,12] In other interesting experiments, Ichimura *et al* (2001) demonstrated the optical control of water droplet on a substrate whose surface is functionalized by an azobenzene containing calix-resorcinarene derivative, utilizing the reversible wettability change of the film surface through photo-isomerization of the azobenzene chromophores. [13] There are many other reports on the photoinduced controlled motion of the nano-objects using the azobenzene polymer films as reconfigurable carpets.[14,15,16]

1.2. Azobenzene polymers in biological systems

Usage of azobenzene polymers is already spread to various branches of biology. For instance, recently in our group several azobenzene containing surfactants are developed for DNA compaction targeting the applications in drug delivery and gene therapy.[17,18,19] Engineering of biological membranes as light-gated ion channels using photo-switching of azobenzene chromophores is an another interesting application being developed actively for the past decade.[20] In a recent review published by group of C. J. Barrett (McGill University, Canada), many other applications of azobenzene containing polymers as an interface with biology are discussed.[21]

Other details of ongoing research and development of applications based upon the azobenzene properties such as photoinduced chirality and photoinduced self-organization could be found in the review of A. Emoto *et al* [8].

1.3. Azobenzene polymers in relief formation

Despite a rapid growth in application of azobenzene containing polymers, fundamentals of various molecular motions originated due to the reversible *cis-trans* photo-isomerization of chromophores is not yet clearly understood. Among the many unexpected physical phenomena related to the molecular motions in azo-modified polymers is the formation of so-called surface relief gratings (SRG) upon the irradiation with an interference pattern.[22] The phenomenon of highly periodic and large amplitude surface relief grating (SRG) formation was first observed in 1995 by two individual groups during their experiments on holographic recording in azopolymer films[23,24]. Ever since the first observation of SRG formation, novel and highly efficient azobenzene containing photosensitive polymers are being synthesized to test the SRG formation efficiency for specific

applications in optical storage, non-linear optics, thin-film optoelectronics, the design of diffractive optical elements, in plasmonics and trapping of light in solar cells, and in many more applications.[25,26,27,28]. Moreover, the optically inscribed SRGs in azobenzene containing polymer films are being studied intensely over a decade due to an unique possibility of structuring the glassy state photosensitive polymer film with highly periodic nano- and micro-sized patterns in one step process at room temperature.[29,30,31] Thus, the process of SRG formation is considered to be a promising alternative to the traditional multistep lithographic techniques[32,33,34] and laser ablation method[35].

The process of SRG formation depends on many parameters such as irradiation wavelength and intensity, chemical nature and molecular weight of the polymer, the content of photosensitive azobenzene groups and the way they are attached to the polymer. In the past decade many theoretical models are proposed based upon the various aspects of surface relief formation in photosensitive polymer film *viz.*, molecular mass transport, gradient of light intensity, pressure, surface tension, molecular reorientation, change in free volume, azobenzene electric dipole interaction with outer electric field, diffusion of azobenzene chromophores from higher to lower isomerization rate etc.[36,37,38,39,40,41,42,43] An overview of all these theoretical models could also be found in the previous dissertations.[44,45,46]

Despite major endeavours to understand the SRG formation phenomenon in photosensitive polymer films, there is no unified concept yet, and many aspects of the SRG formation are still remain unknown. Some of the puzzling questions include,

  i. *How does the topography extrema, i.e. maxima and minima in a relief grating formed, correlate with the distribution of electric field vector with respect to the variation in the intensity- and/or variation in the polarization across the interference pattern.*

Conventionally, the surface relief grating formation (SRG) in photosensitive material using two-beam interferometry and the associated surface relief relaxation[47,48] or photo-induced erasure[49] effects are analysed using the diffraction efficiency method with a linearly or circularly polarized probe beam during the irradiation. Afterwards AFM imaging of the final polymer topography before and after the irradiation process is applied.[50,51,52] The diffraction efficiency method probes for the induced birefringence in the optically anisotropic photosensitive material. However, it has disadvantage to probe the changes in the polymer topography in real time.

In the recent years, attempts were made to connect the SNOM[53] or confocal Raman microscopy[54] with a two beam interferometric optical setup to study the molecular orientation (distribution of chromophores) in the polymer grating and thereby probing the formation mechanism of SRG using different interference patterns. These methods are quite complex and sensitive to the average molecular orientations through the spectral measurements. Observing the changes in polymer topography and the surface relief formation mechanism for all different interference patterns is in general very tedious.

  ii. The origin and the strength of the driving force that can induce such significant deformation of a glassy polymer film at room temperature in air.

Azobenzene containing photosensitive polymer molecules tend to orient themselves perpendicular to the orientation of linear $\vec{E}$-field vector[55,56] and mass transports[57,58] from surface relief grating minima towards maxima in an organized fashion depending upon the intensity or the polarization modulation in the applied interference pattern. This initiation of material flow by absorption of light occurs at room temperature in air, i.e. in a glassy state when the polymer is supposed to be solid-like.

It is known that in order to deform a glassy polymer film far below its glass transition temperature one should apply stresses larger than the yield point of the polymer. For many polymers in practical use it can be located around 50 MPa. This implies that a mere photo-induced process can generate significant mechanical stresses. Viscoplastic theory, for instance, would imply that in order to cause polymer mass transport well below the glass transition temperature, the light-induced stress within the polymer must be far above the yield point of the azobenzene polymer.[59] A theoretical account of SRG formation in non-covalently attached films proposed by Saphianikova *et al*. gives an estimation of about 100 MPa for the striction stress that appears under homogeneous illumination, [42,60] far above the yield stress for conventional polymers uniaxially stretched at small strain rates.[61]

In fact, the forces are so strong that covalent bonds can be broken. Recent research on photosensitive polymer brushes reveals that during SRG formation, covalently tethered polymer chains (decorated with azobenzene containing side chains) are ruptured locally from the areas of receding polymer material.[62,63] The average strength of C-C covalent bond is about 2 nN, the corresponding stress needed for the scission of a polymer chain in a brush of grafting density $1nm^{-2}$ (one chain per nm^2) should therefore be about 2 GPa. A similar value was inferred in the group of Prof. C. J. Barrett in a different context, using a

sophisticated experimental setup where the polymer film was put under uniaxial stress and the change in thickness of the film was detected during irradiation with UV light as a function of applied stress. It was found that up to a level of 1.2 GPa the photo-isomerisation of the azobenzene groups still leads to a noticeable change in polymer thickness.[64] The above mentioned estimations indicate that forces inscribing a topographical pattern into a thin film should be fairly large, but are hard to assess directly.

Further, we have discussed in section 1.1 and 1.2 that the focus on designing and synthesis of novel azobenzene-containing materials is shifted from data storage towards harnessing their photoinduced mechanical effects, for instance applications in artificial muscles and deformable electronics. To achieve it, one needs to have an in-depth understanding on photoinduced motions taking place in azobenzene materials during light irradiation. The photoinduced motion is generally presumed to be a response associated with *cis-trans* isomerisation and molecular re-orientation of azobenzenes to the polarization of light. To verify this presumption experimentally and to check efficiency of novel photosensitive materials, the phenomenon of surface relief grating (SRG) formation is being used as an important tool. Despite a decade spanning efforts, the fundamental processes taking place during SRG formation under irradiation with different light interference patterns still remains a puzzle.

In my thesis, I have focused on developing reliable experimental methods to deal with the above discussed challenges of studying the SRG formation.

This page is intentionally left blank

"We can't solve problems by using the same kind of thinking we used when we created them."

– Albert Einstein

2

Objectives of the thesis

The observation of molecular level processes taking place during the surface relief grating (SRG) formation in photosensitive materials is largely limited due to deficiency in experimental methods. A frequently used diffraction efficiency method to probe the rate of induced anisotropy during SRG inscription in polymer films is not sufficient to observe all the *in-situ* microscopic processes. Moreover, in the past few decades the design and synthesis of novel photosensitive materials is carried out based up on the observed efficiency of photosensitive material during SRG inscription. Thus the process of engineering novel and highly efficient materials appears to be random.

In the current thesis, I am proposing a novel and reliable experimental method to record the change in the topography features of polymer film *in-situ* during the SRG formation. To achieve it, I intend to connect an Atomic Force Microscope (AFM) with the optical setup used for SRG inscription. Following a successful *in-situ* observation of SRG topography changes, it should be possible to correlate the SRG topography extrema (i.e. maxima and minima) with the associated interference patterns. The knowledge of correlation between SRG topography and the interference patterns will be of great help to refine all the existing

theoretical models based up on the behaviour of azobenzene chromophores in presence of the combination of different electric field vectors.

Another important objective is to device an experimental method to probe the localized stresses developed in the polymer film during the SRG formation (photomechanical effects). To achieve it, we have considered depositing a thin metal film on the polymer topography and observing the deformations that may takes place in the metal film during SRG formation (Fig 2.1). Presuming that the stresses developed during the SRG formation are considerably large, ultrathin metal films might respond to local stress distributions, there by facilitating the estimation of localized stresses.
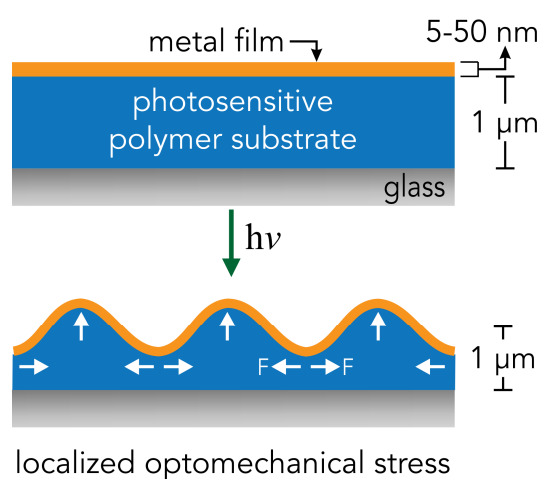
Fig. 2.1. Schematic representation method used to probe the opto-mechanical stresses induced during the SRG formation in photosensitive films.

<div style="text-align: right; font-size: 3em;">3</div>

Experimental Setup and Materials

3.1. Two-Beam Interferometry

Formation of surface relief grating involves the exposure of photosensitive material/polymer film to a light interference pattern and is generally achieved by employing a simple two-beam interferometer in different configurations as shown in Fig 3.1. The principle of interferometry involves a two or more propagating coherent electromagnetic waves of same frequency to interfere each other and the resulting pattern is determined by the phase relations between them. Waves that are in phase undergo constructive interference and waves that are out of phase results in destructive interference.[65]
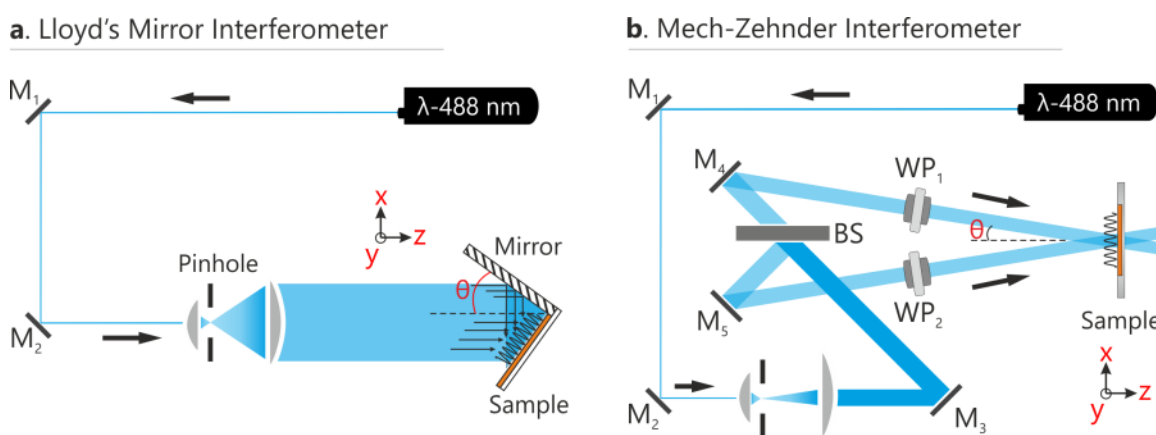
Fig. 3.1. Schemes of general two-beam interferometers used for grating inscription experiments. (a) Lloyd's mirror interferometer with a wavefront division principle. (b) Simplified Mech-Zehnder interferometer with an amplitude division principle. M_1, M_2, M_3, M_4 and M_5 – Mirrors; WP_1 and WP_2 – combination of waveplates and/or polarizers; BS – Beam splitter.

To achieve coherent interfering beams, it is appropriate to choose the waves obtained from single source (monochromatic light). Depending upon the method of achieving the two interfering beams from same source, the interferometers are categorized into two types' *viz.*, wavefront division and amplitude division. An interferometer with wavefront division principle (Lloyd's mirror) is shown in Fig. 3.1a. A Lloyd's mirror interferometer uses single source beam, where one part of the beam from the source interfere with another part of the same beam reflected from a mirror at near-grazing incidence. In the amplitude division principle, the two beams are obtained from a single source by division of the amplitude over the section of the wavefront using a beam splitter as shown in Fig. 3.1b.

If these two beams (plane waves) with amplitudes A₁ and A₂ and the same frequency are propagating in the same direction and polarized in the same plane, for example a vertical linear polarized ($\updownarrow$) and are superposed at an arbitrary point 'O' on a screen as shown in Fig. 3.2a, then the total $\vec{E}$-field and intensity at this point 'O' are given by

$$E = E_1 + E_2$$

$$I = |A_1 + A_2|^2 = A_1^2 + A_2^2 + 2A_1A_2 \tag{3.1}$$

$$= I_1 + I_2 + 2\sqrt{I_1 I_2} \, \cos(\delta_2 - \delta_1)$$

Where I_1 and I_2 are the intensities at arbitrary point 'O' and $\delta = \delta_2 - \delta_1$ is the phase difference between interfering beams. At point 'O' Constructive interference takes place when the beams are in phase (δ=0) and destructive interference occurs if the beams are out of phase by half a period (δ=π).

When two beams meet each other, the resultant "Interference Pattern" (IP) in the region of interference is presented in Fig. 3.2b. Vectorial addition of two coherent beams results in a total field in the superposition region whose intensity and polarization state can be different from either of the interfering beams depending upon the individual polarization of the interfering beams and is modulated along the grating vector. The spatial periodicity (D) of distributed electric field vectors along the grating vector (Fig. 3.2b) is expressed in terms of half of the angle between the two interfering beams (i.e., θ) and the wavelength of the incident beams,

$$D = \frac{\lambda}{2 \sin \theta} \qquad\qquad (\lambda - \text{wavelength}) \tag{3.2}$$

In the past decade, several detailed reports are published on the account of different interference patterns obtained by two linearly (e.g.↕) or circularly (↺) polarized interfering beams[66,67]. A brief discussion of the relevant basics of light polarization and the interference patterns (IP) used throughout the current investigation is presented in the following.
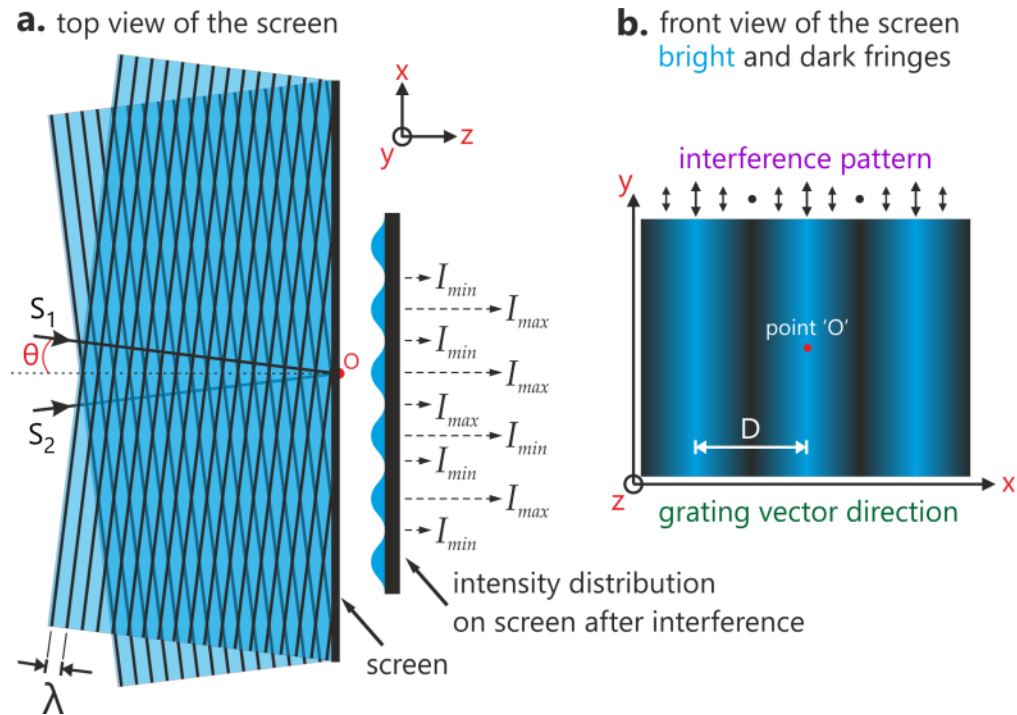
Fig. 3.2. Schematic representation of two beam interference on screen. (a) Top view of the screen: Two plane waves S$_1$ and S$_2$, interfering each other on the screen. (b) Front view of the screen: The bright and dark fringes in XY-plane with the associated field vector distribution along the grating vector as a result of interference is presented. 'D' – The spatial periodicity in the interference pattern.

3.2. Polarization of Monochromatic Light

The polarization state of a monochromatic light beam (plane wave) describes the relative magnitude, direction, and phase of the electric part of the wave. In general, a light wave propagating with two orthogonal fields in the z-direction is given by

$$\vec{E}_x(z,t) = E_{0x}\cos(kz - \omega t)\vec{x}$$

$$\vec{E}_y(z,t) = E_{0y}\cos(kz - \omega t + \delta)\vec{y} \tag{3.3}$$

Here $\vec{x}$ and $\vec{y}$ are unit vectors in the x- and y- directions. The relative phase difference between the two components is denoted by 'δ'.

3.2.1. Linear Polarization

If there is no amplitude in the x-component ($E_{0x} = 0$), then only y-component exists, such wave is known as vertical linearly polarized (VLP:↕) or *s- polarized* in YZ-plane as shown in Fig. 3.3a and is given by

$$\vec{E}_y(z,t) = E_{0y}\cos(kz - \omega t + \delta)\vec{y} \tag{3.4}$$

Here, ω is the angular frequency of the light wave ($\omega = 2\pi v$) and k is the wavenumber ($2\pi/\lambda$). E_{0y} is the amplitude of the wave and δ is the arbitrary phase.

a. Linear Vertical Polarization ($E_{0x}=0$)

b. Linear Horizontal Polarization ($E_{0y}=0$)

c. Linear +45° Polarization ($E_{0x}=E_{0y}=E_0$, $\delta=0$)

d. Linear -45° Polarization ($E_{0x}=E_{0y}=E_0$, $\delta=\pi$)
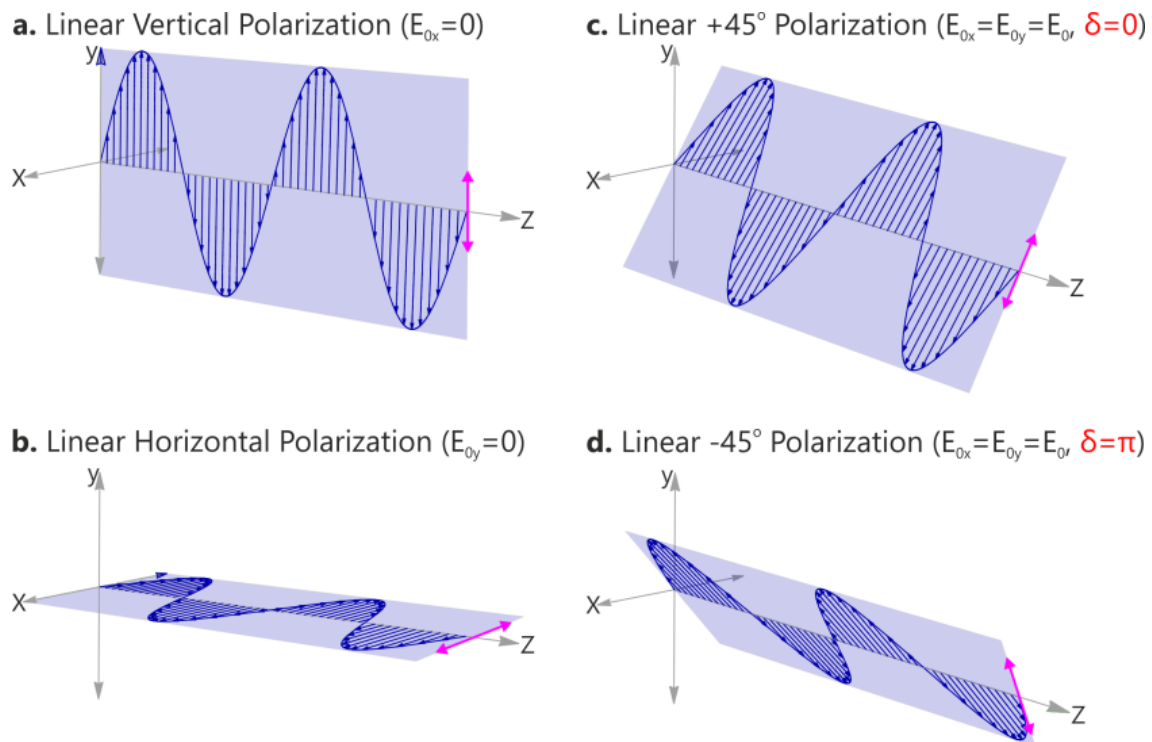
Fig. 3.3. Scheme of different linear polarization states used throughout the current study. The pink arrows represent the polarization direction in XY-plane.

In contrast, if the y-component is zero ($E_{0y} = 0$), and with only x-component the wave is represented as horizontal linearly polarized light (HLP: ↔) or *p- polarized* in XY-plane as shown in Fig. 3.3b. If there is no phase difference between the components (i.e., δ=0) and the x- and y- components are equal ($E_{0x}=E_{0y}$), then $E_x = E_y$ and the resultant wave is represented as +45° linear polarization (+45°: ↗) and with a phase difference of π and $E_x = E_y$, the resultant wave is -45° linear polarized (-45°: ↘) as shown in Fig 3.3(c, d). The linear polarizations are in general given by

$$\vec{E} = \vec{E}_x + \vec{E}_y = (E_{0x}\vec{x} + E_{0y}\vec{y})\,cos(kz - \omega t + \delta) \tag{3.5}$$

Here, the phase difference (δ) is assumed to be 0 or π. However, with δ other than 0 or π, we will obtain either elliptical or circular polarization.

3.2.2. Elliptical Polarization

If the amplitudes of two fields are not equal ($E_{0x} \neq E_{0y}$) and the phase difference is π/2, the tip of the electric field vector from the perspective of the source traces an ellipse giving elliptical polarization and equation 3.5 could be converted using trigonometric identities as follows

$$\left(\frac{E_x}{E_{0x}}\right)^2 + \left(\frac{E_y}{E_{0y}}\right)^2 - 2\frac{E_x}{E_{0x}}\frac{E_y}{E_{0y}}\cos \delta = \sin^2 \delta \quad \text{(equation of an ellipse)} \tag{3.6}$$

An ellipse can be represented by four quantities such as size of the minor and major axes, orientation angle and clockwise (CW) or anticlockwise (ACW).

3.2.3. Circular Polarization

Circular polarization is a special case of an elliptical polarization. Considering a simple plane wave as described in the equation 3.2, if the phase difference (δ) between the components is π/2 and $E_{0x}=E_{0y}$, then the resultant wave is circularly polarized as shown in Fig. 3.4 and equation 3.6 is written as,

$$\left(\frac{E_x}{E_{0x}}\right)^2 + \left(\frac{E_y}{E_{0y}}\right)^2 = 1 \quad \text{(equation of a circle)} \tag{3.7}$$

The left/right handed notation is used throughout the current study to describe the circularly polarized interfering beams. The handedness is determined by the direction of the electric field vector rotation from the point of view of the source.

- *Left Hand Circular Polarization* (LCP – ↺): If the phase difference between the components is ($\pi/2$) + 2mπ, where m is either positive or negative integer or zero

$$\vec{E} = E_{0x} \cos(kz - \omega t)\, \vec{x} + E_{0y} \cos\left(kz - \omega t + \frac{\pi}{2}\right) \vec{y}$$
$$= E_0[\cos(kz - \omega t)\, \vec{x} + \sin(kz - \omega t)\, \vec{y}] \tag{3.8}$$

- *Right Hand Circular Polarization* (RCP – ↻): If the x-component is lagging ($\pi/2$) + 2mπ in phase

$$\vec{E} = E_{0x} \cos(kz - \omega t)\, \vec{x} + E_{0y} \cos\left(kz - \omega t - \frac{\pi}{2}\right) \vec{y}$$
$$= E_0[\cos(kz - \omega t)\, \vec{x} - \sin(kz - \omega t)\, \vec{y}] \tag{3.9}$$
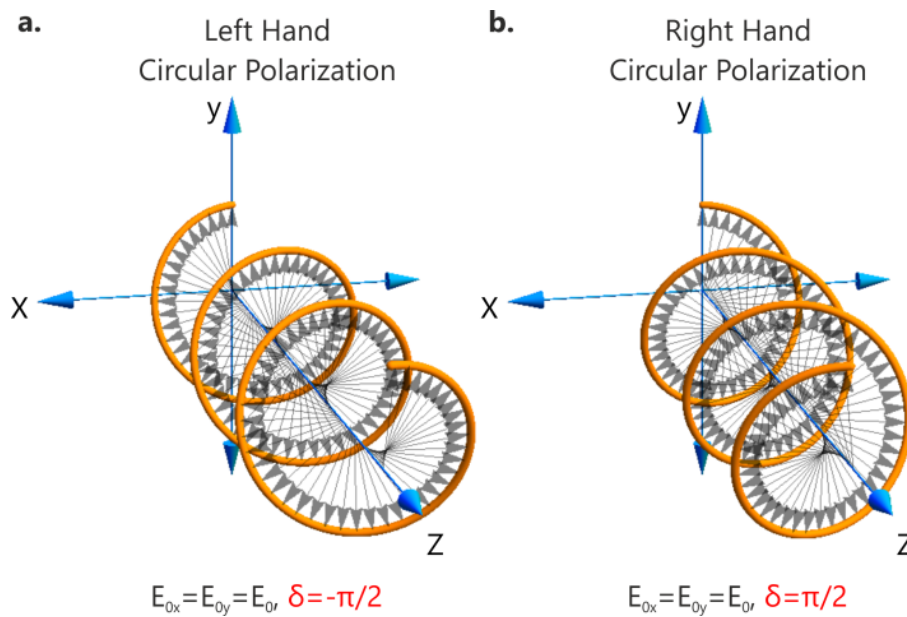
Fig. 3.4. Schematic representation of left (a) and right (b) hand circular polarization state.

3.2.4. Jones Vector

Another simple method to express the polarization of monochromatic light is through Jones vector. Equation 3.2 could be rewritten in complex exponential form as

$$\vec{E} = \begin{pmatrix} E_x \\ E_y \end{pmatrix} = \begin{pmatrix} E_{0x} \\ E_{0y}e^{i\delta} \end{pmatrix} \tag{3.10}$$

In case of linearly polarized light at angle α, the jones vector is written as

$l_\alpha = \begin{pmatrix} \cos\alpha \\ \sin\alpha \end{pmatrix}$ and the angle $\alpha = \tan^{-1}\left(\frac{E_y}{E_x}\right)$.

Similarly, for the circularly polarized light, the jones vector is $\begin{pmatrix} \cos\alpha \\ \pm i\sin\alpha \end{pmatrix}$. Here, the positive sign indicates the right circular polarization and the negative sign indicates the left circular polarization.

The normalized Jones vectors for the polarizations used throughout the current investigation are as follows

Vertical linear polarization: $\begin{pmatrix} 0 \\ 1 \end{pmatrix}$ Horizontal linear polarization: $\begin{pmatrix} 1 \\ 0 \end{pmatrix}$

Linear +45º polarization: $\frac{1}{\sqrt{2}}\begin{pmatrix} 1 \\ 1 \end{pmatrix}$ Linear -45º polarization: $\frac{1}{\sqrt{2}}\begin{pmatrix} 1 \\ -1 \end{pmatrix}$

Left circular polarization: $\frac{1}{\sqrt{2}}\begin{pmatrix} i \\ 1 \end{pmatrix}$ Right circular polarization: $\frac{1}{\sqrt{2}}\begin{pmatrix} 1 \\ i \end{pmatrix}$

3.3. Interference Patterns

In section 3.1, we have discussed that when two coherent beams of arbitrary polarization state are made to interfere, the intensity modulation and/or state of polarization of the total field changes spatially in its magnitude and direction along the grating vector (X-axis in Fig 3.2b) depending upon the phase variations between the two beams. In this section, we are discussing specific interference patterns used throughout current study and also to facilitate the forthcoming discussion of surface relief grating formation in polymer films using these interference patterns (IP), we have considered separating them into two categories as follows

1. Intensity modulated Interference Patterns (or) in short "Intensity Interference Patterns (IIPs)" and
2. Polarization modulated Interference Patterns (or) in short "Polarization Interference Patterns (PIPs).

The intensity interference patterns (IIPs) are obtained by the superposition of two linearly polarized beams with parallel field vectors (*viz., s- : s-; p- : p-; +45° : +45°*), or two right- or two left circularly polarized beams (*viz., RCP : RCP; LCP : LCP*). The polarization interference patterns (PIPs) can be generated by superposition of two linearly polarized beams in orthogonal condition (*viz., s- : p- ; +45° : -45°*) or by interfering right- and left circularly polarized beams (*RCP : LCP*).

For all the interference patterns in following sections 3.3.1 and 3.3.2, we have assumed that the angle of interfering beams is small (paraxial approximation).

3.3.1. Intensity Interference Patterns (IIPs)

In case of all the intensity interference patterns (IIPs) obtained with small interference angle, there is an intensity modulation along appropriate axis depending upon the polarization state of the interfering beams and the polarization state of the interference pattern remains constant.

i)   *s- : s-* **polarization (or) SS**

In this combination, two linearly polarized beams in vertical direction (*s-polarized*) parallel to the Y-axis and perpendicular to the plane of incidence (Fig 3.5) with equal intensities are made to interfere, and the resulting interference pattern or the resultant electric field has only intensity modulation along X-axis, i.e., perpendicular to the grating vector while the polarization state remains

constant over the entire interference region as shown in Table 3.1. This interference pattern is denoted in short for convenience as 'SS'.
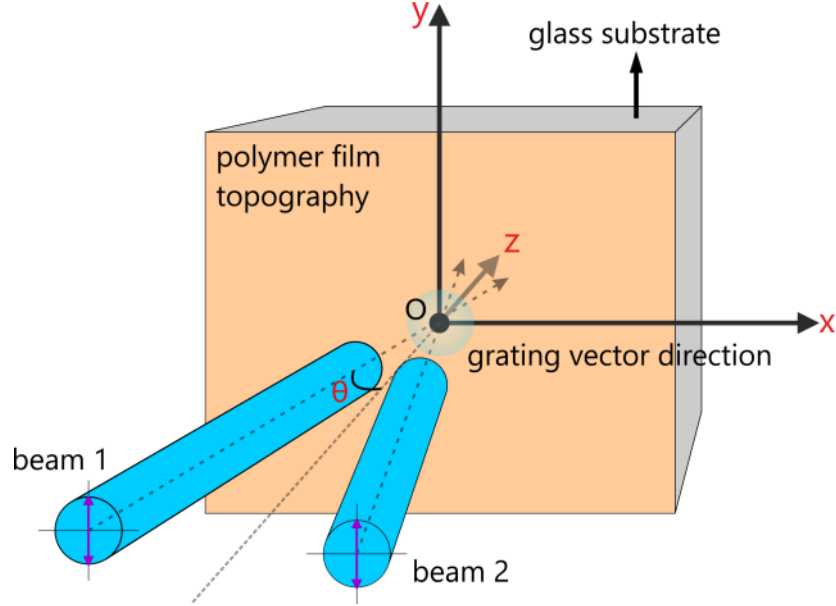
Fig. 3.5. Scheme of two-beam interference. XZ is the plane of incidence and θ is half of the interference angle between two beams. X-axis represents the grating vector direction.

Considering the two plane waves of vertical linear polarized (↕) interfere

$$\vec{E}_1 = E_0 \cos(\omega t - k r_1)\, \vec{y} \; and$$

$$\vec{E}_2 = E_0 \cos(\omega t - k r_2)\, \vec{y}$$

Where, $r_1 = \dfrac{z}{(\cos\theta + x\sin\theta)}$ and $r_2 = \dfrac{z}{(\cos\theta - x\sin\theta)}$

The resulting SS interference pattern is given by

$$\vec{E}_{ss} = \vec{E}_1 + \vec{E}_2 = E_0(\cos(\omega t - k_z z - k_x x) + \cos(\omega t - k_z z + k_x x))\vec{y}$$

$$= 2E_0 \cos(\omega t - k_z z) \cos(k_x x)\vec{y}$$

(3.11)

Here, $k = \dfrac{2\pi}{\lambda}$, $k_x = \dfrac{\pi}{D}$ and $k_z = \dfrac{k}{\cos\theta}$

Polarization of interfering beams				Spatial distribution of polarization along grating vector in the interference pattern (x-axis)									Light Intensity along the grating
beam 1		beam 2		0	π/4	π/2	3π/4	π	5π/4	3π/2	7π/4	2π	
				0	D/8	D/4	3D/8	D/2	5D/8	3D/4	7D/8	D	
S	↑	S	↑	↕	↕	↕	↨	•	↨	↕	↕	↕	$2I\cos^2\delta/2$
S	↑	S	↓	•	↨	↕	↕	↕	↕	↕	↨	•	$2I\sin^2\delta/2$

Table. 3.1. The total electric field vector distribution for the SS interference pattern obtained by two linear vertical polarized interfering beams. The effect of phase difference between beams on the position of maximum and minimum intensity regions also presented.

It is important to note the effect of the phase difference between the interfering beams on the resultant interference pattern. The last two rows of the Table 3.1 describing the effect of phase condition between interfered beams. If the two beams interfere with a phase difference of δ=π (i.e., half a period), the resulting interference pattern also shifts by half a period along the grating vector and this dependency of the phase difference between interfering beams is valid for all the combinations of linearly polarized beams in both the parallel and orthogonal field conditions.

ii)   *p- : p-* **polarization (or) PP**

In this combination, two horizontal linear polarized beams (*p-polarized*) with equal intensities (Fig 3.3b) are made to interfere and the resulting field is modulated along the X- direction as shown in Table 3.2 and considering two *p-polarized* plane waves,

$$\vec{E}_1 = E_0\cos(\omega t - kr_1)\cos\theta\,\vec{x} + E_0\cos(\omega t - kr_1)\sin\theta\,\vec{z}\ and$$

$$\vec{E}_2 = E_0\cos(\omega t - kr_2)\cos\theta\,\vec{x} + E_0\cos(\omega t - kr_2)\sin\theta\,\vec{z}$$

The resulting PP interference pattern is given by

$$\vec{E}_{pp,x} = E_0(\cos(\omega t - k_z z - k_x x)\cos\theta\,\vec{x} + \cos(\omega t - k_z z + k_x x))\cos\theta\,\vec{x}$$

(3.12)

$$= 2E_0\cos(\omega t - k_z z)\cos(k_x x)\cos\theta$$

$$\vec{E}_{pp,z} = E_0(\cos(\omega t - k_z z - k_x x)\sin\theta\,\vec{z} + \cos(\omega t - k_z z + k_x x))\sin\theta\,\vec{z}$$

$$= 2E_0\cos(\omega t - k_z z)\cos(k_x x)\sin\theta$$

(3.13)

If the interference angle θ is small then $\sin\theta \approx 0$ and we could neglect the projection of electric field vector in z-direction (equation 3.13) perpendicular to the XY-plane. However, at large incidence angle the resulting interference pattern could become very complicated.

Polarization of interfering beams				Spatial distribution of polarization along grating vector in the interference pattern (x-axis)									Light Intensity along the grating
beam 1		beam 2		0	π/4	π/2	3π/4	π	5π/4	3π/2	7π/4	2π	
				0	D/8	D/4	3D/8	D/2	5D/8	3D/4	7D/8	D	
P	↔	P	↔	↔	↔	↔	↔	•	↔	↔	↔	↔	$2I\cos^2\delta/2$

Table. 3.2. The total electric field vector distribution for the PP interference pattern obtained by two linear horizontally polarized interfering beams.

Polarization of interfering beams				Spatial distribution of polarization along grating vector in the interference pattern (x-axis)									Light Intensity along the grating
beam 1		beam 2		0	π/4	π/2	3π/4	π	5π/4	3π/2	7π/4	2π	
				0	D/8	D/4	3D/8	D/2	5D/8	3D/4	7D/8	D	
+45°	↗	+45°	↗	↗	↗	↗	↗	•	↗	↗	↗	↗	$2I\cos^2\delta/2$

Table. 3.3. The total electric field vector distribution for the ‡45° interference pattern obtained by two linear +45° polarized interfering beams.

iii) *+45° : +45°* **polarization (or) ‡45°**

In this combination, the electric field vectors of both the interfering beams are oriented at +45° (Fig 3.3c) with respect to Y-axis and the resulting interference pattern along the grating vector has linear polarization oriented at +45° over the
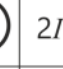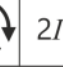
entire interference region as shown in Table 3.3. Further, similar to PP interference pattern, the intensity modulation depends on the angle of the interference. In case of small angle of interference, the interference pattern situation is similar to SS combination.

iv)   *LCP : LCP* **polarization (or) LL**

In this combination, the two interfering beams are left circularly polarized (Fig 3.4a) with rotation symmetry along the propagation axes and the resulting interference pattern remain left circularly polarized with intensity distribution along grating vector as shown in Table 3.4 (second row from the bottom). The interference pattern obtained with two left circularly polarized beams is named as 'LL' in short.

v)   *RCP : RCP* **polarization (or) RR**

Similarly, with two right circularly polarized interfering beams, the obtained interference pattern remains right circularly polarized with intensity modulation along grating vector as shown in the last row of Table 3.4. The interference pattern with two right circularly polarized beams is named as 'RR' in short.

Polarization of interfering beams				Spatial distribution of polarization along grating vector in the interference pattern (x-axis)									Light Intensity along the grating
beam 1		beam 2		0	π/4	π/2	3π/4	π	5π/4	3π/2	7π/4	2π	
				0	D/8	D/4	3D/8	D/2	5D/8	3D/4	7D/8	D	
LCP	↻	LCP	↻	↻	↻	↻	↻	•	↻	↻	↻	↻	$2I\cos^2 \delta/2$
RCP	↺	RCP	↺	↺	↺	↺	↺	•	↺	↺	↺	↺	$2I\cos^2 \delta/2$

Table. 3.4. The total electric field vector distribution for LL and RR interference patterns obtained by two left and right circularly polarized interfering beams respectively. L – Left circularly polarized; R – Right circularly polarized.

3.3.2. Polarization Interference Patterns (PIPs)

In contrast to the IIPs, the polarization interference patterns (PIPs) used in the current study has constant intensity along grating vector with polarization modulation in the interference pattern depending upon the angle of interference

and the polarization in the total electric field near the region of superposition is different from the interfering beams.

i)   *+45º : -45º polarization (or) ±45º*

In this combination, both the interfering beams have linear 45º polarization state with respect to Y-axis but orthogonal to each other (i.e., +45º and -45º; Fig 3.3c and 3.3d respectively).

Polarization of interfering beams				Spatial distribution of polarization along grating vector in the interference pattern (x-axis)									Light Intensity along the grating
beam 1		beam 2		0	π/4	π/2	3π/4	π	5π/4	3π/2	7π/4	2π	
				0	D/8	D/4	3D/8	D/2	5D/8	3D/4	7D/8	D	
+45°	↗	-45°	↘	↕	↻	↺	↺	↔	↻	↻	↻	↕	*I*

Table. 3.5. The total electric field vector distribution for the ±45º interference pattern obtained by two orthogonal linear 45º polarized interfering beams. The interference pattern has purely polarization modulation only when θ=0. For other angle (θ>0), the ±45º interference pattern has both intensity and polarization modulation.

It is important to note that the polarization of both beams is orthogonal only when interference angle between the beams is equal to zero and the resulting interference pattern has only polarization modulation with intensity remains constant across the interference region as shown in Table 3.5. It means that with θ>0, the two-beam interference pattern of ±45º combination always have both intensity and polarization modulation.

ii)   *s- : p-* **polarization (or) SP**

In this combination, the interfering beam 1 is *s-polarized* (parallel to Y-axis) and beam 2 is *p-polarized* (perpendicular to Y-axis) such that the interfering beams are orthogonal to each other. The resulting interference pattern is shown in Table 3.6.

Considering two plane waves of *s-polarized* and *p-polarized*,

$$\vec{E}_1 = E_0 \cos(\omega t - kr_1)\, \vec{y} \; and$$

$$\vec{E}_2 = E_0 \cos(\omega t - kr_2) \cos\theta\, \vec{x} + E_0 \cos(\omega t - kr_2) \sin\theta\, \vec{z}$$

For a small angle of interference, the SP interference pattern is given by

$$\vec{E}_{SP} \approx E_0 \cos(\omega t - kr_1)\, \vec{y} + E_0 \cos(\omega t - kr_2)\, \vec{x}$$

$$= \cos(\omega t - k_z z) \cos(k_x x)\,(\vec{y} + \vec{x}) + \sin(\omega t - k_z z) \sin(k_x x)\,(\vec{y} - \vec{x})$$

(3.14)

Once again, for larger angles of interference the situation is very complicated.

Polarization of interfering beams		Spatial distribution of polarization along grating vector in the interference pattern (x-axis)									Light Intensity along the grating
beam 1	beam 2	0	π/4	π/2	3π/4	π	5π/4	3π/2	7π/4	2π	
		0	D/8	D/4	3D/8	D/2	5D/8	3D/4	7D/8	D	
S ↕	P ↔	↗	↗ ↻	↻	↺	↘	↺	↻	↺	↗	*I*

Table. 3.6. The total electric field vector distribution for the SP interference pattern obtained by two orthogonal linear polarized interfering beams (beam 1 is *s-pol* and beam 2 is *p-pol*). The interference pattern has purely polarization modulation.

Polarization of interfering beams		Spatial distribution of polarization along grating vector in the interference pattern (x-axis)									Light Intensity along the grating
beam 1	beam 2	0	π/4	π/2	3π/4	π	5π/4	3π/2	7π/4	2π	
		0	D/8	D/4	3D/8	D/2	5D/8	3D/4	7D/8	D	
RCP ↻	LCP ↺	↔	↔	↗	↗	↕	↘	↘	↔	↔	*I*

Table. 3.7. The total electric field vector distribution for SP interference pattern obtained by two orthogonal linear polarized interfering beams (beam 1 is *s-pol* and beam 2 is *p-pol*). The interference pattern has purely polarization modulation.

iii)   *RCP : LCP* polarization (or) RL

In this combination, beam 1 is right circularly polarized (Fig 3.4b) and beam 2 is Left circularly polarized (Fig 3.4a) and the resulting polarization of the interference pattern depending upon the relative phase of the two interfering beams. With angle between the interfering beams is 90°, the polarization is perfectly orthogonal and the resulting interference pattern is purely polarization modulation as shown in Table 3.7.

Considering the interference of right and left circularly polarized waves,

RCP: $\vec{E}_1 = E_0 \cos(\omega t - kr_1) \cos\theta\,\vec{x} + E_0 \sin(\omega t - kr_1)\,\vec{y} - E_0 \cos(\omega t - kr_1)\sin\theta\,\vec{z}$

LCP: $\vec{E}_2 = E_0 \cos(\omega t - kr_2) \cos\theta\,\vec{x} - E_0 \sin(\omega t - kr_2)\,\vec{y} + E_0 \cos(\omega t - kr_2)\sin\theta\,\vec{z}$

For a small angle of interference, the RL interference pattern is given by

$$\vec{E}_{RL,x} = E_0(\cos(\omega t - kr_1) + \cos(\omega t - kr_2))\vec{x}$$
$$= 2\,E_0 \cos(\omega t - k_z z) \cos(k_x x)\,\vec{x}$$

(3.15)

$$\vec{E}_{RL,y} = E_0(\sin(\omega t - kr_1) - \sin(\omega t - kr_2))\vec{y}$$
$$= -2\,E_0 \cos(\omega t - k_z z) \sin(k_x x)\,\vec{y}$$

(3.16)

At x=0 we obtain a horizontal electric field vector and at x=D/2 a vertical electric field vector as shown in Table 3.7.

A complete list of all the interference patterns discussed in the section 3.3.1 and 3.3.2 are presented in Table 3.8 in two groups (IIP & PIP). It is interesting further to understand how all these different interference patterns contribute in the formation of a simple Surface Relief Grating (SRG) geometry in a photosensitive polymer film.

	Polarization of interfering beams				1	2	3	4	5	6	7	8	9	10
					Spatial distribution of polarization along grating vector in the interference pattern (x-axis)									Light Intensity along the grating
	beam 1		beam 2		0	π/4	π/2	3π/4	π	5π/4	3π/2	7π/4	2π	
					0	D/8	D/4	3D/8	D/2	5D/8	3D/4	7D/8	D	
A	Intensity interference pattern (IIP)													
1	S	↕	S	↕	↕	↕	↕	↕	•	↕	↕	↕	↕	$2I\cos^2 \delta/2$
2	P	↔	P	↔	↔	↔	↔	↔	•	↔	↔	↔	↔	$2I\cos^2 \delta/2$
3	+45°	↗	+45°	↗	↗	↗	↗	↗	•	↗	↗	↗	↗	$2I\cos^2 \delta/2$
4	L	↺	L	↺	↺	↺	↺	↺	•	↺	↺	↺	↺	$2I\cos^2 \delta/2$
5	R	↻	R	↻	↻	↻	↻	↻	•	↻	↻	↻	↻	$2I\cos^2\delta/2$
B	Polarization interference pattern (PIP)													
6	S	↕	P	↔	↗	↺	↻	↺	↘	↺	↻	↺	↗	I
7	+45°	↗	-45°	↘	↕	↺	↻	↔	↔	↺	↻	↺	↕	I
8	R	↻	L	↺	↔	↗	↗	↗	↕	↘	↘	↔	↔	I

Table. 3.8. Spatial distributions of polarizations along the grating vector of all interference patterns used in the current investigation, for small interference angle (θ). 'δ' is the phase difference between two interfering beams and is the function of position along the grating vector (X) and the grating periodicity (D). $\delta = 2\pi X/D$

3.4. *In-situ* Interferometric Atomic Force Microscopy (IIAFM)

In section 3.1 and Fig. 3.1, we have discussed briefly about two configurations of optical schemes to achieve a two-beam interferometer (*viz.*, wavefront and amplitude division). Comparing these two configurations, it is clear that the amplitude division allows more flexibility to control many experimental parameters related to SRG formation such as polarization of the interfering beams, periodicity of grating, and phase difference between the beams. Thus, throughout the current investigation we have employed a simplified Mech-Zehnder Interferometer to inscribe the SRG in photosensitive polymer film. Further to facilitate the *in-situ* observation of surface relief grating formation, we have aligned the Mech-Zehnder Interferometer with an Atomic Force Microscope as shown in Fig. 3.6.
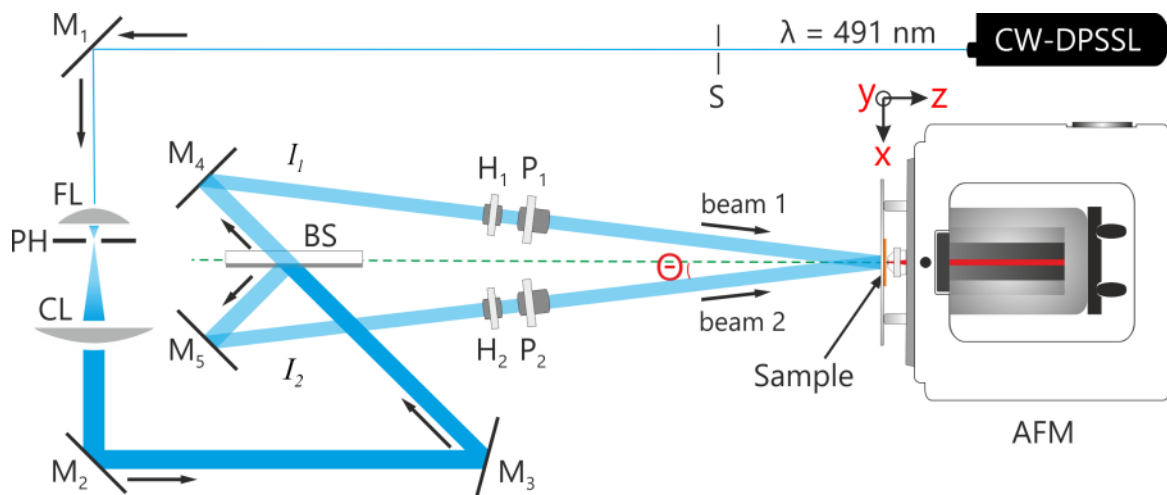
Fig. 3.6. Experimental setup for recording SRG formation: (M_1, M_2, M_3, M_4 and M_5) – mirrors; BS - beam splitter; (H_1 and H_2) - half wave plates; (P_1 and P_2) – polarizer; (I_1, I_2) – intensities of beams; S – computer controlled shutter; FL – focusing lens; PH – pinhole; CL – collimating lens; and AFM – Atomic Force Microscope.

To inscribe the surface relief in polymer film, a continuous wave-diode pumped solid state laser (CW-DPSSL) operating in a single longitudinal mode with a wavelength of 491 nm and oscillating in vertical linear polarization state (↕) is used (Cobalt Calypso™). The laser beam is spatially expanded and then collimated with a pair of focusing and collimating lenses and a pin hole. The uniform 5 mm diameter central part of collimated Gaussian beam profile is used

for interference experiments. The collimated beam is split into two parts with equal intensities using a non-polarizing beam splitter and the two beams are aligned to interfere at the polymer sample positioned with the AFM (PicoScan, Agilent, USA; see appendix A.1c) for *in-situ* measurements of the grating formation as shown in Fig. 3.6.

3.4.1. Optical scheme to achieve linearly polarized beams

During *in*-situ AFM measurements, the polarization state of each beam is controlled with a polarizer (P_1 and P_2) as shown in Fig. 3.6. Despite the beam from the laser source oscillates in vertical linear polarization state ($\updownarrow$) and the polarization state could be controlled by a half wave plate, an extra set of polarizers P_1 and P_2 are used as shown in Fig 3.6. These polarizers (P_1 and P_2) are used as optical filters to allow only required linear polarization state and blocks waves of other polarizations in both beams. Half wave plates H_1 and H_2 are placed behind the polarizers (in the path towards sample) as shown in Fig 3.6, to control the intensity of beams passing through polarizers based upon the Mauls's law ($I = I_0 \cos^2 \phi$). Using single frequency laser mode, equal intensities in the interfering beams, stable optical mounts and good control in polarization state of the beams, a fairly good fringe contrast, $\left(v = \dfrac{I_{max} - I_{min}}{I_{max} + I_{min}} \right)$ is achieved in all the intensity modulated interference patterns (IIPs). Using the optical scheme presented in Fig 3.6, we have achieved SS, PP, ‡45º (IIPs) and SP, ±45º (PIPs).

3.4.2. Optical scheme to achieve circularly polarized beams

It is well known that a linearly polarized light whose electric field is 45º to the principle axes of a quarter wave plate ($\lambda/4$) will emerge from this plate as circularly polarized light. Thus to achieve a circularly polarized beam using the linearly polarized source beams, we have added an extra set of quarter wave plates (Q_1 and Q_2) after polarizers (P_1 and P_2) as shown in Fig 3.7.

In the present study, it is important to explain comprehensively the difference between optical periodicity and polymer grating periodicity. The optical periodicity 'D' is the distance between two adjacent regions of maximum (I_{max}) or minimum (I_{min}) intensity of light within the interference pattern as shown in Fig 3.2. The polymer grating periodicity (d) is the distance between two adjacent peaks (maxima) or valleys (minima) of SRG. The optical periodicity ($D = \lambda/2\sin\theta$) of the surface relief is controlled by the angle θ between two interfering beams.
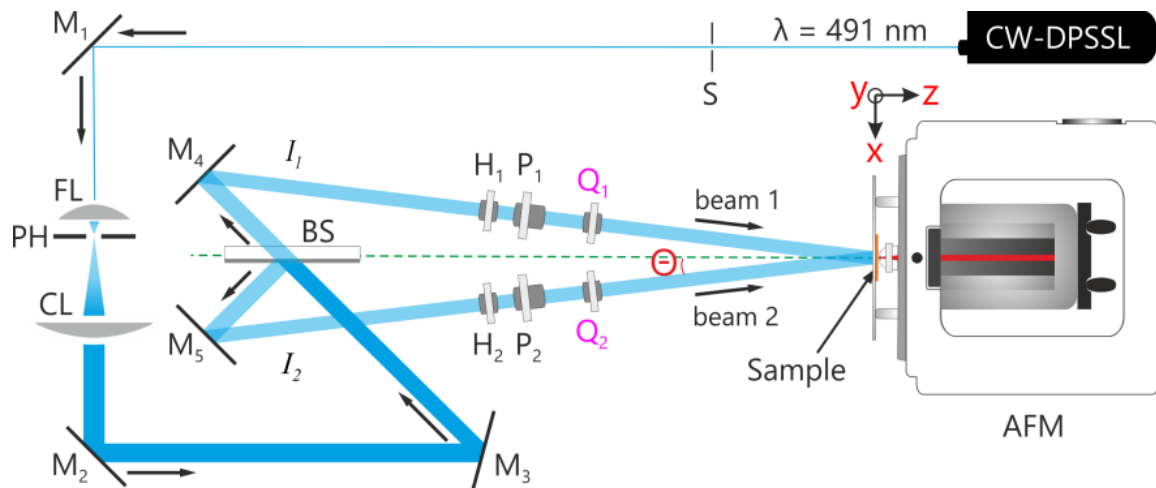
Fig. 3.7. Experimental setup for recording SRG formation with circularly polarized interfering beams. (Q_1 and Q_2) - Quarter wave plates ($\lambda/4$).

The combination of a two-beam interferometer and an AFM allows for the acquisition of changes in polymer topography while the film is being irradiated. In our setup, the interfering beams reach the sample from the glass (back) side (see appendix A.2) such that they are not disturbed by the AFM cantilever. The AFM is oriented horizontally and aligned with the interfering laser beams in such a way that the interference plane is parallel to the sample surface and the tip scanning is in XY–plane (appendix A.1). All the *in-situ* AFM measurements were performed with 1 Hz scan speed and each scan requires 9 minutes to complete. The AFM scan cycle is toggled to maintain continuous up and down scanning during *in-situ* measurements across a used scan area, so that topography variations running upward and downward in the AFM images represent the topography changes across the whole polymer surface. The scanning directions in the AFM images then correspond to a time axis.

3.4.3. Photosensitive Materials

In the current study, we have chosen two photosensitive materials based upon their molecular weight to observe and compare the SRG formation with different interference patterns. One of the materials is a commercially available polymer with high molecular weight and approximately 40 repeated azobenzene units connected to a backbone chain named in short as PAZO as shown in Fig 3.8a, and the second material is a low molecular weight azobenzene containing dendritic material (three azobenzene units bounded to the core) as shown in Fig 3.8b.
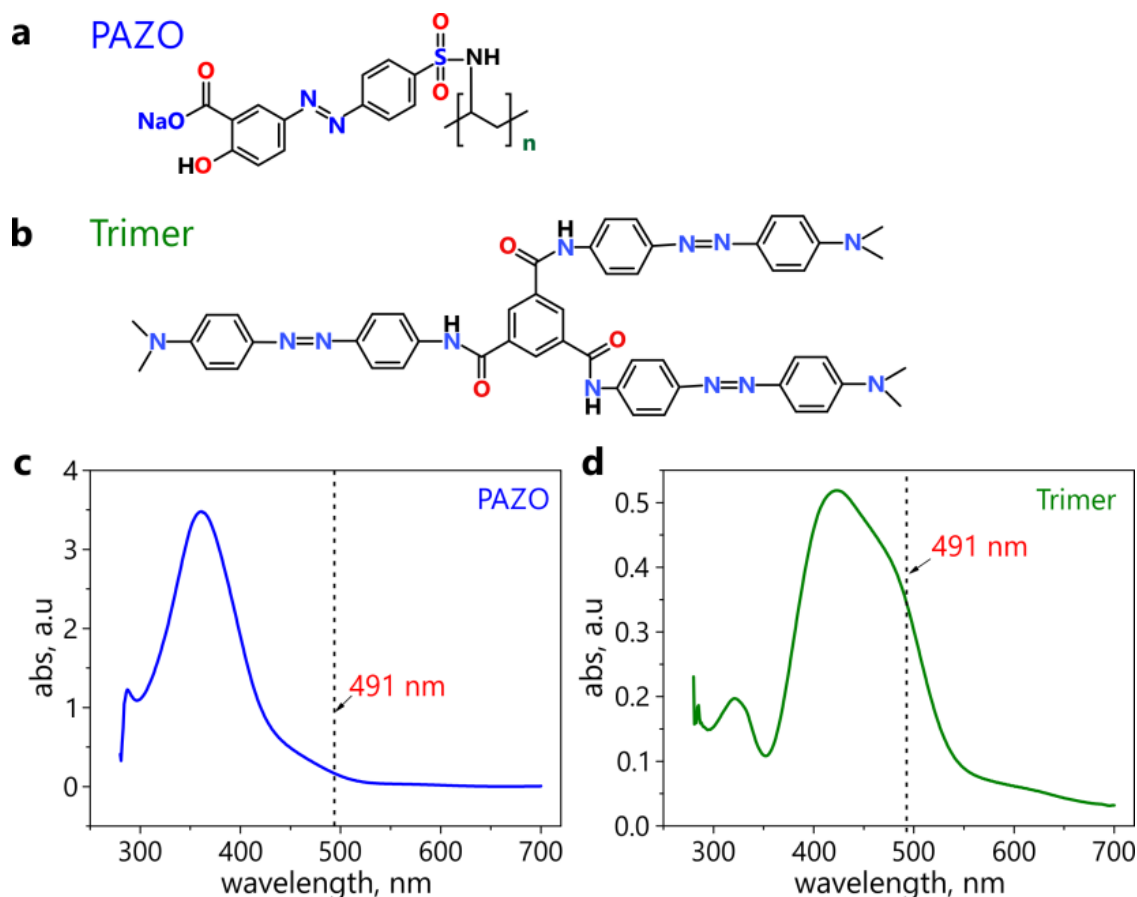
Fig. 3.8. Chemical structure of photosensitive materials and their UV-Vis absorption spectrum. (a) PAZO chemical structure. (b) Trimer chemical structure. (c) The absorption spectrum of PAZO (blue curve) and (d) Trimer (green curve). The dotted line represents the wavelength of laser source in the absorption spectrum of photosensitive material.

a. PAZO

Commercially available azobenzene-containing photosensitive polymer PAZO (poly{1-[4-(3-carboxy-4-hydroxyphenylazo)benzenesulfonamido]-1,2-ethanediyl,sodiumsalt}) is purchased from Sigma-Aldrich. The polymer solution is prepared by dissolving PAZO in a mixture of 95% methoxyethanol and 5% Ethylene glycol. The molecular weight of PAZO is estimated by GPC analysis to be $M_n = 1.4 \times 10^4$ g/mol (ca. 40 repeat units). PAZO is also soluble in water and it contains negatively charged azobenzene moieties in its side chain. The absorption spectrum of PAZO is presented in Fig 3.8c (blue curve) and the maximum absorption is observed at 365 nm wavelength.

b. Trimer

An azobenzene containing trimer is shown in Fig. 3.8b. The material is prepared by amide formation through the reaction of 1,3,5-benzenetricarbonyl trichloride (Alfa Aesar, 0.26 mmol) with *N,N*-Dimethyl-4,4′-azodianiline (Aldrich, 0.78 mmol) in anhydrous dimethoxyethane (Aldrich) at room temperature in the presence of triethyl amine (Aldrich, 0.78 mmol) according to the described procedure elsewhere[68]. The solution was filtered through 0.45 μm Nalgene filter. The absorption spectrum of trimer is also presented in Fig 3.8d (green curve) and the absorption maximum is at 400 nm wavelength.

3.4.4. Polymer film (sample) preparation

To obtain different film thicknesses, appropriate volume of photosensitive material is spin coated on a glass substrate at controlled rpm. For instance, 1 μm thick PAZO film is prepared by spin casting of the polymer solution of 250 mg/ml concentration on a glass substrate (Schott D263M glass, thickness – 130 μm) at 11,000 rpm during 1 minute. We are able to achieve PAZO films at required thickness conveniently; however maximum achievable Trimer film thickness is limited to ~ 350 nm due to restriction on synthesis procedure. The glass substrate used to prepare all samples in the current study has 95 % transmittance for the wavelength used (λ – 491 nm). [69]

3.4.5. Index of refraction

It is well known that the birefringence could be induced in azobenzene containing photosensitive materials and there will be decrease in the refractive index parallel to the polarization of light and an increase in the orthogonal direction proportionally.[65] Here we are presenting the refractive index measured on isotropic polymer films before inscription of SRG.

The complex index of refraction of PAZO and trimer is determined using Diffuse Reflectance Accessory (DRA) available with VARIAN UV-Vis-NIR spectrometer (Cary 5000). We have measured the relative spectral reflectance and transmission of the uniformly coated thin polymer film on glass substrate and determined the refractive and extinction coefficient using transfer-matrix method with acceptable probability controlled simulated annealing algorithm.[70] For all the experiments in the current study, we have used a laser wavelength of 491 nm to inscribe surface relief grating. For PAZO and trimer the complex index of refraction at 491 nm is $1.84 \pm i0.01325$ and $1.946 \pm i0.27536$ respectively.
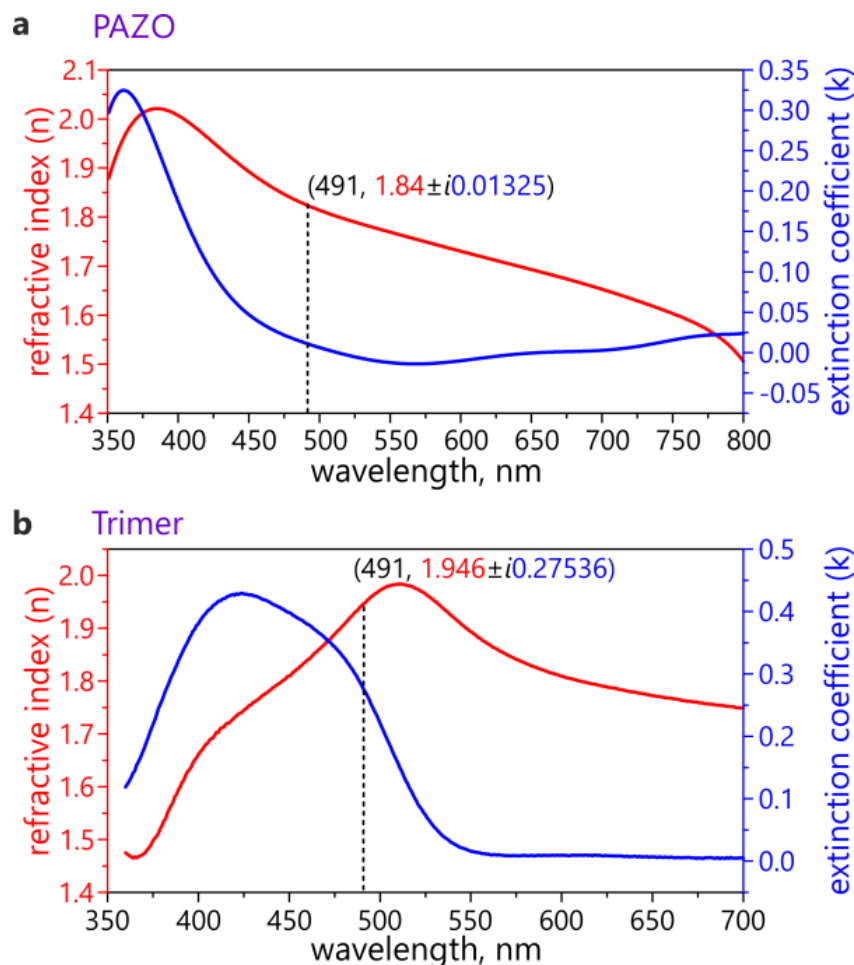
Fig. 3.9. Complex index of refraction for PAZO (a) and trimer (b) measured using transmission/reflection spectroscopy.

3.4.6. *In-situ* AFM recording of SRG formation

A micrometre thick PAZO film is prepared on a glass substrate (2×2 cm²) and the sample is inserted in the *in-situ* AFM setup as shown in Fig. 3.6. Irradiation is performed from the glass side and the polymer topography is scanned by the AFM tip such that the irradiation process does not influence the AFM tip scanning. As a first step, the polymer topography is scanned continuously without irradiation (in dark). During the scan progress, the irradiation beams are switched ON (see red dotted line in Fig. 3.10) to interfere at the sample and the immediate changes in polymer surface topography as a response to the interference pattern is recorded as shown in Fig. 3.10a.
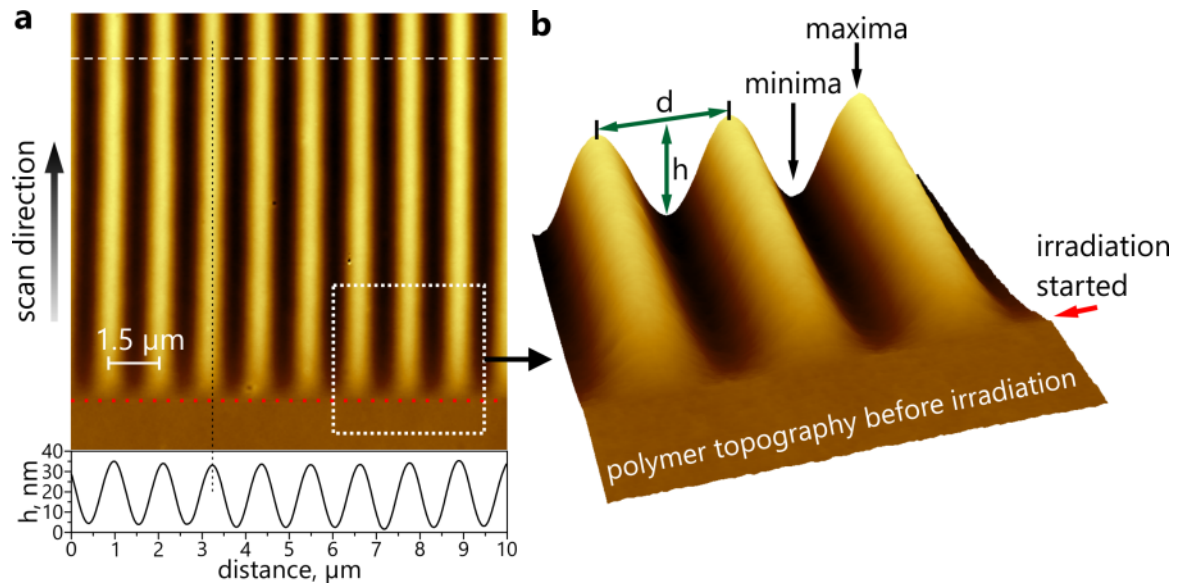
Fig. 3.10. *In-situ* AFM measurement. (a) 1 µm thick PAZO film is irradiated using an intensity interference pattern with a periodicity (D) of 1.5 µm at an intensity 100 mW/cm². Irradiation started at red dotted line while AFM scan of polymer topography is in progress. The profile at the bottom represents the topography cross section taken at white dashed line. (b) Three dimensional view of dotted box region in (a). Grating periodicity 'd', grating height 'h', grating minima and maxima are defined as shown.

From Fig 3.10b, it is evident that the photosensitive material reacts instantaneously to develop a SRG upon irradiation. This is the first successful *in-situ* observation of SRG formation in photosensitive materials using AFM and our experimental setup (IIAFM) offers many advantages to study the complex process of SRG formation in more detail as we would see in the following chapters.

This page intentionally left blank

In-situ Observation of Surface Relief Grating Formation

In the previous chapter, we have observed the possibility to study the SRG formation in *in-situ*. Here, we are extending the application of this method to study the SRG formation using many combinations of different experimental parameters *viz.,* photosensitive materials, interference patterns, and periodicity (D). A constant irradiation intensity of 100 mW/cm² is used for all experiments unless otherwise mentioned.

4.1. Comparison of SRG formation in PAZO and trimer

4.1.1. Intensity Interference Patterns (IIPs)

Our preliminary studies on comparing the SRG formation during the first 5 minutes of irradiation with PAZO and trimer using different intensity interference patterns revealed interesting results as shown in Fig 4.1. All the measurements started from top to bottom scan direction and each scan started with plain polymer (isotropic) topography and the irradiation with particular interference pattern started at position pointed by white arrow (see Fig 4.1a). Here, we used 4 μm periodicity for all gratings inscribed in PAZO (thickness, *z*-500 nm) and 2 μm periodicity for all the gratings inscribed in trimer (*z*-350 nm). We would like to mention that from our experimental observation, the comparison presented in Fig 4.1 is valid for any arbitrary optical periodicity (D).

   i)   *SS* (↕↕)

Comparing the SRG formation using SS interference pattern, PAZO shows strong response and the grating developed instantaneously with grating periodicity (d) equal to optical periodicity (D) (see Fig 4.1a). We have observed a 10 nm grating height immediately after switching ON the interfering beams and the grating height continued growing rapidly until it reached saturation in < 30 min. In case

of trimer, the reaction to SS interference pattern is very poor and during the first 30 seconds of irradiation, the AFM micrograph shows that two separate arms merging together to form a final grating position. The two arms started exactly half a period away from both ends of final grating maximum position as shown in Fig 4.1e. The process may indicate the role of mass transport in creating a surface relief grating in photosensitive materials.

ii)   ‡45° (↗↗)

Comparing to SS interference pattern, ‡45° pattern is relatively efficient for grating formation in both PAZO and trimer. Similar to SS, the grating formation for PAZO started instantaneously with 15 nm (Fig 4.1b). In case of trimer, the process of merging two arms is more clearly visible for 2 minutes of duration before the final grating position completely revealed. The associated cross section profiles presented in Fig 4.1f are confirming the phenomenon of mass transport to create a final grating position.

iii)   PP (↔↔)

The observation of SRG formation using PP interference pattern for both PAZO (4.1c) and trimer (Fig 4.1g) are similar to ‡45° except that the grating formation efficiency is increased almost in two times for both the materials compared to SS. And particularly for trimer, the observation of mass transport is more clearly visible.

iv)   LL (↺↺) or RR (↻↻)

Both LL and RR interference patterns has similar impact on the grating formation efficiency in PAZO, the starting height of SRG after switching the irradiation beams ON is ~ 50 nm. In contrast, the grating formation efficiency in trimer is the same as in case of PP, LL and RR interference patterns.

Observing the formation of surface relief in PAZO and trimer using different intensity interference patterns (SS, ‡45°, PP, LL and RR), it is evident that PAZO is very sensitive to intensity modulation in the interference pattern and the polarization of electric field in the interference pattern helps to increase the grating formation efficiency. In contrast, trimer response to the intensity modulation is very weak, but we observed important information of molecular mass transport process. Further, the comparative study of SRG formation in PAZO and trimer offers deeper insight into the concept of free volume change during the irradiation of photosensitive material film due to azobenzene *cis-trans* isomerization processes[71,72].
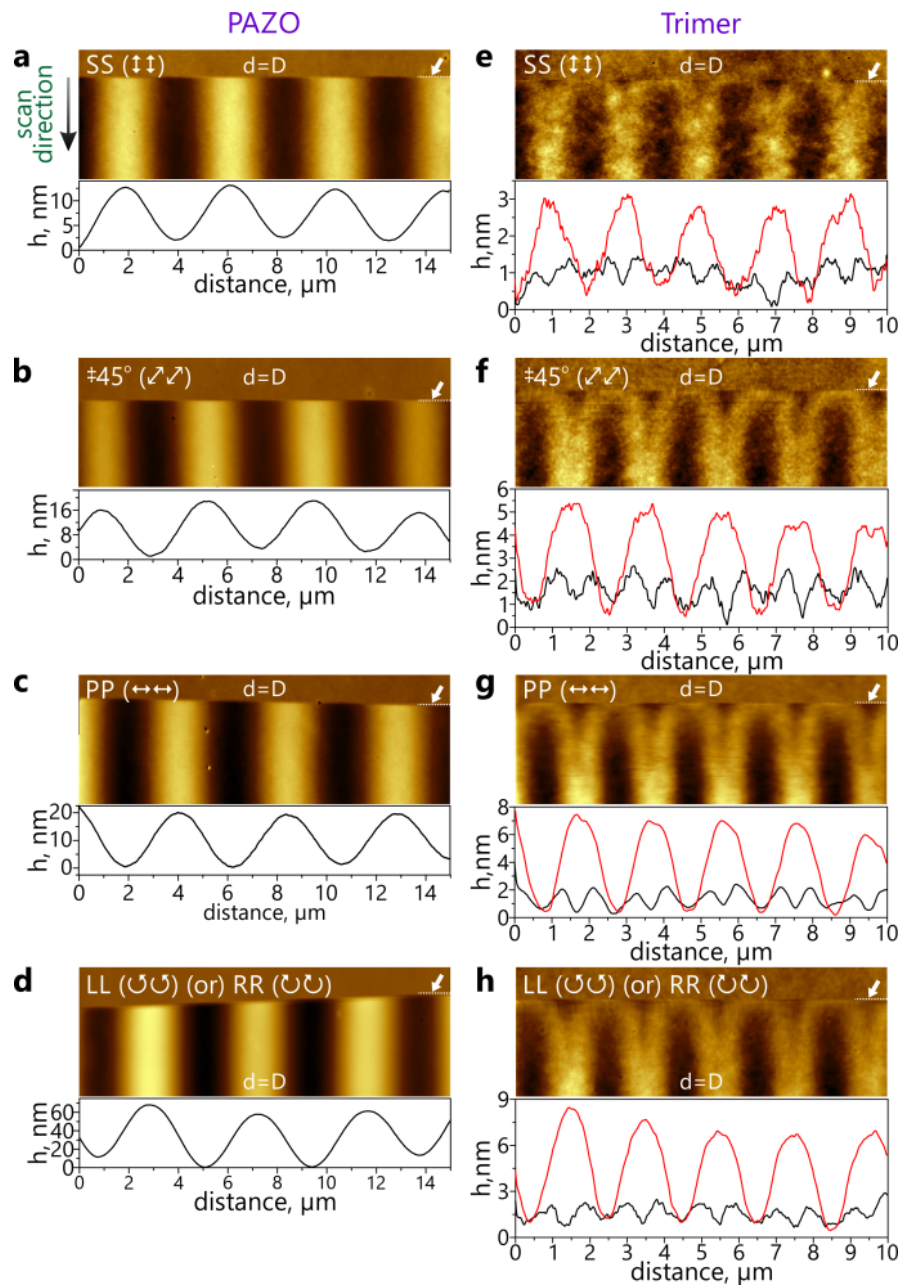
Fig. 4.1. Comparison of SRG formation using intensity interference patterns (IIP) in PAZO and trimer in the first 5 min of irradiation. (a), (b), (c) and (d) SRG formation with a periodicity 'D' of 4 μm in PAZO using SS, ‡45°, PP and LL or RR respectively. The associated cross sectional profiles are taken immediately after the irradiation started. (e), (f), (g) and (h) SRG formation with a periodicity 'D' of 2 μm in trimer using SS, ‡45°, PP and LL or RR respectively. The associated cross sectional profiles are taken immediately after irradiation started (black) and after 5 min of irradiation (red). White arrow at the left-top corner of each AFM micrograph pointing the position when the irradiation is switched ON. Scan direction for all the measurements is from top to bottom.

4.1.2. Free volume change in photosensitive polymer film

Azobenzene molecules undergo photo-isomerisation transitions from trans- to the cis configuration during irradiation with light. This transition is completely reversible and can be interconverted by light or heat.[73,74,75,76] The changes of the azo-molecular properties during isomerisation reaction are significant. For instance, the size of the molecules change by almost a factor of two (Fig 4.2), requiring for the cis configuration more free volume. At the same time, the dipole moment of the azobenzene molecules changes from 0 Debye for trans- more stable configuration to 3 Debye for the cis-isomer.[77,78]
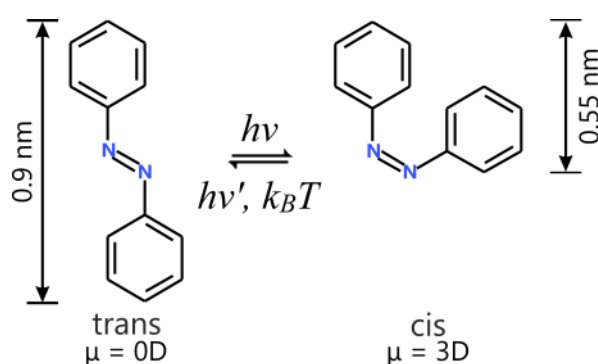
Fig. 4.2. Azobenzene *cis-trans* isomerization.

In the AFM micrographs presented in Fig 4.1(e-h), the trimer molecules immediately undergo cis-trans isomerization upon irradiation and the change in free volume occurs at intensity maxima (bright) regions and no reaction takes place in the intensity minima (dark) regions. Thus we observed a primary grating for short time then followed by mass transport towards the original grating position. At this stage, it is possible to assume that the SRG maxima for trimer film correspond to the intensity minima of interference pattern. However, to confirm this assumption more experimental evidence is necessary.

It might be possible that due to high grating formation efficiency of PAZO (see Fig 4.1(a-d), we are unable to observe the changes in the free volume or mass transport phenomenon similar to trimer (see Fig 4.1(e-h)).

4.1.3. Polarization Interference Patterns (PIPs)

In the previous section, we have studied the formation of surface relief grating using IIPs *in-situ* and found that PAZO responses stronger, while trimer response is weaker to intensity modulation.

As we discussed in section 3.3.2, there is no intensity modulation in PIPs at considerably short angle of incidence. In the following, we discuss the SRG formation using polarization interference patterns (PIPs) and compare the grating formation behaviour to purely polarization modulation and purely intensity modulation conditions.

i)   ±45° (↗↘)

The experiments are conducted similar to the procedure described in section 4.1.1. Grating formation is observed during the first 5 min of irradiation. For ±45° interference pattern, the results of PAZO and trimer are presented in Fig 4.3a and Fig 4.3d respectively. The grating formation is more efficient in case of trimer (Fig 4.3d) compare to PAZO with pure polarization modulation. Surprisingly, the results describe an opposite phenomenon compared to the observation in section 4.1.1 with intensity modulation. Trimer has no mass transport phenomenon (see Fig 4.3(d-f)) during the initial stages of grating formation. In contrast, PAZO has exhibited a unique grating phase transitions during the SRG formation. For the first 5 minutes, the grating periodicity is half of the optical periodicity (d=D/2) as shown in Fig 4.3a. The initial grating (labelled as 1) continued to disappear with time while the new grating (labelled as 2) replaces it exactly half a period away. This is the first time these unique transitions during grating formation are recorded. During the complete experiment, we found that only for the first 5 to 10 minutes (depending upon d and *I*), the grating exhibits a transition between the initial and final grating positions (Fig 4.3a) and the final grating periodicity is equal to the optical periodicity.

ii)   SP (↕↔)

The first report on SRG formation using SP interference is published in 1998 for the side chain azobenzene polyesters[79]. Following this report, very few studies were carried out to further elucidate the effects of the SP polarization combination, probably due to the low grating foramtion efficiency as reported before[80,81]. SP interference pattern reported to produce a polymer grating periodicity (d), which is half of the used optical periodicity (D). In the current study, we have also observed the same phenomenon for both PAZO and trimer

(Fig. 4.3(b, e)). The polymer grating periodicity is half of the optical periodicity (d=D/2).
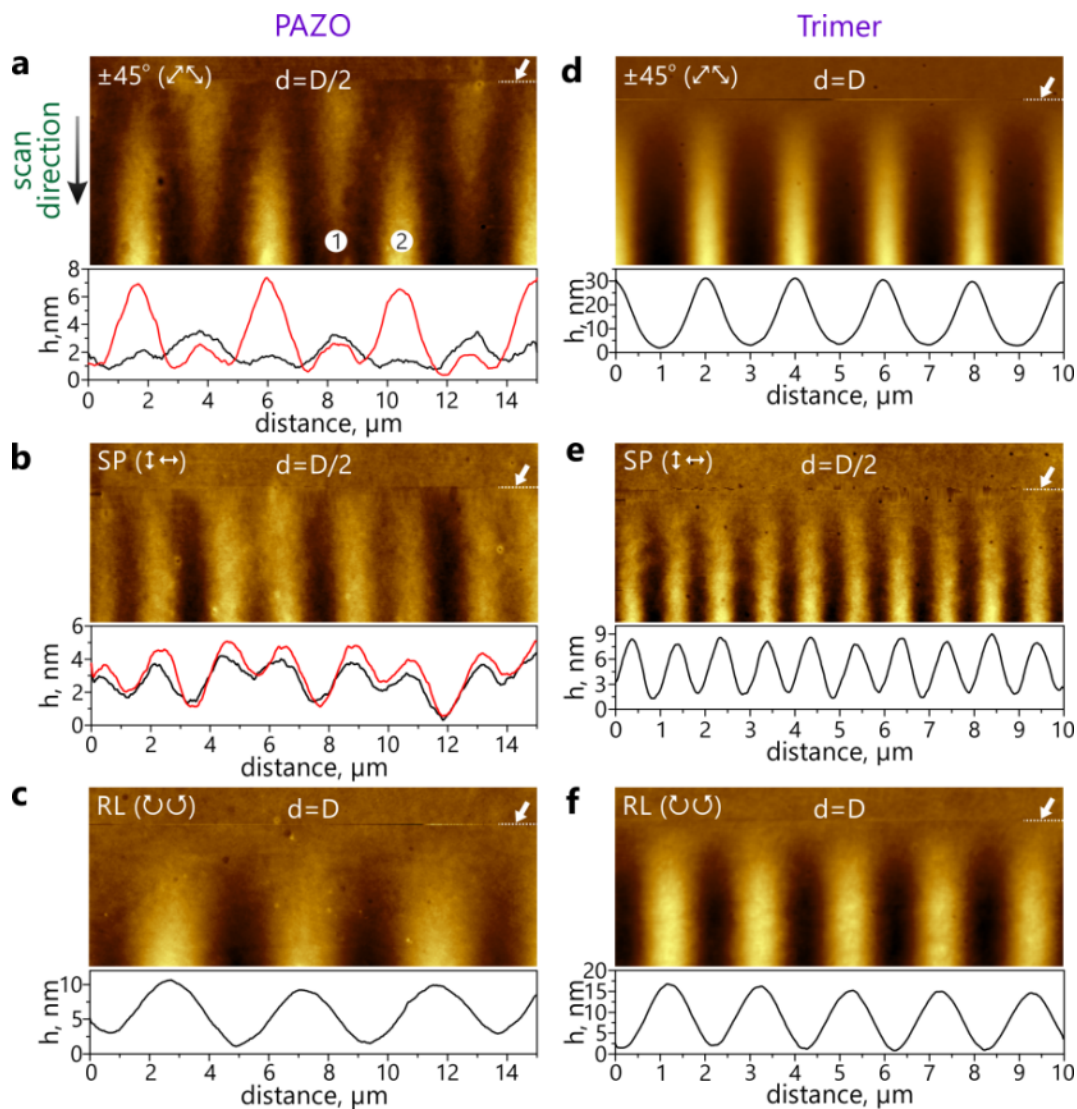
Fig. 4.3. AFM micrographs: Comparison of SRG formation using polarization interference patterns (PIP) in PAZO and trimer in the first 5 min of irradiation. (a), (b) and (c) SRG formation a periodicity 'D' of 4 μm in PAZO using ±45°, SP and RL respectively. The cross sectional profiles are taken after irradiation started (black) and after 5 min of irradiation (red) (d), (e) and (f) SRG formation with a periodicity 'D' of 2 μm in trimer using ±45°, SP and RL respectively. Scan direction for all the measurements is from top to bottom. White arrows at the right-top corner of each AFM micrograph pointing the position when the irradiation is switched ON.

Comparing the grating developed with SP and ±45° interference patterns, in case of PAZO (Fig 4.3(b, c)) both has grating periodicity equal to half of the optical periodicity (d=D/2) in first few minutes of irradiation. However, in case of ±45° pattern the final grating periodicity is equal to optical periodicity (d=D) and for SP pattern the final grating periodicity continued to be half of the optical periodicity (d=D/2). Further, from Table 3.5 and 3.6 the only difference between SP and ±45° interference patterns is the angle of linearly polarized electric field vectors. To understand these intriguing grating formation behaviour using SP and ±45° interference patterns, it is very important to know which $\vec{E}$- field vector of these patterns is responsible for different grating positions (i.e., minima, maxima, slopes etc). This point we solved as discussed in chapter 6.

iii)   RL (↶↺)

In Fig 4.3(c, f) we have presented the surface relief formation for PAZO and trimer using RL interference pattern. We have observed a normal grating formation with 'd' being equal to 'D' throughout the irradiation time and the efficiency of grating formation is observed to be high in case of trimer than PAZO.

4.2. SRG Growth Kinetics

It was mentioned in section 3.4.2 that the scan direction during *in-situ* AFM measurement represents the time dependent changes in the polymer topography and each scan requires 9 minutes to complete. Up and Down scanning in AFM is toggled to record the changes in polymer topography until the grating formation process (grating growth) is saturated. Thus the AFM scan information of polymer topography could be converted to reveal the grating growth kinetic as shown in Fig 4.4.
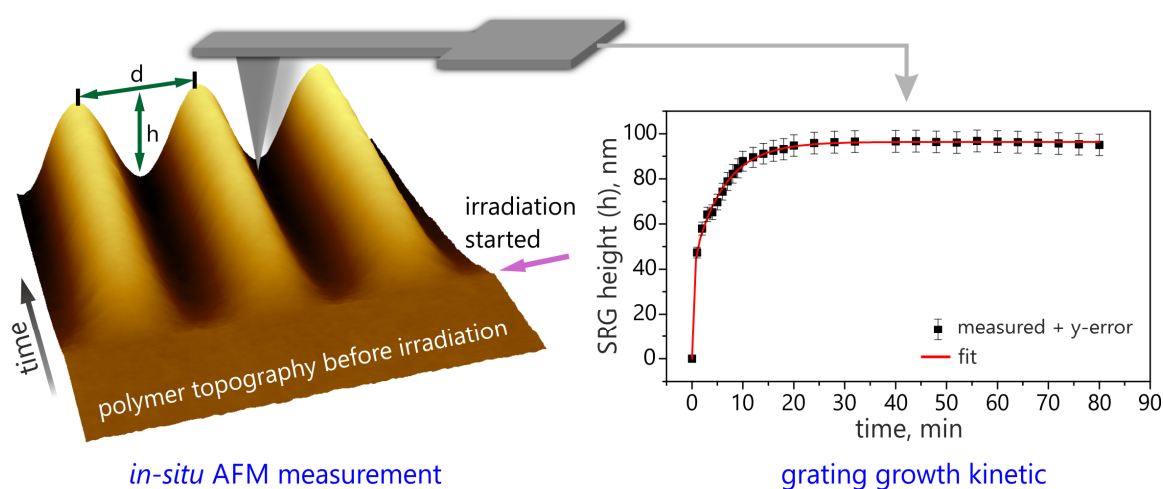
Fig. 4.4. SRG growth kinetic. The height information from AFM scan is plotted as duration of measurement (time) *vs.* grating height (h).

4.2.1. *In-situ* recording of grating growth kinetics

Fig 4.5 shows the topography change of trimer film (h = 150 ± 10 nm) during *in-situ* irradiation using ±45° interference pattern with 1 μm optical periodicity (D). After switching ON the irradiation (see red dotted line in the Fig. 4.5b), an immediate change of the topography is observed. The growth of grating height proceeds rapidly within the first 10 minutes (Fig 4.5d), reaching a maximum in SRG height of 200 nm, while still leaving 100 nm of film at the bottom of grating (see insert in Fig. 4.5e). The optical periodicity 'D' in this case exactly corresponds to the grating periodicity 'd' in the photosensitive film. Further irradiation within the next 60 minutes does not influence the height of the grating but its cross sectional profile, which changes with time from a sinusoidal to an anharmonic shape. The anharmonicity is known to appear at higher deformations even if one

assumes that the inscribing force is a sinusoidal function with the optical periodicity D.
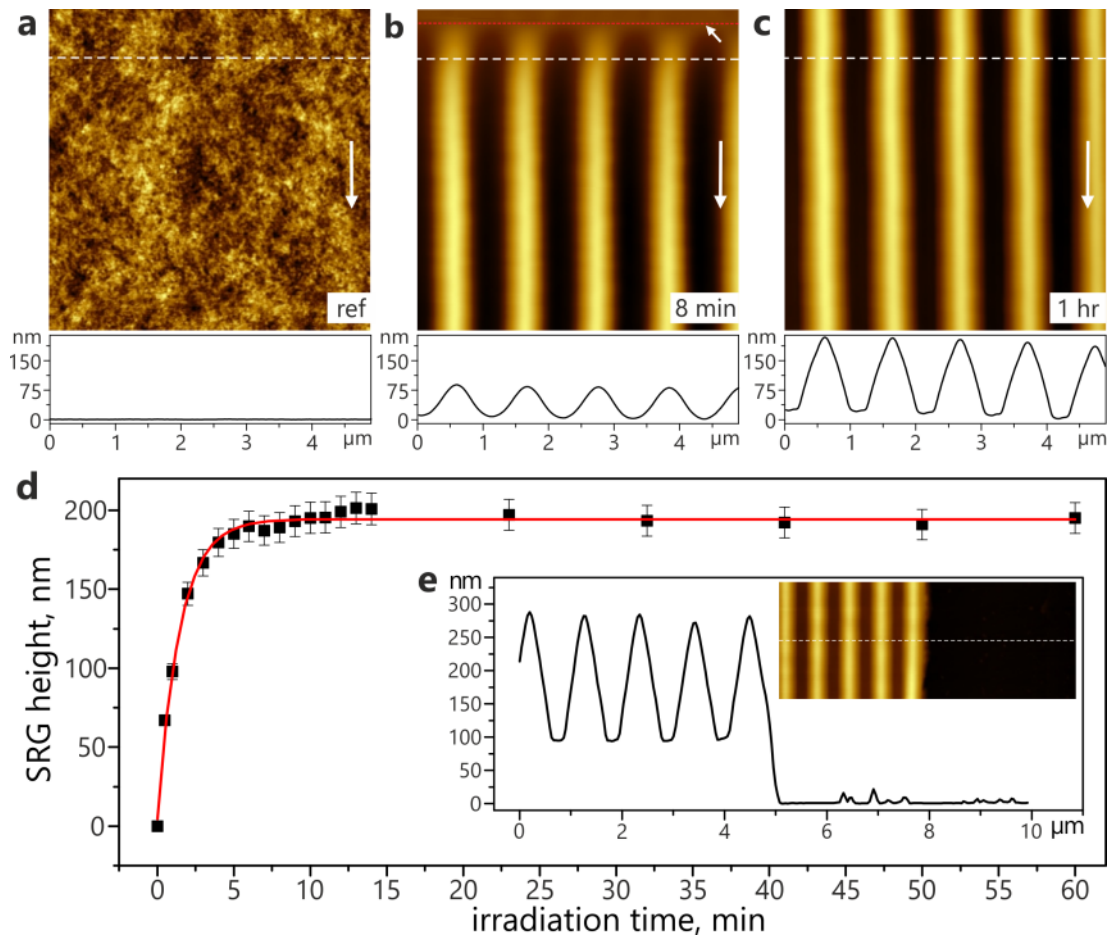
Fig. 4.5. AFM micrographs of trimer film recorded as a function of irradiation time. The polarization combination is ±45 (PIP), the periodicity of the interference pattern is 1 µm. (a) Reference scan before starting irradiation. The direction of scanning is shown by the white arrow on each micrograph. (b) During scanning from top to bottom the irradiation is switched ON at the position marked by white dotted line. (c) AFM micrograph after 60 min of continuous illumination. (d) Dependence of the SRG height on irradiation time as extracted from the AFM measurements. (e) The inset shows the AFM scratch analysis of the film thickness. The white dotted lines represent the cross sectional profile shown at the bottom of corresponding AFM micrograph. Irradiation intensity, I = 100 mW/cm².

It has been shown before that the grating starts to deviate from a sinusoidal one at relative deformations exceeding 20% due to a complex shift of volume elements along the grating vector. [41] Additionally, absorption effects, which lead to a strong dependence of the inscription force on the penetration depth, may play a role in the appearance of anharmonicity. On the other hand, the saturation of the grating growth observed at long inscription times can be explained by taking into account the surface tension force. The saturation is reached when the surface force counterbalances the inscription force.

4.2.2. Dependence of SRG growth on experimental parameters

Many experimental parameters contribute to the SRG formation *viz.,* interference pattern (IIP or PIP), grating periodicity (d), type of photosensitive material, irradiation intensity (*I*), duration of irradiation (time), and photosensitive film thickness (*z*). In order to determine how these parameters contribute to the formation of SRG in more details, we have studied comprehensively the dependence of grating height by varying each parameter separately as described in the following sections.

i)   Influence of irradiation time & interference patterns (IP)

Over the past decade, varieties of photosensitive materials are synthesized and in order to test their efficiency/photosensitivity, observing the inscription rate of SRG is a favourite choice for many researchers. Due to the lack of efficient techniques to study the SRG growth *in-situ* the irradiation time is kept arbitrary (< 60 min). In some experiments, the grating growth rate is studied in *ex-situ* by irradiating the samples in steps ranging from few seconds to few minutes.[82] Further, the irradiation time is considered by observing the "Diffraction efficiency" of a probe laser during SRG formation. Considering much inefficiency in available techniques, maximum achievable SRG height and possible growth phases remained a puzzle and the observed photosensitivity of new materials may be not completely reliable.

Using our experimental setup (IIAFM), for the first time we are able to reveal the time dependent behaviour of SRG formation. We have performed the experiments with *in-situ* observation of SRG formation until the grating growth rate saturates completely.

Fig 4.6 shows the grating growth kinetic for 1μm thick PAZO film using different interference patterns. In case of all the intensity interference patterns (IIP), the grating growth rate is observed to be exponential during the first 10–15 minutes and reached a saturation phase with no further growth in SRG height. Thus while

using IIPs, the irradiation time needed to reach maximum SRG height is ~30 min. We have also determined that RR interference pattern is very efficient compared to other IIPs. The maximum achieved grating height is ~300 nm for 1 µm thick PAZO film using RR pattern at an irradiation intensity of 100 mW/cm².

Following several repeated experiments, the SRG formation efficiency using different IIPs is observed to be

$$RR \geq LL > PP > \ddagger 45^o > SS \qquad (4.1)$$
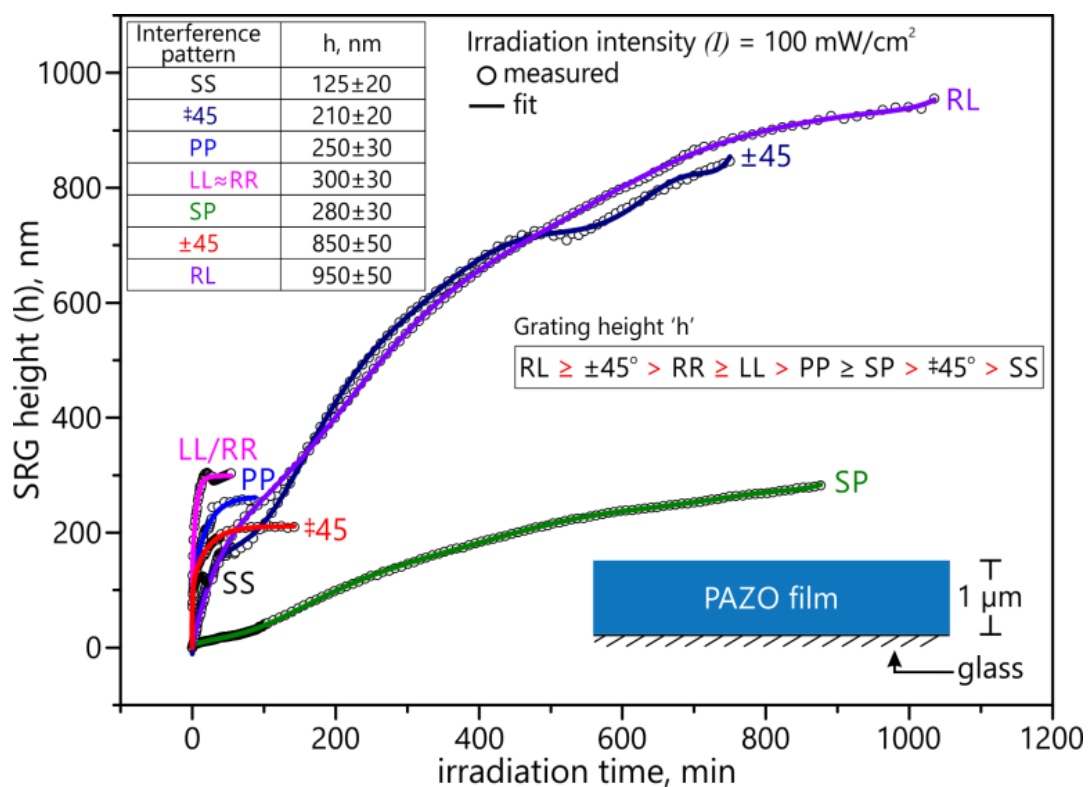
Fig. 4.6. Dependence of SRG height on irradiation time for 1µm thick PAZO film for different interference patterns. For IIPs, the maximum irradiation time required is ~30 to 45 min. For PIPs, the irradiation time is ca. 24 hrs.

In case of PIPs, the SRG growth rate is very slow and continues to growing for longer duration. The SRG continued growing for above 25 hours of irradiation. Among PIPs, RL interference pattern is efficient resulting to maximally attainable SRG height of h = 1 µm. The SP interference pattern results to smallest SRG height among PIPs. However, during comparison one should consider the fact that the SP gratings periodicity is always half of the optical periodicity (d=D/2)

thus to compare SP interference pattern with other PIPs, suitable grating periodicity should be used. Thus the irradiation time required for complete SRG formation in case of PAZO using PIPs is more than 24 hours. The maximum achievable grating height is more than a 1μm for RL and ±45° and from the experimental observation, the achievable grating height of PIPs could be expressed as follows

$$RL \geq \pm 45° > SP \tag{4.2}$$

ii)   Influence of grating periodicity (d) & film thickness (z)

The limits of maximum achievable SRG height should depend on number of azobenzene molecules excited by irradiation. In turn, this depends on the amount of material available during irradiation with particular interference pattern. The area is defined by the grating periodicity (d) of the interference pattern (i.e. the distance between two adjacent intensity maxima or minima). The amount of available material locally is defined by film thickness.

In Fig 4.7 we have presented a comprehensive study on the influence of film thickness (z) and grating periodicity (d) on SRG growth for PAZO films. Both film thickness and grating periodicity are modulated simultaneously by keeping the intensity (100 mW/cm^2) and interference pattern (±45°) constant for all experiments. All measurements are performed until the grating height reach a near saturation phase. The film thickness is changed in relation to the source wavelength of 491 nm i.e. ~1.0 μm (z = 2λ), ~0.5 μm (z = λ), and ~0.25 μm (z = λ/2) and the grating periodicity is modulated between 0.5 μm and 5 μm for each film thickness.

In Fig 4.7a, the grating growth kinetic is presented for different grating periodicities using a constant film thickness of 1.0 μm (z = 2λ) and in Fig 4.7b, we have plotted the maximum achieved grating height (h) against the grating periodicity (d). The third degree polynomial fitting (Fig 4.7a, green curve) of data shows the dependency of grating height on periodicity. When we increase the grating periodicity gradually from 0.5 μm (d = λ) till 4.0 μm, the maximum achievable grating height also increased. Beyond 4.0 μm periodicity the grating height decreases. Thus, for 1 μm thick film the maximum grating height is achieved at 4.0 μm grating periodicity. In Fig. 4.7c, we have reduced the film thickness to 0.5 μm (z = λ) and the kinetic for different periodicities are presented. Fig 4.7d shows the relation between maximum achieved grating height for each periodicity. Surprisingly, we observed a maximum grating height with 3.0 μm periodicity.

Fig. 4.7. Dependence of SRG height on grating periodicity 'd' and film thickness 'z' for PAZO film using ±45° interference pattern. (a) Grating growth kinetic for different periodicities using 1.0 μm thick PAZO film. (b) Relation between d and h for 1.0 μm thick PAZO film. (c) Grating growth kinetic for different periodicities using 0.5 μm thick PAZO film. (d) Relation between 'd' and 'h' for 0.5 μm thick PAZO film. (c) Grating growth kinetic for different periodicities using 0.25 μm thick PAZO film. (d) Relation between 'd' and 'h' for 0.25 μm thick PAZO film. Intensity (100 mW/cm^2).

We have reduced the film thickness to 0.25 μm ($z = \lambda/2$) for kinetics presented in Fig 4.7e and the relation between 'h' and 'd' are plotted in Fig 4.7f. The maximum grating height is obtained at ~ 1.5 μm periodicity.

Comparatively, one shall mention that with increase in film thickness (z) the maximum grating height (h) is achieved at larger periodicity (d). In order to prove if this phenomena of dependency between 'z', 'd' and 'h' could be generalized, we have repeated the above described experiments with ‡45° and PP interference patterns. The results are presented in appendix A.3.

Despite the differences in the grating formation behaviour, we have observed a similar relation between the parameters *viz.* z, h, and d for different interference patterns (IIPs & PIPs). Further increasing the film thickness above 1.0 μm ($z > 2\lambda$), the relation between z, h, and d remains similar to $z = 2\lambda$.

In our experimental setup, we irradiate all samples from the glass side. When two interfering beams pass through glass into the polymer film with an angle of incidence (θ) and interfere to create an interference pattern thereby SRG, we could also expect a secondary interference at glass polymer interface due to back reflections based upon the interference conditions for thin film in the order of the source wavelength. The interference conditions at the glass/polymer interface are as follows

Destructive interference $\qquad 2nz \cos\beta = m\lambda$ $\qquad\qquad\qquad$ (4.3)

Constructive interference $\qquad 2nz \cos\beta = \left(m - \dfrac{1}{2}\right)\lambda$ $\qquad\qquad$ (4.4)

Where, z is film thickness; n is the refractive index, m is the orders of wavelength, β is the angle in the film.

The effect of this secondary interference in the bulk of the photosensitive material is not understood clearly. Also, due to the lack of clear understanding on the molecular level dynamics for azobenzene containing photosensitive materials under light irradiation conditions, we could not explain this dependency between z, h, and d at this stage of investigation. However, it is one possibility that the volume element (between two adjacent grating minima) playing key role during material mass transport to define a maximum achievable grating height. Another possibility to explain this relation (z, h, and d) is the convection fluid

flow model in material between local minima of polymer grating.[*] Thus, more theoretical studies are required to further understand the influence of grating periodicity and film thickness on SRG formation.

iii)   Influence of photosensitive material

From figure 4.6, we have understood that the irradiation time required to achieve maximum grating height (h) depends up on the interference pattern. To generalize these observations, it is essential to test another photosensitive material. Thus we have repeated the experiments with trimer (see Fig 3.8b) until the grating growth kinetic saturates for ‡45° (IIP) and ±45° (PIP) interference patterns.
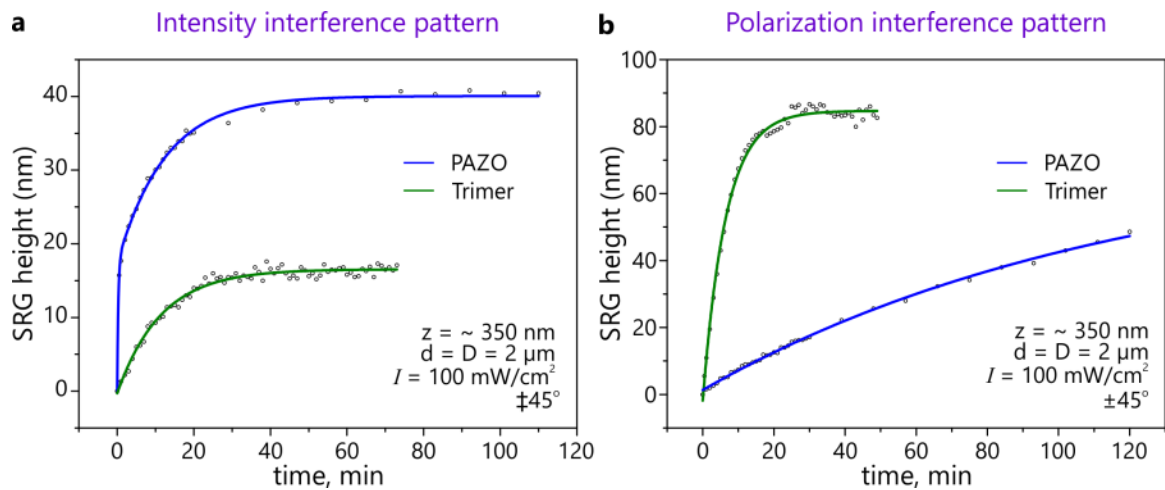
Fig. 4.8. Dependence of SRG height on photosensitive material. (a), (b) PAZO and trimer are compared for two interference patterns (‡45° and ±45°). Film thickness is kept constant to be ~350 nm. An intensity of 100 mW/cm² is used for all the measurements.

The grating growth kinetic using ‡45° (IIP) and ±45° (PIP) for both PAZO and trimer are compared in Fig 4.8. The results confirm the observations in section 4.1. The photosensitivity of azobenzene containing materials depends up on the pure intensity or pure polarization modulation in the interference patterns. The film thickness (~350 nm) and the intensity (100 mW/cm²) are kept constant for the

measurements in Fig 4.8(a, b). In case of ±45° interference pattern, PAZO has gradual growth rate. In contrast trimer has exponential growth rate in the first 20 min followed by stationary growth phase. In case of ‡45° PAZO has an exponential growth followed by stationary phase, however trimer response to intensity interference pattern is very low. The difference between PAZO and trimer is the molecular weight. In literature, there are no comparative studies available for different interference patterns based upon number of azobenzene chromophores grafted onto a backbone chain. To understand this intriguing behaviour of photosensitive material choice towards pure intensity or pure polarization modulation, more detailed experimental studies are required by modifying the chemical structure of azobenzene containing photosensitive material.

At this stage of investigation, we could only speculate in the frame of orientation approach.[†] MD simulations of model side-chain azobenzene-containing polymers revealed that the sign of photo-induced deformation under homogeneous illumination depends strongly on the molecular architecture. In particular, when azobenzenes are attached to a main chain via a very short spacer of two cites, the reorientation of azobenzenes perpendicular to the electric field vector ($\vec{E}$) causes reorientation of main chains parallel to $\vec{E}$ and the sample elongation along $\vec{E}$. It is known that polymers with very short spacers do not exhibit LC effects and thus are amorphous. PAZO has the architecture very similar to the model amorphous polymer. Therefore, for the case of pure IIP grating with ‡45° pattern one would expect a considerable stretching of polymer in the regions with maximum intensity along the grating vector. This explains the appearance of grating peaks in the non-illuminated regions (dark regions of IIP) in this geometry. It is not obvious why a relatively high grating appears at the first minutes of illumination. Such an effect would be observed when the kinetics of trans-cis photo-isomerization events will be fast enough to provide a noticeable reorientation of chromophores at the very beginning of illumination. Interestingly, the pure PIP pattern with ±45° is very unfavourable for the inscription of SRGs on PAZO films. At careful inspection one notices a competition between the regions with the horizontal polarization (having the electric field vector parallel to the grating direction) and those with the circular polarization. In the latter regions the azobenzenes are expected to be reoriented perpendicular to the film surface and

---

[†] The paper is submitted for publication by the author of current dissertation. The MD simulation and theoretical explanation presented above and next page is provided by Dr. Marina Saphiannikova from Leibniz Institute of Polymer Research Dresden, who is also a co-author of the paper.

thus to cause an in-plane orientation of the polymer chains. The dynamics of the chain reorientation in the regions with the circular reorientations seems to be faster than in the regions with the horizontal polarization, as this would lead to a build-up of material in the regions with horizontal polarization coming from the neighbouring regions with the circular polarization. With time however the reorientation of chains in the regions with the vertical polarization slightly wins and the most of material is distributed into the direction of the vertical polarization. In overall, the mutual competition between the regions suppresses the grating inscription.
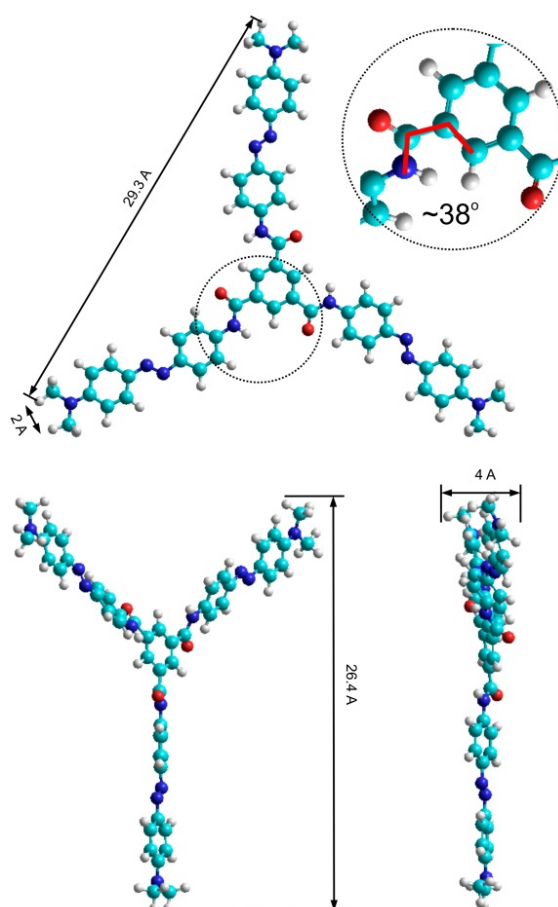
Fig. 4.9. Simulation of trimer molecule using Hyperchem.

Contrary to amorphous PAZO, the trimer is a low molecular weight compound that is not able to undergo stretching under illumination. Therefore, one would expect a local deformation of the trimer film due to a pure geometrical reason, i.e. due to repacking of trimers caused by reorientation of the three azobenzene

arms. The simulation with the Hyperchem software revealed that even in the absence of illumination the trimer is not flat: its arms protrude at the angle of about 40° from the plane of a core benzene ring as shown in Fig 4.9. Further, attachment of the arms to the core is not rigid and can be adjusted under application of the external force.

Thus, reorientation of the trimer will strongly depend whether it is illuminated by a linear or a circular polarized light. The illumination with the ‡45° pattern seems to cause only a slight adjustment of the arm positions which does not result in a considerable repacking of trimers as a whole. Moreover, this process is localized mostly in the region with the highest intensity. Such local adjustment is able to produce only a weak deformation at the beginning of illumination with the build-up of material on the other sides of the region with the highest intensity. This explains the appearance of double peaks in the very beginning of illumination and their gradual fusion with time.

The pure PIP ±45° pattern is considerably more favorable for the inscription of SRGs on the trimer films as can be seen from Fig. 4.3d. It is definitely causes a considerable repacking of trimers as a whole in the regions with a circular polarization. Therefore, from a start, the deformation carries a global character being assisted by the adjustment of trimer positions in the region with the horizontal polarization.

These two examples nicely show that the efficiency of grating inscription depends strongly on the intricate interplay between a particular polarization pattern and a particular molecular architecture.

iv) Influence of intensity (*I*)

Not only film thickness and periodicity influence the SRG process, but also the intensity of the incident light.

A micrometre thick PAZO film is used for all measurements in Fig 4.10. The intensity increased gradually in 100 mW/cm^2 steps from 50 to 600 mW/cm^2. Observing the growth kinetic it is evident that increase in the irradiation intensity will increase the SRG inscription rate proportionally as shown in Fig 3.19b. It is important to control intensity when testing the efficiency of the new photosensitive materials. In literature many photosensitive materials are reported with higher photosensitivity, however the intensity parameter is not studied relative to other photosensitive materials for more reliable assessment. As we could see from Fig 4.10a, more than 600 nm grating height is achieved in less than 2 hours of irradiation using 600mW/cm^2 for a micrometre thick film.
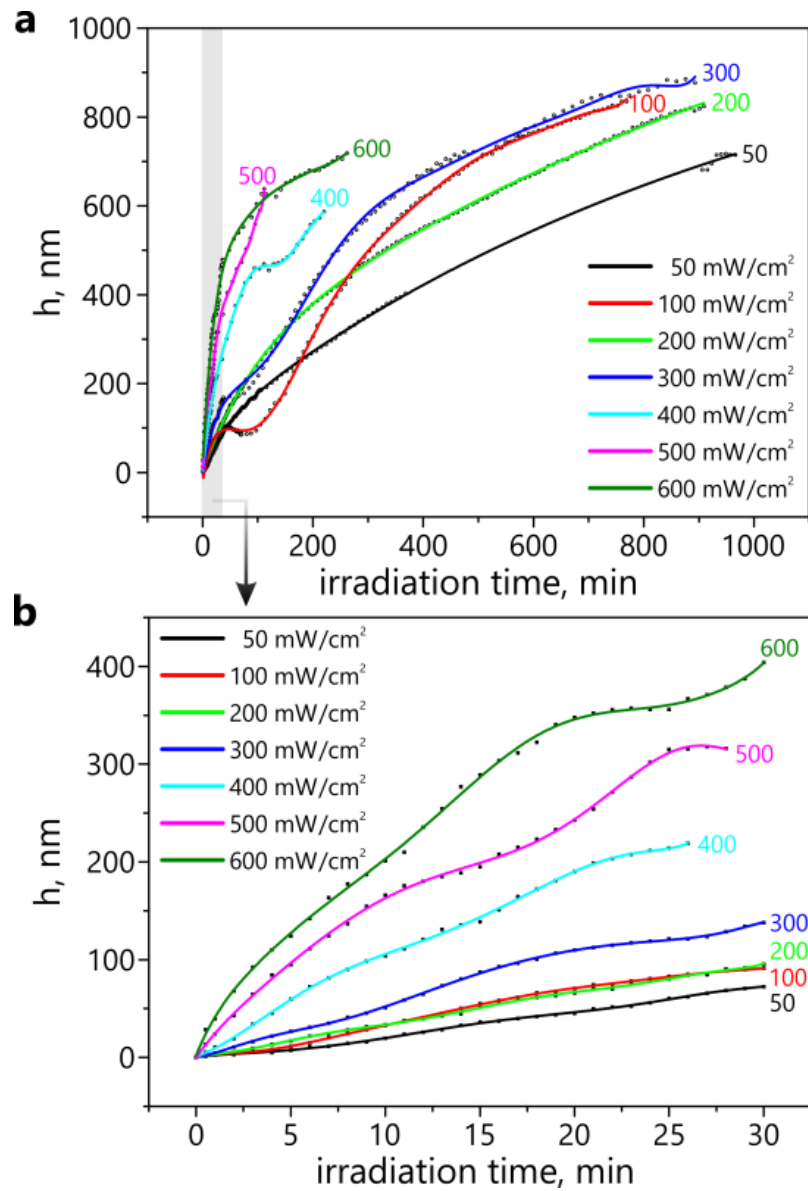
Fig. 4.10. Dependence of SRG height on Irradiation intensity (50 – 600 mW/cm²) for PAZO. (a) Complete growth kinetic in long irradiation duration. (b) First 30 min of Irradiation.

4.3. Summary

In a short overview of this chapter, using our novel/unique experimental setup (IIAFM), we have observed the surface relief grating formation *in-situ*. Which also made possible to observe the grating growth kinetic *in-situ* and to study the influence of many experimental parameters *viz.*, interference pattern (IIPs & PIPs), film thickness (z), grating periodicity (d), irradiation time, photosensitive material, and irradiation intensity (*I*) on the SRG formation. Due to lack of complete understanding on the molecular level dynamics of azobenzene chromophores under light irradiation conditions, we are unable to explain few observations in detail as described in relavent sections. However, we believe the experimental data presented here paved a way for future in-depth theoretical and experimental works.

In a comparative observation of the SRG formation in PAZO and Trimer using different interference patterns (IIPs & PIPs), we have found that the PAZO is more efficient to pure intensity modulation while the trimer is very efficient to pure polarization modulation. This is the first report on characterizing a photosensitive material to be sensitive to certain interference pattern (i.e., pure intensity or pure polarization modulation). And we have also found intriguing grating formation behaviour (see Fig 4.1 and 4.3) for different interference patterns. To explain these results more experimental studies are required. The challenge here is to further elucidate the role of different $\vec{E}$-field vectors (viz., linear, elliptical and circular) in different interference patterns to the formation of surface relief grating in photosensitive materials.

SRG Formation by Intensity Interference Patterns*

The photoinduced orientation of azobenzene chromophores is understood to be one of the three important criteria for inscription of surface relief grating. The remaining two criteria include the molecular architecture of azobenzene containing photosensitive materials (i.e. the rigidity of the main chain and the length of the spacer in side-chains) and the effect of temperature.[83] The orientation of azobenzene chromophores is directed by the external electric field and it was found that the azobenzene chromophores tend to orient perpendicular to the linearly polarized electric field vector in order to attain a steady state (no further absorption of photons) and the individual *trans* form of azobenzene chromophores could be excited only following a relation of $\cos^2 \omega$, here ω is the angle between the electric field vector of the incident light and the transition moment of the photochromic moiety which coincides with its long molecular axis as shown in Fig 5.1.[84]

Detailed reports are available in literature, explaining the azobenzene chromophore orientation with respect to a linearly polarized light. Further, the light induced molecular reorientation is considered to be the driving force for molecular mass transport during the SRG formation.[83]

In order to understand these intriguing SRG formation phenomena, it is essential to assign the local orientation of electric field vector in different interference patterns to the polymer grating positions (i.e. maxima, minima etc). Observing the SRG formation in trimer films with IIPs (Fig 4.1(e-h)) we have made a primary assumption that the grating maxima might correspond to the intensity minima of IIP (section 4.1.2). From the Table 3.8, we could see that all the

---

intensity interference patterns (SS, PP, ‡45°, LL, RR) have only intensity modulation along the grating vector while the polarization of electric field remains constant. Thus knowing the response of PAZO and trimer towards intensity maxima or minima regions (i.e. photosensitive material mass transporting towards or away from light?) could offer a possibility to assign one complete period of different IIPs with the corresponding polymer grating positions.
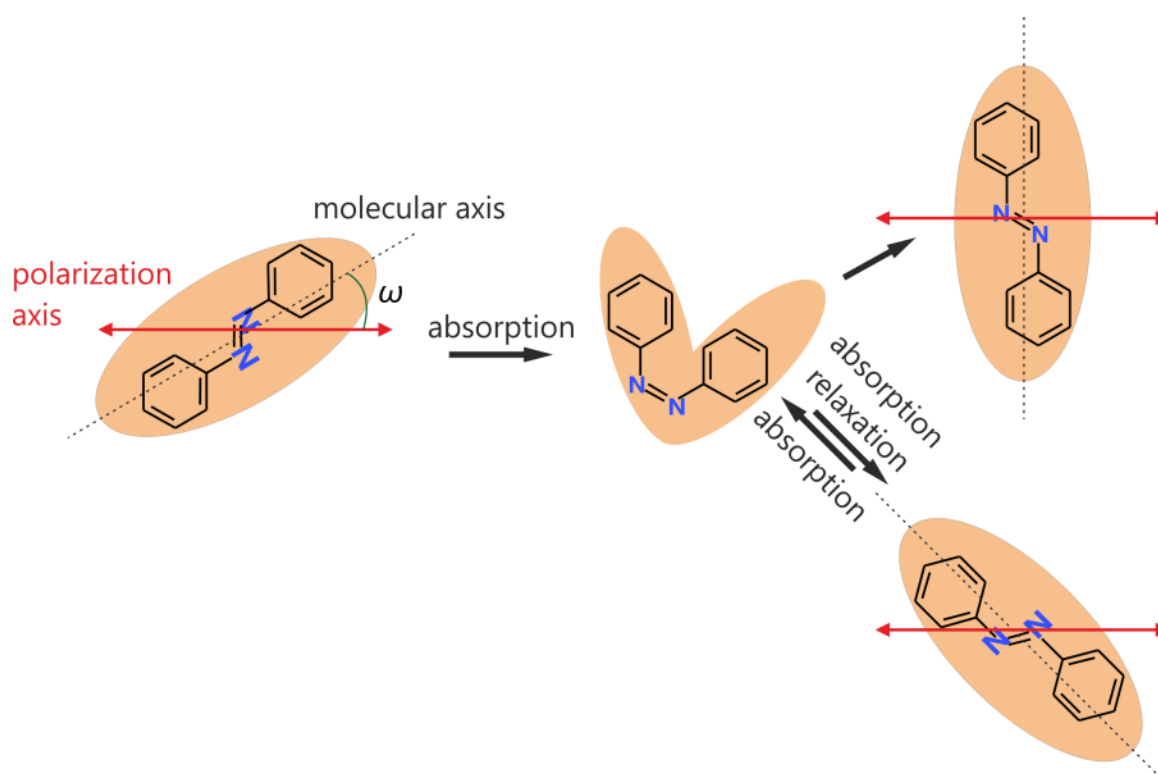
Fig. 5.1. Schematic representation of photoinduced reorientation and *cis-trans* isomerisation processes.

5.1. Mass transport response of photosensitive material to the light intensity

It is known that different photosensitive polymers will respond differently by mass transporting towards or away from light intensity.[85] To probe the photoinduced mass transport response of PAZO and trimer, we used a chromium mask with 100 nm thick chromium layer on glass substrate consisting of square (5×5 μm²) and circle (5 μm in diameter) arrays as both holes (Fig 4(a,

e)) and posts (Fig 4(i, m)). The chromium free regions of mask allows the maximum light to transmit through while blocking the light in Cr filled regions, thereby creating the bright and dark regions to probe the material flow.

Fixed Parameters	Intensity - 100 mW/cm^2	PAZO film thickness - 1±0.05 µm
	45° linear polarization (red arrow)	Irradiation from glass side (back side)
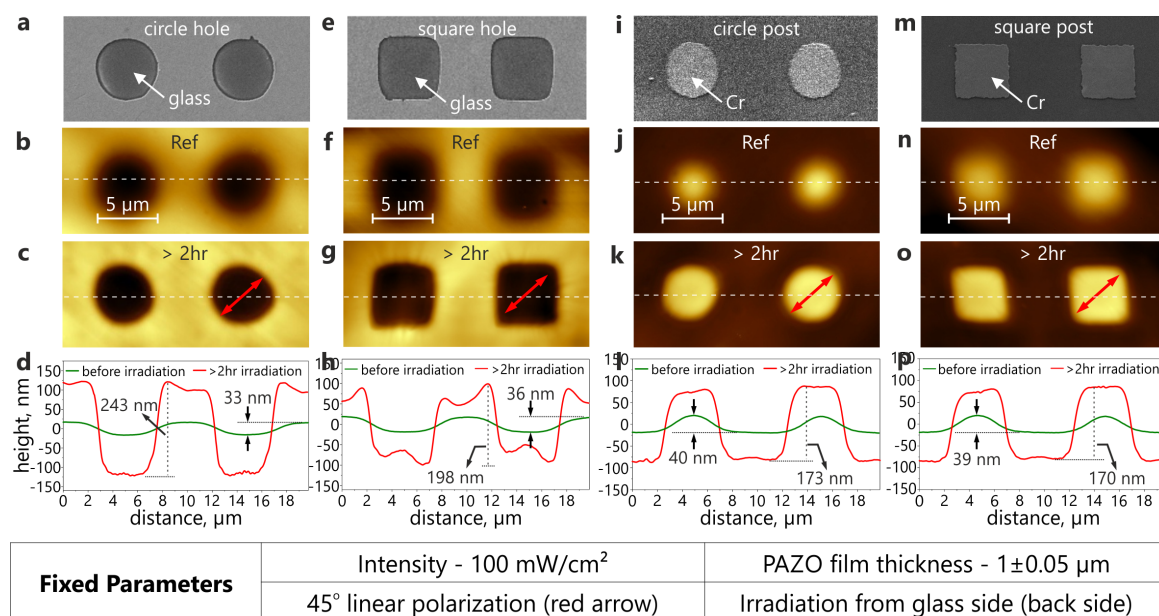
Fig. 5.2. Chromium mask experiment to determine the response of PAZO to the light intensity. a) Cr mask with circular apertures (holes). b) The AFM micrograph reveals the position of Cr apertures in a micrometre thick PAZO layer before irradiation. c) PAZO film after 2 hrs of irradiation with homogenous light. d) Comparison of extracted profiles from AFM micrographs in figure 'b' and 'c'. Green colour profile represents the cross section of polymer topography before irradiation and the red colour profile represents the polymer surface after irradiation with homogenous light. e), f) g) and h) shows the same experiment repeated with Cr mask having square aperture regions. i), j) k) and l) shows the Cr mask experiment with circular posts. m), n) o) and p) shows the Cr mask experiment with square posts.

A micrometre thick PAZO film, spin coated directly on the Cr mask is used for all the experiments presented in Fig 4. An *in-situ* AFM experiment is set up similar to the section 3.4.2, except that we used a linearly polarized homogenous light (single beam) to irradiate the sample from glass side while the polymer topography is scanned continuously with AFM tip. Fig 4(b, f, j, n) shows the topography of the polymer film on chromium mask before irradiation. The AFM micrographs of polymer topography before irradiation revealed the regions of

square and circular features, allowing us to observe the mass transport during *in-situ* measurement. The irradiation is continued until the topography changes (mass transport) were saturated. The PAZO film topography after 2hrs of irradiation is presented in Fig 4(c, g, k, o). The corresponding cross sectional profiles of polymer topography before (green) and after (red) irradiation are presented in Fig 4(d, h, l, p). The comparative analysis confirms the fact that the photosensitive material flowing (or) mass transporting away from light towards dark regions. We have repeated the similar Cr mask experiments with trimer as shown in appendix B.1. The results confirmed once again the observation made in chapter 4 (Fig 4.8), the trimer response with linearly polarized light is very weak. Despite a weak response, the result shows that the trimer also mass transports towards lower intensity or dark regions.

In addition to the study on intensity dependent mass transport behaviour of PAZO and trimer, we have also recorded the multiple wave interference patterns as a result of Fresnel diffraction through the above mentioned micro apertures, presented in appendix B.2.

Now we know that the photosensitive materials, PAZO and trimer are mass transporting away from the maximum light intensity regions, we could support our previous assumption, i.e. the SRG maxima might corresponds to the minimum intensity positions in the corresponding intensity interference patterns (Ch. 4, Section 4.1.2). However, experimental observation is still necessary to assign one complete period of different IIPs with the corresponding polymer grating (SRG) positions without further ambiguity. To overcome this challenge, once again we have employed our IIAFM setup in a unique way by switching between different interference patterns while following the corresponding changes in the polymer film topography during a single *in-situ* AFM measurement as described in the following section.

5.2. SRG formation in PAZO by intensity interference patterns (IIPs)

The experimental setup used to switch between different interference patterns (SS, PP, ‡45°) obtained by any linearly polarized interfering beams while simultaneously observing the polymer topography changes is presented in Fig 5.3. Before conducting the actual experiments, it is important to verify the reliability of the experimental setup and any possible artefacts in the measurements.

(i)   Extra λ/2 waveplates

Comparing to the optical scheme presented in Fig 3.6, we added an extra set of λ/2 plates (H_3 and H_4) in the path of interfering beams and a computer controlled shutter is placed (S) in front of sample as shown in appendix Fig B.3. Although the polarization state could in principle be controlled by the polarizers (P_1 and P_2) alone as we did for all the experiments in chapter 3, the extra wave plates (H_3 and H_4) are used to control the polarization state of each beam due to the specific experimental requirement of generating several subsequent interference patterns (viz. SS, PP, ±45° etc) at fixed interference point on sample surface in a single experiment. During *in-situ* AFM measurement, it is important to rotate the polarizer or waveplate in order to change the phase difference or polarization combination between the interfering beams.

Rotating the polarizer (calcite prisms) to adjust polarization state of the beams will alter the beam intensity and there by alters the fringe contrast in the interference pattern. Such rotation will also affect the beam path due to the air gap between the calcite prisms and results in the shifting of interfering beam position at the sample surface by few tens of micrometres. Thus, during *in-situ* AFM measurement, the observation of changes in polymer surface topography will be unreliable due to many artefacts. To overcome these problems, we chose to use the above mentioned extra λ/2 plates (H_3 and H_4), which are antireflection coated and have a maximum transparency at 491 nm wavelength. So while rotating the waveplate, the position of beams at the point of interference on polymer surface remains fixed and only the required phase or polarization state of the beam alters and the observed polymer topography variations during switching between interference patterns will be experimentally reliable.

In brief, polarizers (P_1 and P_2) are fixed with the transmission axis to allow only vertical linear polarization state while filtering any other noise during all the switching experiment presented in this and the following chapter 6. The purpose of λ/2 plates (H_1 and H_2) is only to maintain equal intensity in the interfering beams following Maulus's law. Finally, to switch the interference pattern during *in-situ* AFM measurements, it is essential to alter the polarization state of interfering beams or their phase difference (e.g. SS to PP or $SS^{\uparrow\uparrow}$ to $SS^{\uparrow\downarrow}$ etc). To achieve this, we used the extra λ/2 plates (H_3 and H_4) as shown in appendix Fig B.3.

The computer controlled shutter (S) is placed just in front of the sample to turn ON/OFF the interfering beams while switching between the interference patterns during *in-situ* AFM measurements.
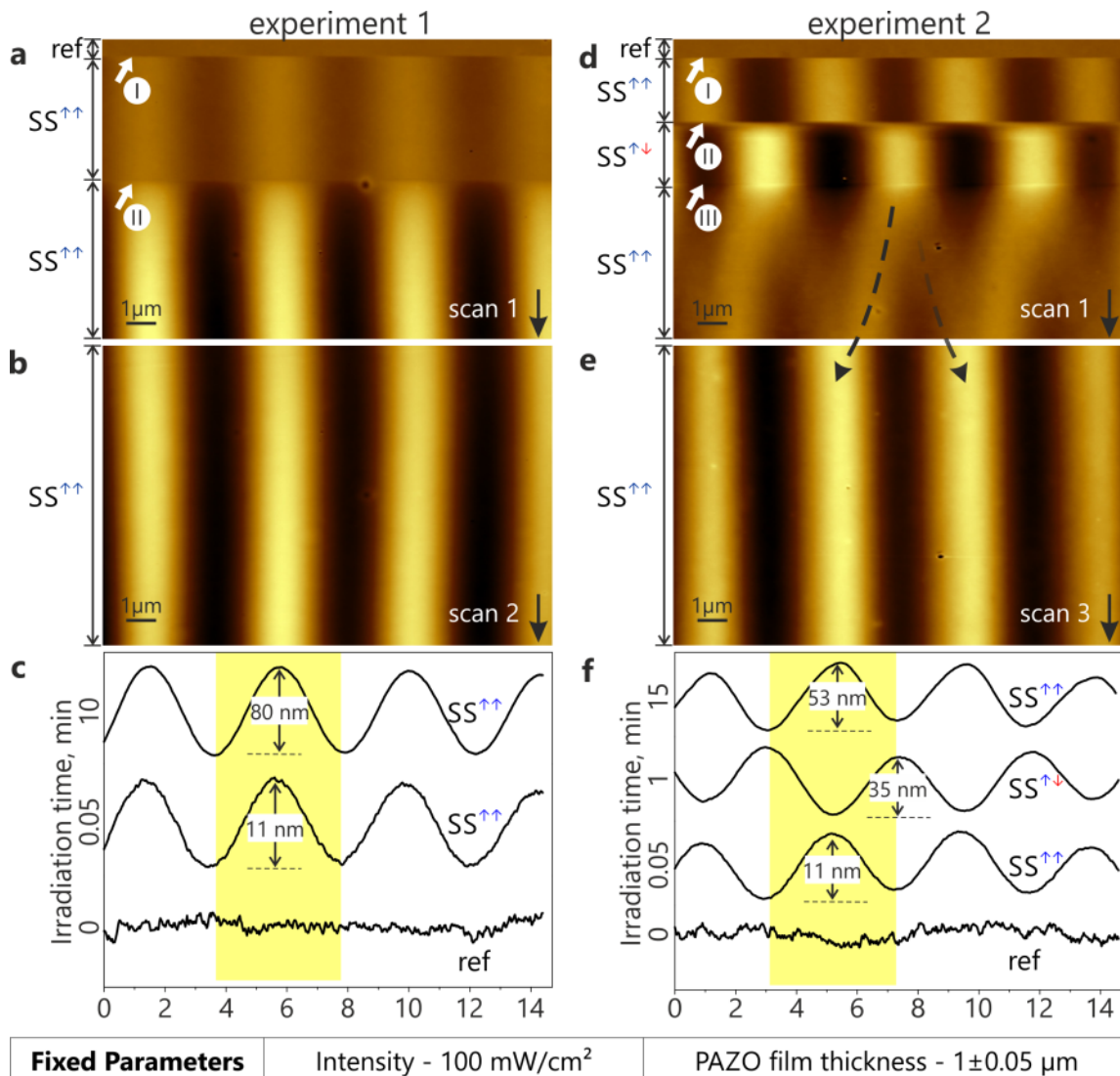
Fig. 5.3. AFM micrographs of the polymer topography recorded within a selected area. While the polymer topography is scanned, the polarization state of the interfering beams is changed in *in-situ*. Experiment 1 (a, b, c): topography change under irradiation with $SS^{\uparrow\uparrow}$ interference pattern. (a) The first irradiation event lasts only 5 seconds, followed by 3 minutes scanning in dark (till position "II"). At the level marked "II" irradiation with the same interference pattern ($SS^{\uparrow\uparrow}$ polarization) was resumed. (b) Continuous scan during irradiation. (c) Comparison of AFM cross-sectional profiles. Experiment 2 (d, e, f): The effect of 180° out of phase condition and reversible switching behaviour. (d) Switching between $SS^{\uparrow\uparrow}$ - $SS^{\uparrow\downarrow}$ - $SS^{\uparrow\uparrow}$ marked by "I", "II", and "III", respectively. (f) The grating migration behaviour presented with extracted cross section profiles from AFM micrograph. The black

arrows besides the scan number at the bottom right side of each AFM micrograph represent the AFM scan direction. The y-axis of (c) and (f) denotes the time of irradiation used for each combination before switching.

(ii)   Phase difference between the interfering beams

The state of the two interfering beams (plane waves) being in phase defines the point or position of the intensity maxima (constructive interference) and minima (destructive interference) in the intensity interference patterns assuming that the two interfering beams are in same polarization state in parallel as shown in appendix Fig B.4. If constructive or destructive interference is to continue occurring constantly at an arbitrary point 'P_0', at the centre of interfering beams on the photosensitive polymer film, the sources of the waves must be coherent sources. Two sources are coherent if the waves they emit maintain a constant phase relation. Effectively, this means that if the two interfering beams assumed to be in 0º phase to each other at an arbitrary point 'P_0' resulting a constructive interference and if one of the beam is rotated by 180º to become out-of-phase with respect other beam at the arbitrary point 'P_0', the interference pattern shifts by half a period (see appendix Fig B.4).

Simple notation was adapted to represent two interfering beams are in phase with 0º or out of phase by 180º to each other. With respect to an arbitrary point 'P_0' as shown in appendix Fig B.4, when two beams are assumed to be in phase with each other, two upward arrows are used in superscript of particular polarization combination 'SS$^{\uparrow\uparrow}$' to represent in phase condition. When one of the beams is rotated with the help of a half wave plate (H$_3$ or H$_4$) to achieve 180º out of phase or antiphase with respect to point 'P_0', inverted arrow (red) is used in superscript 'SS$^{\uparrow\downarrow}$'. It is important to note that when we create a phase difference of 0º or 180º using a $\lambda/2$ plate, the polarization state of the beam remains constant.

(iii)   Test experiment

To test the accuracy of our optical alignment, precision of feedback loop during the *in-situ* AFM scan and the influence of interfering beams on the AFM scan stability, we have performed an experiment as presented in Fig 5.3 (a-c). The *in-situ* experiment is started with scanning a polymer surface (1 μm thick PAZO film on glass substrate) without irradiation from top to bottom. After 30 sec of the reference scan, the interfering beams (in phase relation) are switched on with the first interference pattern (SS$^{\uparrow\uparrow}$) for a relatively short time of 5 seconds (marked as "I" in Figure 5.3a) and switched off quickly with an automated computer controlled shutter. The initiation of polymer film deformation is observed

immediately, i.e. in the first second of scanning under irradiation and the film forms a surface relief grating (SRG) with an average height of 10 ± 2 nm.

While the AFM scan is in progress, after four minutes the shutter reopened for rest of the experiment (marked as 'II') with the same interference pattern (SS$^{\uparrow\uparrow}$). In the subsequent scan (starting from mark 'II'), the position of the maxima and minima of the SRG stays in the same position while the height grows continuously until 80 ± 5 nm and reached a stationary growth phase. In figure 5.3c, the cross sectional profiles from the AFM micrographs during two stage of irradiation with SS$^{\uparrow\uparrow}$ pattern are compared.

The results presented in experiment 1 (Fig 5.3(a-c)) confirms the stable alignment of experimental setup and the precision of AFM scan feedback loop during the *in-situ* measurements. When the interference pattern is switched ON/OFF with the help of a shutter, there is no shift in the SRG position during the ongoing scan and also no significant influence of interfering beams on AFM tip is observed.

5.2.1. Switching between SS$^{\uparrow\uparrow}$ and SS$^{\uparrow\downarrow}$ interference patterns

The observation of SRG formation, while changing the phase difference between interfering beams (i.e. SS$^{\uparrow\uparrow}$ to SS$^{\uparrow\downarrow}$) is an important tool to make sure that the change in polymer topography indeed related to the changes in the corresponding interference pattern. In addition, it also help to observe the mass transport mechanism in photosensitive polymer film and to assign the $\vec{E}$-field vector distribution in different intensity- and polarization interference patterns with the corresponding polymer grating positions.

In section (5.2*ii*), we have discussed the shift in interference pattern by half a period when we alter the phase difference between the interfering beams from 0o to 180o. It is interesting to see if the polymer grating also shifts its position by half a period when we switch the interference pattern between SS$^{\uparrow\uparrow}$ and SS$^{\uparrow\downarrow}$.

Experiment 2 in Fig 5.3(d–f) shows a reversible switching behaviour and the SRG formation during the change in phase difference between two interfering beams (SS$^{\uparrow\uparrow}$ to SS$^{\uparrow\downarrow}$). After 30 seconds of reference scan the laser beams are switched ON (marked as 'I') with SS$^{\uparrow\uparrow}$ for <5 seconds and switched OFF with automatic shutter. While the cantilever tip is scanning polymer surface in dark, beam1 was altered with the help of λ/2 plate (H₃) to achieve 180o out of phase condition relative to beam2 keeping polarization state of both the beams same (SS). During the scan progress at 3ʳᵈ minute (marked as 'II'), the beams are switched on with SS$^{\uparrow\downarrow}$ interference pattern for a period of one minute and switched OFF. We observed an immediate shift in the polymer topography by half a period relative to the

previous SRG position and continued growing in new position until the irradiation is switched OFF.

Following the irradiation with $SS^{\uparrow\downarrow}$, while the AFM scan continues in dark, the beam1 is switched back to $0°$ phase condition and at 5th minute of scanning (marked as 'III'); the beams are switched on with original $SS^{\uparrow\uparrow}$ interference pattern for the remaining experiment. The extracted profiles from the AFM micrographs in Fig 5.3d and 5.3e are compared in Fig 5.3f.

The AFM micrograph in Fig 5.3d visualizing the effect of phase difference between the interfering beams. The reversible switching of the polymer grating between $SS^{\uparrow\uparrow}$ to $SS^{\uparrow\downarrow}$ and back to $SS^{\uparrow\uparrow}$ shows different kinetics at each step. During the first switching step from $SS^{\uparrow\uparrow}$ to $SS^{\uparrow\downarrow}$ the induced molecular anisotropy in PAZO film is weaker due to <5 seconds of irradiation. In contrast, due to one minute long irradiation with $SS^{\uparrow\downarrow}$ the induced anisotropy in polymer film is stronger. Thus, the reversible switching condition between $SS^{\uparrow\downarrow}$ - $SS^{\uparrow\uparrow}$ took another 15 minutes of irradiation to reveal the final SRG position. Nevertheless, the reversible switching behaviour clearly demonstrates the mass transport phenomenon in photosensitive polymer film during SRG formation due to interference pattern and the further analysis is provided in Fig 5.4.
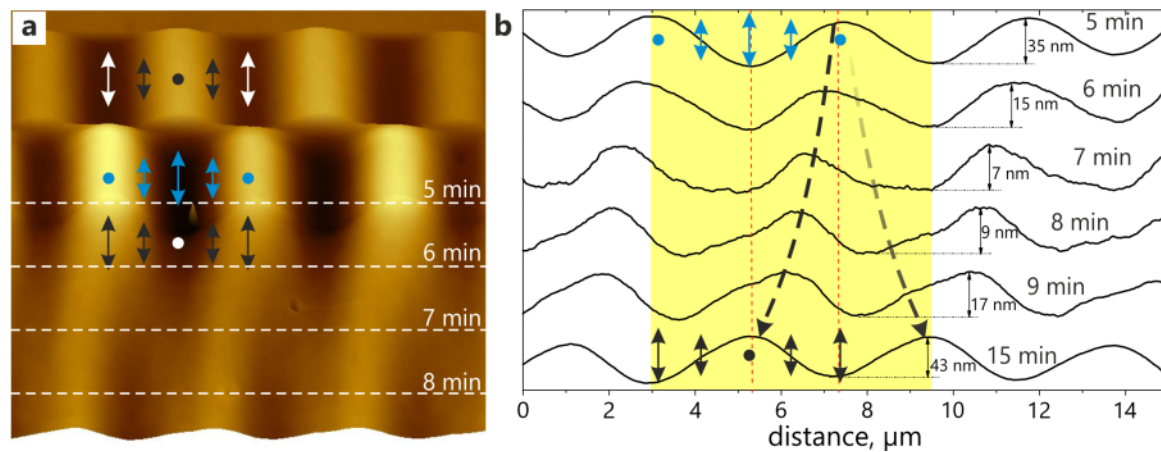
Fig. 5.4. Mass transport behaviour in photosensitive polymer film while switching between $SS^{\uparrow\uparrow}$ - $SS^{\uparrow\downarrow}$ - $SS^{\uparrow\uparrow}$. The grating migration behaviour presented with extracted cross section profiles from AFM micrograph.

From section 5.1, we know that the PAZO goes away from light intensity and combing our understand with the experiments presented in Fig 5.3, we could

assign the $\vec{E}$-field vector distribution of SS interference pattern with the polymer grating positions as shown in Fig 5.3d. The grating minima correspond to the intensity maxima and vice versa. Figure 5.3b presents the mass transport behavior of surface relief maxima towards new grating positions. Following the switching of interference pattern from SS$^{\uparrow\downarrow}$ - SS$^{\uparrow\uparrow}$ the SRG maxima immediately starts mass transport towards the lowest intensity regions. The grating shape clearly indicates the sliding behaviour of maxima towards new position and also the splitting of actual maxima into two half portions migrating towards the adjacent new lowest intensity regions. The grating height reduced during the sliding phenomenon from 40nm to 6nm before it starts growing at new positions. The mass transport effect is the result of intensity modulation (I_{max} and I_{min}) but not the polarizing vector due to only the intensity modulates in the SS interference pattern.

From the experiments presented in Fig 5.3, we would like to mention that the accuracy of our experimental setup and *in-situ* AFM measurement allows us to relate polymer topography changes precisely to the corresponding interference patterns.

The general protocol or experimental steps for all the upcoming experiments in this and following chapter 6 involving switching between difference interference patterns will be same as described in the current section.

5.2.2. SRG formation in PAZO by SS, PP and ‡45º interference patterns

In the intensity modulated interference patterns (SS, PP, ‡45º, LL, and RR) the polarizing vector remains constant with only intensity oscillating along the grating vector in the XY-plane as shown in Table 3.8. If two plane waves interfering at the arbitrary point 'P_0' with the same intensities but only the polarization of each beam rotated by 90° from vertical linear to horizontal linear polarization state (i.e., from SS to PP) maintaining a constant in-phase relation between them, the position of bright (I_{max}) and dark fringes (I_{min}) will not change in the resulting interference patterns. To confirm this theoretical understanding, we have performed several switching experiments between all the IIPs as described in the following.
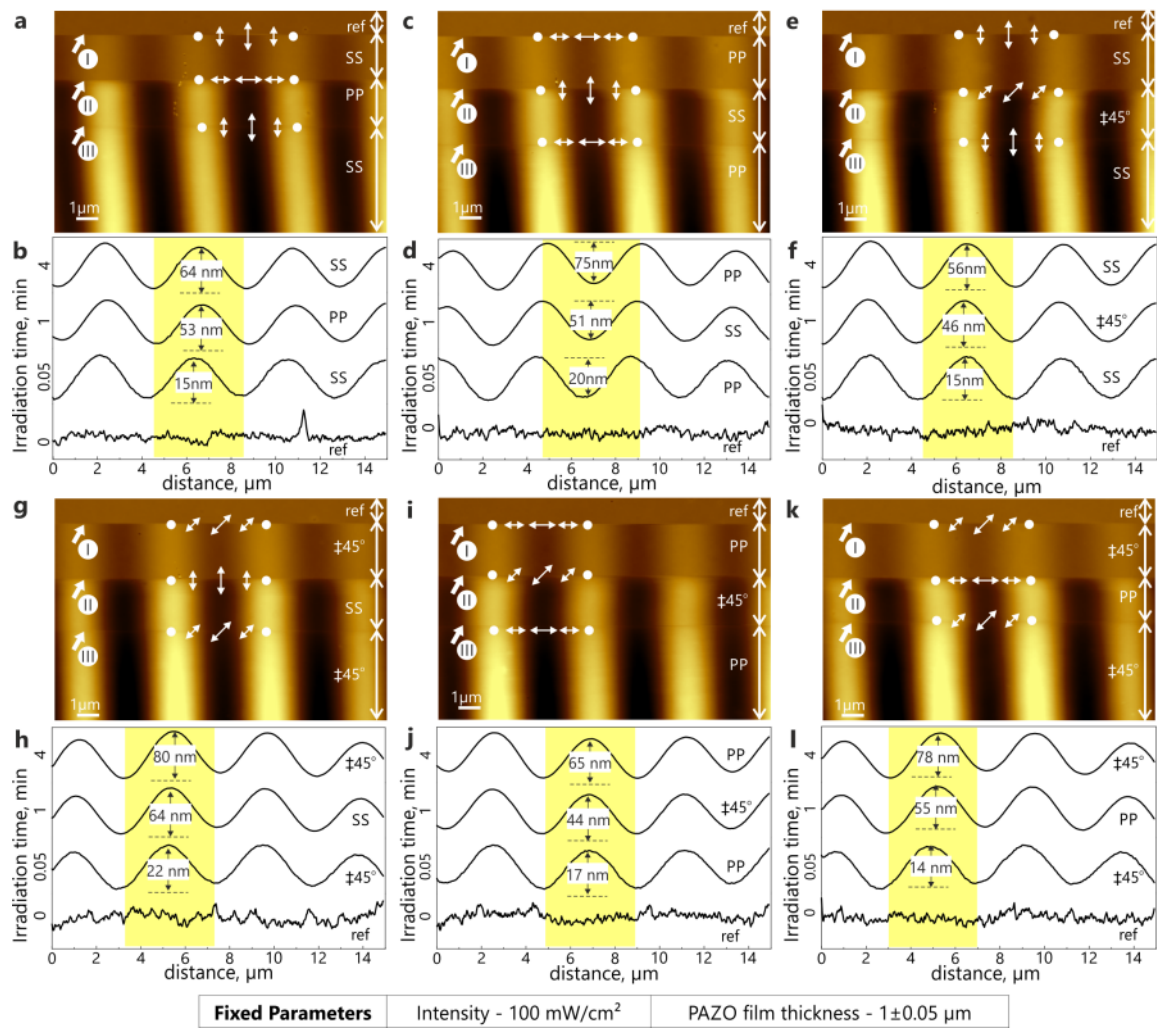
Fig. 5.5. *In-situ* AFM measurements of the topography change under irradiation with IP of different combinations: SS, PP and ‡45° in single measurement. (a) The scan starts with reference scan from top towards bottom, at a position "I" the irradiation with SS combination is switched on for 5 seconds. At the position marked by "II" the polarization is changed to PP combination, followed by reversible switching to SS combination at point "III". b) comparison of extracted profiles from figure a. (c) Reversible switching experiment between PP–SS–PP. d) comparison of extracted profiles from figure c. (e) Reversible switching experiment between SS–‡45°–SS. f) comparison of extracted profiles from figure e. (g) Reversible switching experiment between ‡45°–SS–‡45°. h) Comparison of extracted profiles from figure g. (i) Reversible switching experiment between ‡45° –PP–‡45°. j) Comparison of extracted profiles from figure (i). (k) Reversible switching experiment between PP–SS–PP. l) Comparison of extracted profiles from figure k. The scan direction for all the experiments is from top to bottom. The y-axis of (b), (d), (f), (h), (j) and (l) denotes the time of irradiation used for each combination before switching.

Fig 5.5 shows a set of six experiments, in which all the intensity modulated interference patterns obtained with linearly polarized interfering beams (SS, PP and ‡45º) in-phase condition are mixed with reversible switching between every two combinations. All the measurements started with a reference scan in first 30 sec from top to bottom. In Fig 5.5a, reversible switching experiment is performed between SS–PP–SS similar to the experiments presented in section 5.2.1. During *in-situ* AFM measurement, while switching from SS to PP and back to SS, the grating position remains unchanged. Combing all other possible combinations between SS, PP and ‡45º shows the same result (Fig 5.5). In appendix Fig B.5, we presented a single measurement, SS and PP and ‡45º patterns are switched simultaneously and the results observed are remain same without any change in grating position.

In some of the AFM micrographs presented in Fig 5.5, the grating position seems to be slightly deviating from the starting position during downward scan direction. In our *in-situ* AFM design, the AFM body is round in shape and is mounted on supporting legs as shown in appendix Fig B.6. The cantilever scanning direction is set to 0º by default and the cantilever holder should orient perpendicular to the optical Table to achieve scanning of sample topography perpendicular to the polymer grating lines (SRG). Due to manual alignment procedure, sometimes the AFM body is positioned a few degrees away from 0º alignment, as a result the scan direction also tilt few degrees. This small rotation of AFM body will not affect the *in-situ* AFM measurement, but the acquired image looks as shown in Fig 5.5.

5.2.3. SRG formation in PAZO by LL and RR interference patterns

Until now, we have discussed the SRG formation using IIPs obtained by interfering two linearly polarized beams in parallel. In this section, we will use the IIPs obtained by two circularly polarized beams knows as LL (*LCP:LCP*) and RR (*RCP:RCP*) interference patterns. Comparing to the optical scheme presented in Fig B.3, we added an extra set of $\lambda/4$ plates (Q_1 and Q_2) in the path of interfering beams. The scheme of experimental setup used to switch between circularly polarized interference patterns is presented in appendix Fig B.7.
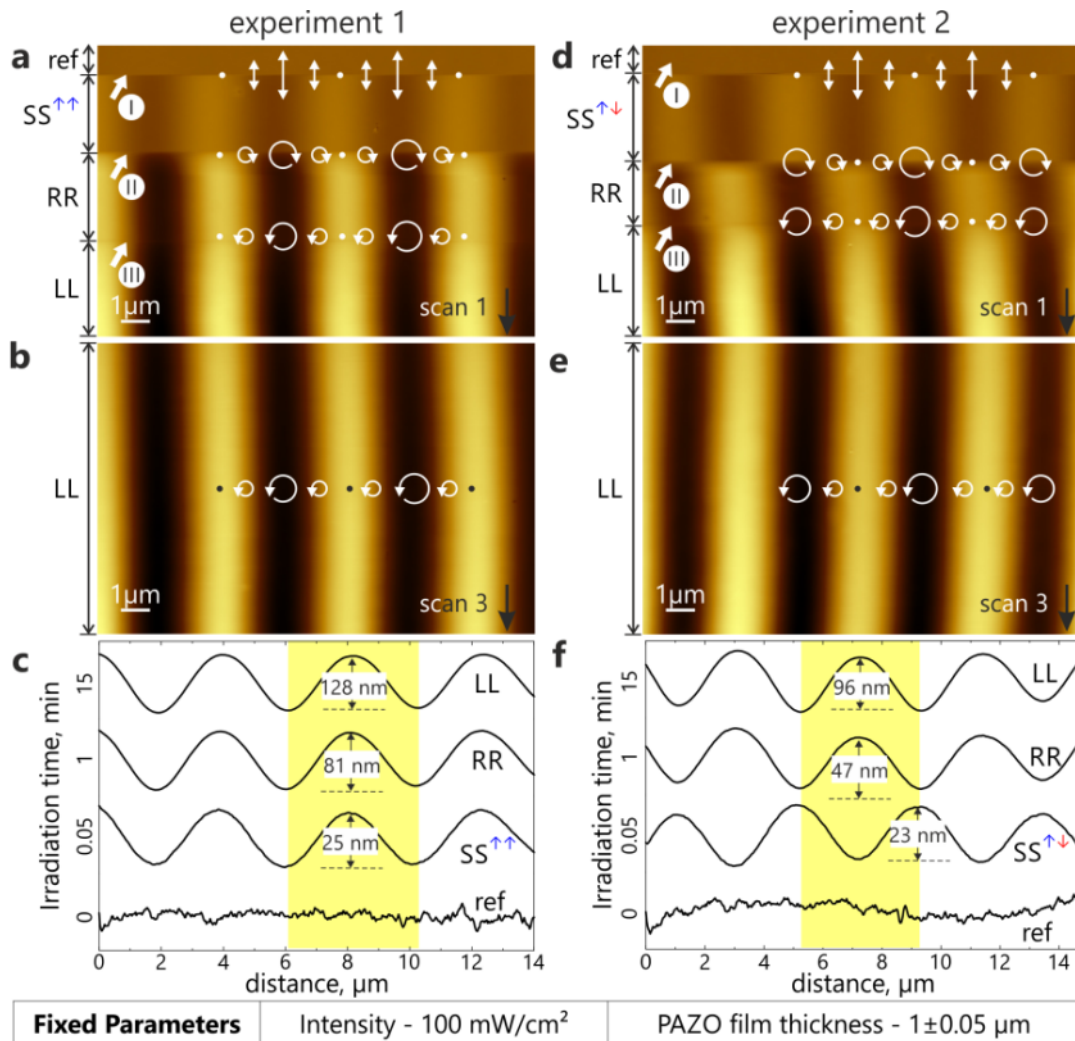
Fig. 5.6. SRG formation while switching the interference patterns from SS$^{\uparrow\uparrow}$ to LL to RR and from SS$^{\uparrow\downarrow}$ to LL to RR. Experiment 1 (a, b, c): topography change under irradiation with SS$^{\uparrow\uparrow}$ interference patterns. (a) The first irradiation event lasts only 5 seconds, followed by 3 minutes scanning in dark (till position "II"). At the level marked "II" irradiation with LL interference pattern was started. At level marked "III" the interference pattern is switched to RR. (b) Continuous scan during irradiation with RR pattern. (c) Comparison of AFM cross-sectional profiles. Experiment 2 (d, e, f): The effect of 180° out of phase condition and the SRG formation by LL RR patterns. (d) Switching between SS$^{\uparrow\downarrow}$ – LL – RR marked by "I", "II", and "III", respectively. The distribution of $\vec{E}$-field vector on the polymer surface is shown. The black arrows besides the scan number at the bottom right side of each AFM micrograph represent the AFM scan direction. The y-axis of (c) and (f) denotes the time of irradiation used for each combination before switching.

The extra $\lambda/2$ plates mentioned in appendix Fig B.3 are still used though only $\lambda/4$ plates (Q_1 and Q_2) after polarizers are sufficient to achieve circularly polarized beams. The reason for this choice is to conveniently switch between any linearly polarized interference pattern to any circularly polarized interference pattern and vice versa (e.g. switching between SS to LL), without disturbing the position of interference on sample.

Once again to check the accuracy of the optical alignment (new waveplate combination) and to assign $\vec{E}$-field vector distribution of the LL and RR interference patterns with the corresponding SRG positions in polymer film, we choose to perform switching experiments from $SS^{\uparrow\uparrow}$ to LL to RR and from $SS^{\uparrow\downarrow}$ to LL to RR as presented in Fig 5.6.

In experiment 1 [Fig 5.6(a-c)], while switching from $SS^{\uparrow\uparrow}$ to LL to RR no change in grating position is observed thus confirming the fact that if two plane waves interfering at the arbitrary point 'P_0' with the same intensities but only the polarization of each changed (i.e., from SS to LL to RR) maintaining a constant in-phase relation between them, the position of bright (I_{max}) and dark fringes (I_{min}) will not change in the resulting interference patterns.

To further validate the above said result and the functionality of new waveplate combinations we have performed experiment 2 as shown in Fig 5.6(d-f) by switching the interference pattern from $SS^{\uparrow\downarrow}$ to LL to RR. As we expected, when we are switching the interference patterns from 180° out of phase condition to an in-phase condition, the interference pattern will switch by half a period and thereby SRG position.

5.2.4. SRG formation in trimer by IIPs

The experiments presented in Fig 5.5 and 5.6 shows that using any intensity interference pattern (*viz.*, SS, PP, ‡45°, LL, RR) for PAZO the SRG maxima corresponds to the local intensity minima of associated interference pattern and vice versa. To generalize this observation, here we have studied the SRG formation behaviour in trimer using all the IIPs.

The experimental procedure is repeated similar to the previous sections (5.2.2 and 5.2.3). In Fig 5.7, we have presented two experiments involving the switching between IIPs obtained by linearly polarized beams (i.e. SS, PP and ‡45°) and switching between IIPs obtained by circularly polarized beams. Fig 5.7a shows the trimer film topography before irradiation. The SRG formation in trimer while switching between different intensity interference patterns is presented in Fig

5.7(b, d). From the AFM micrographs and the cross sectional profiles, we could conclude that there is no change in SRG position in trimer films while switching between different intensity interference patterns. Using the Cr mask experiment, we know that trimer also mass transports away from the light intensity. Thus, the results observed with trimer are similar to that of PAZO except that the SRG formation efficiency.

The grating maxima occur at the intensity minima regions of IIP. This phenomenon can be explained using recent approaches which are based on free energy and the symmetry considerations for amorphous azobenzene containing materials.[42,80] In the case of homogeneous illumination, the minimum of free energy can be achieved if the sample stretches or contracts itself along the polarization direction, the sign of deformation depends on the chemical structure of azobenzene containing molecules.[79] However, in the case of intensity interference patterns, in particular SS and PP, the total free energy, integrated over one grating period, is shown to be minimized if the material moves in the direction of the local free energy decrease.[80] This direction coincides with the direction of decreasing light intensity.

Comparatively, PAZO is very sensitive to the intensity gradient in the interference pattern while trimer response is significantly weaker for intensity gradient. This phenomenon is possibly due to the difference in the molecular weight. PAZO is a high molecular weight polymer with approximately 40 repeated azobenzene units attached to the backbone chain, while trimer consists of only three azobenzene units to a core benzene ring. The molecular reorientation and the associated mass transport processes are much stronger in PAZO due higher rate of molecular level dynamics in single chain and between neighbouring molecules. In contrast trimer might experience a weak force for molecular mass transport process.
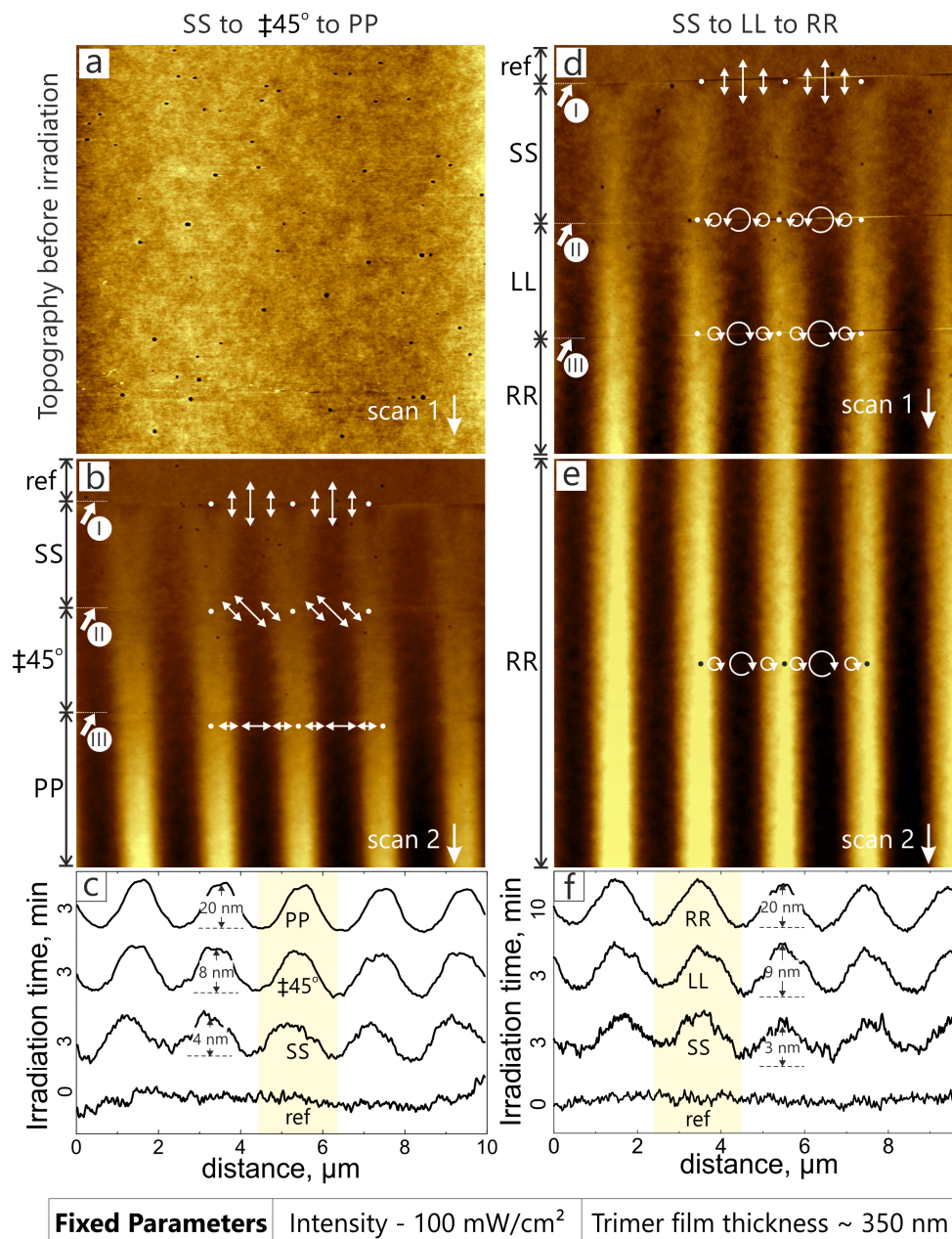
Fig. 5.7. AFM micrographs of the trimer film topography change recorded *in-situ* during switching the polarization combination of the interfering beams. (a) Topography before irradiation. (b) By scanning from top to bottom, the irradiation with SS combination is switched ON at the point marked by "I" (white arrow). At positions "II" and "III" the irradiation is changed to ‡45° and PP, respectively. d) By scanning from top to bottom, the irradiation with SS combination is switched on at the point marked by "I". At positions "II" and "III" the irradiation is changed to LL and RR, respectively. (c) Cross sectional profiles from the AFM micrograph in (b). (f) Cross sectional profiles from the AFM micrographs in (d) and (e).

5.3. Visualization of pure intensity and pure polarization modulation in the interference patterns

In section 3.5.4, we have mentioned that the maximum achievable film thickness for trimer is restricted to ~ 350 nm due to the limitation in the synthesis. When the components of chemical mixture slightly varied, the precipitation starts immediately, making the trimer solution unstable (see Fig 5.8 a, c). However, this turned out to be an advantage to prove that the SRG maxima correspond to the intensity minima in the interference pattern. In addition, we are also able to visualize the intensity modulation in both the IIPs and PIPs as shown in Fig 5.8.

In theory, we know that the IIPs are purely intensity modulated (constant polarization) and PIPs are purely polarization modulated (uniform intensity) with paraxial approximation. To prove it experimentally, either we should use a beam profiler or we need a good chemical probe. Here, we used the trimer film containing the aggregates of azo dye to study the quality of interference patterns. We used PP and ±45° interference patterns to represent IIP and PIP respectively with a grating periodicity of 4 μm (7° of angle between interfering beams), fulfilling the paraxial approximation.

From Table 3.8, we know that all the intensity interference patterns supposed to have an intensity gradient with good fringe contrast, $\left(v = \dfrac{I_{\max} - I_{\min}}{I_{\max} + I_{\min}} \right)$ which is periodical modulation of bright and dark regions. We could assume that in the dark regions of PP interference pattern, no photo isomerization takes place in trimer film. We could observe this result in Fig 5.8b, where the trimer film is irradiated for 1hr with PP interference pattern. Due to photo isomerization and molecular mass transport processes, all the holes are filled up or vanished except at the SRG maxima, where no reaction takes place due to dark zones. This also supports the reliability of our optical setup with good fringe contrast and proves once again that for all the intensity interference patterns, the SRG maxima correspond to the intensity minima of associated interference pattern.

 Intensity remains contestant throughout the irradiation area for polarization interference patterns (PIPs), thus reaction takes places throughout the film due to the modulation of localized $\vec{E}$-field vector as shown in Table 3.8. We could observe this phenomenon in Fig 5.8d, where we have presented the SRG formation in trimer film after 1hr of irradiation with ±45° interference pattern. However, we are yet to understand how the SRG topography (i.e. maxima or minima) corresponds to the polarization modulation in the PIPs. We will deal with this task in detail in following chapter 6.
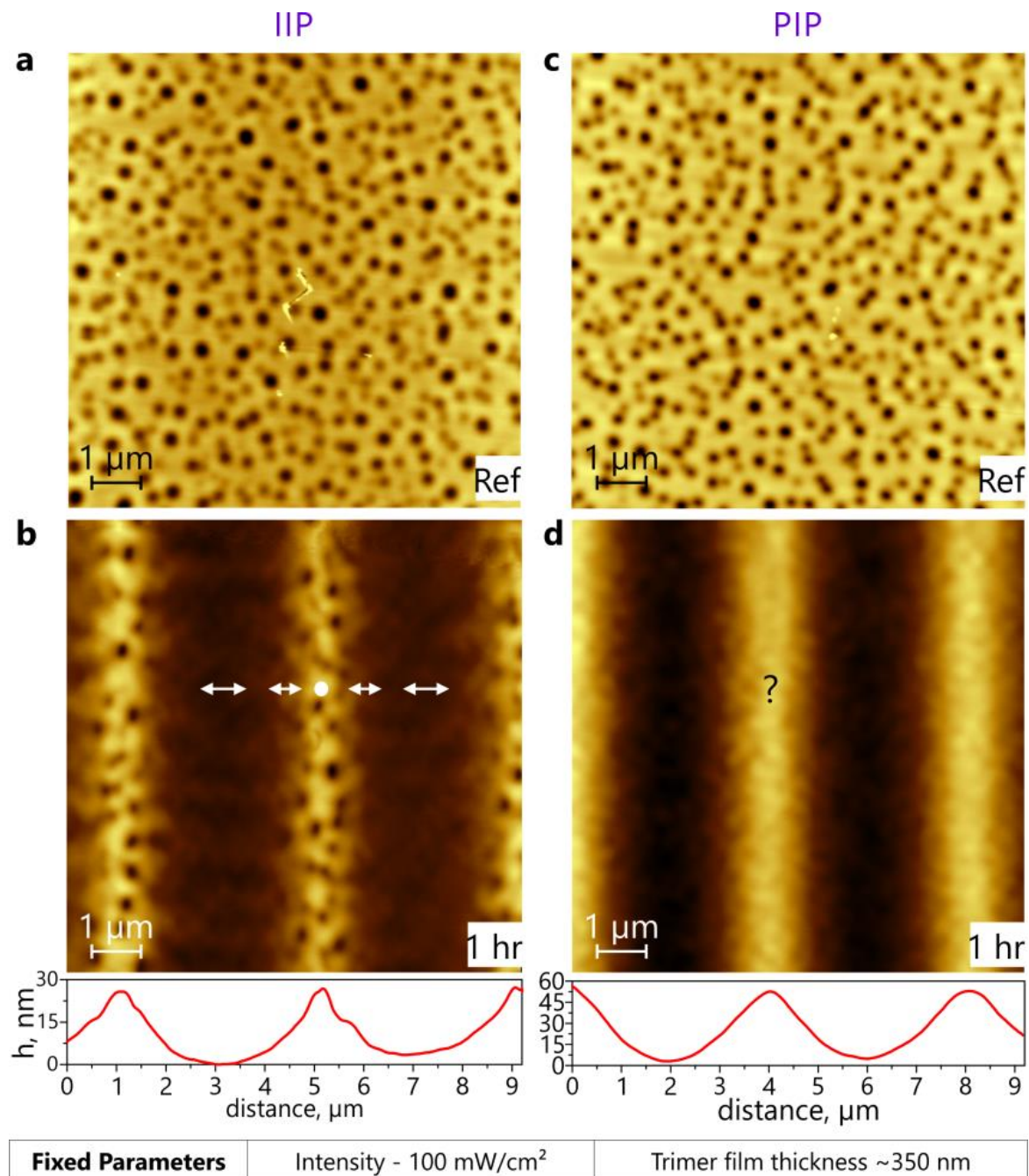
Fig. 5.8. (a), (c) Trimer film topography before irradiation. (b) Trimer topography after 1 hr of irradiation with PP interference pattern and its cross sectional profile. The interference pattern is also shown corresponding to the SRG topography. (d) Trimer topography after 1 hr of irradiation with ±45° interference pattern and its cross sectional profile. We are yet to correlate the local $\vec{E}$-field vector of PIP interference pattern with the SRG topography.

5.4. Local $\vec{E}$-field vectors of the IIPs *vs.* the SRG topography

In the intensity modulated interference patterns, the position of I_{max} and I_{min} remains unchanged when switching from one interference pattern to the other with constant phase relation. Thus for all the intensity modulated interference patterns (IIPs) such as SS, PP, ‡45°, LL, and RR the PAZO surface relief maxima and minima positions are correspond to the intensity minima (I_{min}) and maxima (I_{max}) respectively as shown in Table 5.1.

The assignment presented in Table 5.1 is only valid when the photosensitive material mass transports away from light intensity. For instance, a photosensitive material mass transports towards light intensity, then the surface relief maxima and minima correspond to the intensity maxima (I_{max}) and minima (I_{min}) in the associated intensity interference pattern.

Table 5.1. Experimentally derived SRG positions as a function of different intensity interference patterns. This table is only valid for any photosensitive material mass transports away from light intensity.

5.5. Summary

In a short overview of this chapter, here we apply our IIAFM setup as shown in Fig B.3 and Fig B.7 to study the correlation between surface relief topographies of azobenzene containing polymer films and the $\vec{E}$-field vector distribution of the intensity interference patterns (IIPs). The analysis is carried out for two photosensitive materials, PAZO and trimer.

We used a Cr mask consisting square and circle apertures in both hole and post configurations, defining the bright and dark regions to probe the mass transport response of PAZO and trimer towards light intensity and found that both PAZO and trimer flows away from light intensity towards dark regions. Using our IIAFM setups, we have acquired the local changes in topography of the polymer surface while at the same time switching between different types of interference patterns (Figs 5.3, 5.5, 5.6 and 5.7). The studies with all intensity interference patterns (IIPs) show that

- The position of intensity minima corresponds to the topography maxima, whereas the positions of the intensity maxima can be related to the topography minima.
- The SRG maxima and minima positions are determined purely by intensity gradient in the interference patterns.
- The polarization of interference patterns only contribute to the grating formation efficiency.
- PAZO is very sensitive to the intensity modulation and has better grating formation efficiency compared to the trimer.

SRG Formation by Polarization Interference Patterns*

In the previous chapter, we have learnt that intensity gradient in the interference pattern (IIP) plays major role to inscribe the surface relief grating in PAZO films. In contrast, trimer response towards IIPs is significantly weaker. Similarly, in Fig 4.8, we have learnt that SRG formation is very efficient in trimer compared to PAZO using polarization interference patterns (PIPs). Particularly, in case of trimer films, efficient grating formation is observed even in 100 nm thin films using PIPs (±45° and RL) and SRG formation efficiency in 100 nm thin PAZO films is insignificant using any interference pattern possibly due to its high molecular weight. In addition to these observations, we have seen intriguing SRG formation behaviour in case of ±45° and SP interference patterns as shown in Fig 6.1.

In Fig 6.1, we have presented a comparative observation of SRG formation behaviour using IIP (PP) and PIP (±45°, and SP) interference patterns. For PP interference pattern (Fig 6.1a) a rapid growth rate of 117 nm is observed in the first three minutes and the growth rate saturates after 30 minutes. In contrast, for ±45° and SP patterns a gradual growth rate was observed throughout the irradiation time (refer fig 4.6 for the grating growth kinetics). Further, there are significant differences in the grating formation behaviour.

As reported in literature,[79,80,81] the polymer grating periodicity (d) using SP interference pattern is always half of the optical periodicity (d=D/2). The reason for such unique grating formation behaviour using SP interference pattern is not clearly understood and very few reports are published in the past decade. We

---

have also observed similar result in both the PAZO and trimer films using SP interference pattern as shown in Fig 6.1c and Fig 4.3(b, e).
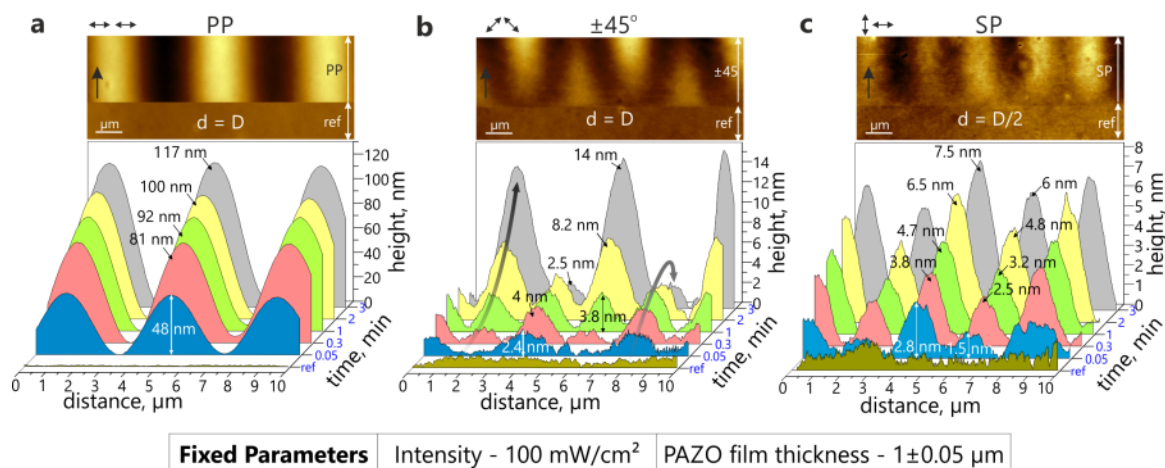
Fig. 6.1. Comparison of intensity and polarization interference patterns. The black arrows in the AFM micrographs represent the scan direction. (a) PP is an intensity interference pattern (IIP) and the growth of grating within the first 3 minutes of irradiation shows exponential growth behaviour and the optical periodicity (D) is equal to the observed polymer grating periodicity 'd'. (b) ±45° pattern is a polarization interference pattern (PIP) and the grating growth rate is gradual with phase transitions between the appearing and disappearing surface relief peaks in the first 3 minutes. The final polymer grating periodicity is equal to optical periodicity (d ~ D). (c) SP is also a polarization interference pattern and the grating growth behaviour is gradual with polymer grating periodicity is always half of the optical periodicity (d ~ D/2).

In-situ observation of the SRG formation in PAZO films using ±45° interference pattern revealed more intriguing behaviour with the grating being initiated with half of the actual optical periodicity (d=D/2) as shown in Fig 6.1b, however the final grating periodicity tend to be equal to the optical periodicity (d=D). In the AFM micrographs, this is perceived as a transition between appearing and disappearing grating lines or peaks. This phenomenon appears to be independent of the periodicity of interference pattern as shown in Fig 6.2. However, the grating peak transition behaviour is absent in trimer films where the grating periodicity is always equal to the optical periodicity (d=D) as shown in Fig 4.3b.

74

With a relatively short angle between the interfering beams, we could expect that there is no intensity modulation in the PIPs (see Table 3.8 and Fig 5.8b). This fact leads us to the assumption that the SRG formation using PIPs might be governed by the local $\vec{E}$-field vector in whole. Thus as a first step to understand the unique SRG formation behaviour in PAZO films using SP and ±45° interference patterns and the associated microscopic processes, it is important to correlate the $\vec{E}$-field vector distribution of PIPs with the SRG topography similar to the Table 5.1. Once again, we have started the study of SRG formation using PIPs by observing the influence of phase difference between the interfering beams.
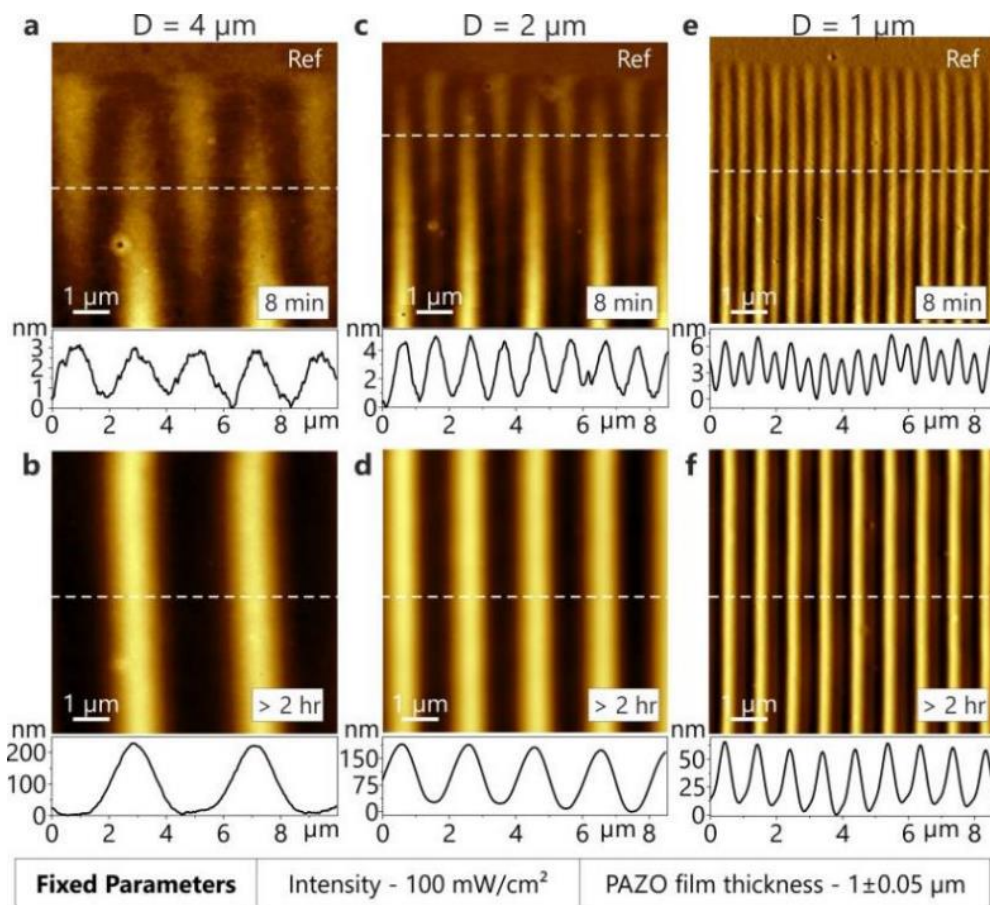
Fig. 6.2. Comparison of phase transitions in ±45° interference patterns at different optical periodicities (D). a), c) and e) showing the phase transitions with ±45° interference pattern in polymer gratings in first 8min for 4μm, 2μm and 1μm periodicities respectively. b), d) and f) showing the final grating with ±45° interference pattern in polymer gratings for 4μm, 2μm and 1μm periodicities respectively.

6.1. Effect of phase difference between the interfering beams on SRG formation

Similar to the experiment performed with switching between SS$^{\uparrow\uparrow}$ and SS$^{\uparrow\downarrow}$ (Section 5.2.1), the effect of phase difference between orthogonal interfering beams could be easily analysed with *in-situ* AFM measurements. In experiment 1 (Fig 6.3(a-c)), we have presented the SRG formation behaviour while switching the interference pattern from ±45↗↖ to ±45˅ combination. The grating peaks continued developing in the same positions, describing the fact that both ±45↗↖ and ±45˅ patterns are similar. In experiment 2 (Fig 6.3(d-f)), we have switched the interference pattern from ±45↗↖ to ±45↗↘ combination during *in-situ* AFM measurement. From the Fig 6.4b, we could observe that when the interference pattern switched from ±45↗↖ to ±45↗↘ the grating phase transitions are shifted to invert the appearing and disappearing peaks, proving the 180º out of phase condition.

Experiment 3 (Fig 6.3(g-i)) demonstrates the effect of 180º phase difference between the interfering beams in SP polarization combination on the SRG formation. Due to double grating formation behaviour (d=D/2), the SP interference pattern represent a mirror image situation. Despite switching SP interference pattern between in-phase and 180º out of phase conditions, the double grating position remains unchanged as shown in Fig 6.3(g, h). Thus, there is no influence of phase difference between the interfering beams in SP combination on the SRG formation.

Similar experiments are performed using trimer films and observed the same results as in Fig 6.3. For instance, as presented in appendix Fig C.1, when the interference pattern is switched from ±45↗↖ to ±45↗↘ combination during *in-situ* AFM measurement, the SRG peak positions are revealed to be switched immediately while the original peak positions erased slowly.

The study of phase difference between interfering beams presented here will help us to setup the switching experiments between different IIPs and PIPs carefully and to correlate the SRG topography with the $\vec{E}$-field vector distribution in the associated interference pattern.
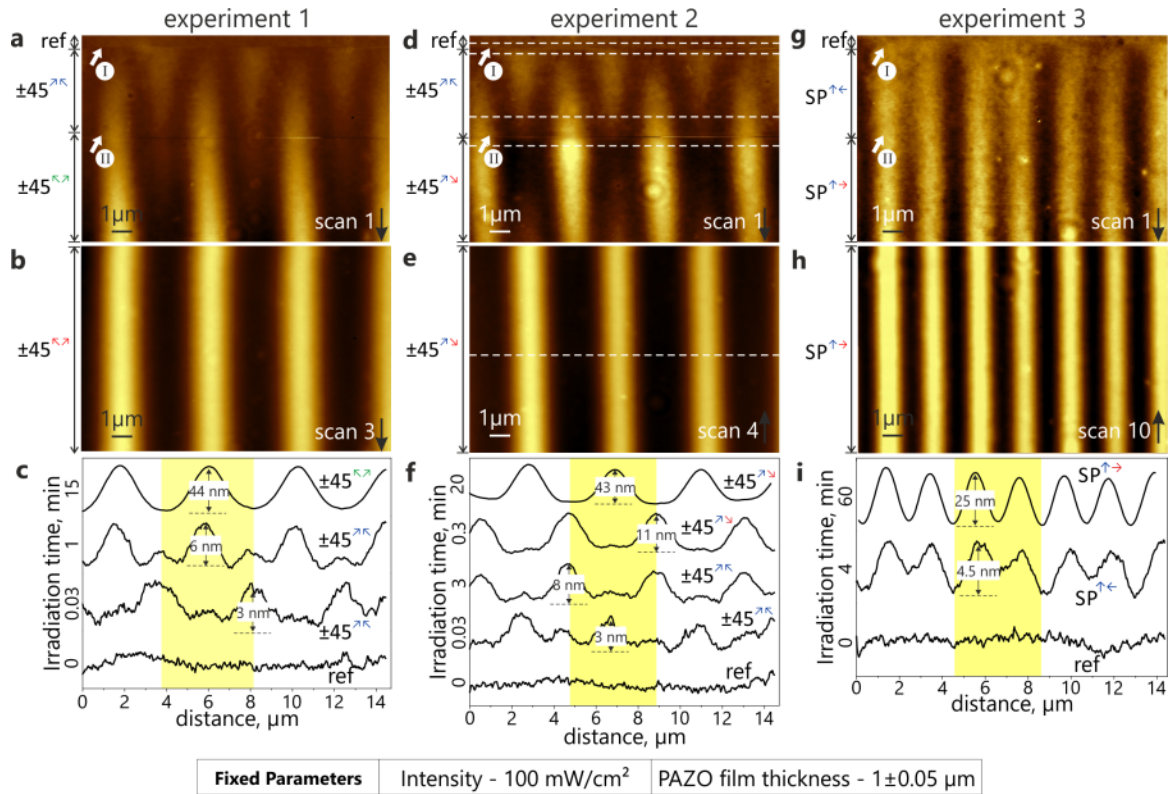
Fig. 6.3. *In-situ* AFM analysis of mixing two beam interference of polarization modulated interference combinations in a sequence in single experiment. a), b), and c) shows experiment with combination between ±45↗↖ and ±45∨. Both of these combinations are orthogonal linear polarizations in phase and they are same. d), e) and f) shows experiment with one beam 180° out of phase as ±45↗↘. Changing from ±45↗↖ to ±45↗↘ shifted the polymer grating by half a period and the phase transitions are inverted as shown in figure d. g), h) and i) shows the out of phase condition relation between SP↑← and SP↑→. The y-axis of (c) (f) and (i) denotes the time of irradiation used for each combination before switching.

6.2. SRG formation by ±45° and SP interference patterns

The difference between ±45° and SP interference patterns is the polarizing vector distribution as shown in Table 3.8 (rows 6 and 7). In case of ±45° configuration, the $\vec{E}$-field vector distribution changes from vertical linear to circular, horizontal linear, orthogonal circular and so on; for SP configuration, the vertical and horizontal linear $\vec{E}$-field vectors are replaced by orthogonal +45° oriented linear $\vec{E}$-field vectors. To understand the contribution of similarities and the differences

between these interference patterns on SRG formation, we have performed several experiments by switching between different interference patterns as described in the following sections.

6.2.1. Switching between ±45º and SP patterns

Experiment 1 in Fig 6.4(a-d) shows the switching behavior between SP$^{\uparrow\leftarrow}$ and ±45$^{\nearrow\nwarrow}$. In Fig 6.4a, following reference scan, SP$^{\uparrow\leftarrow}$ interference pattern is switched on for 4 minutes resulting in double grating formation with d=D/2. At the 4th minute of AFM scan, the configuration switched to ±45$^{\nearrow\nwarrow}$ resulting in transitions of appearing and disappearing peaks. The peak transitions occur exactly in the position of double grating peaks of SP$^{\uparrow\leftarrow}$ interference pattern.

To confirm the grating peak positions, we have performed another experiment by switching the interference pattern in reverse from ±45$^{\nearrow\nwarrow}$ to SP$^{\uparrow\leftarrow}$ as shown in experiment 2 [Fig 6.4 (e-h)]. The observed results are similar in both experiments (1 and 2), that is the grating maxima positions of SP$^{\uparrow\leftarrow}$ interference pattern always matches with the grating appearing and disappearing peaks of ±45$^{\nearrow\nwarrow}$ interference pattern. The same results were observed when the switching studies were performed between ±45$^{\nearrow\searrow}$ and SP$^{\uparrow\rightarrow}$ with out of phase condition (data not presented). Similarly, we have also performed switching experiment between ±45º and SP patterns using trimer film as presented in appendix Fig C.2.

These experiments clearly revealing the fact that the surface relief formation with ±45º and SP share some common features and one of the grating peak which sustained in case of SP$^{\uparrow\leftarrow}$ double grating is actually disappearing in case of ±45$^{\nearrow\nwarrow}$ interference pattern. As we discussed before, the similarities between these interference patterns is the circular (↻) or elliptical polarized regions and the difference is the linearly polarized $\vec{E}$-field vectors regions ($\updownarrow$, $\leftrightarrow$, $\searrow$) (see Table 3.8; rows 6 and 7).
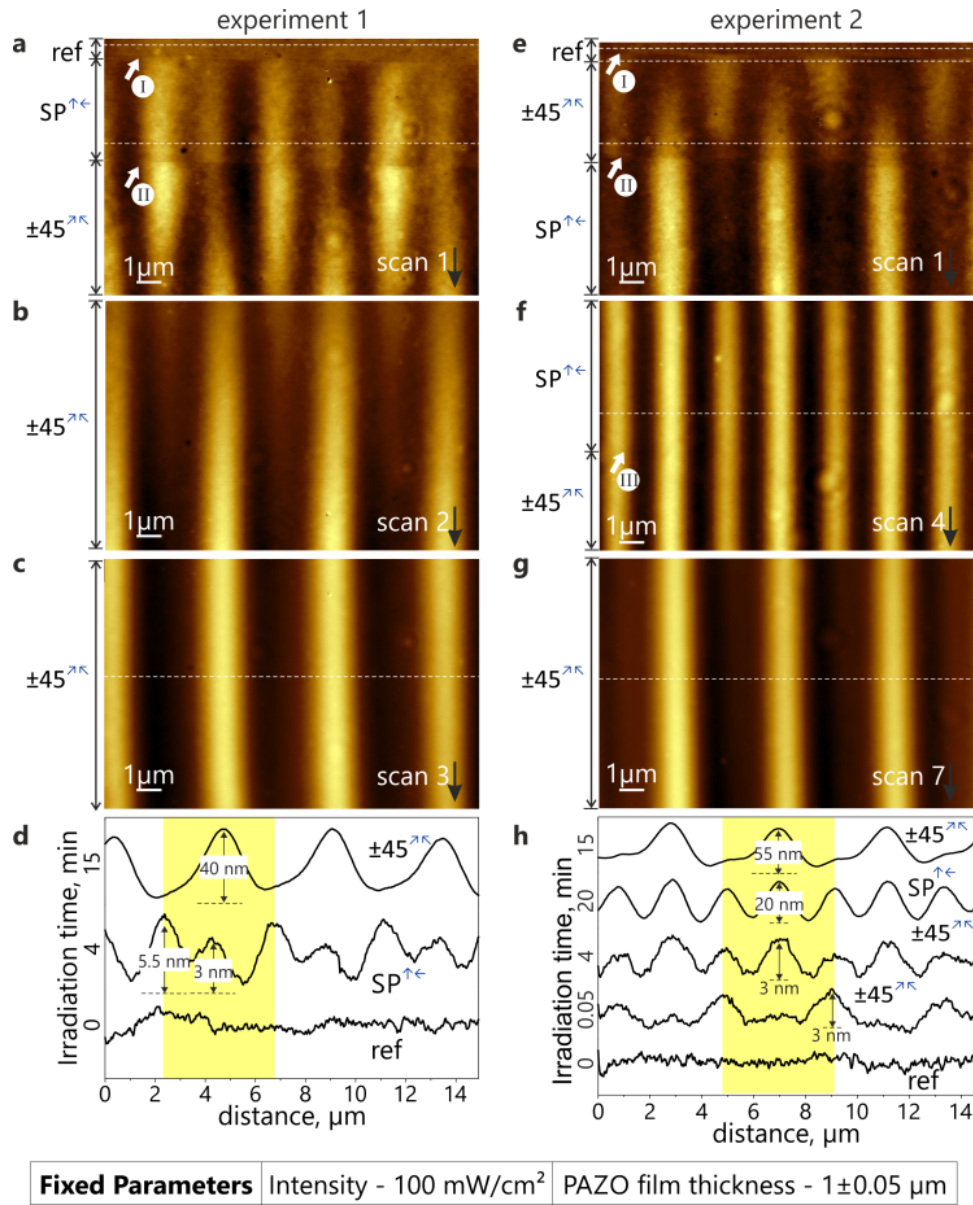
Fig. 6.4. AFM micrographs of polymer topography acquired in-situ during consequent changing of polarization combinations of two interfering beams. (a, b and c) The first step of irradiation (started at the point marked by "I") is performed with SP$^{\uparrow\leftarrow}$ combination, at a point marked by "II" the polarization is switched to ±45$^{\nearrow\nwarrow}$ combination. (e) The surface first irradiated by the ±45$^{\nearrow\nwarrow}$ polarization combination followed by switching to SP$^{\uparrow\leftarrow}$ pattern ("II"). The surface relief grating peak which disappears in case of ±45 sustained in SP grating (f). (f, g) By switching back to initial combination of ±45$^{\nearrow\nwarrow}$ ("III"), one of the topography maxima vanishes. (d and h) The corresponding cross-section of polymer topography taken along scans marked by dashed white lines is presented as a function of irradiation time and polarization combinations. The y-axis of (d) and (h) denotes the time of irradiation used for each combination before switching.

6.2.2. *In-situ* AFM measurement of grating formation while switching between IIPs and SP$^{\uparrow\leftarrow}$ interference pattern

In the Table 5.1, we have correlated the IIPs with the SRG topography profile. The SRG maxima correspond to the local intensity minima of IIP and vice versa. This knowledge might be valuable for us to correlate the SRG topography with the $\vec{E}$-field vector distribution of PIPs. In the appendix Fig B.3, we have presented a graphic to describe the interference of two waves at an arbitrary point "P_0". Let us assume this arbitrary point "P_0" to be the center in the region where two beams interfere on the polymer surface. If two vertical linearly polarized waves ($\updownarrow$) meet each other with constructive interference at this arbitrary point "P_0" the resultant local $\vec{E}$-field vector is the sum of individual wave vector, and is also vertical linearly polarized ($\updownarrow$). Now if we rotate one of the waves by 90º ($\leftrightarrow$), we will obtain the SP polarization combination ($\updownarrow$, $\leftrightarrow$) and the resultant $\vec{E}$-field vector at the arbitrary point "P_0" is a 45º tilted linearly polarized vector ($\nearrow$) as shown in Table 3.8 (row 6, column 1). Similarly if two orthogonal 45º oriented waves ($\nearrow$, $\searrow$) interfere at the arbitrary point "P_0", the resultant $\vec{E}$-field vector is vertical linearly polarized ($\updownarrow$) as shown in Table 3.8 (row 7, column 1) and section 3.3.2*i*.

Combining the knowledge discussed above with our *in-situ* AFM experiments, if we switch the interference pattern from IIP (e.g. SS$^{\uparrow\uparrow}$) to a PIP (e.g. SP$^{\uparrow\leftarrow}$), we could experimentally determine the orientation of local $\vec{E}$-field vector with respect to an arbitrary point "P_0" during the SRG formation. For instance, let us consider a polymer grating inscribed using SS$^{\uparrow\uparrow}$ interference pattern and fix an arbitrary point "P_0" being any grating minima in the recorded AFM micrograph. Now, if we switch the interference pattern to SP$^{\uparrow\leftarrow}$, by following the new grating positions, we could correlate the local orientation of $\vec{E}$-field vector and the polymer grating with respect to the arbitrary point "P_0".

We have performed these experiments as shown in Fig 6.5, where we observed the polymer grating formation when we switch the interference pattern from an IIP (in-phase) to SP$^{\uparrow\leftarrow}$. In experiment 1 [Fig 6.5(a-c)], following the reference scan we have switched ON the SS$^{\uparrow\uparrow}$ pattern for few seconds and switched OFF while the AFM scan continues in the dark. During the scan progress in dark, the half wave plates (see H$_3$ and H$_4$ in appendix Fig B.3) are rotated to achieve SP interference pattern. At level marked as "II" we have switched ON the SP interference pattern for the rest of experiment. As shown in Fig 6.5a, the primary grating (SS$^{\uparrow\uparrow}$) is slowly erased during irradiation with SP interference pattern and new double grating appeared slowly after several minutes. The erasure process could be easily explained by the molecular reorientation and the associated mass transported processes due to change in the interference pattern.
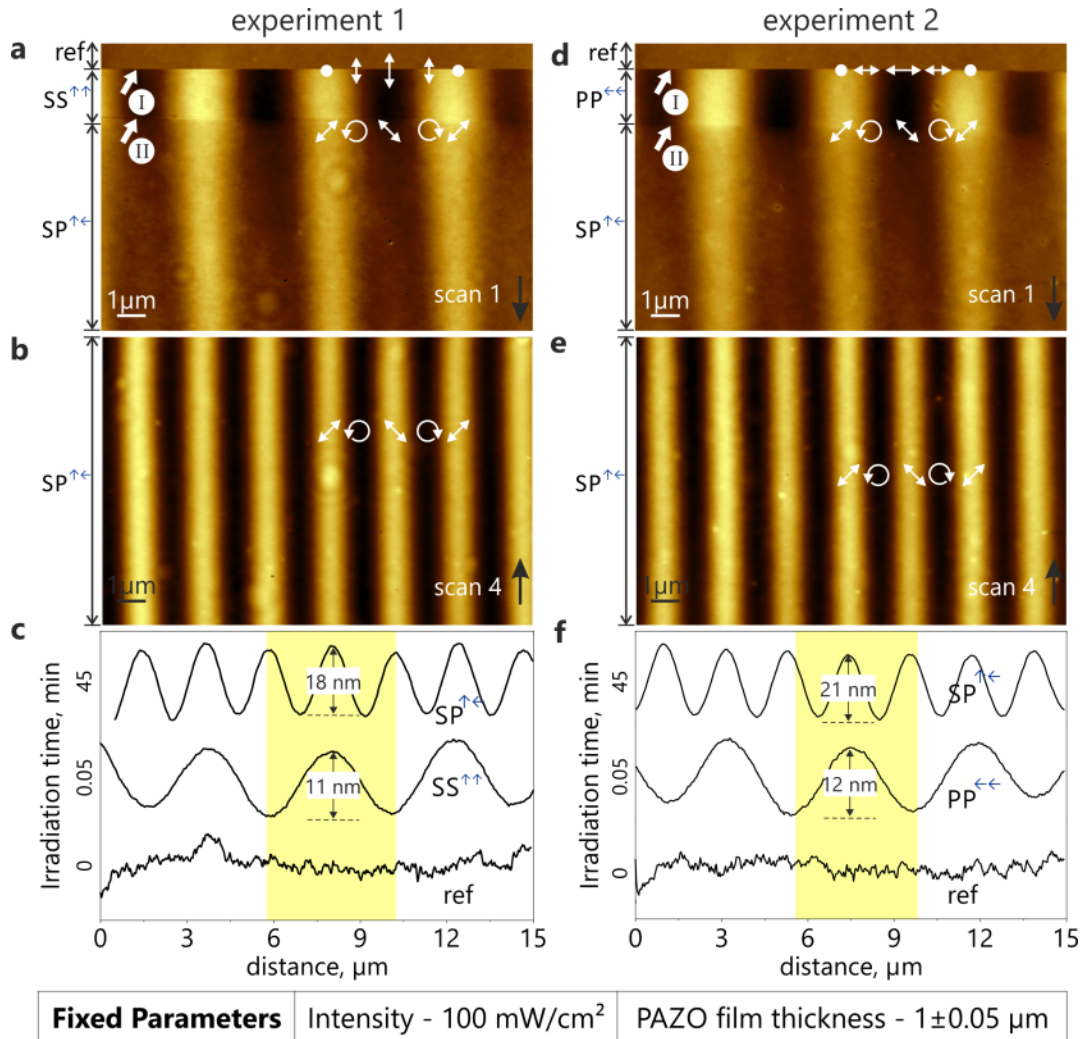
Fig. 6.5. *In-situ* AFM analysis of polymer topography while switching the interference patterns from IIPs to $SP^{\uparrow\leftarrow}$ in a sequence in single experiment. a), b), c) demonstrate the changes in polymer topography while switching the interference pattern from $SS^{\uparrow\uparrow}$ to $SP^{\uparrow\leftarrow}$. The linearly polarized $\vec{E}$-field vector positions in the interference pattern of $SP^{\uparrow\leftarrow}$ leads to the polymer grating peaks. d), e), f) shows the AFM micrographs of polymer topography while switching from $PP^{\leftarrow\leftarrow}$ to $SP^{\uparrow\leftarrow}$. The y-axis of (c) and (f) denotes the time of irradiation used for each combination before switching.

The changes in polymer topography with SP interference pattern revealed a double grating as shown in Fig 6.5(b, c). Comparing the AFM micrographs in Fig 6.5(a, b), one of the double grating peaks of SP interference pattern remain in the original grating maxima position of $SS^{\uparrow\uparrow}$, while the second grating maxima of SP

pattern appeared at the original grating minima of SS$^{\uparrow\uparrow}$ pattern. From Table 3.8 Fig 6.5 (a-c), we could now correlate the $\vec{E}$-field vector distribution of the SP interference pattern with the polymer grating topography as shown in Fig 6.5a. The grating maxima of SP interference pattern appear with the 45° linear $\vec{E}$-field vectors (i.e. ↗ and ↘). To confirm this observation, we have repeated the same experiment by switching the interference pattern from PP$^{\leftarrow\leftarrow}$ to SP$^{\uparrow\leftarrow}$ as shown in Fig 6.5(d-f) and ‡45$^{\nearrow\nearrow}$ to SP$^{\uparrow\leftarrow}$ (data not shown) and obtained similar result.
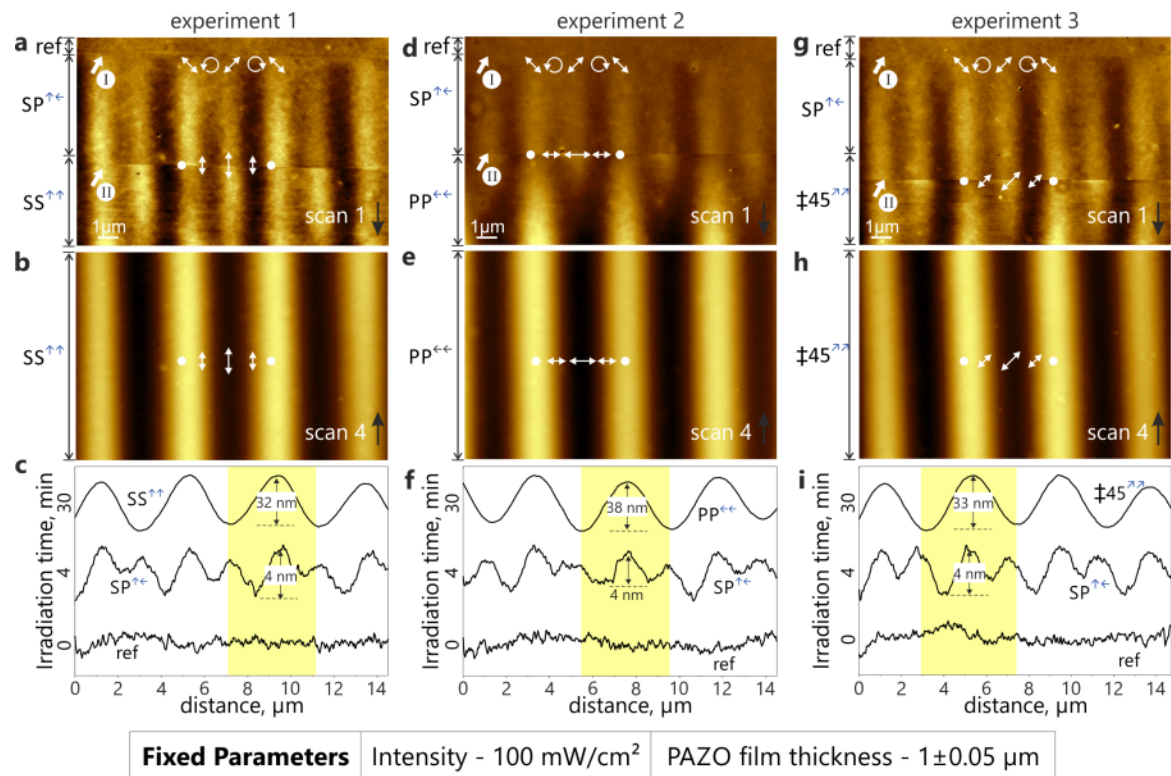
Fig. 6.6. *In-situ* AFM analysis of mixing two beam interference of polarization (SP$^{\uparrow\leftarrow}$) versus Intensity modulated interference combinations in a sequence in individual experiments. a), b), c) and d) showing the switching between SP$^{\uparrow\leftarrow}$ and SS$^{\uparrow\uparrow}$. e), f), g) and h) showing the switching between SP$^{\uparrow\leftarrow}$ and PP$^{\leftarrow\leftarrow}$. i), j), k) and l) showing the switching between SP$^{\uparrow\leftarrow}$ and 45$^{\nearrow\nearrow}$. The y-axis of (c), (f) and (i) denotes the time of irradiation used for each combination before switching.

Once again, to have a solid experimental observation without any further ambiguity in SP interference pattern associated SRG formation (d=D/2), we have performed more *in-situ* AFM measurements while switching the interference patterns from SP$^{\uparrow\leftarrow}$ to IIPs as shown in Fig 6.6 (*reverse order to the experiments in*

Fig 6.5). When we switch the interference pattern from SP$^{\uparrow\leftarrow}$ to SS$^{\uparrow\uparrow}$ (Fig 6.6a), to PP$^{\leftarrow\leftarrow}$ (Fig 6.6d), and to 45$^{\nearrow\nearrow}$ (Fig 6.6g) during the *in-situ* AFM measurements, one of the double grating peaks continued growing while the other grating maxima is erased. In the appendix Fig C.3, we have presented similar experiment with trimer film and the same result is observed.

> *"Thus, we could now firmly conclude that the linear 45ᵒ $\vec{E}$-field vectors (i.e. ↗ and ↘) of SP interference pattern corresponds to the maxima of associated polymer grating and the circular $\vec{E}$-field vectors (i.e. ↺ and ↻) corresponds to the grating minima."*

6.2.3. *In-situ* AFM measurement of grating formation while switching between IIPs and ±45$^{\nearrow\nwarrow}$ interference pattern

Here, we are focusing on the SRG inscribed using ±45ᵒ interference pattern. Similar to the experiments performed in the previous section, we have observed the changes in the polymer grating topography while switching the interference patterns from IIPs to ±45$^{\nearrow\nwarrow}$ as shown in Fig 6.7.

In experiment 1 (Fig 6.7(a-c)), PAZO film is irradiated with SS$^{\uparrow\uparrow}$ pattern followed by ±45$^{\nearrow\nwarrow}$ in sequence and the result shows that the final grating maxima of the ±45$^{\nearrow\nwarrow}$ configuration are migrated to the grating minima of the primary grating (SS$^{\uparrow\uparrow}$). In other words, the grating maxima are migrating half a period away from the previous maxima position. From Table 3.8, we know that when we switch the interference pattern from SS$^{\uparrow\uparrow}$ to ±45$^{\nearrow\nwarrow}$, the local $\vec{E}$-field vector at position "0" (Table 3.8: column 1) will remain vertical linearly polarized (↕). In chapter 5, we learnt that for the SS interference pattern (Table 5.1), the minima of grating topography correspond to position "0" (maximum of intensity). Observing the grating migration by half a period while switching the interference pattern from IIP to ±45$^{\nearrow\nwarrow}$, we could describe that the SRG maxima correspond to the vertical linear $\vec{E}$-field vector (↕) and the SRG minima corresponds to the horizontal linear $\vec{E}$-field vector of the ±45$^{\nearrow\nwarrow}$ interference pattern. A similar result is obtained when switching the interference pattern from PP$^{\leftarrow\leftarrow}$ to ±45$^{\nearrow\nwarrow}$ as shown in Fig 6.7 (d-f) and from 45$^{\nearrow\nearrow}$ to ±45$^{\nearrow\nwarrow}$ (data not shown).

More experiments are performed as shown in Fig 6.8 to validate the above described result by observing the changes in polymer grating topography while switching the interference patterns from ±45$^{\nearrow\nwarrow}$ to any IIP (*reverse order to the experiments in Fig 6.6*).
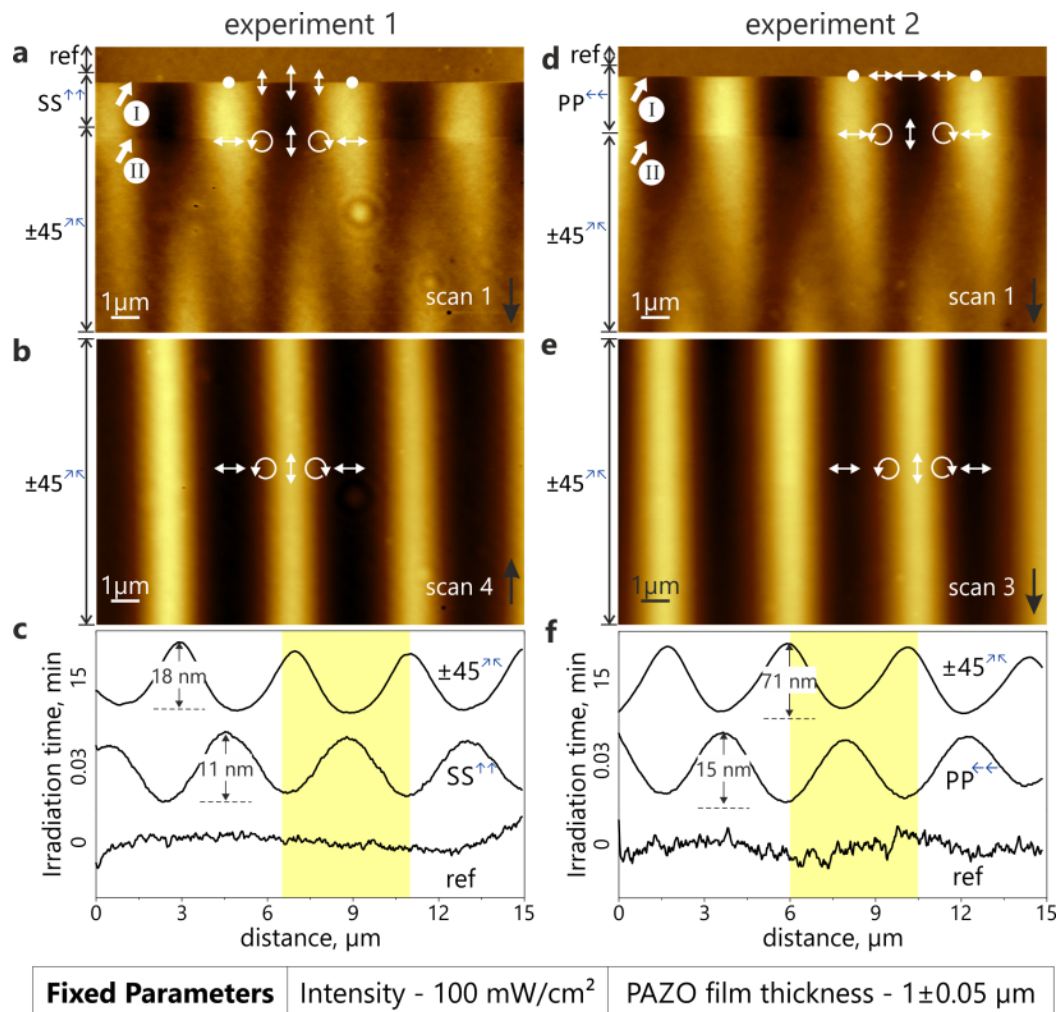
Fig. 6.7. *In-situ* AFM analysis of mixing two beam interference of Intensity versus polarization modulated interference combinations in a sequence in single experiment. a), b), c) shows switching the interference pattern from SS$^{\uparrow\uparrow}$ to ±45$^{\nearrow\nwarrow}$. d), e), f) shows the switching between PP$^{\leftarrow\leftarrow}$ to ±45$^{\nearrow\nwarrow}$. The vertical linearly linearly polarized $\vec{E}$-field vector positions in the interference pattern of ±45$^{\nearrow\nwarrow}$ leads to the sustained polymer grating peaks and the horizontal linear $\vec{E}$--field vectors leads to the disappearing peaks. The y-axis of (c) and (f) denotes the time of irradiation used for each combination before switching.

In Fig 6.8(a, d, g), the primary grating (marked "I") is inscribed using ±45$^{\nearrow\nwarrow}$ pattern during 4 minutes of irradiation time and we have observed the appearing and disappearing phase transitions of grating lines. At 4$^{\text{th}}$ minute (marked as "II"), the pattern is switched from ±45$^{\nearrow\nwarrow}$ to SS$^{\uparrow\uparrow}$ (Fig 6.8a), to PP$^{\leftarrow\leftarrow}$ (Fig 6.8d), and

to 45↗↗ (Fig 6.8g). Immediately after switching, one could see that the growing peak of primary grating is erased while the disappearing peak of primary grating start growing as a sign of new grating peak migrating half a period away from original position.
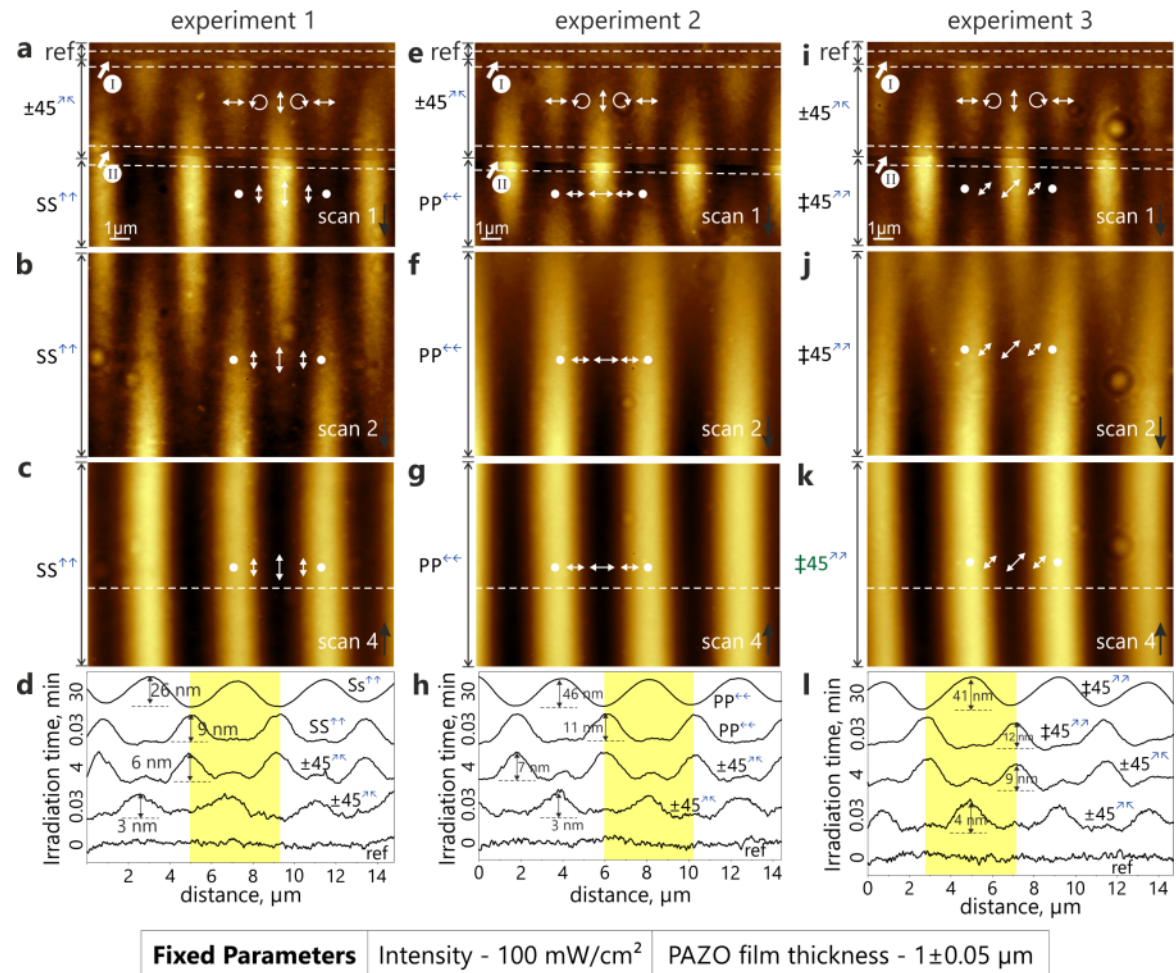
Fig. 6.8. AFM micrographs showing the topography change under irradiation while switching the polarization combination from (a, b, c) ±45↗↖ to SS↑↑; (e, f, g) from ±45↗↖ to PP←←, and (i, j, k) from ±45↗↖ to (h) 45↗↗. (d, h, l) The corresponding cross-sections are shown as a function of irradiation time. The inserted $\vec{E}$-field vector pattern is assigned to the topography features. The y-axis of (d), (h) and (l) denotes the time of irradiation used for each combination before switching.

Similarly, experiments are repeated with trimer films by observing the grating topography changes while switching the interference pattern from SS$^{\uparrow\uparrow}$ to ±45$^{\nearrow\nwarrow}$ and from PP$^{\leftarrow\leftarrow}$ to ±45$^{\nearrow\nwarrow}$ as shown in appendix C.4. The results observed with trimer films are similar to Fig 6.7 and Fig 6.8.

> "*Thus, we could now firmly conclude that the vertical linear $\vec{\boldsymbol{E}}$-field vectors (i.e. $\updownarrow$) of ±45° interference pattern corresponds to the maxima of associated polymer grating and the horizontal linear $\vec{\boldsymbol{E}}$-field vectors (i.e. $\leftrightarrow$) corresponds to the grating minima.* "

It is an interesting question, why the grating maxima appear with the linearly polarized $\vec{\mathbf{E}}$-field vectors instead of circular $\vec{\mathbf{E}}$-field vectors. One possible explanation is the azobenzene chromophores tend to reorient themselves perpendicular to the linearly polarized light to achieve a stable state[84]. However, in case of circularly polarized light, the azobenzene chromophore has no specified orientation to attain stable ground state. The continuous modulation of $\vec{\mathbf{E}}$-field vectors from linear to elliptical to circular and so on, results in the reorientation and mass transport of azobenzene chromophores towards regions with linear $\vec{\mathbf{E}}$-field vectors.

Observing the SRG formation by SP and ±45° interference patterns, the role elliptical and circular $\vec{\boldsymbol{E}}$-field vectors ($\circlearrowleft$) appear to be a driving force to push molecules towards the more stable regions of linear $\vec{\boldsymbol{E}}$-field vectors. To understand this effect further, we need to use a PIP which contains only linearly polarized $\vec{\boldsymbol{E}}$-field vectors without intensity gradient.

In section 3.3.2*iii*, we have discussed the interference of orthogonal circularly polarized beams and the resultant interference pattern contains only linearly polarized $\vec{\boldsymbol{E}}$-field vector modulation with constant intensity as shown in Table 3.7. We call this interference pattern in short as RL and studying the SRG formation with this interference pattern might reveal some details about the role of elliptical and circularly polarized $\vec{\boldsymbol{E}}$-field vectors in SP and ±45° interference patterns.

6.3. SRG formation by RL interference pattern

Experiment 1 in Fig 6.9 shows the *in-situ* observation of SRG formation while switching the interference pattern from SS$^{\uparrow\uparrow}$ to RL. Following the reference scan, the primary grating is inscribed by irradiating with SS$^{\uparrow\uparrow}$ interference pattern for few seconds as shown in Fig 6.9a (marked as "I"). At level marked as "II", the interference pattern is switched to RL for rest of the experiment. In Fig 6.9a, we

could observe that the primary grating is completely erased before the new grating maxima and minima positions are developed.
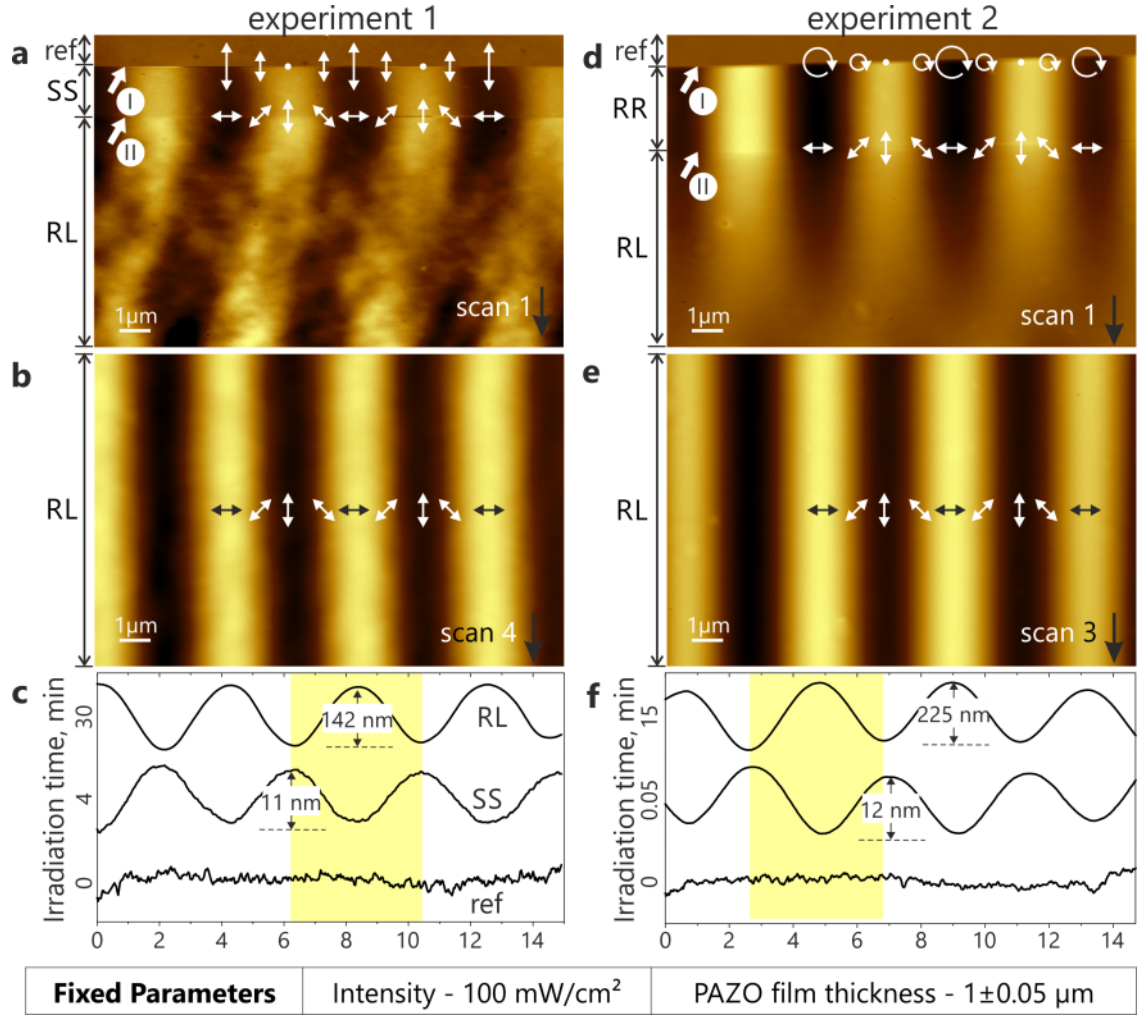
Fig. 6.9. *In-situ* AFM analysis of mixing two beam interference of Intensity versus polarization modulated interference combinations in a sequence in single experiment. a), b), c) shows switching between $SS^{\uparrow\uparrow}$ to $RL^{\circlearrowleft\circlearrowleft}$. d), e), f) shows the SRG formation while switching the interference pattern from $RR^{\circlearrowleft\circlearrowleft}$ to $RL^{\circlearrowleft\circlearrowleft}$. The y-axis of (c) and (f) denotes the time of irradiation used for each combination before switching.

From Table 3.8, we know that when we switch the interference pattern from $SS^{\uparrow\uparrow}$ to $\pm 45^{\nearrow\nwarrow}$, the local vertical linear polarized $\vec{E}$-field vector ($\updownarrow$) at position "0" (Table 3.8: column 1) will become horizontal linearly polarized ($\leftrightarrow$). Observing the final grating maxima position in Fig 6.9 (b, c) using RL irradiation demonstrate that

the SRG maxima corresponds to the horizontal linear $\vec{E}$-field vector ($\leftrightarrow$) and the grating minima corresponds to the vertical linear $\vec{E}$-field vector ($\updownarrow$). Similarly, in experiment 2 [Fig 6.9(d-f)] we have observed the SRG formation while switching the interference pattern from RR ($\circlearrowright$,$\circlearrowright$) to RL ($\circlearrowright$,$\circlearrowleft$) and confirmed the same result that the SRG maxima using RL interference pattern correspond to the horizontal linear $\vec{E}$-field vector ($\leftrightarrow$).

In order to confirm this observation, we have repeated several experiments using trimer films as shown in appendix Fig (C.5 to C.10). We have observed SRG formation by switching between RL and every possible IIP (appendix Fig C.5 to C.8) and PIP (appendix Fig C.9 and C.10) interference patterns. All the experiments confirm the same result as presented in Fig 6.9. The grating maxima for RL pattern corresponds to the horizontal linear $\vec{E}$-field vector ($\leftrightarrow$).

6.4. Azobenzene chromophores *vs.* favourable $\vec{E}$-field vectors

We know that in polarization interference patterns (PIPs) the intensity along the grating vector remains constant. As a result, intensity is not a driving force for SRG formation using SP, $\pm45^{\circ}$, and RL interference patterns and is purely governed by local $\vec{E}$-field vector of these PIPs.

In case of SP interference pattern, the grating maxima appeared wherever orthogonal 45° oriented $\vec{E}$-field vector ($\nearrow$ and $\searrow$) appeared throughout the irradiation area along grating vector, which is twice per optical periodicity (D) resulting in double grating phenomena. The polymer molecules are driven away from the regions of circularly polarized $\vec{E}$-field vector towards linearly polarized $\vec{E}$-field vectors.

In case of $\pm45^{\circ}$ interference pattern, when the beams are switched on, the surface relief peaks appeared initially at regions with horizontal $\vec{E}$-field vector ($\leftrightarrow$) and with time these peaks erased and the new maxima developed with vertical $\vec{E}$-field vector ($\updownarrow$). The molecules remain unstable and undergoing mass transport away from regions with circularly polarized $\vec{E}$-field vector. Comparing the $\pm45^{\circ}$ interference pattern with SP, it is a puzzling behavior of SRG formation. The orientation of $\vec{E}$-field vector decides the direction of molecular mass transport.

In contrast to $\pm45^{\circ}$ and SP interference patterns, the grating maxima for RL interference continued growing with horizontal $\vec{E}$-field vector ($\leftrightarrow$). This key observation raises more questions about the role of elliptical and circularly polarized $\vec{E}$-field vectors of $\pm45^{\circ}$ and SP interference patterns.

Though single azobenzene chromophore tend to reorient itself perpendicular to the linear $\vec{E}$-field vector, the combination of both linear and circular $\vec{E}$-field vectors in the interference patterns appears to create an organized driving force. The nature of driving force might strongly depend up on the combination of linear and/or circular $\vec{E}$-field vectors. Further, it is possible that depending upon the combination of $\vec{E}$-field vectors, the favorability of molecules to mass towards or away from certain linear $\vec{E}$-field vector is decided.

At this stage of investigation, it is not possible to investigate the in-depth molecular dynamics. However we believe the results presented here pave a way for more theoretical and experimental works soon.

6.5. Experimentally derived grating table

Based upon the detailed experimental analysis presented in Chapter 5 and the current chapter 6, the correlation between the surface relief grating topography (i.e. maxima and minima etc.) and the $\vec{E}$-field vector distribution of different interference patterns is summarized as shown in Table 6.1.

6.6. Summary

In a short overview of this chapter, we have presented experiments to study the polarization interference patterns (PIPs) in detail utilizing the appearing/disappearing peak transition behaviour of ±45° polarizing combination and the double grating formation behaviour of SP polarization combination as tools. From Fig 6.4, it is clear that the grating formation behaviour of SP and ±45° share several common features. While switching from SP to ±45° interference pattern as shown in Fig 6.4a, one of the grating peaks of SP combination continued growing while the other grating maxima disappears. Comparing the $\vec{E}$-field vector distribution of polarization interference patterns, (Table 3.8: row 6 and row 7) it is evident that the grating maxima for ±45° and SP combinations occur with either linearly polarized $\vec{E}$-field vector or circularly polarized $\vec{E}$-field vectors. To solve this puzzle more experiments are performed by switching the polarization combinations from IIP to PIP (e.g. SS to ±45° and SS to SP) as shown in Fig 6.5 and Fig 6.7. From these experiments and comparing with the interference patterns in Table 3.8 (rows: 1, 6 and 7), we found that the grating maxima using ±45° and SP occurs with linearly polarized $\vec{E}$-field vectors. For SP the grating maxima occur with linear $\vec{E}$-field vectors(↗ and ↘) and for ±45° the

grating maxima appears with vertical linear $\vec{E}$-field vector (↕) while the disappears maxima during transient behaviour occurs with horizontal $\vec{E}$-field vector (↔). To support this understanding we presented more experiments in Fig 6.6, 6.8 and appendix Fig C.1 to Fig C.4. Observing the PIPs in Table 3.8 lead us to study RL interference pattern to understand the role of linear and circular $\vec{E}$-field vector in PIPs. The experiments presented in Fig 6.9 and appendix Fig C.5 to Fig C.10 shows that the grating maxima using RL pattern appear with horizontal linear $\vec{E}$-field (↔). A comparative study highlighted the unique favorability of azobenzene containing molecules to mass transport specifically towards certain linear $\vec{E}$-fields leading to the double grating phenomena using SP interference pattern and appearing/disappearing peak transitions in case of ±45º pattern. However more experimental and theoretical understanding is required to find the role of elliptical and circularly polarized $\vec{E}$-fields in SP and ±45º interference patterns. Finally, based up on the detailed experimental analysis in Chapter 5 and 6, we have summarized the correlation between different interference patterns (IIPs and PIPs) and SRG topography in Table 6.1.

Table 6.1 is a valuable addition of knowledge to the community studying the photo responsive nature of azobenzene chromophores for variety of applications in optoelectronic industry

	Polarization of Interfering beams				1	2	3	4	5	6	7	8	9
					Spatial distribution of polarization along grating vector of interference pattern (x-axis)								
	beam 1		beam 2		-D	-3D/4	-D/2	-D/4	0	D/4	D/2	3D/4	D
A	Intensity Interference Pattern (IIP)												
1	SRG position				(wave)								
2	S	↕	S	↕	↕	↕	•	↕	↕	↕	•	↕	↕
3	P	↔	P	↔	↔	↔	•	↔	↔	↔	•	↔	↔
4	+45°	↗	+45°	↗	↗	↗	•	↗	↗	↗	•	↗	↗
5	L	↺	L	↺	↺	↺	•	↺	↺	↺	•	↺	↺
6	R	↻	R	↻	↻	↻	•	↻	↻	↻	•	↻	↻
B	Polarization Interference Pattern (PIP)												
7	SRG position				(wave)								
8	+45°	↗	-45°	↘	↕	↻	↔	↻	↕	↺	↔	↻	↕
9	R	↻	L	↺	↔	↗	↕	↘	↔	↗	↕	↘	↔
10	SRG position				(wave)								
11	S	↕	P	↔	↗	↻	↘	↺	↗	↻	↘	↺	↗

Table 6.1 Experimentally derived SRG positions as a function of different intensity interference patterns. The assignment for IIPs presented here is only valid for any photosensitive material mass transports away from light intensity.

This page is intentionally left blank

<div style="text-align: right; font-size: 4em;">7</div>

Surface Relief Structures below Diffraction Limit using Far Field[*]

Structuring the photosensitive polymer topography below diffraction limit is very interesting for data storage and nanofabrication related applications. To achieve it, there are plenty of different techniques ranging from laser assisted and mask-free fabrication to conventional photolithography. [86,87] Enormous progress has been made recently in the field of nanofabrication, and one can now-a-days inscribe structures of characteristic sizes about a few tens of nanometers. The fabrication methods involve very short wavelengths such as deep UV (DUV)[88], or extreme UV (EUV), with a wavelength down to 10 nm.[89] In these approaches one is bound to utilize specially designed materials that show an adequate photo-chemical reaction at these small wavelengths. However, we could not exploit the unique properties of azo-molecules, as they absorb at wavelengths between 300 to 500 nm. As an alternative, near field- or plasmonics-based nanolithographic methods have recently been proposed to arrive at structural dimensions below the diffraction limit down to a few tens of nanometers [5,85,90,91,92,93,94,95,96]. Although this approach is very promising and still under development, the main drawback here is the fabrication of metal nanostructures that are able to generate the near field distribution.

The advantage in using azobenzene polymer films is that usually one can render the patterning reversible; the underlying process is photo-physical in nature. In addition, variety of structural features could be achieved easily, such as linear gratings, orthogonal gratings, 2D dimple arrays using three-bam interference,[31] tetragonal, hexagonal patterns – 2D gratings,[97,98] 10-fold surface relief quasi-crystal[99], and 3D structures as well[100]. However, the disadvantage as mentioned above is that the spatial resolution of the SRG is diffraction limited. One cannot

---

[*] Parts of the data presented in this chapter and associated appendix is published by the author of current dissertation in *Appl. Phys. A* **113**, 263 (2013)

inscribe patterns with topography variations smaller than half of the incident wavelength.

In chapter 6, we have studied the double grating formation (d=D/2) phenomenon using SP interference pattern in both the PAZO and dendrimer films. Logically, if the phenomenon observed with SP pattern is reproducible for any arbitrary optical periodicity (D), we should be able to inscribe topography patterns with the size smaller than the diffraction limit by using the lowest optical periodicity, i.e. half of the laser source wavelength. We choose to study both the linear and orthogonal grating structural features as presented in the following sections.

7.1. Linear gratings below diffraction limit

To study the formation of below diffraction limit structures using SP pattern, we have performed a series of experiments comparing both the photosensitive materials (PAZO and trimer), for three different optical periodicities (D – 1 μm, 0.5 μm, and 0.3 μm) using three different interference patterns (‡45°, ±45°, and SP) as presented in Fig 7.1 and Fig 7.2. A constant polymer film thickness of 250 ± 20 nm is used for all measurements. Interference beam intensity kept constant at 100mW/cm². All the sample are irradiated for 1hr duration.

In Fig 7.1 (a–c), the grating formation in PAZO film at different periodicities using ‡45° interference pattern (IIP) is shown. While the grating periodicity is reduced from 1 μm to 0.3 μm, the grating height is also observed to be reduced, possibly due to the less space available to accommodate the molecules. Here, the optical periodicity is equal to grating periodicity (d=D). Changing the interference pattern from IIP to a PIP, i.e. to ±45° pattern as shown in Fig 7.1 (d–f), similar grating height is observed for 1.0 μm and 0.5 μm periodicities; however insignificant grating is developed for 0.3 μm periodicity. Though the grating could not be observed almost, the surface roughness has changed significantly, indicating the molecular mass transport locally. A single PAZO molecular backbone chain length is approximately 8–10 nm long and using 0.3 μm optical periodicity (D), the local linear and circular E-field vectors are located too close and may fail to produce a definite molecular mass transport. This could be a reason for the lack of the SRG formation for 0.3 μm periodicity (Fig 7.1f). Similarly the SRG formation in PAZO film using SP pattern is studied in Fig 7.1 (g–i). As one would expect, the irradiation with SP pattern results in the grating with half of the optical periodicity (d=D/2). For 1.0 μm and 0.5 μm periodicities we have observed double grating formation behaviour, but with very low grating formation efficiency. In case of 0.3 μm periodicity, clearly the polymer topography remains absolutely flat. Comparing the topography in Figs 7.1(f and

i), it is clear that with 0.3 μm grating periodicity using SP pattern, grating formation is not possible in PAZO films. The reason for lack of grating formation in Fig 7.1i in PAZO film might be the might molecular weight of PAZO.

We have repeated the above described experiments with trimer films as shown in Fig 7.2. In chapter 3, we have learnt that trimer is very efficient for PIPs compare to IIPs. The grating formation efficiencies vary depending upon the film thickness, interference pattern and molecular weight. Considering the small molecular structure of trimer (three azobenzene units attached to a centre benzene ring), efficient grating formation observed compared to PAZO. Interestingly, using trimer films we have observed pronounced gratings at the smallest optical periodicities (0.3 μm). As shown in Figs 7.2 (f and i), using 280 nm optical periodicity, we have observed a grating of ~ 140 nm periodicity. The wavelength of the interfering beams is 491 nm, the diffraction limit is 245 nm. The grating periodicity in Fig 7.2i is 140 nm, which is close to half of the diffraction limit.
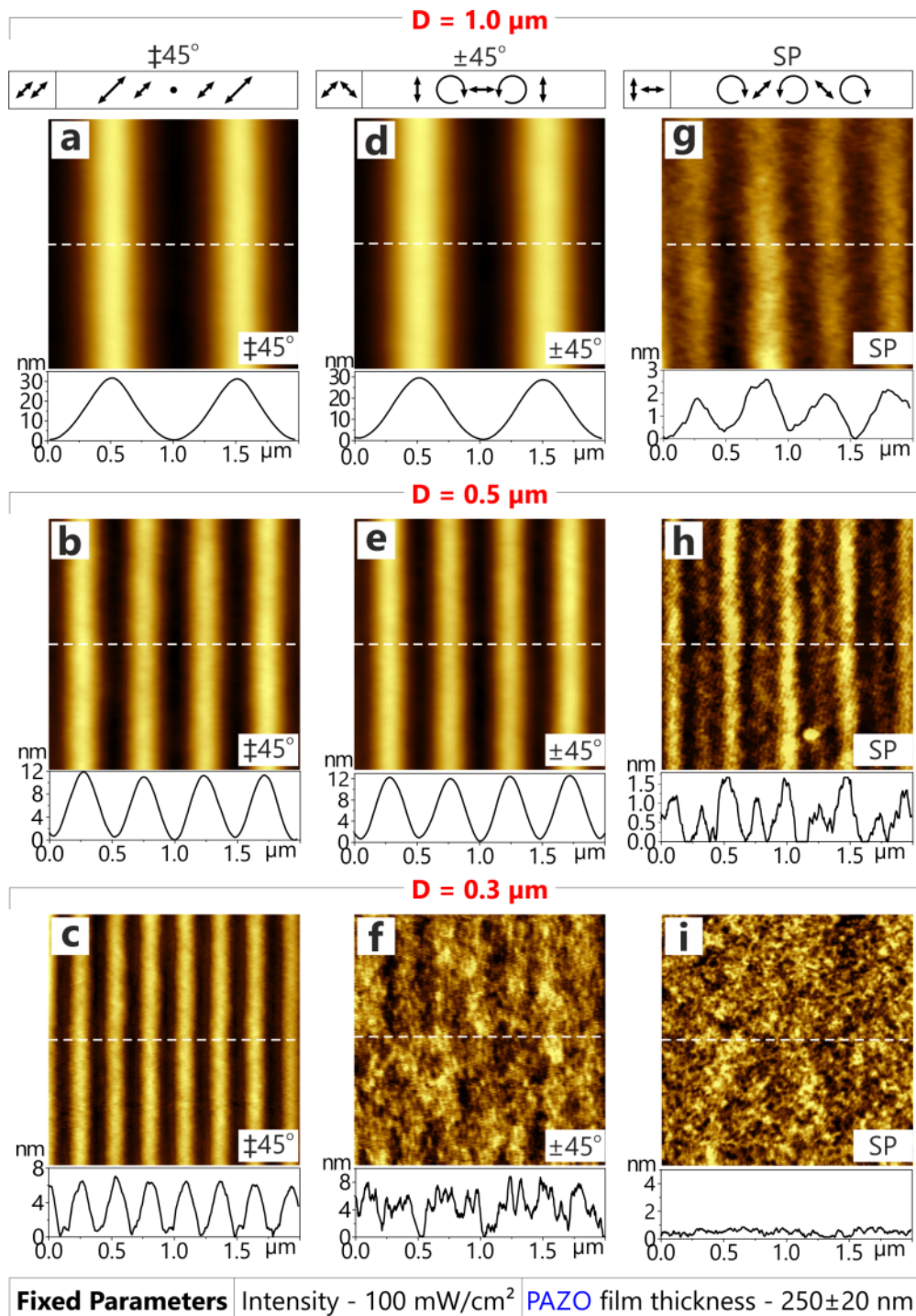
Fig. 7.1. Comparison of grating formation at varying periodicities (1, 0.5, 0.3 μm) and varying interference patterns (‡45°, ±45° and SP). a), b), c) SRG formation due to pure intensity grating (‡45°) with periodicities 1, 0.5, 0.3 μm, respectively. d), e), f) The SRG formation by pure polarization grating (±45°) periodicities 1, 0.5, 0.3 μm, respectively. g), h), i) SRG formation by SP interference pattern with double grating phenomena periodicities 1, 0.5, 0.3 μm respectively.
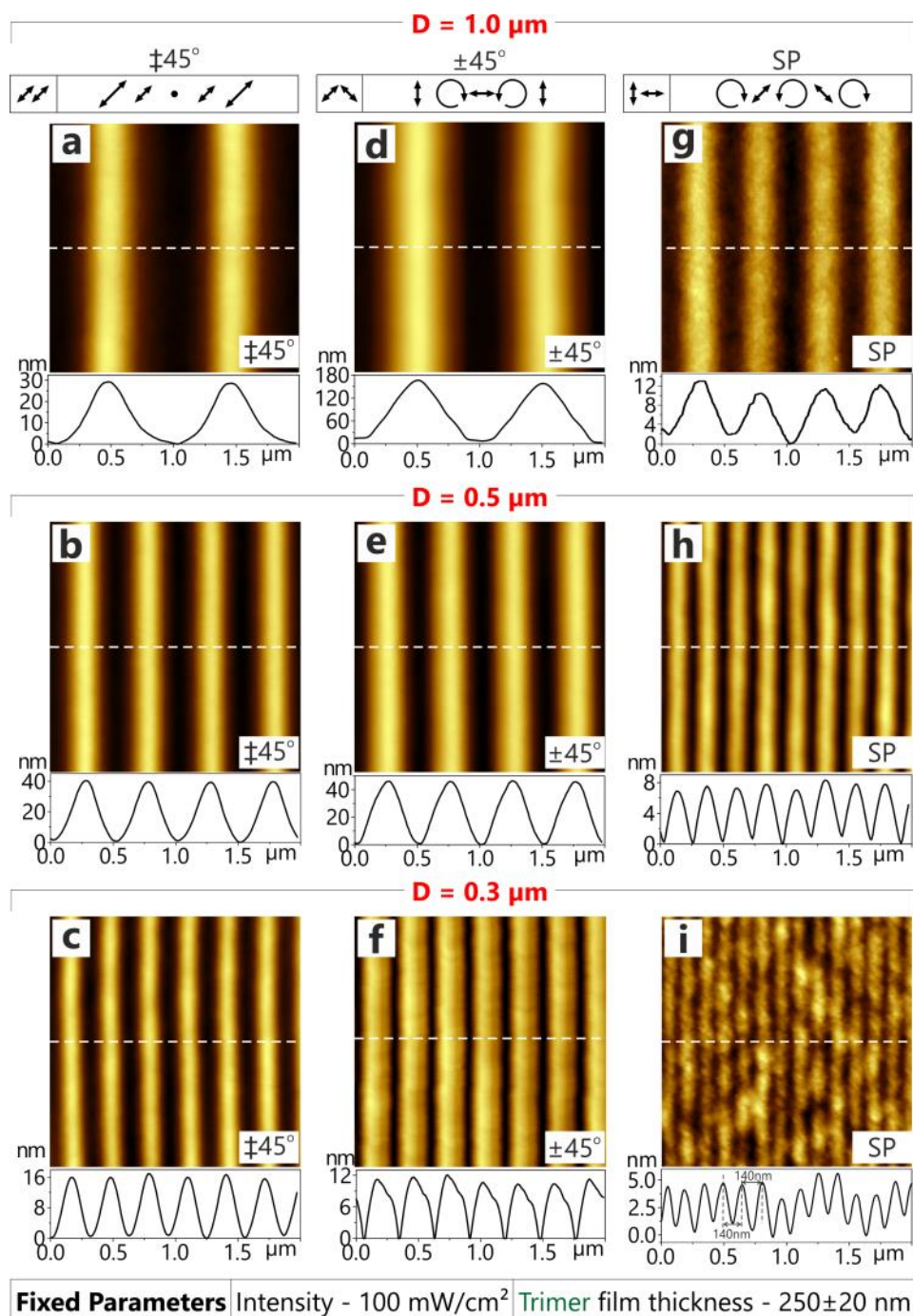
Fig. 7.2. Comparison of grating formation at varying periodicities (1, 0.5, 0.3 μm) and varying interference patterns (‡45°, ±45° and SP) using ~250 nm thick trimer film. a), b), c) SRG formation due to pure intensity grating (‡45°) with periodicities 1, 0.5, 0.3 μm, respectively. d), e), f) SRG formation by pure polarization grating (±45°) periodicities 1, 0.5, 0.3 μm, respectively. g), h), i) SRG formation by SP interference pattern with double grating phenomena periodicities 1, 0.5, 0.3 μm respectively.

7.1.1. Exploiting SP interference pattern for nano-patterning

Irradiation with an SP ($\updownarrow$, $\leftrightarrow$) interference pattern of 280 nm periodicity resulted in a surface relief grating of around 140 nm periodicity, i.e. already more than 3 times smaller than the wave length of the incident light. Fig. 7.3 shows the SRG generated during irradiation with the SP pattern at four different optical periodicities: 510 nm, 420 nm, 350 nm and 280 nm, that results in surface relief with half of optical periodicity, 255 nm, 210 nm, 175 nm, and 140 nm, respectively (Fig. 7.3(a–d)).
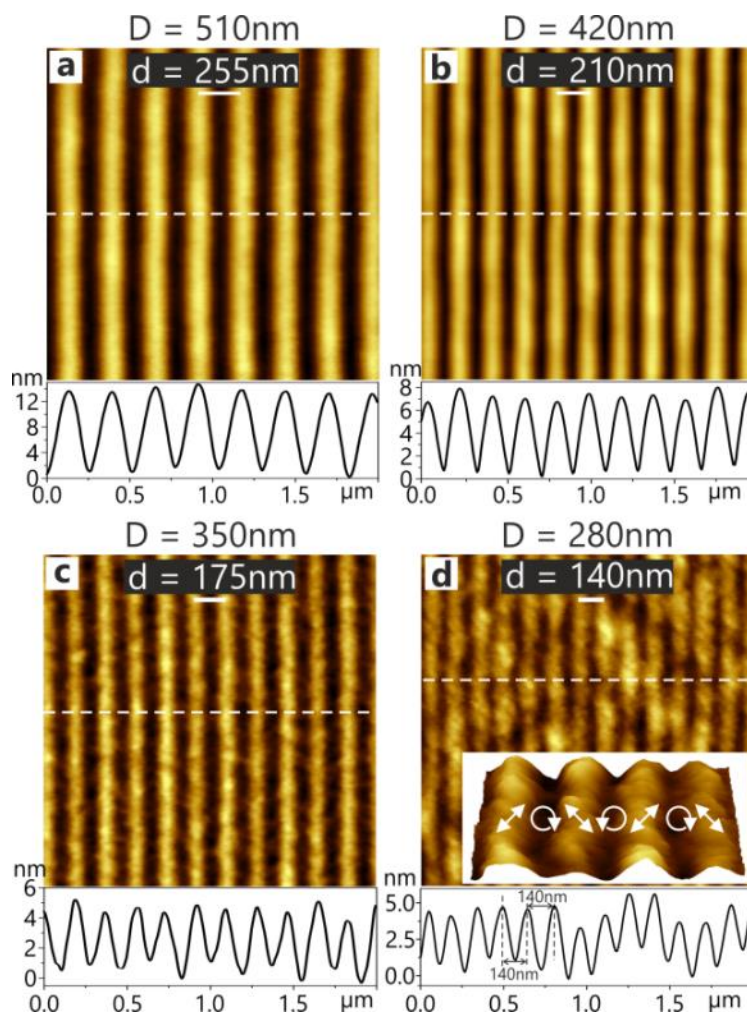
Fig. 7.3. AFM micrographs of the SRG inscribed by SP polarization combination for different optical periodicities. 510 nm (a), 420 nm (b), 350nm (c), 280nm (d) results in 255nm, 210nm , 175nm and 140nm grating periodicity, respectively.

7.1.2. Influence of interfering beam intensity on the grating periodicity

In past, different groups published treatise on polarization holography and provided a detailed description on effect of interfering beam intensity on $\vec{E}$-field vector modulation in the SP interference pattern outside the paraxial approximation (i.e. large angle between the interfering beams).[101,102] In Fig 7.4b, we have compared the local orientation of the $\vec{E}$-field vector of SP pattern when the two interfering beams are with equal intensities (i.e. $I_1 = I_2$; row 2) and when one of the beams has half the intensity of the second beam (i.e. $I_1 = 2I_2$; row 3).
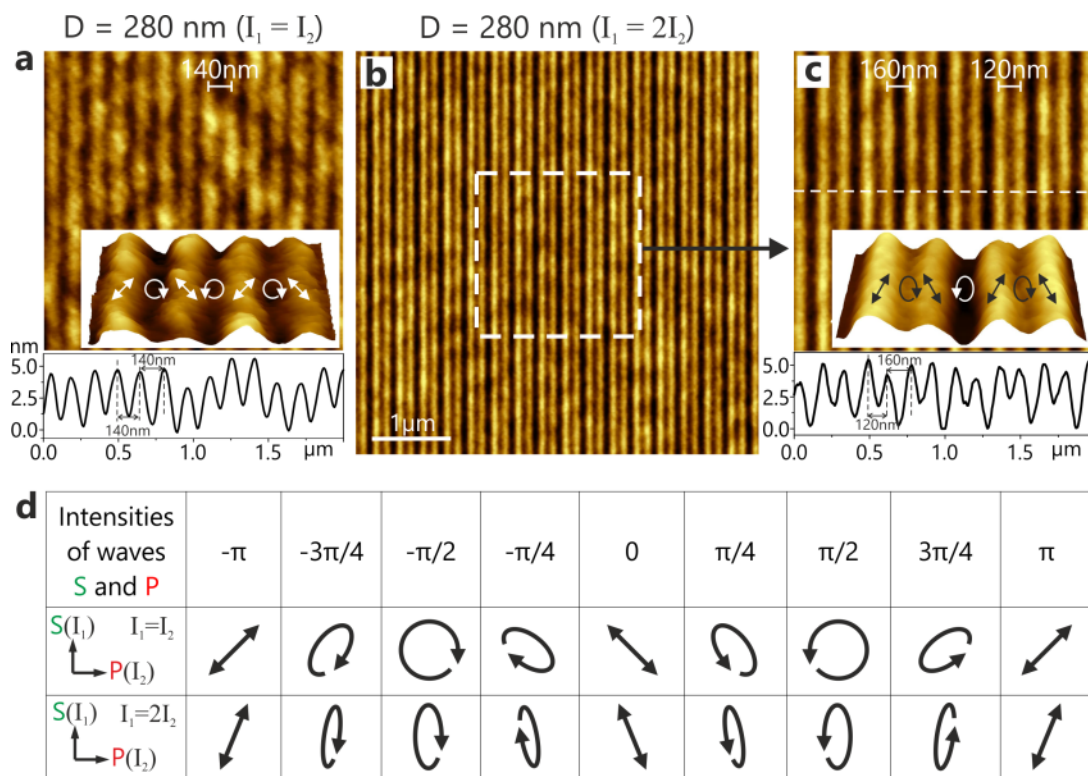
Fig. 7.4. Effect of intensity on SP grating periodicity (a) 150 nm grating periodicity with 300 nm optical periodicity with equal intensity of two interfering beams. (b) dual grating periodicity effect at 300nm optical periodicity when the intensities of two interfering beams are unequal. (d) The SP interference pattern of two waves with orthogonal linear polarization with equal intensities (row 2) and different intensities (row 3) of interfering beams.[101]

Fig 7.4a shows the SRG below diffraction limit using SP interference pattern with both the interfering beams of equal intensity. For an optical periodicity of 280 nm,

we have obtained a grating periodicity of 140 nm throughout the irradiation area. The double grating formation phenomena using SP pattern is well studied in previous chapters. In Fig 7.4b, we have presented a dual grating periodicity effect observed when the interfering beams of SP interference pattern has intensities of $I_1 = 2I_2$. For a grating periodicity of 280 nm, we observed two different periodicities, the small periodicity is observed to be 120 nm while the larger periodicity is measured to be 160 nm. The dual grating periodicity is observed even for larger periodicities when the intensity of the beams has condition of $I_1 \neq I_2$. Comparing the interference patterns presented in Fig 7.4d, it appears to be that the mass transport of molecules is guided by a mutual contribution between the linearly and circularly polarized $\vec{E}$-field vectors. To understand the double grating periodicity effect we need more theoretical and experimental studies for a detailed understanding over the response of trimer molecules in the presence of various linear, circular and elliptical $\vec{E}$-field vectors.

7.1.3. Linear gratings below diffraction limit using a different photosensitive material

In the above sections, we have seen the formation of SRG with the size below diffraction limit. To observe the reproducibility of this phenomenon, we have considered testing another photosensitive material.

As an alternative, we used the poly(ethylene imine)-(Methyl red, Na salt), code named as GL2360, the chemical structure is shown in Fig 7.5a. The synthesis of the polymer is described elsewhere.[103] To prepare a 250 nm thin polymer film, the polymer sample was spin-coated at 3000 rpm during 1 minute on a glass substrate from a 5 mg/ml MeOH solution. The UV-Vis absorption spectrum for this polymer is provided in supporting information Fig C.11 with the absorption maximum at 420 nm.

The molecular weight of GL2360 is relatively high compare to trimer, but similar to PAZO. Irradiating this polymer film with 250 nm periodicity using SP interference pattern resulted in the formation of 125 nm grating periodicity as shown in Fig 7.5b, which is three times smaller than the actual source wavelength of 491 nm. Despite the low efficiency of gratings presented in Figs (7.4 and 7.5), using a suitable photosensitive material and experimental parameters, it should be possible to achieve very efficient gratings at periodicities below diffraction limit.
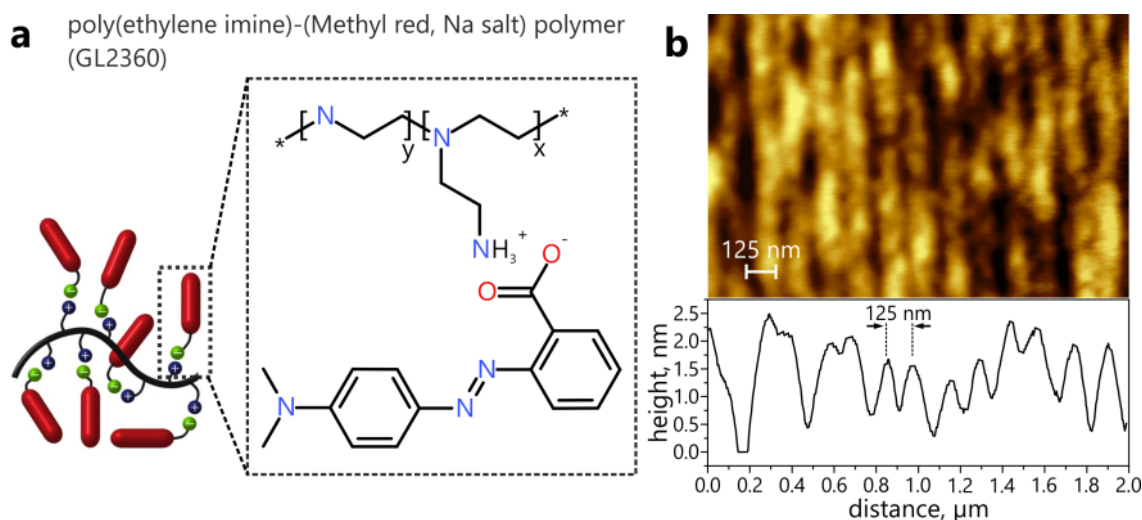
Fig. 7.5. (a) Chemical structure of poly(ethylene imine)-(Methyl red, Na salt). (b) AFM micrograph of the SRG with 125 nm grating periodicity inscribed by SP (PIP) with D = 250 nm optical periodicity.

7.2. Orthogonal structures

To demonstrate the potential of double grating formation phenomenon during irradiation with SP interference pattern, we inscribe square array topography into a photosensitive film. For this, we apply a two-step irradiation procedure.

Figure 7.6a shows the scheme of experimental steps followed to achieve the square arrays. Fig 7.6b shows the AFM image of the surface relief structures when two gratings are recorded orthogonally to each other at the same location in a sequence. Polymer film thickness of 250 ± 20 nm is used for all measurements presented in the current section. First surface relief is inscribed with 0.5 μm periodicity (D), intensity of 100 mW/cm^2 with ±45° interference pattern for a time period of 60 min. Then, the sample is rotated orthogonally (90°) to the initial grating lines and another 60 min of irradiation performed with same irradiation parameters. The dimensions of square lattice (orthogonal grating) are shown in Fig 7.6b. The depths of the gratings formed in typical cases are in the range of 130 ± 20 nm. The distance between two adjacent bell structures is measured as 490 ± 10 nm while the diagonal distance between any two bell structures of single square unit is measured as 650 ± 50 nm.

101
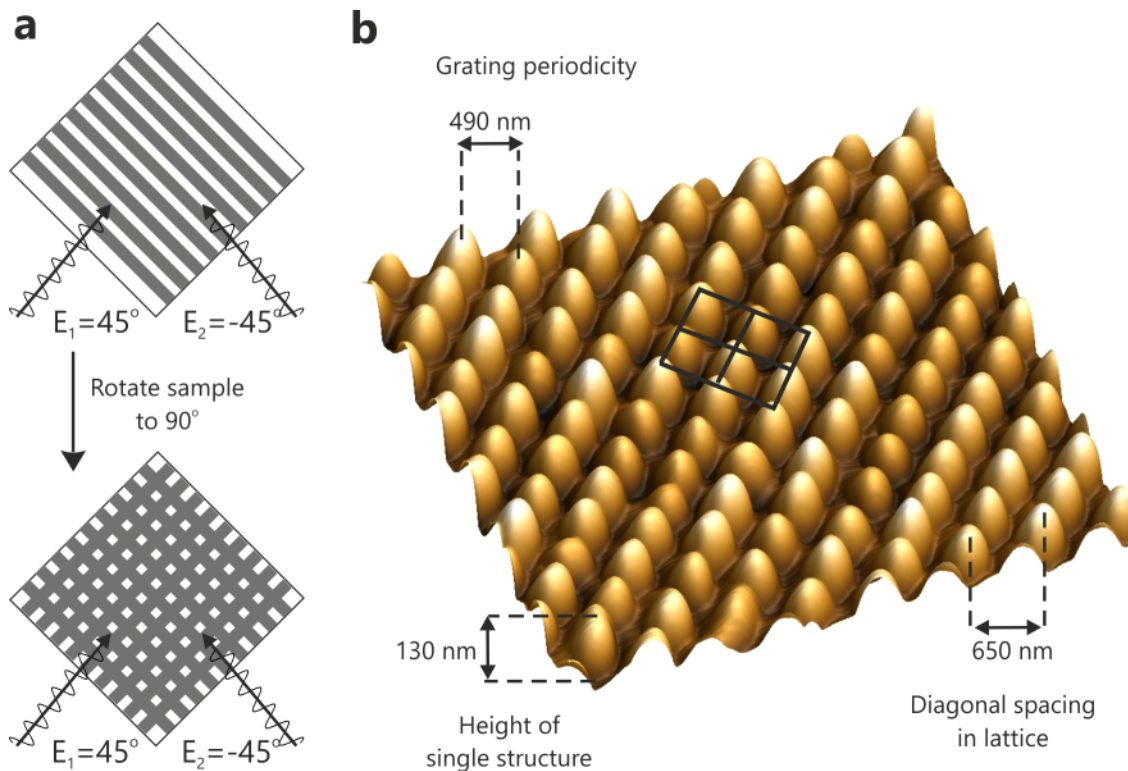
Fig. 7.6. Orthogonal gratings generated using successive cross irradiation with the ±45º interference pattern. (a) The schematic picture highlights the production steps: the SRG is inscribed in the first step of irradiation, followed by a second cross irradiation. (b) AFM micrograph of the topography pattern.

7.2.1. Orthogonal structures using SP interference pattern

In the previous section, we have seen the orthogonal gratings with an optical periodicity of 500 nm using ±45º interference pattern. Here, we are presenting the same experiment using SP interference pattern.

For an optical periodicity of 500 nm, resulting lattice has a periodicity of 250 ± 5 nm and the grating height of 25 ± 5 nm as shown in Fig. 7.7. The squared ordered arrays are homogeneous all over the irradiation area of 5×5 mm².

Fig. 7.7. Orthogonal gratings generated using successive cross irradiation with the SP interference pattern. (a) AFM micrograph of the topography pattern with orthogonal grating at diffraction limit of 250 nm periodicity with 491 nm wavelength. (b) inset and (c) detailed analysis of individual structures.

7.2.2. Square arrays below diffraction limit

The orthogonal grating experiments presented above are repeated with SP interference pattern at periodicities of 350 nm and 280 nm. Fig 7.8 shows the square arrays with grating periodicity of 175 nm, the height of each bell structure is 4 nm.

The asymmetric double grating phenomena could also be well exploited to achieve more complex and periodically arranged square arrays as shown in supporting information S4. Using a cross irradiation with the SP polarization combination using optical periodicity of 280 nm, we are able to produce square arrays with a smallest periodicity of 140 ± 20 nm at 1cm² area (supporting information Fig C.12), which is four times below the diffraction limit of the source wavelength (491 nm). A detailed AFM analysis of the size and periodicity of orthogonal gratings is shown in the Fig C.12b. We observe different periodically aligned features with larger square structures surrounded by rectangular and small square features. For better illustration we mark different pattern by proper color on the scheme inserted in the Fig C.12a (inset) and on the

103

AFM micrograph in the Fig C.12b. The smallest distance between any two neighboring bell structures in square arrays is measured to be 100 ± 10 nm. The depth of each bell structure is only between 2 and 5 nm. Despite very weak growth rate, the double grating phenomena could be fully exploited by tailoring the suitable materials.
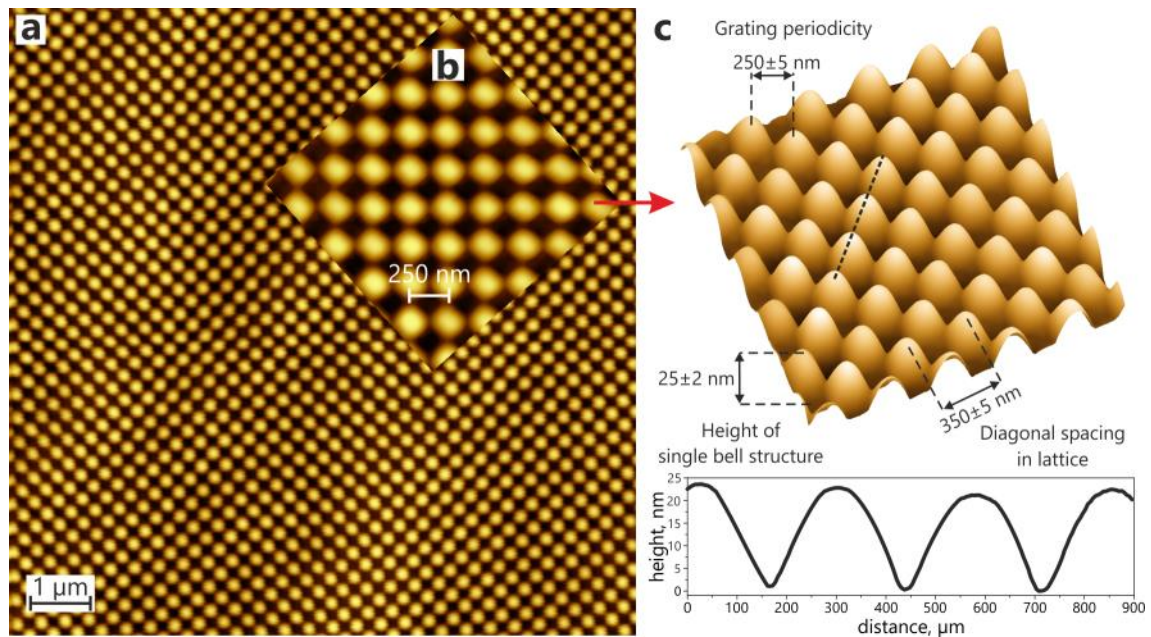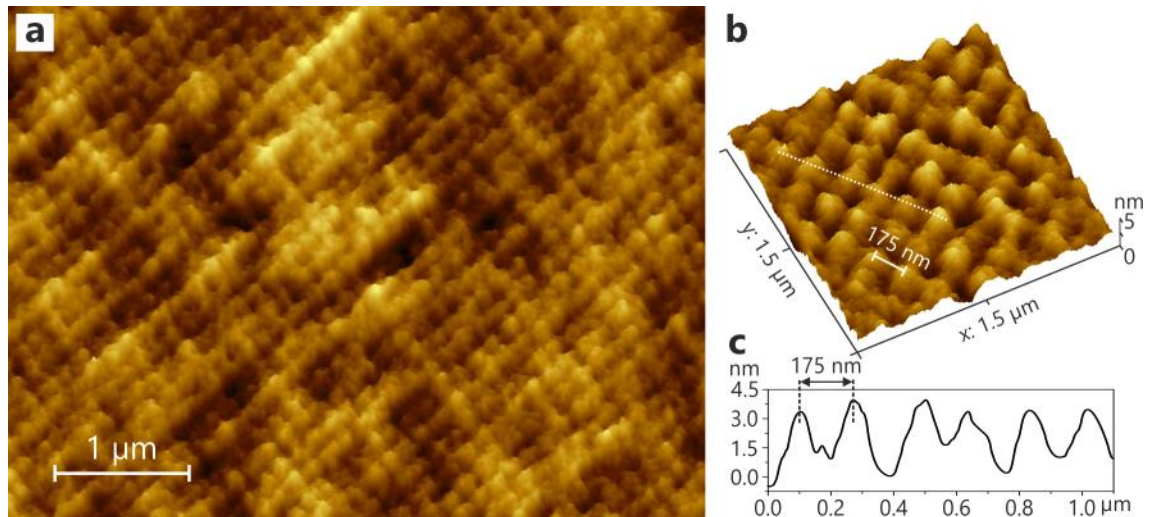

Fig. 7.8. Orthogonal gratings generated using successive cross irradiation with the SP interference pattern. (a) AFM micrograph of the topography pattern with orthogonal grating at diffraction limit of 175nm periodicity with 491nm wavelength of the inscribed light. (b) Cross sectional profile.

7.3. Summary

In a short overview of this chapter, we have shown that using SP (↕, ↔) interference pattern, it is possible to achieve linear and orthogonal gratings with the size below the diffraction limit. We have tested three different photosensitive materials, *viz.* PAZO, trimer, and GL2360. The effects of interfering beam intensity on the periodicity of the polymer gratings using SP pattern are visualized for the first time. We have obtained reproducible linear and orthogonal gratings of 140 nm periodicity, which is three times smaller than source wavelength of 491 nm.

<div align="right">

8

</div>

Probing Opto-Mechanical Stresses
Induced during the SRG Formation[*]

To probe opto-mechanical stresses associated to the mass transport phenomena during SRG formation, we have considered depositing a thin metal film on top of the photosensitive polymer film (1 μm thick PAZO film) to see if the metal layer could be deformed; the observations are presented in the following sections.

8.1. Deformation of thin gold films on PAZO during the SRG formation

A thin gold film of 25 ± 2 nm is deposited on a micrometre thick PAZO film at a deposition rate of 0.25 nm/sec via physical vapour deposition (PVD) process using Leybold Oerlikon Univex 350. Fig 8.1b shows a high resolution SEM image of Au/PAZO/glass interface acquired with advanced Zeiss Supra 40VP Scanning Electron Microscope, operated at the "Interdisciplinary Resource Center for Nanotechnology, St. Petersburg, Russia".

A gold film of 25 nm thick should offer considerable constrain/resistance to the deformation of relatively soft polymer underneath. To observe the impact of SRG formation on the gold film and vice versa, we set up an *in-situ* AFM measurement. The experimental setup described in Fig 3.6 is applied to perform the *in-situ* observation of metal film deformation during SRG formation. To choose an appropriate interference pattern (*i.e.* IIP or PIP) for the polymer film irradiation, the possible change in surface area of polymer film topography before and after the irradiation as shown in Fig 8.1a is considered as a decisive parameter.

---

[*] Parts of the data presented in this chapter are published by the author of current dissertation in *ACS Appl. Mater. Interfaces* **5**, 7743 (2013), *ACS Appl. Mater. Interfaces* (2014) – DOI: 10.1021/am501870t and submitted for publications in other journals.
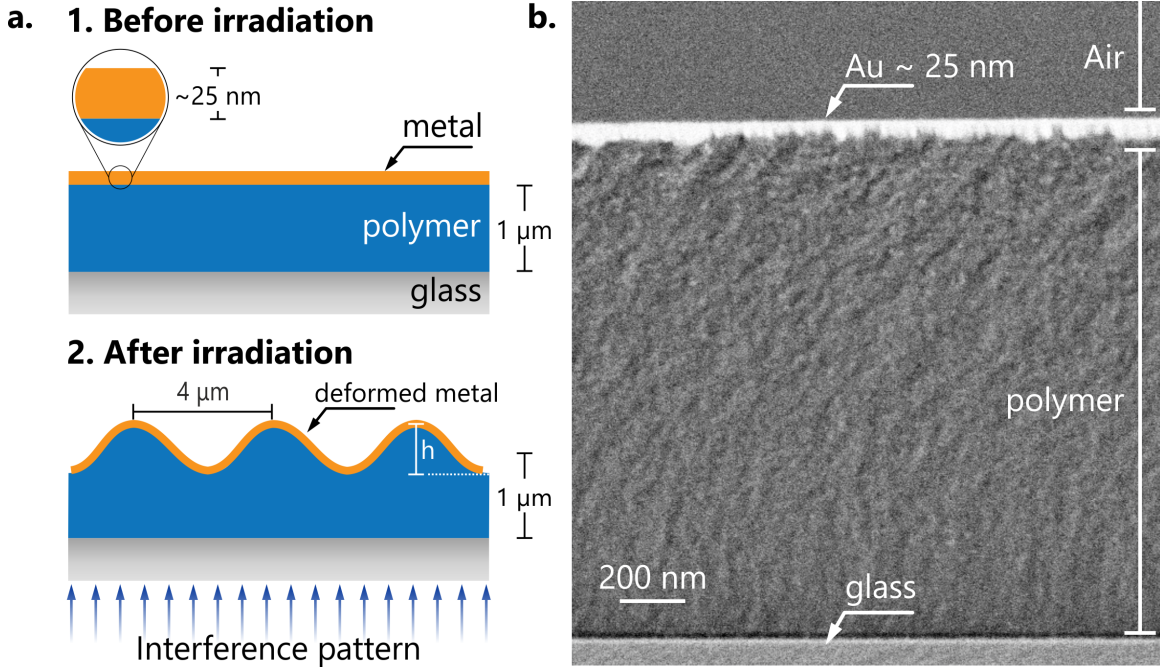
Fig. 8.1. (a) Scheme of experimental plan to test the deformation of metal layer during SRG formation in PAZO film. (b) SEM image of sectioned sample showing deposited gold film (bright region) on PAZO film before irradiation.

8.1.1. Change in surface area

To calculate the change in surface area, we assume sinusoidal profile of the SRG: $z(x) = A_o \sin \frac{2\pi x}{d}$, where A_o, d are half of the grating height (amplitude) and the periodicity of the SRG; we can then calculate the arc length 's' for the one period as

$$s = \int_0^d \sqrt{1 + [z'(x)]^2} \, dx = \int_0^d \sqrt{1 + A_o^2 \frac{4\pi^2}{d^2} \left(\cos \frac{2\pi x}{d} \right)^2} \, dx \qquad (8.1)$$

In section 4.2.2*i*, we have discussed in detail the influence of different interference patterns on the SRG growth kinetic in PAZO films. Using the maximum achievable grating height, we have determined the change in surface area of polymer topography for one period of SRG as shown in Fig 8.2. Comparing the Tables in Fig 8.2 (b and d), it is observed that a grating periodicity of 4 µm results in a maximum change in surface area using ±45° interference pattern in a micrometre thick PAZO film. From Fig 4.6 the RL interference also appears to be

suitable to induce maximum possible deformation in metallised photosensitive polymer films.
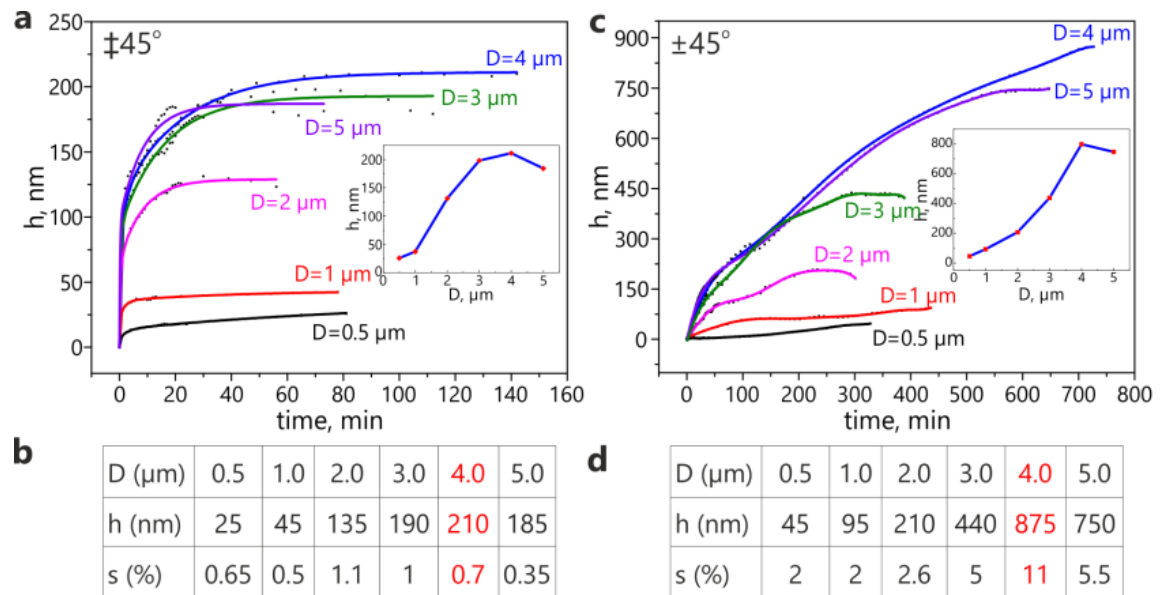
Fig. 8.2. Comparison of grating growth kinetics for different interference patterns. (a) Growth kinetics for IIP interference pattern (↗↗). The inset graph shows the change in height with respect to change in periodicity. (b) Change in the surface area with respect to the change in periodicity determined from the IIP growth kinetics. (c) Growth kinetics for PIP interference pattern (↗↘). The inset graph shows the change in height with respect to change in periodicity. (d) Change in surface area with respect to the change in periodicity determined from the PIP growth kinetics.

Thus, to observe the *in-situ* deformation of metal film during the SRG formation, we used a grating periodicity of 4 μm, PAZO film thickness of 1 μm, 25 ± 2 nm thin film of gold deposited on PAZO film, ±45° interference pattern (↗↘), and 100 mW/cm² irradiation intensity as experimental parameters. The gold film coated PAZO sample is inserted in the experimental setup as shown in Fig 3.6 and the irradiation continued for 12hr to compare the SRG formation in PAZO film with and without gold film on top.

Interestingly, considerable deformation of gold film is observed in *in-situ* AFM measurements during the irradiation of Au/PAZO film with ±45° interference pattern. The SRG formation is recorded as shown in the Figure 8.3 (a, b). The grating growth kinetic presented in Fig 8.3a reveal two important effects of

deposited gold film on polymer. First, the influence of a possible back reflection of light from the gold film into the PAZO causing the developing grating to suppress during the first 30 minutes of irradiation (grey colour bar in Fig 8.3a). Second, constrain of the 25 nm thin gold film to the SRG formation in PAZO film. Comparing the SRG growth kinetic in PAZO film for 4 μm grating periodicity with and without gold film on top (see Fig 8.3a), the maximum achievable grating height in 12hr of irradiation period reduced from 850 nm to 400 nm.
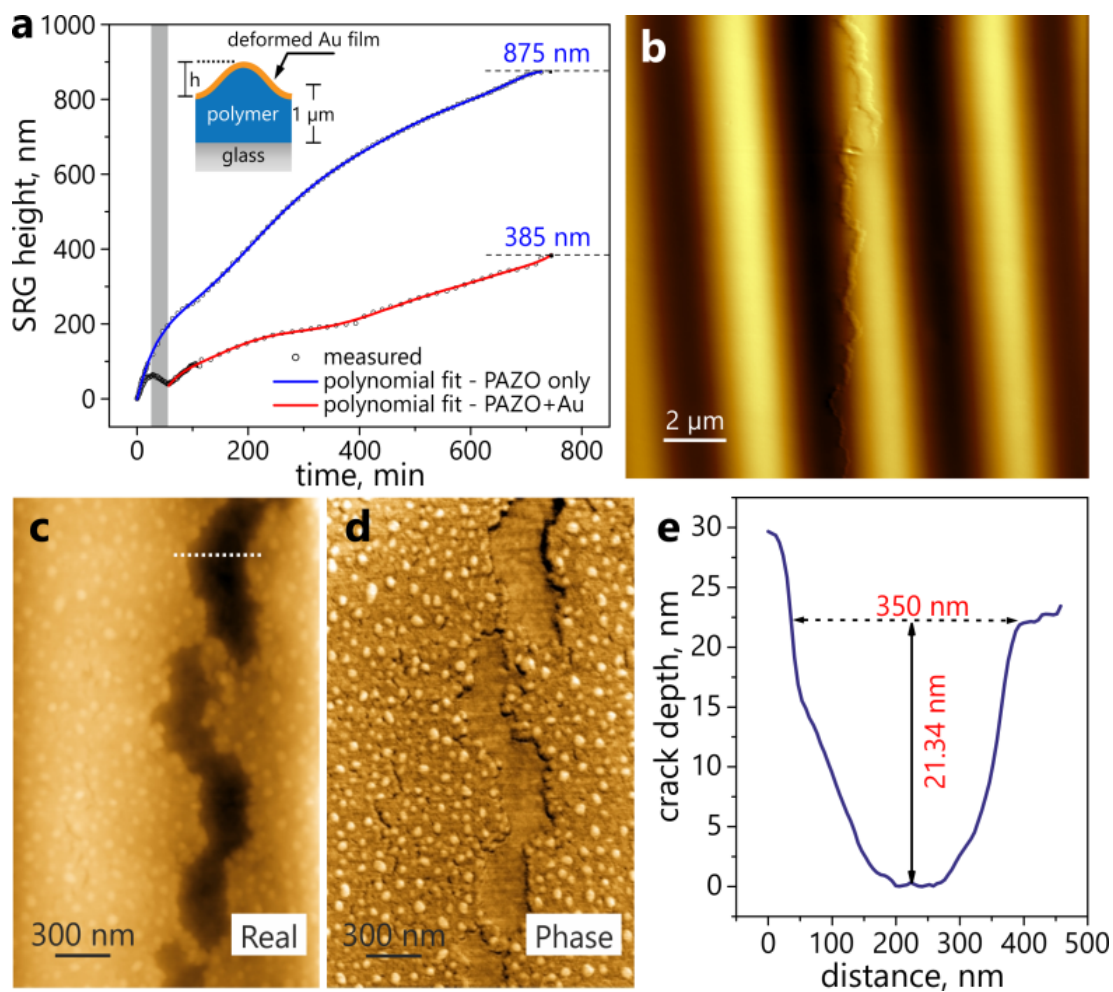
Fig. 8.3. *In-*situ AFM measurement of 25 nm thin gold film deformed during the SRG formation in a micrometre thick PAZO film. (a) SRG growth kinetic of Au/PAZO film. (b) AFM micrograph of deformed metal film topography with observable crack parallel to the grating line. (c) *Ex-situ* AFM Analysis: AFM topography image of deformed gold film with crack. (d) Phase image. (e) Cross-sectional profile of crack highlighted with white dotted line in (c).

In addition to the gold film deformation during the SRG formation, another interesting result is observed as shown in Fig 8.3b (AFM micrograph). A wide crack appeared almost parallel to the SRG line. The width of the crack varies between 50–350 nm from edge to centre. In order to confirm the crack formation, an *ex-situ* AFM analysis is performed on the same sample as shown in Fig 8.3 (c–e). High resolution AFM micrograph presented in Fig 8.3c revealed the topography of gold film with large aggregates of Au particles spread across metal film. The cross sectional analysis of the crack presented in Fig 8.3e (correspond to the white dashed line in Fig 8.3c) confirms the thickness of the deposited Au film to be around 25 nm. During the *ex-situ* AFM analysis, it is observed that similar cracks spread across the irradiation area at random positions; however most of the cracks appear to be parallel to the grating lines.

Experimental Parameters	Intensity - 100 mW/cm²	±45° interference pattern
25 nm thin Au layer on 1 µm thick PAZO film		Irradiation time - 12 hrs
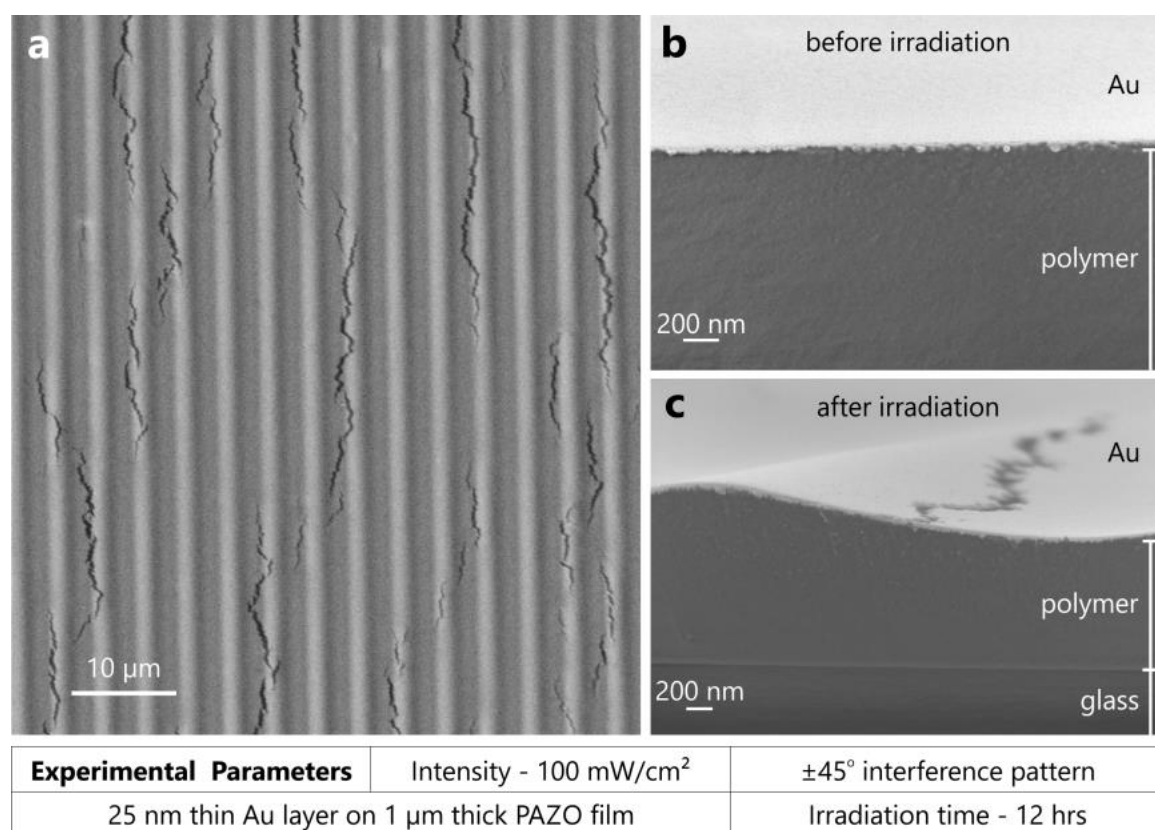
Fig. 8.4. (a) SEM analysis of randomly ruptured 25 nm thin gold film during the SRG formation in PAZO film with 4 µm grating periodicity. (b) Topography of the deposited gold layer on the polymer film before irradiation. (c) Topography of the gold film as adopted neatly on the developed SRG after irradiation.

To visualize the cracks in more detail, SEM analysis is performed as shown in Fig 8.4. Randomly positioned cracks are found through the irradiation area and clearly the cracks are parallel to the grating lines (perpendicular to the grating vector). The crack formation observed in Fig 8.4a is similar to the macroscopic tensile load test applied on a much thicker metallised polymer films (170 nm thick Cu film on several hundred micrometres of polymer substrate), studied elsewhere[104]. Au film topography before and after the irradiation is also presented in Fig 8.4 (b, c). To perform the SEM imaging of interface, the Au/PAZO/glass sample is carefully bisected by applying the breaking pressure towards gold layer to keep the Au/PAZO interface undamaged. We have also repeated the same experiment with 25 nm thin Au layer deposited on the PAZO film using 5 μm grating periodicity and observed similar crack formation (see appendix Fig D.1).
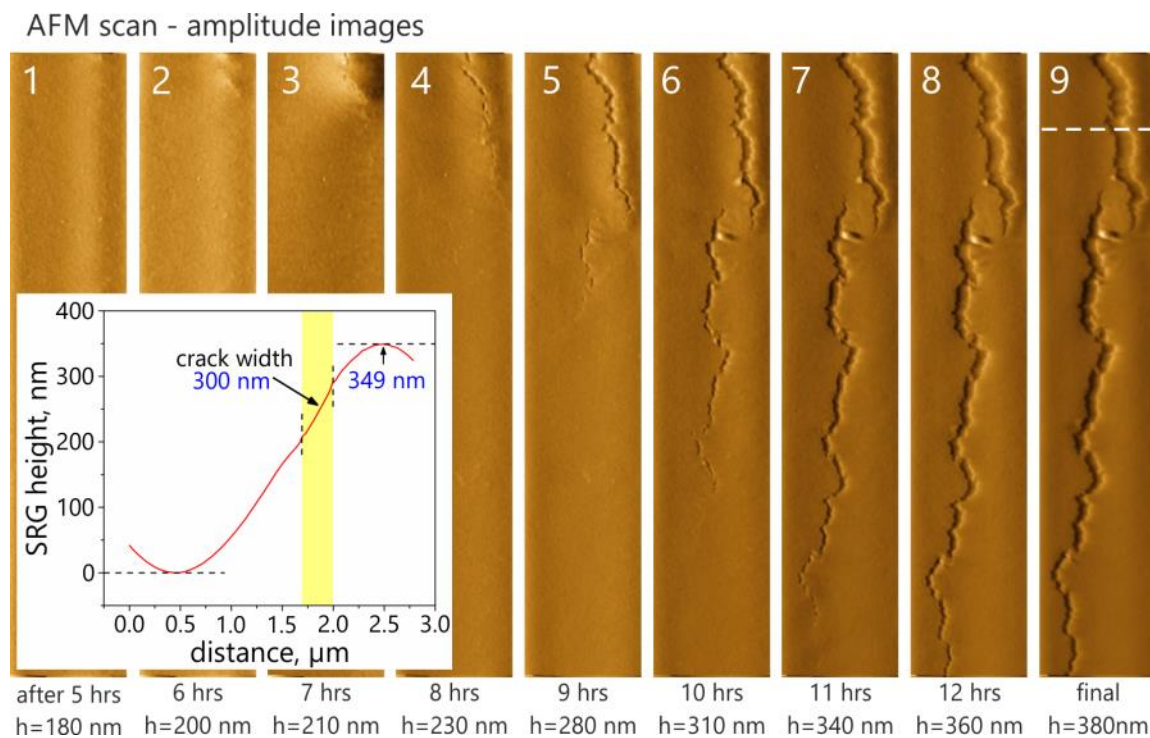
Fig. 8.5. AFM amplitude images: *In-situ* analysis of 25 nm thick metallic film rupturing with ±45° interference pattern at 4μm grating periodicity. The inset graph corresponds to the white dashed line in AFM micrograph 9 and shows the crack position between the SRG maxima and minima. The cross sectional profile is taken from AFM topography image.
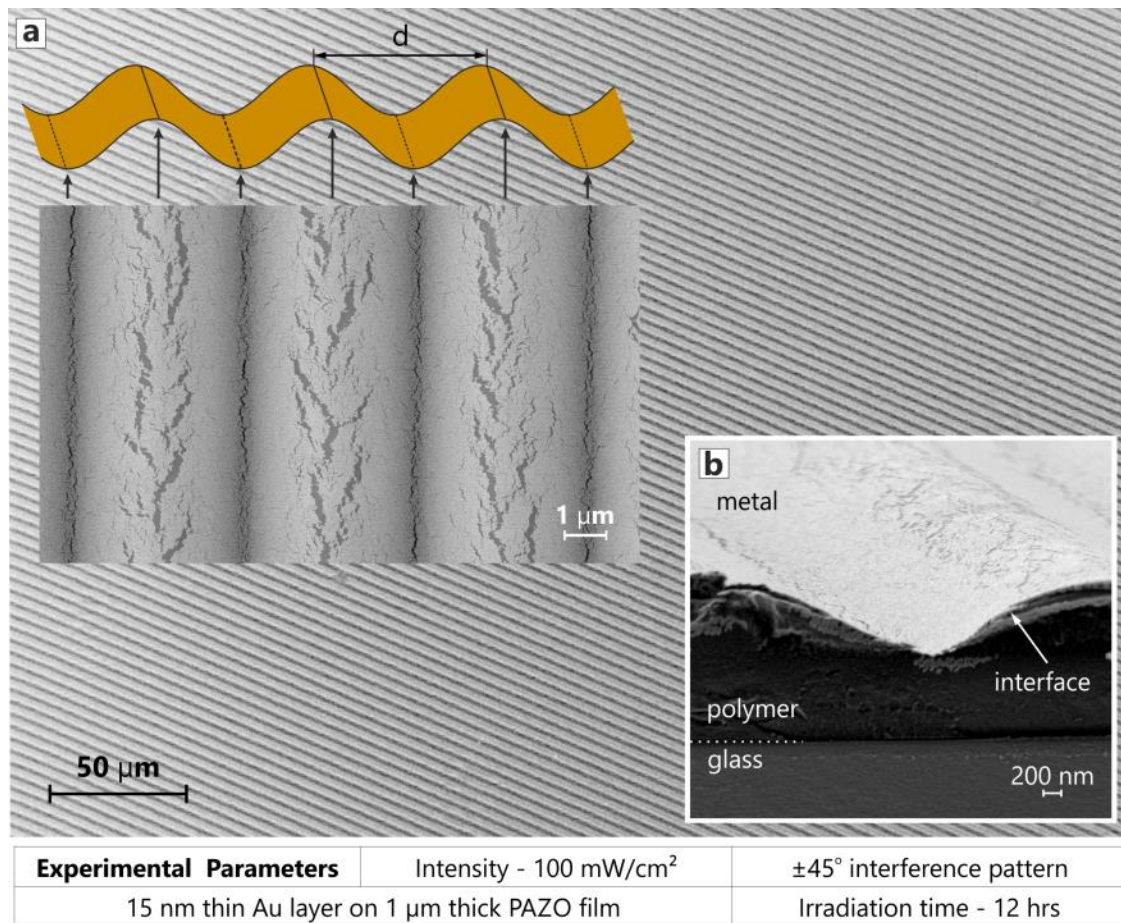
In addition to the above observations, our AFM connected experimental setup made it possible to record the propagation of the crack *in-situ*. In Fig 8.5, we have a set of AFM amplitude images showing the crack propagation at varying irradiation time and grating height. Amplitude images are an alternative to the AFM topography or height images and they correspond to the AFM tip deflection as it encounters the sample topography features. However, the z-scale in the amplitude images is not reliable or meaningless.

The first crack is initiated at a grating height of approximately 180 nm (5 hrs. of irradiation) and is equal to a change in surface area of 0.5 %. A pronounced crack is observed at a change in surface area of 3 %. For a much larger metal film thickness (> 50 nm), the required strain is reported to be more than 10 %.[100] Following 12 hrs of irradiation, a crack width of ~ 300 nm is measured and the crack length varies between 10–30 μm.

8.2. Periodic rupturing of ultra-thin Au films

The metal film deformation and rupturing behaviour observed in Fig 8.4 appears to be similar to the macroscopic tensile load test, where the loads are applied at both the ends of metallised polymer substrates. The nature of load applied in a macroscopic tensile load test is global and non-uniform on the whole substrate. However, intuitively one could presume that SRG formation takes place due to the mass transport of material from local minima towards local maxima. Thus the nature of load applied on metal film during the SRG formation might be periodic and localized at a periodicity of 4 μm.

To understand the origin of stresses lead to the observed crack formation in the previous section, we have reduced the Au film thickness from 25 ± 2 nm to 15 ± 2 nm with deposition rate of 2.5 Å/sec. The advantage of depositing a thin gold film on polymer substrate is that one could easily achieve a continuously coated conductive metal film on polymer surfaces without seeding layer.[105,106] Despite reduced film thickness, 15 nm thin Au layer neatly covered on the whole PAZO surface (see appendix Fig D.2). The sample is then irradiated with ±45° interference pattern and 4 μm grating periodicity for 12 hrs. The *in-situ* analysis of film deformation revealed that the maximum achievable grating height dropped from 875 ± 50 nm to 650 ± 30 nm (Fig 8.7a) compared to 400 nm in case of 25 nm thick Au film. Obviously 15 nm thin Au film offers less resistance to the deformation compared to 25 nm thin Au layer.

Experimental Parameters	Intensity - 100 mW/cm²	±45° interference pattern
15 nm thin Au layer on 1 µm thick PAZO film		Irradiation time - 12 hrs

Fig. 8.6. (a) Periodically ruptured Ultra-Thin Au film (15 nm) during SRG formation in PAZO with ±45° interference pattern. The SRG maxima and minima are compared with the SEM micrograph. (b) 3D view of the periodically ruptured 15 nm thin Au film. The background large scale SEM micrograph corresponds to the same sample with many grating lines.

SEM analysis of the deformed 15 nm thin gold film revealed an interesting phenomenon: the gold layer is ruptured periodically all over the irradiation area (Fig 8.6). The rupturing is homogeneous along the stripes and appears twice a period, i.e. at the topography maxima and minima (Fig 8.6 (a, b) and appendix Fig D.3) confirming the presumption that the stresses are localized at every 4 µm periodicity due to the local mass transport of material during SRG formation. From Fig 8.6a, one could observe that the shape and the size of the formed cracks differ depending on their position on the SRG. Zigzag cracks appear at the maximum of each grating line on the polymer topography and have characteristic orientations at angles between 50° and 60° to the grating vector. In

the valleys, the cracks are confined along a line perpendicular to the grating vector. The width differs as well, to be larger (up to 400 nm) at maximum of the SRG.
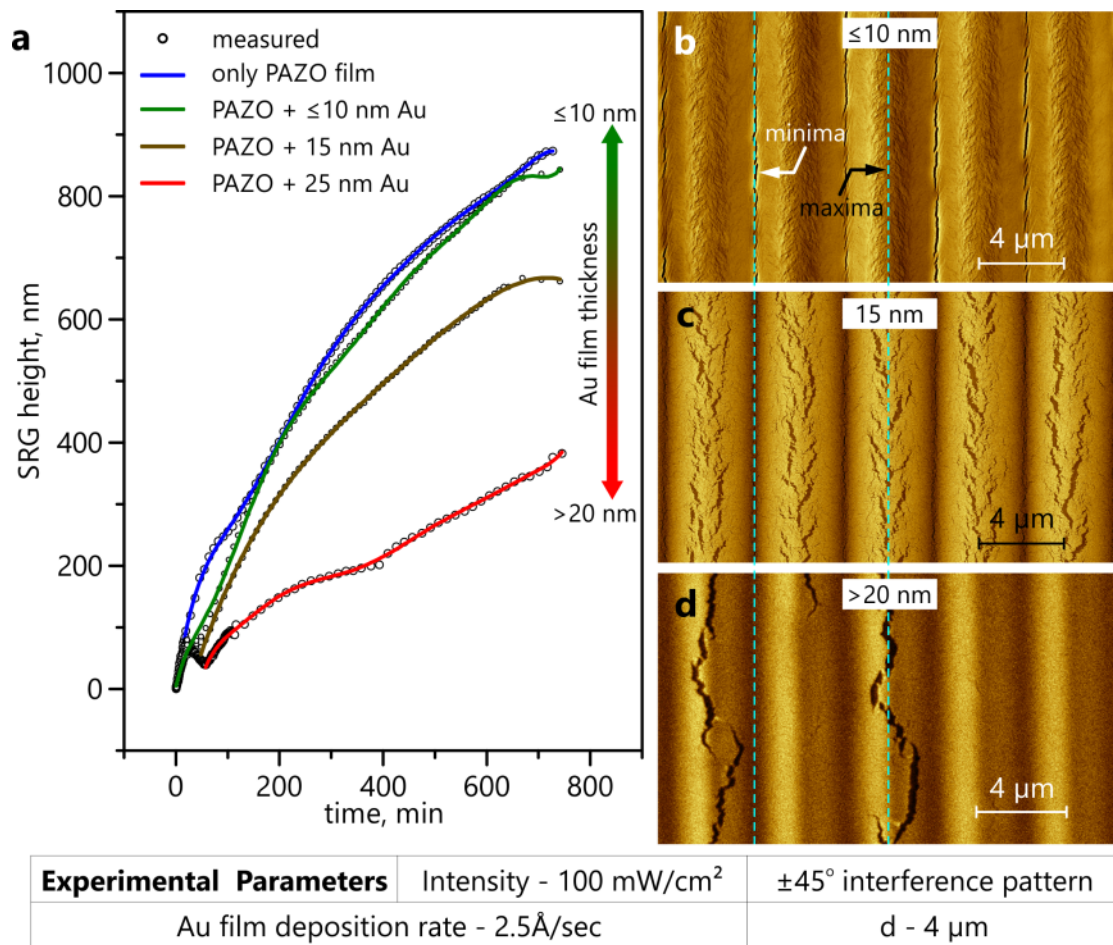
8.2.1. Influence of Au film thickness on the crack formation

The primary goal of using a metal film on PAZO is to probe the stresses induced or developed during the SRG formation in polymer. The cracks in metal films observed in Figs (8.4 and 8.6) appear to be the imprint of localized stresses induced during the SRG formation. However, more experiments are necessary to validate this assumption.

Here, we have studied the crack formation by varying the Au film thickness between 5–30 nm. The observations are briefed in Fig 8.7. Continuously coated and good conductive metal films of as thin as 5 nm are deposited on PAZO surface. The dependency of SRG growth kinetic during the SRG formation is presented in Fig 8.7a. Obviously, the maximum achievable strain in metal film increases with decrease in the metal film thickness. From the growth kinetic in Fig 8.7a, we could see that there is no significant mechanical resistance on the SRG formation in PAZO film using a metal film thickness of ≤ 10 nm. Using a metal film thickness of > 10 nm, the mechanical resistance to the polymer deformation increased rapidly and beyond 50 nm thin Au films, the polymer deformation is completely restricted.

Fig 8.7 (b, c, d) compares the crack formation in Au films of different thicknesses with a grating periodicity of 4 μm using ±45° interference pattern. Randomly positioned cracks are observed for the Au films of between 20–30 nm (Fig 8.7d), however, beyond 25 nm the density of cracks in the irradiation area are reduced, and no cracks are observed for Au films beyond 35 nm thick. Up to 50 nm thick gold films, considerable deformation of h = >50 nm is observed. For the Au film thickness between 10–20 nm, a periodic crack formation is observed (Fig 8.7c). Though cracks appeared twice a period, more pronounced cracks are observed at the maxima and a thin perturbation is seen at the grating minima. Further, as the metal film thickness approaches close to 10 nm, more pronounced crack appeared at grating minima while a local perturbation is seen at the grating maxima (Fig 8.7b). This observation of changes in the crack formation for different film thicknesses is intriguing and puzzling.

Also noticing the growth kinetics of pure PAZO film and PAZO with ≤ 10 nm thin films, the effect of back reflection on the first 60 min of SRG formation is suppressed. The width of cracks in each case varied between 200–500 nm.

Fig. 8.7. Influence of Au film thickness on the crack formation during SRG formation. (a) SRG growth kinetic for only PAZO film (blue curve), ≤ 10 nm Au on PAZO (green), 15 nm Au on PAZO (brown), and > 20 nm Au on PAZO film (red). (b) SEM image: Periodically ruptured 10 nm thin Au film with pronounced crack at the grating minima. (c) SEM image: Periodically ruptured 15 nm thin Au film with pronounced crack at the grating maxima. (d) SEM image: Random cracks in > 20 nm thin Au film.

8.2.2. Influence of interference pattern on the crack formation

The results presented in Fig 8.7 supports our initial assumption that the cracks seen are probably the imprint of localized stress distribution induced during the SRG formation. Intuitively, one could say that the local stresses are due to the mass transport of material and is controlled by the applied interference pattern.

To see if the change in interference pattern could alter the mass transport processes underneath the SRG formation and there by the nature of crack formation, here we compared the SRG formation with ±45° and RL interference patterns as shown in Fig 8.8.
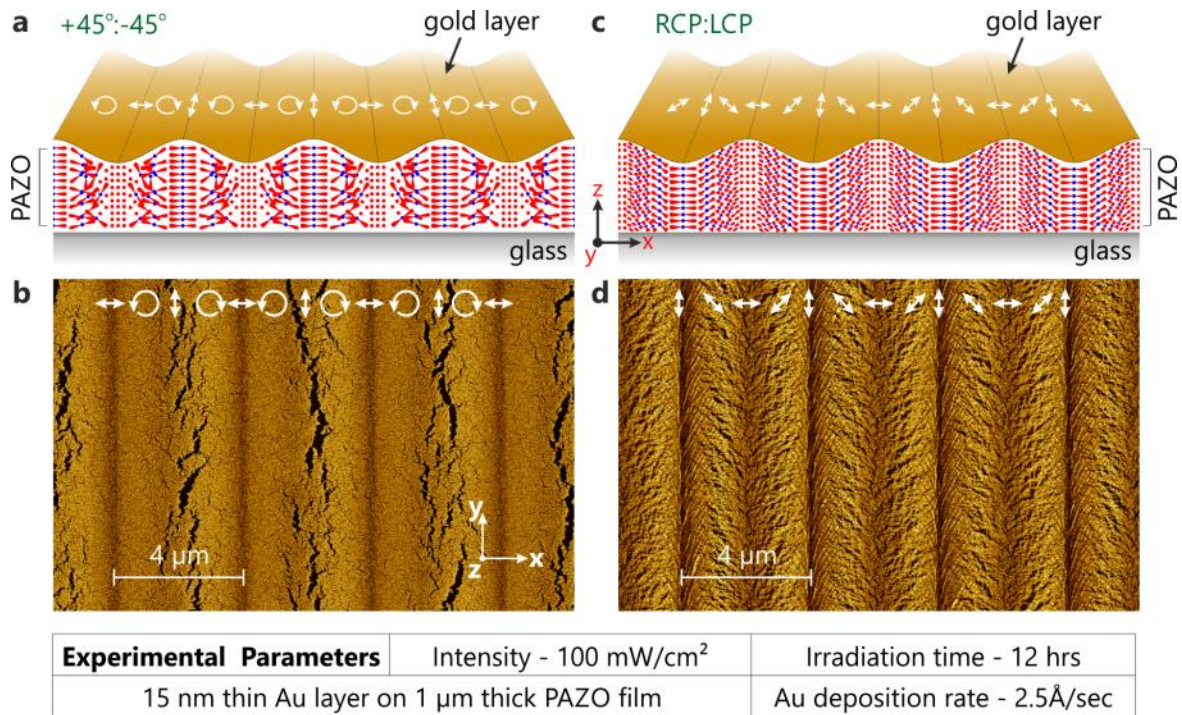
Fig. 8.8. SEM micrographs of the 15 nm thin Au layers deformed on the polymer film during inscription of the surface relief grating using two different polarization states of the interference pattern: (b) ±45° and (d) RL. The distribution of the $\vec{E}$-field vector relative to the topography variation is depicted by white arrows. (a), (b) For both cases the schematically representation of azobenzenes orientation in the polymer film after irradiation is shown above the SEM micrographs.

When the SRG is inscribed by interference pattern of different polarization states, for instance RL, the metal layer is also ruptured as shown in Fig 8.8d. However, at the same change in the height and periodicity (see Fig 8.9f) of the grating, i.e. the same induced strain, the morphology of the deformed metal layer differs significantly. Thus, when comparing the meal layer deformed by irradiation with ±45° (Fig 8.8a, b) and RL (Fig 8.7c, d), one may immediately recognizes that in the first case the metal ruptured only at the SRG maxima. In the case of RL deformed metal, at the slopes of the SRG there are densely spread cracks progressing from

grating minima towards maxima at an angle of 65º with respect to the grating vector. We have also observed the crack formation for both the interference patterns at different grating height in *ex-situ* SEM analysis as shown in Fig 8.9.
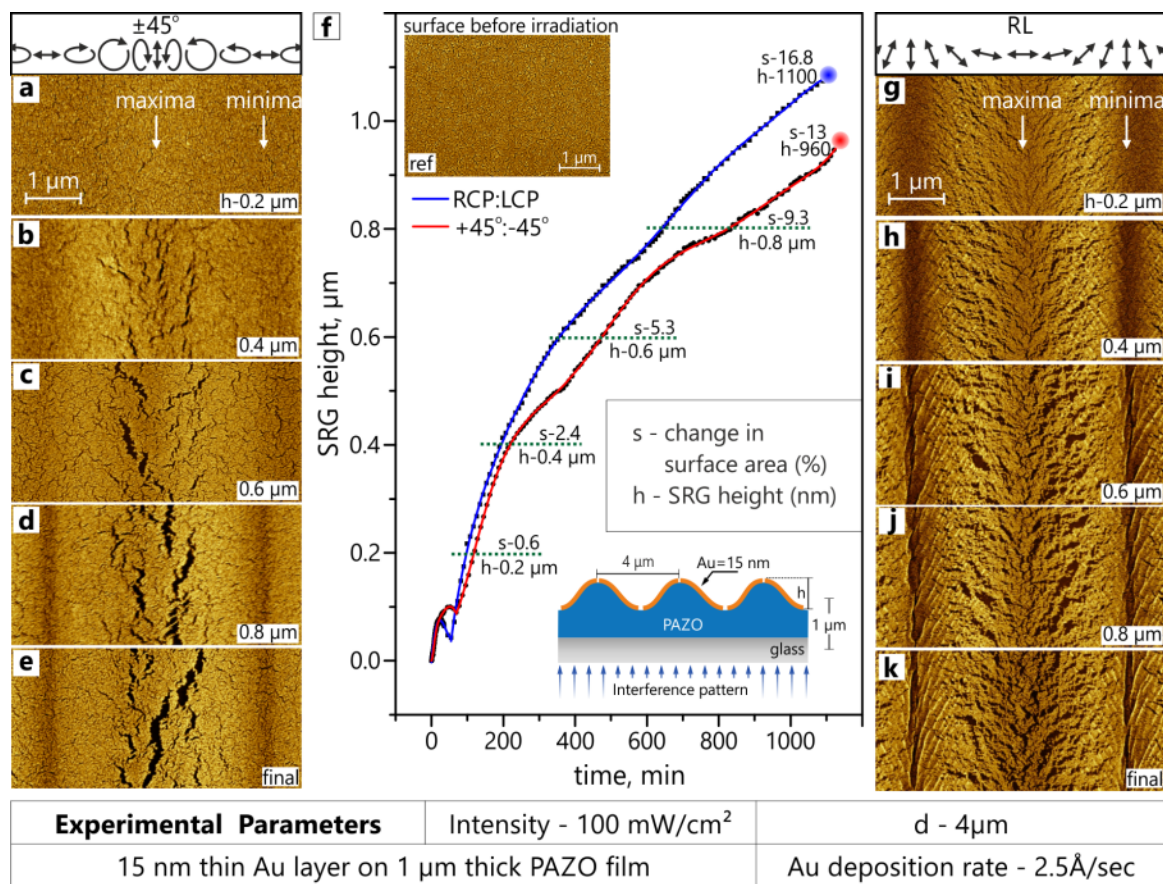
Fig. 8.9. Comparison of crack formation for 15 nm gold film with polarization modulated interference patterns (±45º and RL) as a function of grating height (h). (a–e) development of crack formation at different stages of grating growth is presented through ex situ experiments for ±45º interference pattern. f) Comparison of grating growth profiles for ±45º and RL interference patterns. In the top left corner, inset shows the SEM image of topography of the gold film surface on polymer substrate before irradiation. The bottom right corner shows the scheme of common sample and grating parameters. (g–h) development of crack formation at different stages of grating growth is presented through ex situ experiments for RL interference pattern.

The cracks discussed until now for different experimental parameters start to appear only after several minutes of irradiation when the grating height increases

more than half of the maximally attainable height (Fig 8.9). For instance if the irradiation proceeds 200 minutes (see growth kinetic in the Fig 8.9f), the metal layer with inscribed SRG topography stays intact. Additionally, metal wrinkles at the topography minima are detected when the metal film ruptured with RL pattern (see Fig 8.9(g–k)). SEM images of cracks spread across larger scan area are included in the appendix Fig D.4. From this observation one can conclude that at the same applied strain and kinetic of the deformation the local distribution of the strength and direction of the opto-mechanical load (stress distribution) should be different for different polarization state of the interference patterns.

Thus, the periodic crack formation phenomenon presented in sections 8.2.1 and section 8.2.2 should be an imprint of localized stress developed within the polymer film during SRG formation. In addition, features like convenient adaptability of metal film on the deforming polymer surface and the wrinkles presented in Fig 8.9k posing more interesting questions about the nature of bonding layer near the ultra-thin metal/polymer interface. One could presume that there should be a strong bonding layer. However, probing the bonding layer experimentally is a challenging task. Here we solve this problem by first looking for the existance of any diffused layer at the Au/PAZO interface using Neutron Reflectometry, followed by studying the ashesion of metal polymer interface using an extra interface of multi-layered graphene between Au and PAZO as described in the following sections 8.3 and 8.4.

8.3. Diffused layer at the Au/PAZO interface[*]

To understand the Au/PAZO interface, we have performed neutron reflectivty measurements on 10 nm thin metal films deposited on a micrometer thick PAZO film spin coated on glass substrate. A micrometer thick polymer film is prepared by spin coating of PAZO solution with 250 mg/ml concentration onto a glass substrate (5×7 cm^2) followed by the physical vapour deposition of 10 nm thin gold film on top. The samples are then used for obtaining neutron reflectivity curves at the time of flight reflectometer REFSANS Instrument (Fig 8.10) operated at MLZ in Garching near Munich. The instrument is operated with an incident wavelength spectrum ranging from 2 to 10 Å with a $\frac{\Delta\lambda}{\lambda}$ resolution of 3 %. The opening of the beam defining slits, were selected as to keep the total $\frac{\Delta Q}{Q} = 6$ % and the reflectivity was measured using three consecutive overlapping

---

measurements at incident angles 0.3º, 0.6º and 1.4º over the q range extending to 0.2 Å⁻¹.
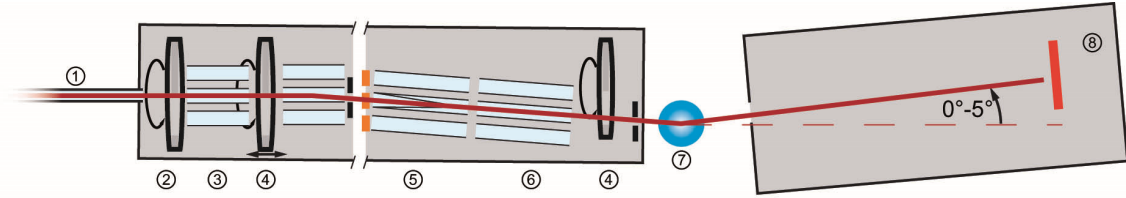
Fig. 8.10. Scheme of REFSANS instrument at MLZ.[107] (1) Neutron guide NL 2b. (2) Master chopper. (3) Neutron guide elements. (4) Slave chopper 1+2. (5) Changeable polarizer. (6) Neutron guide elements. (7) Sample position. (8) Detector.

For the modelling of neutron reflectivity curves from the given set of parameters we used the so called matrix formalism described in details elsewhere[108,109].

Neutrons obey everywhere the stationary wave equation given by,

$$\nabla^2\psi + k_0^2\psi - V\psi = 0 \qquad (8.2)$$

where, ψ is a wave function, k_0 is the magnitude of the wave vector in free space and $V = k_0^2(1 - n^2)$ is a potential of a homogeneous medium characterized by refractive index n, which depends on its scatttering length density.

The Fresnel theory yields the exact eigenstate for the homogeneous layer

$$\psi(r) = C\,[T\exp(ikr) + R\exp(ik'r)] \qquad (8.3)$$

where, k' is a wave vector of the secularly reflected beam, C is a normalization constant, R and T are the Fresnel reflection and transmission coefficients.

The boundary conditions at every interface allow to obtain the system of linear equations in matrix form which connects the Fresnel coefficients above the sample surface with the coefficients in the substrate. Generally, the interface between two neighbouring layers is described as a random Gaussian variable $z(x, y)$ with standard deviation σ. The description works correctly only in the case when $\sigma \ll t$, where t is a layer thickness. We do not consider in this work the case when interfacial profile has lateral and height correlations. In this case the roughness become also a source of the strong diffuse scattering. When σ is too

large one considers graded, but smooth interfaces, where the scattering length density is a function of z. The interface is divided into thin slabs with a maximum thickness $t_s < 2\pi/Q_{max}$, wher Q_{max} is a maximum scattering vector in the experimental data. In neutron reflectivity, the instrumental resolution $\Delta Q/Q$ is a function of both the angular divergence of the incident beam and its wavelength spread. This leads to a broadening of the characteristic scattering from the sample as expressed by the resolution function, which in many cases is a Gaussian profile. The standard deviation of the resolution function is given by two parts

$$\Delta Q^2 = Q^2 \left(\frac{\Delta\lambda}{\lambda}\right)^2 + (\Delta\theta)^2 \qquad (8.4)$$

where, the wavelength spread contribution is larger at larger Q and angular divergence $\Delta\theta$ is constant.

In order to simplify the analysis of the experimental data, we performed neutron reflectivity measurements on a pure glass substrate, PAZO/glass sample and Au/PAZO/glass. We present in particular the modelling procedure applied to the data from all three samples and the obtained parameter.

i. *Pure glass*

The experimental reflectivity curve and fitting result for the pure glass substrate are shown in Fig 8.11. Fitting of experimental data lead to the following optimized values of glass SLD and roughness respectively $3.565\times10^{-6} \pm 0.001 \times10^{-6}$ Å^{-2} and $\sigma = 8.00 \pm 0.02$ Å.

ii. *PAZO/glass*

Simulations of the data from PAZO/glass sample (Fig 8.12) has shown that the profile of the rough air-polymer interface tends effectively to a form of square root gradient with the following parameters scattering length density of PAZO film at $z = 0$ ρ_{PAZO} $(z = 0) = 1.135 \times 10^{-6} \pm 0.005 \times 10^{-6}$ Å^{-2}, gradient thickness 125.94 ± 0.50Å and mean SLD of PAZO $= 2.246\times10^{-6} \pm 0.003\times10^{-6}$ Å^{-2}. The scattering length density of glass substrate and its roughness were taken from previous fit of the data for pure glass sample.

iii. *Au/PAZO/glass*

The model of PAZO in the above section shows that the surface of the polymer is not perfect and its profile tends to a square root gradient. The AFM surface roughness analysis of 5×5 µm^2 demonstrates much smaller surface roughness of around 1 nm. However, neutron beam at low angles covers larger surface given

by the opening of the beam and gives more averaged information compared to AFM.
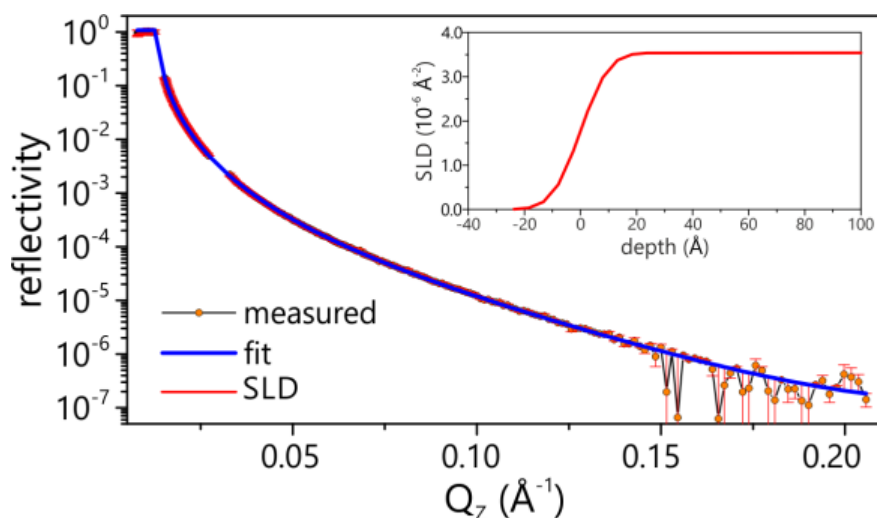
Fig. 8.11. Levenberg-Marquardt fit of a calculated neutron reflectivity curve of a glass substrate (scattering length density ϱ = 3.565$\times$10^{-6} $\pm$ 0.001$\times$10-6 Å^{-2}, roughness σ = 8.00$\pm$0.02 Å). The model scattering length density profile is depicted in inset.
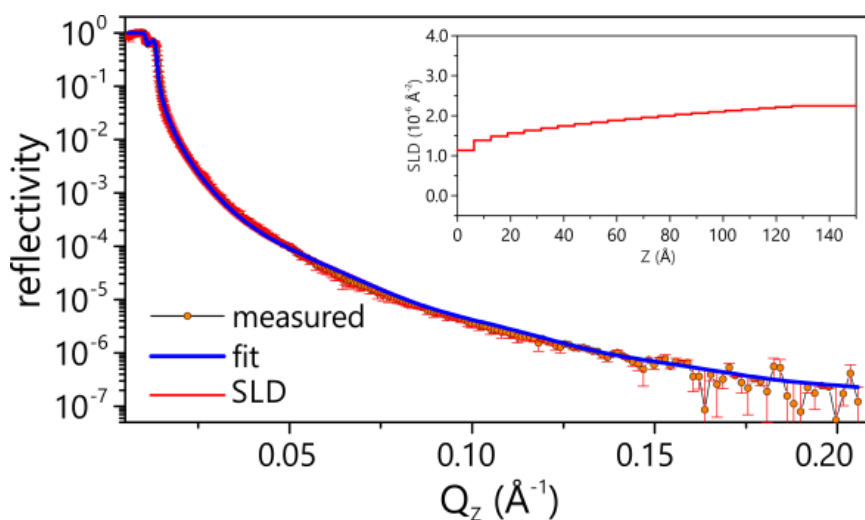
Fig. 8.12. The model where PAZO-air interface has a form of square-root function. This model is in a good agreement with experimental curve. The obtained parameters are SLD at z = 0, 1.135$\times$10^{-6} $\pm$ 0.005$\times$10^{-6} Å^{-2}, gradient thickness t_g = 125.94 $\pm$ 0.50 Å, mean SLD of PAZO ρ_{PAZO} = 2.246$\times$10^{-6} $\pm$ 0.003$\times$10^{-6} Å^{-2}.
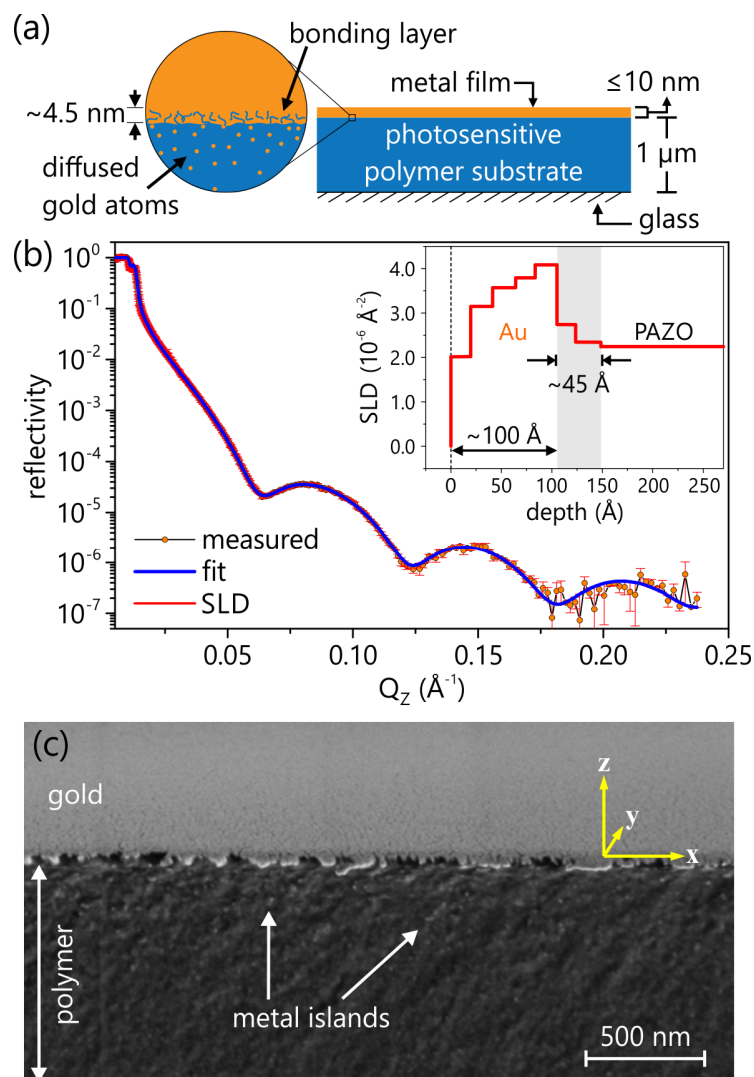
Fig. 8.13. Neutron reflectivity analysis of bonding layer at metal/polymer interface. a) Scheme of bonding layer. b) The final scattering length density profile (embedded image) and fit results of the corresponding calculated neutron reflectivity curve. SLD and thickness of the sub-layers were optimized by Levenberg-Marquardt algorithm. c) SEM image depicting the metal polymer interface.

To simulate a profile of gold layer and gold/PAZO interface we used the following procedure. The first 200 Å of the scattering length density profile including the Au layer and the interface between the gold layer and PAZO film were split into 10 slices. The parameters of every slice were optimized independently with physical constrains for the slice thickness and SLD, the

former could possess the values in the range from zero to 25 Å, defined by the maximum experimental scattering vector Q_{max} and the latter was limited from the upper side by 5×10^{-6} Å^{-2}, which is larger than caluclated value of the scattering length density of gold 4.5×10^{-6} Å^{-2}. The result in Fig 8.13b shows perfect agreement between the curves. The final density profile is presented in the inset of Fig 8.13b.

The scheme in Fig 8.11a shows the gold/polymer interface and the estimated diffused layer to be ~45 Å. In addition to neutron reflectivity, we performed SEM imaging of bisected Au/PAZO/glass sample (breaking pressure applied towards gold layer to avoid particle from gold layer being distributed within the polymer). The SEM image in Figure 4c shows few single metal grains diffused deep into the polymer film. Metal particles are observed up to 500 nm deep in the polymer film, however, these small grains of metal particles are invisible for detection using neutron reflectivity due to lack of significant particle density.

8.4. Bonding layer at the Au/PAZO interface

The neutron reflectivity results presented in the above section clearly indicate a ~45 Å thin diffused Au layer into the PAZO surface. However, to confirm the cracks observed in section 8.2 to be the imprints of local stress distribution during SRG formation, the diffused Au layer should create a good bonding/adhesion between Au and PAZO films. To address this question, we considered to study the crack formation in metal layer when the Au/PAZO interface is separated by multi-layered graphene (G-ML). It is well known that there will not be any penetration of the gold through the graphene multi-layer.[110,111] Thus, we presume that G-ML creates a good isolation layer between the Au-PAZO layers and allow us to observe the crack formation behaviour in Au layer during SRG formation with and without the G-ML at the Au/PAZO interface.

To analyse the crack formation with and without G-ML during SRG formation, an important questions arises here about the deformation of G-ML on PAZO during SRG formation. Unless the G-ML deforms on PAZO during SRG formation similar to the Au film, the comparison of crack formation will not be appropriate. Thus in the first step, we have studied the possibility of deforming the G-ML on PAZO during SRG formation as described in the following section.

8.4.1. Multilayer Graphene (G-ML) deformed on PAZO

Multi-layer graphene (G-ML) has been transferred onto a micrometer thick PAZO surface using method of mechanical exfoliation from high purity and highly oriented pyrolytic graphite (HOPG) purchased from Momentive™. The

process of mechanical exfoliation involves a gentle physical rubbing of graphite piece on the polymer surface, which results in the multi-layered graphene flakes/pieces dispersed on to the polymer surface at random positions. We used AFM to analyse the thickness of G-ML flakes in a definite area marked for irradiation in subsequent steps. The AFM analysis revealed a wide range of G-ML pieces of thickness between 10–50 nm. Our IIAFM setup up shown in Fig 3.6 is used to irradiate the G-ML/PAZO film. *In-situ* AFM observation of multi-layered graphene deformation during SRG formation with ±45° interference pattern is presented in Fig 8.14.
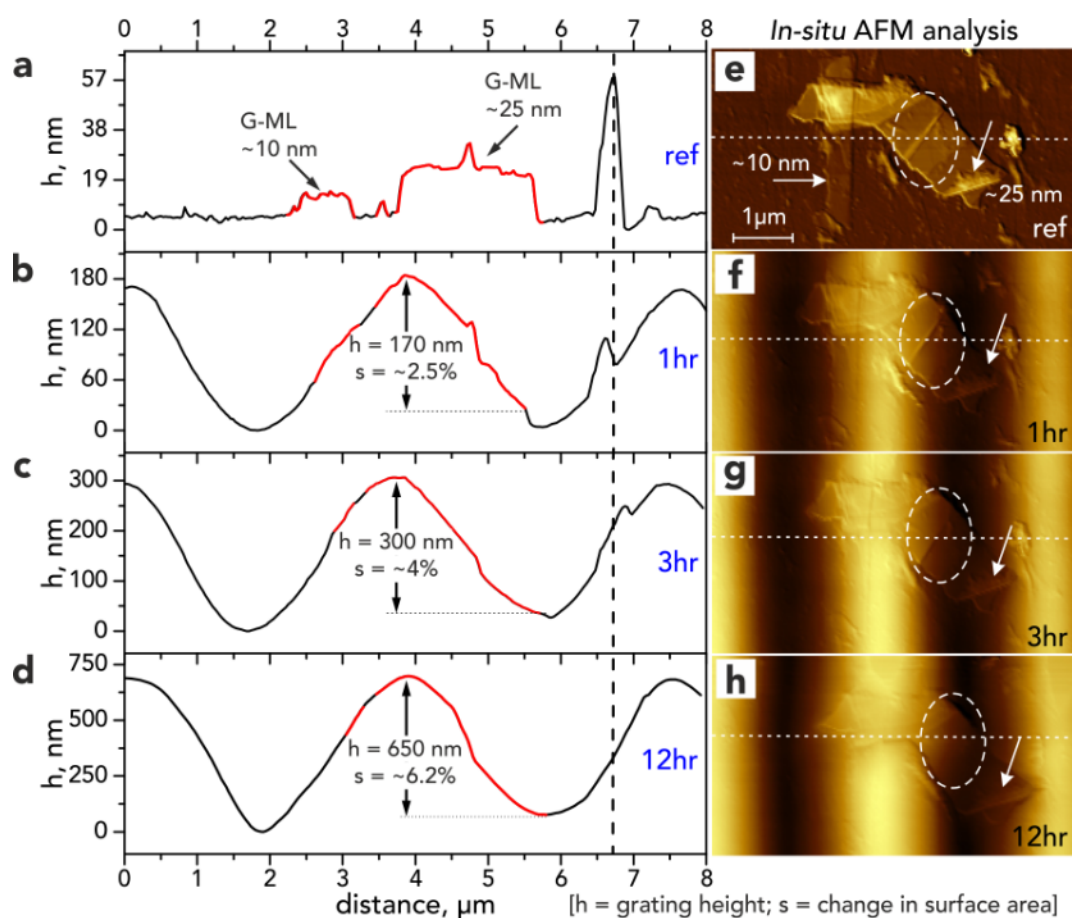
Fig. 8.14. *In-situ* AFM measurement of multi-layered graphene deformation on the photosensitive polymer film during SRG inscription. (a–d) The AFM cross-sectional analysis of the SRG development as a function of irradiation time taken along the white dotted line in (e). The red line in the profile of indicates the multi-layered graphene piece shown in AFM picture. The black line of the profile represents the polymer surface. (e–h) Corresponding AFM micrographs.

During irradiation with interference pattern the polymer topography changes resulting in a formation of the SRG. The height of the SRG increases gradually up to h = 650 nm after 12 hours of irradiation. The graphene piece deforms as well following the topography change. Fig 8.14e shows the polymer surface with a piece of multilayer graphene of 25 nm thickness. There are two folds (marked by the dashed ellipse and an arrow) of the graphene piece resulting from the transfer procedure. With the change in the surface area during the SRG formation these folds flatten as shown in the Fig 8.15. The deformation of G-ML as a function of the SRG height, i.e. increase in the surface area, s, is presented in the Fig8.14 (e–h) with the corresponding cross-sectional analysis of the topography change (Fig 8.14(a–d)).
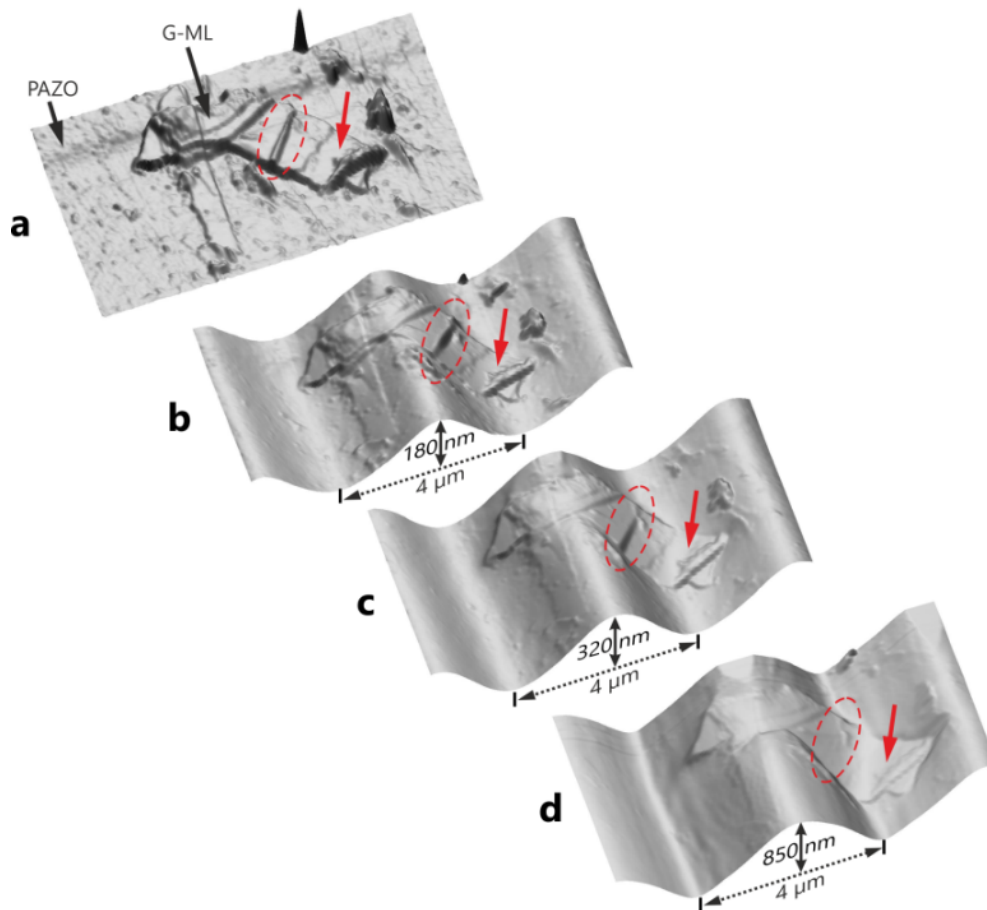

Fig. 8.15. *In-situ* AFM measurement of multi-layered graphene deformation on the photosensitive polymer film during SRG inscription. (a–d) AFM micrographs in 3D. The red coloured circle and the arrow indicates the unfolding regions of graphene during the deformation.

The deformation of G-ML not only restricted to small pieces in the range of grating periodicity, but much larger and thicker graphite flakes are also observed to be deformed along with SRG topography. Fig 8.16 and appendix Fig D.5 shows the ex-situ AFM analysis of much larger and thicker graphene flakes, deformed and adopted neatly on the developed SRG.
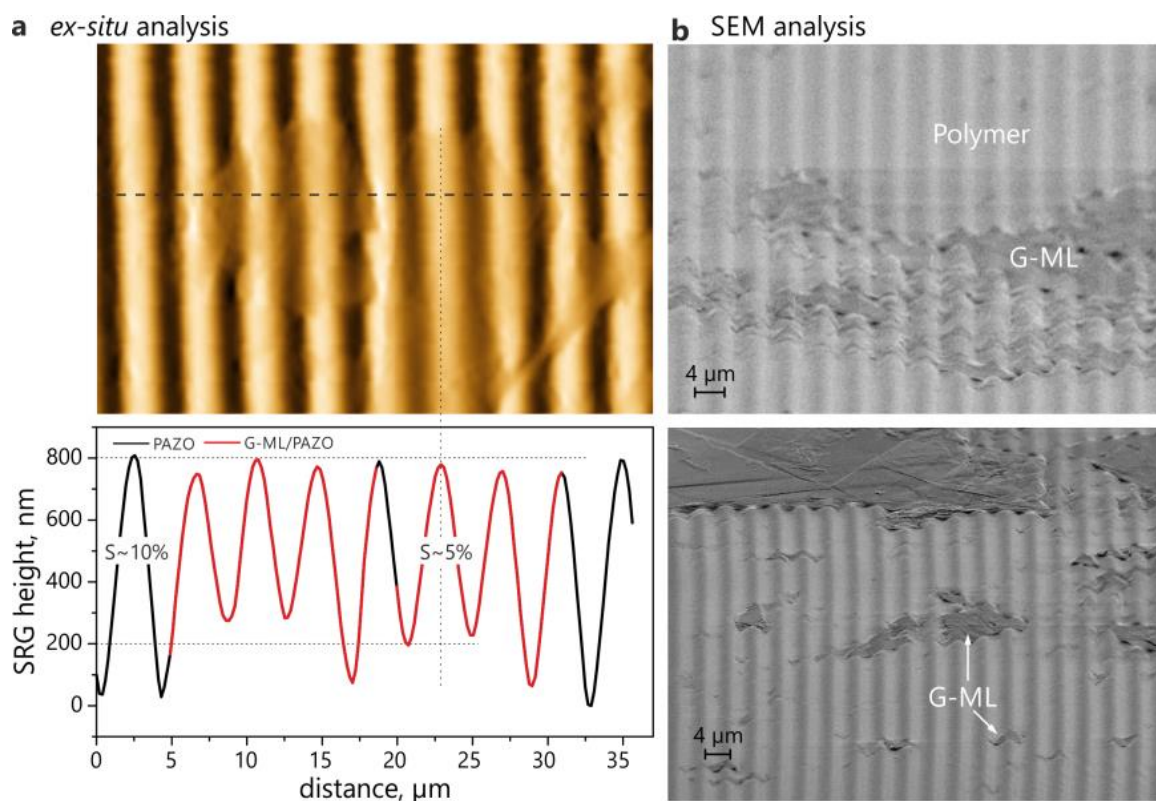
Fig. 8.16. (a) AFM analysis of multi-layer graphene deformed on photosensitive polymer. The sinusoidal profile in graph corresponds to the cross-section taken at black dotted line in AFM picture. The red colour region in the sinusoidal profile corresponds to the G-ML regions. 'S' represents the change in surface area from flat to a grating profile. (b) SEM analysis of deformed G-ML.

Observing the Figs (8.14, 8.15, and 8.16), intuitively one could presume that the G-ML pieces has considerable adhesion with the PAZO film. In addition, the red regions in the profiles of Fig 8.14 (a–c) indicate that the G-ML piece is adopting neatly on PAZO during the grating formation. To probe the strength of interaction between the polymer and grephene, we have performed RAMAN

measurements in collaboration with our project partners.[*] Using Raman spectroscopy we have found that the photosensitive polymer interacts with the graphene hexagons via the azobenzene side groups. This interaction is evidenced in specific Raman bands as a shift of the centre of mass on the order of 1-2 cm^{-1}. We have also showed that on polymer chromophores this molecular interaction is centered with the aromatic rings. This suggests an interaction due to charge redistribution between the aromatic rings of chromophores in the polymer surface layer and the graphene layer.

In a short overview, here we have confirmed that multi-layered graphene could be deformed anisotropically on the SRG topography similar to the ultra-thin gold films.

8.4.2. Au/G-ML/PAZO interface

With the understanding on nature of G-ML during SRG formation, here we proceed to prepare and test the Au/G-ML/PAZO interfaces.

As first step, AFM analysis is performed and marked regions of interest with approximately 10–30 nm thick multi-layered graphene dispersed on PAZO film, followed by deposition of 10 nm thin Au film at 2.5 Å/sec (Fig 8.17a-I). The morphology of the gold layer on the G-ML and the polymer surface differs significantly allowing us to track exactly the position of the graphene piece (Fig 8.17b).

The SEM analysis after grating inscription in Au/G-ML/PAZO sample with ±45° and RL interference patterns is presented in Fig 8.17(c, d) and Fig 8.18. In section 8.4.1, we have seen that G-ML piece of the width around one SRG period does not alter the height of the grating topography. However, the Au layer on G-ML remains undisturbed and cracks appear only in the regions where gold layer is in the direct contact with PAZO (Fig 8.18). This observation confirms that the diffused gold layer at Au/PAZO interface created a strong bonding/adhesion layer and the observed cracks are direct imprint of local stress distribution in the polymer film during grating formation. In other words, we could infer that the bonding layer at Au/PAZO interface serves as a transducer of the local stress distribution in the polymer film to a metal layer.
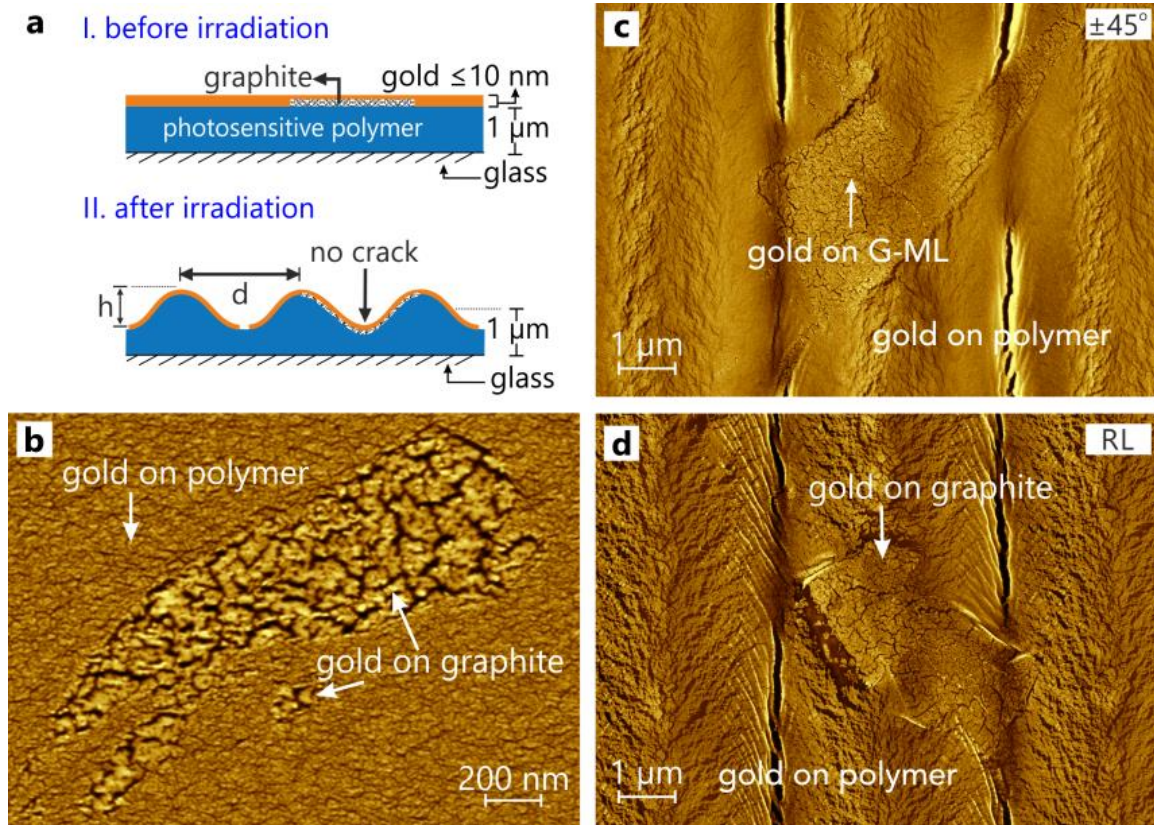
Fig. 8.17. Study on metal-polymer bonding layer effect on crack formation with ±45° and RL interference patterns. a) Schematic representation of sample properties. Figure a-I shows the arrangement of glass/polymer/G-ML/Au layers. Small graphite flakes are dispersed on photosensitive polymer film and gold film is deposited on G-ML dispersed polymer film. Figure a-II shows the sample after grating formation. b) SEM image shows the 10 nm thin gold film topography deposited on polymer and G-ML layers. c) Comparison of 10 nm thin gold film rupturing on polymer and G-ML areas for ±45° interference pattern. d) Comparison of 10 nm thin gold film ruptured on polymer and G-ML areas for RL interference pattern.
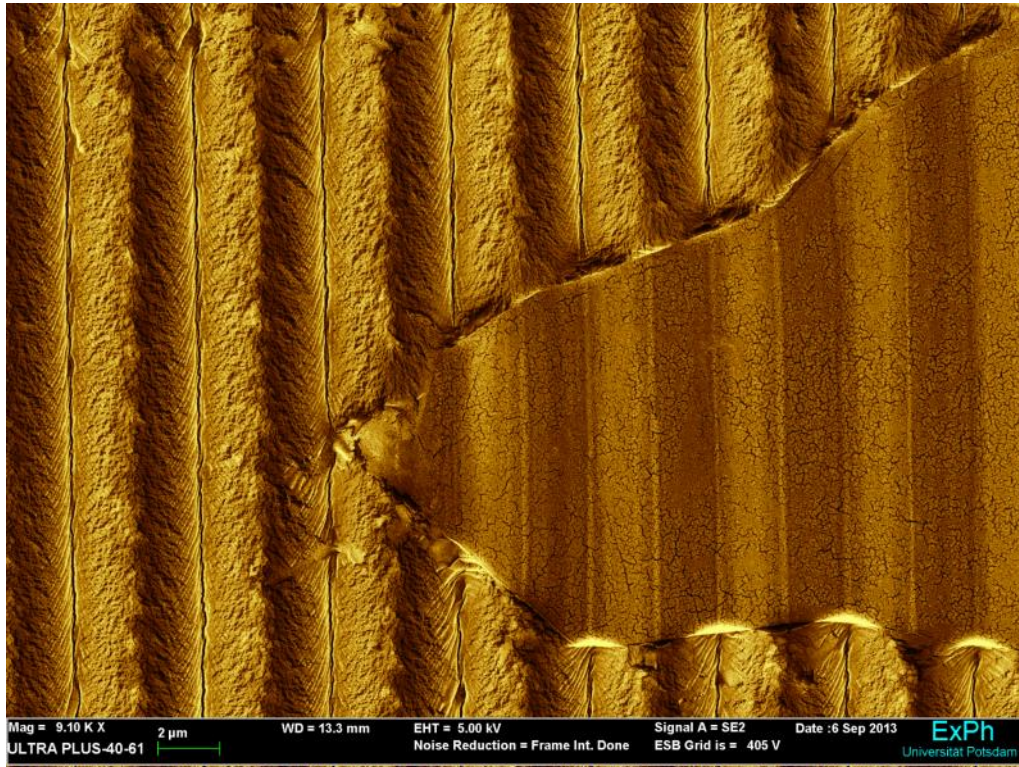
Fig. 8.18. SEM image of 10 nm thin deformed gold film on polymer and G-ML regions.

8.5. Influence of Au film quality on the crack formation

Here, we have observed the dependency of Au film morphology on the rate of film deposition. When we reduce the 10 nm thin metal film deposition rate from 2.5 Å/sec to 0.5 Å/sec, the morphology of the Au films varied significantly as shown in Fig 8.18(a, d). With higher deposition rate of 2.5 Å/sec, typical 10 nm thin gold film has connected networks of Au aggregates (inset of Fig 8.18d). In contrast, with lower deposition rate of 0.5 Å/sec, a typical 10 nm thin film has individual islands of grain size varying between 20–50 nm (inset of Fig 8.18a). Despite the differences in the film morphology, the electrical conductivity of 10 nm films deposited on PAZO remain similar in the rage of 175 ± 5 Ohm, compared to the infinite resistance of only PAZO film.
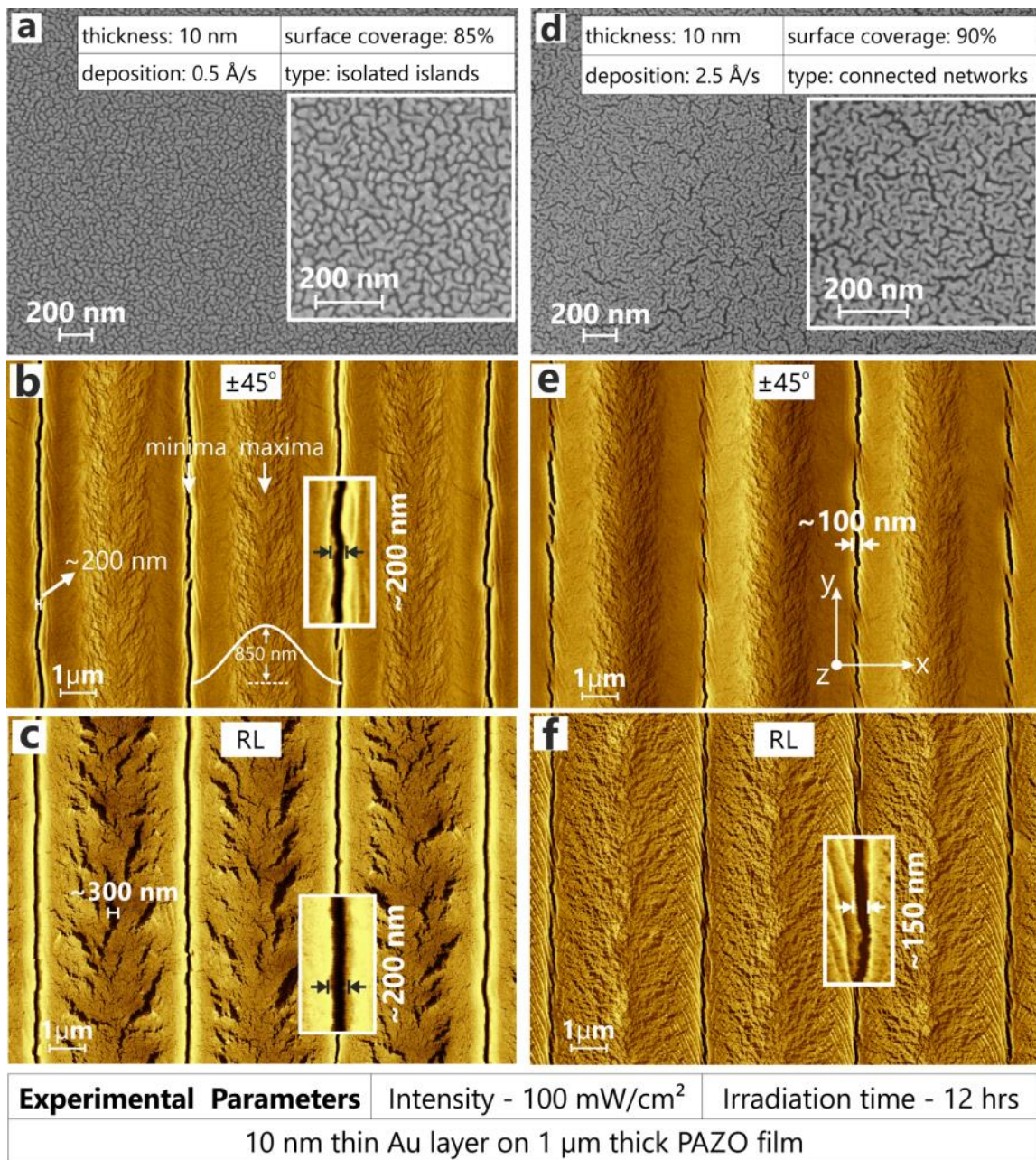
Fig. 8.19. Influence of Au film quality on rupturing behaviour using ±45° and RL interference patterns. a) **Island film**: SEM images of 10 nm thin Au film deposited on PAZO at 0.5 Å/sec evaporation rate. (b) SEM image showing the periodic rupturing of 10 nm thin island film with ±45° interference pattern. (d) SEM image showing the periodic rupturing of 10 nm thin island film with RL interference pattern. (d) **Network film**: SEM images of 10 nm thin Au film deposited on PAZO at 2.5 Å/sec evaporation rate. (e) SEM image showing the periodic rupturing of 10 nm thin network film with ±45° interference pattern. (d) SEM image showing the periodic rupturing of 10 nm thin network film with RL interference pattern.

It is interesting to know how these films of different morphology responds to the applied strain during the SRG formation in PAZO. Thus, we have inscribed the SRG in these films using both the PIPs (±45° and RL) as shown in Fig 8.19. The height of SRG is kept constant for all measurements at 850 ± 30 nm and associated the growth kinetic is also observed to be similar. Fig 8.19 (b, e) shows the crack formation in 10 nm thin island and network quality films using ±45° interference pattern and the rupturing behaviour in both the films is observed to be similar. However, a more pronounced crack at the grating minima is observed using island quality metal film (Fig 8.19b). In contrast, the crack formation using RL interference pattern in both the island and network quality films display huge differences (Fig 8.19(c, f)). Using network quality film (2.5 Å/sec rate), we have observed a straight crack along the each grating minima and a continuous thin riffle from SRG minima towards maxima. Using the island quality film (0. 5 Å/sec rate), a wide and well pronounced crack appeared at the grating minima and randomly positioned strong cracks also appeared at the maxima, at angle of ~ 60° to the grating vector. Comparatively, from the observed crack pattern, one might infer that the island quality gold films (0.5Å/sec) appear to be less resistant to the mechanical deformation compared to the network quality films. Another important question need to be addressed is the origin of these cracks and we leave it for discussion in the forthcoming sections.

8.6. Controlled opto-mechanical stresses in photosensitive polymer films

8.6.1. Opto-mechanical stresses induced by ±45° pattern

In section 8.2.1, we have seen that while reducing the film thickness form 15 nm to 10 nm, the pronounced crack position shifted from SRG maxima to minima using ±45° interference pattern. It is an intriguing phenomena and possibly indicating the location of maximum stress induced regions during the SRG formation, unique to ±45° interference pattern. Interestingly, testing two 15 nm thin Au films deposited on PAZO surfaces using 0.5 Å/sec and 2.5 Å/sec also displayed a similar result (Fig 8.20(b, c)).

In chapter 6, we showed that the maxima and minima positions of SRG using ±45° interference pattern corresponds to the vertical linear (↕) and horizontal linear (↔) $\vec{E}$-field vectors and the slopes corresponds to the circularly oriented $\vec{E}$-field vector (↺ and ↻) in the XY–plane. To understand the role of these linear $\vec{E}$-field vectors in the SRG formation, we have compared the growth kinetic of SS and PP interference patterns (Fig 8.20e). In case of IIPs, we know that intensity

modulation plays significant role and is supported by the orientation of $\vec{E}$-field vector of the interference pattern. Using SS pattern, we achieved a SRG height of 100 nm with an irradiation intensity of 100 mW/cm². In case of PP interference pattern, at same irradiation intensity the observed SRG height is double (250 nm) that of SS pattern.
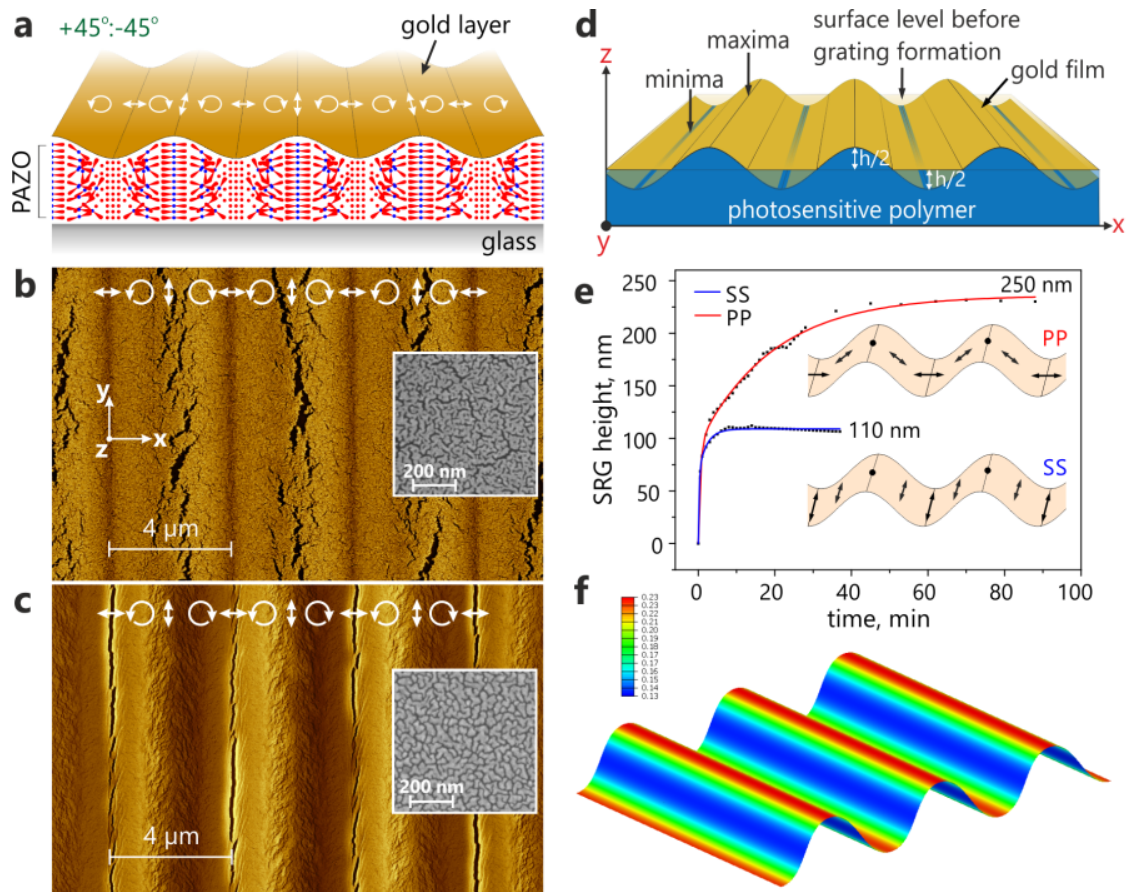
Fig. 8.20. (a) Scheme of azobenzenes orientation in the polymer film after irradiation with ±45° pattern. (b) SEM images of ruptured gold film at the SRG maxima of the grating for 15 nm film deposited at 2.5Å/sec rate. Inset: SEM image of 15 nm gold sample before irradiation. (c) SEM image of ruptured gold film at the SRG minima of the grating for 15 nm film deposited at 2.5 Å/sec rate. Inset: SEM image of 15 nm gold sample before irradiation. (d) Scheme of deformed metal film on polymer surface during SRG formation (notice the surface level before and after irradiation). (e) Growth kinetics of SRG inscribed with SS and PP interference patterns to understand the role of vertical (↕) and horizontal (↔) $\vec{E}-$field vector of ±45° interference pattern. (f) FE simulation: Stress distribution along the grating vector.

The only difference between the SS and PP interference patterns is the orientation of $\vec{E}$-field vector along the grating vector. The grating growth kinetic in Fig 8.20e indicates that the horizontal linear $\vec{E}$-field vector ($\leftrightarrow$) doing significant amount of work compare to vertical linear $\vec{E}$-field vector ($\updownarrow$).

The crack formation behaviour seen with different Au films of island and network qualities appear to probe the interplay between the mechanical resistance of the metal film to the deformation and the molecular mass transport processes between linearly polarized $\vec{E}$-field vectors (i.e. $\updownarrow$, $\leftrightarrow$). Irrespective of the metal film quality, one might presume that maximum reaction taking place at regions with horizontal linear $\vec{E}$-field vector ($\leftrightarrow$), which result in the molecules mass transport towards vertical linear $\vec{E}$-field vectors ($\updownarrow$) there by SRG formation takes place. Carefully following the effect of film quality on the crack formation behaviour, one may infer that the Au film with networks should offer more resistance to the deformation compared to the island quality films. Thus one could assume that at the initial stages of grating formation, if the metal film offers considerable resistance to the local necking or dislodging at the grating minima, the elastic energy should build up at the Au/PAZO interface due to the bonding layer and eventually as a result of bulging effect at the grating maxima, the cracks might appeared as seen in Fig 8.20b. In contrast, the island quality metal film offers less resistance to the initial stresses developed at the minima during SRG formation and allows seeding the crack formation at very initial stages of grating formation, thus releasing the excess elastic energy that might be stored in the metal film. The result might be a well pronounced crack at the SRG minima and considerable perturbation at the SRG maxima due to bulging effect.

i. FE Simulations*

To shed light on the crack patterns observed in the gold nanolayer, we assume that its deformation behaviour can still be understood through a continuum mechanics approach. Let's consider a thin elastic sheet ($L_0, W_0 \gg t = 15\ nm$) laying on a deforming substrate. Considering the perfect bonding at the metal/polymer interface, the photo-induced SRG of the polymer translates to an imposed vertical sinusoidal displacement at the bottom face of the metal sheet. Equation (8.1) gives the averaged longitudinal strain at the bottom of the sheet:$\langle \varepsilon_{xx}(z=0)\rangle_x$, which grows from 0 to approximately 10% as the polymer film is changing its height. A simple finite-element (FE) simulation is

implemented in Abaqus to confirm the localization of maximum stretching strain on the peaks and valleys of an elastic sheet subjected to an imposed vertical sinusoidal displacement on its bottom face (Fig 8.20f). The calculation performs a static step, taking nonlinear geometry into account, on a cuboid with dimensions $L_0 = W_0 = 4\,\mu m$ and $t = 15\,nm$ assigned with isotropic linear elastic properties with a nominal Young modulus of $1\,nN/nm^2$. In the scheme of Fig 8.20d, one could notice the difference between the surface level before and after SRG formation in sinusoidal fashion. From Fig 8.20f, it is evident that deforming a metal film in sinusoidal profile results in maximum stress at the surface relief maxima and minima. That is, during bending of metal film by surface relief formation, the cracks are possible to appear at both the maxima and minima. However, observing the cracks in Fig 8.20(b, c) a pronounced crack appears either at the SRG minima or maxima indicating that the stresses developed with the vertical and horizontal linear $\vec{E}$-field vectors is not uniform/equal. Moreover, it appears that maximum reaction takes place at the grating minima where a horizontal $\vec{E}$-field vector is located. If this assumption is true, one should be able to accelerate or decelerate this rate of reaction by increasing the irradiation intensity of ±45° interference pattern, which may result in overcoming the mechanical resistance of metal film and the cracks might appear at local minima instead of local maxima.

ii.   Influence of irradiation intensity on the crack position using ±45° pattern

To experiment on the possibility of controlling the opto-mechanical stresses associated with horizontal linear $\vec{E}$-field vector (↔), we have varied the irradiation intensity between 100–400 mW/cm2, and the resulting crack formation behaviour in 15 nm thin network quality gold films is shown in Fig 8.21.

Increasing the intensity from 100 mW/cm² to 200 mW/cm² results in increased rate of reaction at the minima as shown in Fig 8.21f growth kinetics. More stress is induced by linear horizontal $\vec{E}$-field vectors (↔) to push the molecules away rapidly causing the deformation of the metal film at minima regions. As the stress working on the deformation of metal film at the valleys, the stress distribution varied the maxima considerably causing different rupturing behaviour as shown in Fig 8.21b.

Further increasing the intensity to 300mW/cm² and 400mW/cm², the rate of reaction accelerated at the minima regions confirming the linear horizontal $\vec{E}$-field vectors (↔) to be the primary stress inducing regions as shown in Fig 8.21(c, d, f). Figure 8.21e presents a 3D SEM image of 300mW/cm² film deformation confirming the location of cracks at the maxima and minima. Thus, the crack

intensity increases at the valleys leads to releasing stress, and causing weak deformation at the maxima regions.

It is also very interesting to cross check the reproducibility of above observed phenomena on 15 nm gold films with 0.5 Å/sec deposition rate. Fig D.6 shows the deformation behaviour of 0.5 Å/sec gold films at different intensities. And further increasing intensity to 200, 300 and 400 mW/cm² clearly confirms that for ±45° interference pattern, the stress inducing regions are linear horizontal $\vec{E}$-field vectors (↔) at the grating valleys, thus causing the SRG formation in photosensitive polymer films.
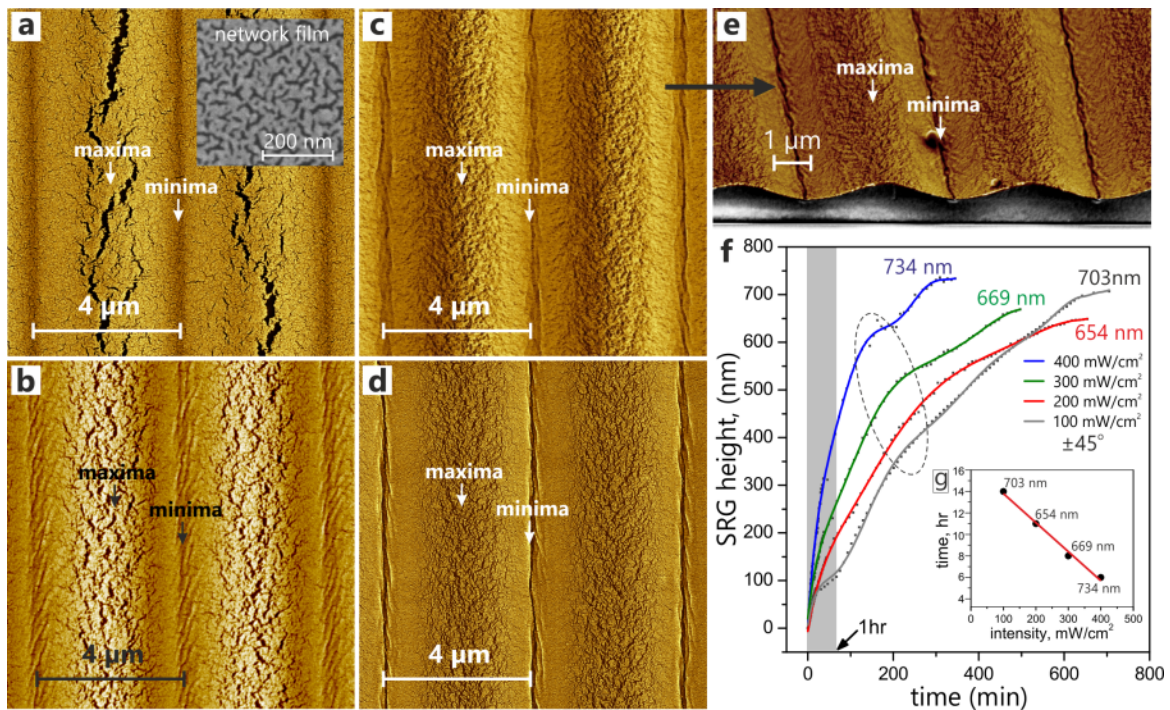
Fig. 8.21. Visualizing the effect of horizontal linear $\vec{E}$–filed vector by controlling the rate of reaction through varying intensity. All the experiments are for 15 nm thin gold film, deposited with 2.5 Å/sec rate. a) Rupturing only at the grating maxima with 100mW/cm². b) Deformation at the valley and the rupturing at the maxima with 200mW/cm². c) Weak rupturing and deformation at the valleys and peaks with 300mW/cm². d) Strong rupturing at valleys and weak deformation at the peaks with 400mW/cm². f) Grating growth kinetics for different intensities.

Briefly describing the above observed phenomena, an optical field induces a spatially varying stress across the metal film at defined locations (↔) through

organized mass transport in photosensitive polymer material (opto-mechanical stresses). However, the major challenge is estimating or measuring the magnitude of stress locally to be able to map the stress distribution along grating vector. We have discussed this issue in section 8.6.3.
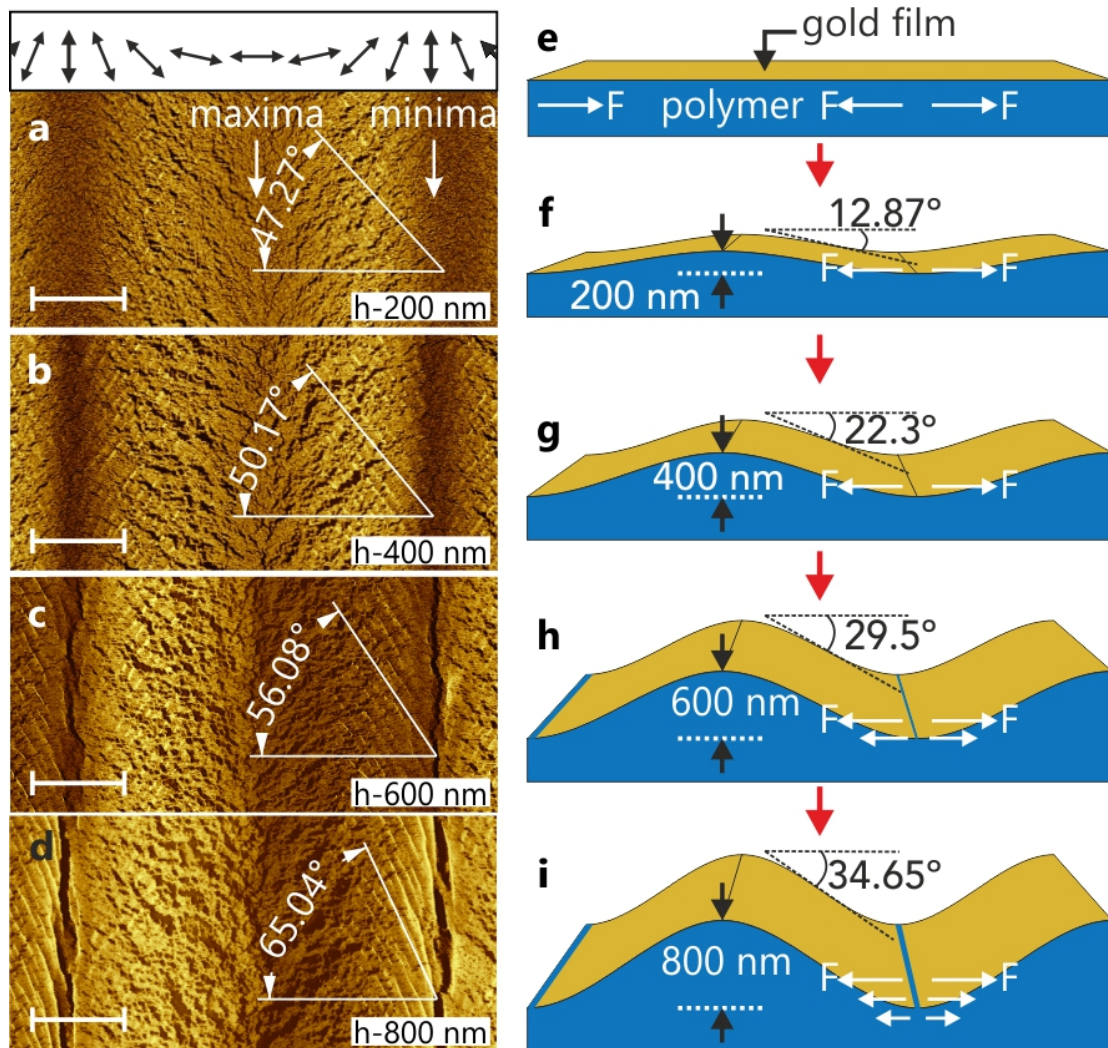
Fig. 8.22. *Ex-situ* SEM analysis of crack formation with characteristic strain features near grating minima. (a–d) SEM images of new work quality metal film topography at different stages of grating development (*viz.*, h – 200, 400, 600 and 800 nm). The angle of the strain features is measured with respect to the grating vector (x-axis). The white line represents the scale bar of 1 μm. The local $\vec{E}$-field vector during grating formation is presented in the scheme at the top. (**e–i**) The deformed metal film on PAZO is presented in graphics with estimated inclination angle to the horizontal surface.

## 8.6.2. Opto-mechanical stresses induced by RL pattern

Taking a closer look at the grating minima of Fig. 8.9k, we could clearly observe the folding features which are strongly appearing on one side of the grating minima at a characteristic angle of 65° with respect to the grating vector using RL pattern. In the repeated experiments, we observed that these folding features always oriented towards upward direction to the developing grating and strongly positioned at any one side of the grating minima, while similar weak riffle could be seen on the neighbouring side. Though, the reason behind particular choice of folding orientation is not clear at this stage of investigation, we further carried *ex-situ* analysis of the appearing folding as a function of grating height, presented in Fig. 8.22.

Our system consists of a thin metal film, confined to a polymer film. During the SRG formation (plastic deformation) the polymer exerts a force (Fig 8.22e) on the metal due to its material mass transport perpendicular to the grating lines. Because the surface deforms over time, the force does not act directly in this direction on the metal. To make analysis simpler we modelled the sinusoidal surface by planes at an inclination angle to the horizontal as presented in Fig 8.22(f–i). The angle is defined by the horizontal and the tangent line on the slope of the SRG. The force along the metal surface is derived as demonstrated in Fig. 8.23b.

It is known that a stress, applied to a hard material gives rise to a shear force at an angle to the original stress-direction (Fig 8.23a) due to the slip or dislocation of metal grains during plastic deformation[112]. Furthermore we know that a compound of a soft material and a harder material layer, when put exposed to stress, shows wrinkles on its surface. In Fig 8.22(a–d), wrinkles can be found, that we assigned to the effect just described. Knowledge of the angle of the wrinkles with the grating and the angle defined by the tangent on the surface's slope enables us to calculate the ratio of the initial force exerted by the polymer and the resulting shear force on the metal.

$$\frac{F_A}{F_S} = \frac{\cos \alpha}{\sin \gamma} \qquad \text{(or)} \qquad \frac{F_S}{F_A} = \frac{\sin \gamma}{\cos \alpha} \qquad\qquad (8.5)$$

Assuming that the polymer is always driven by the same force we can plot the qualitative development of the shear force over the grating height and it is obvious that while the metal gets damaged during crack propagation, shear force will increase as shown in Fig. 8.23c. Thus, one could conclude the fact that the observed cracks and shear folding features are indeed the imprints of microscopic opto-mechanical tensile load originated during grating formation.
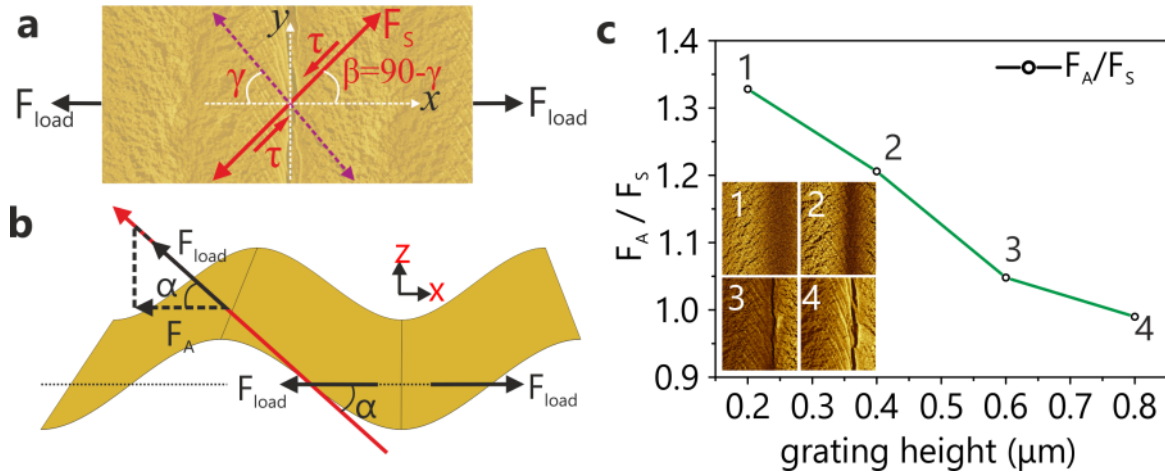
Fig. 8.23. Model to explain the shear strain near grating minima during SRG formation. (**a**) A tensile load F_B produces a shear stress, τ, on an inclined plane in the stressed metal film. Generally, shear stresses in a material have their maximum value on planes at 45° to the tensile axis. (**b**) The angle 'α' is the inclination angle of plane to the horizontal line along applied tensile load and the tangent line on the slope of the SRG. (**c**) Drop in shear force during the grating formation due to the appearance of crack.

8.6.3 Estimation of stresses

It is presumably quite complicated to estimate the stresses during the SRG formation because it might consist of several competing mechanisms. At this stage we can only speculate about the actual mechanism of crack formation and rupture. For this we may employ, for example, some standard models frequently employed in material science in order to estimate the stresses that the polymer exerts on the metal film. In fact, there are plenty of fundamental studies on the deformation and stability of hybrid materials consisting of metal film deposited on a flexible polymer substrate, as it is of fundamental importance for industrial applications such as flexible electronics. A mechanism of fast fracture would imply that the elastic energy stored in the deformed metal sheet is released into the formation of cracks. This model appears to be supported by the conductivity measurements where an instantaneous drop of conductivity is observed, although the deformation of polymer film is continuous and takes a long time.[113]

According to this approach the stress needed to form a crack is $\sigma = \sqrt{\frac{EG_c}{\pi a}} \approx$ $0.4\,GPa$, where E, G_c, $\sqrt{EG_c}$ and a are the Young modulus, toughness, fracture

toughness and crack length, respectively. For a typical value of fracture toughness of gold thin films[114] $\sqrt{EG_c}$ = 0.7MN/m$^{3/2}$ and a crack length of 1μm as measured from SEM images, the stress exerted from the polymer film on a gold layer evaluates to be ~0.4 GPa. On the other hand, one might apply a model frequently used for metal laminated polymer substrates that are put under tensile strain. In this model transverse cracks form by a local rupturing of the metal sheet as a result of necking, i.e. local thinning.[115] From a standard equation: $\sigma = K\varepsilon^N$, we may estimate local stress to be σ = 0.1 GPa. Here we use values for the strain, ε=0.024 calculated as described above; for the prefactor, K = 114 MPa and the hardening exponent, N = 0.02, which are typical for a weakly hardening metal.[116]

The rupturing phenomenon reported in this study should be much more complicated to model because in contrast to a global transverse load the strains in our system occur locally as can be seen from the different shape and size of the cracks formed at the valleys and ridges of the polymer topography. Also, bending of the metal film and thus its stiffness should play a role. However, even the rough estimations put forward above give reasonable values of the stresses exerted by the polymer on the adsorbed metal film during mass transport. These values are in the range of several hundreds of MPa, and are in good agreement with the theoretically predicted stress.[117] The forces inscribing a topographical pattern into a thin film are hard to assess experimentally and this work could be a starting point for the use of thin metal films to probe and characterize the extent and strength of material flow locally.

8.7. Influence of temperature on the crack formation

It is possible to assume that 12hr long irradiation with laser beams might increase the heat in the metal films there by crack formation takes places due to the internal stresses and due to thermal expansion coefficient mismatch. To address this question, we have also analysed any possible contribution of heat generated at metal/polymer interface during long time exposure to light, causing metal film ruptured.

Our experiments are performed in the laboratory atmosphere that ensures a constant air temperature around the sample of roughly 20° C. At the sample surface we have constant interfering beam power of 20 mW. Measurements showed that about 10% of that power does not transmit through the sample. We also measured that most of the light that is not transmitted is being (whatever light is absorbed might heat up the sample) reflected by the glass/polymer/metal interfaces. So the actual sample material absorbs roughly 1% of the incoming

light power that is 0.2 mW. If the sample would heat up significantly, it would directly give off the heat to the surrounding air which then because of the density changes would be replaced by cooler air. Assuming that 1mm thick air layer being "attached" to the sample surface and acting as a thermal insulator we can calculate the heat being conducted away from the sample based up on the Fourier law:

$$\Delta Q = k\frac{A}{b}\,\Delta T \qquad\qquad (8.6)$$

Where, 'k' is heat conductivity of air = 0.024 W/mK, 'A' is the contact area = 0.3 cm², 'b' is distance over which the heat needs to be transferred; and 'ΔT'-temperature difference of 10 K, which we chose arbitrarily as a realistic value that is well below glass-transition temperature of PAZO. Using these values, we determined a possible heat transfer from the sample of 7.2 mW. This value exceeds the power input of 0.2 mW to a great extent. Thus we conclude that no significant rise in temperature for our samples during the long time exposure to the light.

8.8. Influence of grating periodicity on the crack formation

We have tested the deformation of 10 nm thin gold films using ±45° and RL interference patterns at varying grating periodicities (1 μm, 2 μm, 3μm and 4 μm) and observed that the combination of strain and the interference pattern are significant parameters to rupture the metal films (Fig 8.23). When the Au/PAZO films are irradiated with grating periodicity below 3 μm, the maximum achievable strain reduced to less than 4 % (Fig 8.2d), however we know from the SRG growth kinetics that a minimum of 3% strain is essential to initiate cracks in ~ 10 nm thin Au films using ±45° pattern (Fig 8.24c) and a minimum of 2 % is sufficient for RL pattern (Fig 8.24b). Pronounced cracks are observed with RL even at 1 μm grating periodicity. However for 1 μm grating periodicity, no cracks are observed with ±45° pattern. No cracks are observed with IIPs as the strain is limited to less than 1.5 %.
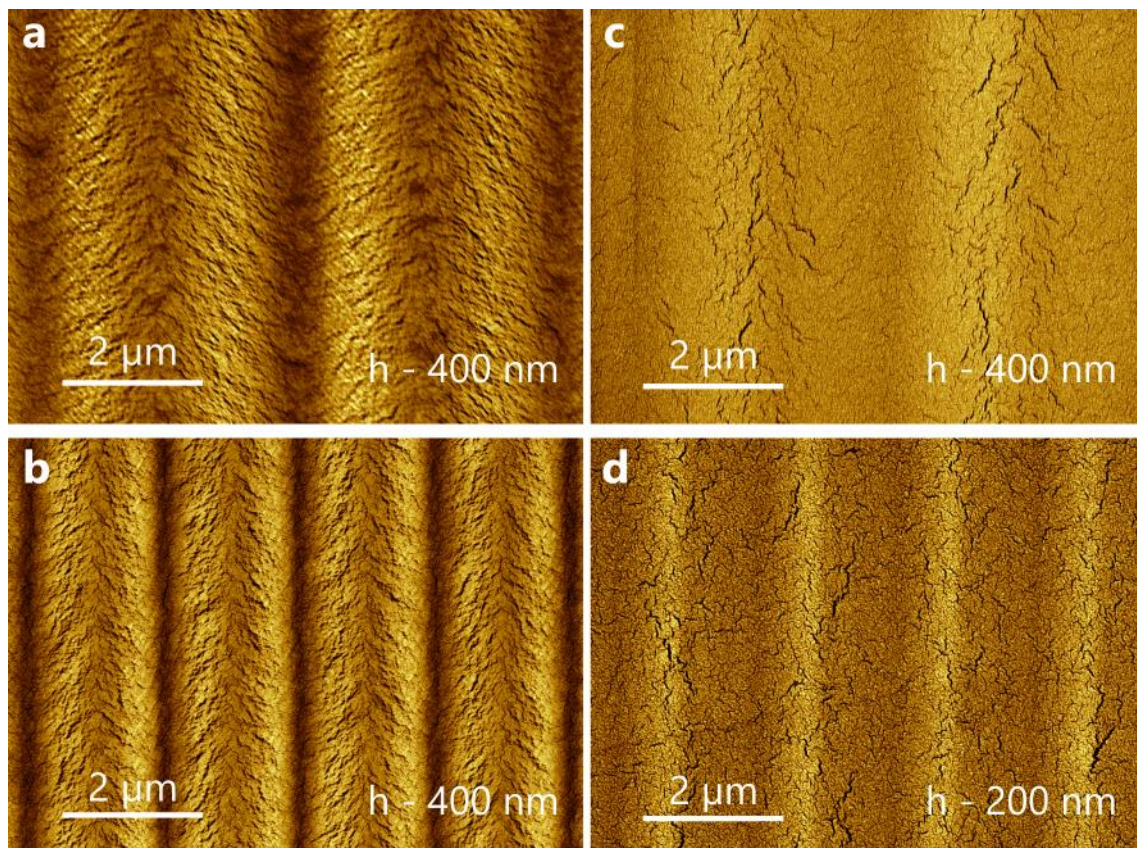
Fig. 8.24. 10 nm thin Au film deformed by RL (a, b) and ±45° interference pattern with 4 μm grating periodicity (a, c) and 2 μm grating periodicity (b, d). Maximum achievable grating height for ±45° pattern with 2 μm grating periodicity is limited to ~ 200 nm.

8.9. Photo-patterning of ultra-thin gold films

Reversible switching is one of the unique properties of some photosensitive polymers. Opto-mechanical stress could be induced in polymer substrates in repeated stages to apply loads in more controlled fashion as desired and also to achieve some unique features in large area with less fabrication steps. Here we tested the possibility of reversible switching by applying opto-mechanical load in repeated stages and simultaneously achieved unique features in metal film as presented in Fig 8.25.

Initially, grating is inscribed in only PAZO film (Fig 8.25b), followed by deposition of thin metal film (Fig 8.25c). After deposition of metal film on polymer grating, an orthogonal grating (grating lines induced perpendicular to the initial polymer grating) is inscribed in PAZO film confirming the possibility

140

of reversible switching. In addition, by varying the thickness of the deposited metal film (Fig 8.25d-1 and 8.255d-2), unique photo-patterning features are achieved. Applying orthogonal grating with 20 nm thin metal films results in 150 nm wide and 50 nm deep folding features in metal film. In contrast, reducing the film thickness to 10 nm and inducing the orthogonal gratings leads to periodic 200 nm wide crack formation. The reversible switching processes are even possible for multistage photo-patterning as demonstrated in Fig 8.25(e–h). Fig 8.25 demonstrates the advantage of easy photo-patterning of thin metal films on photosensitive polymers into a variety of structural features, *viz.*, folding, square lattice, hexagonal lattice and weaved thread like structures.
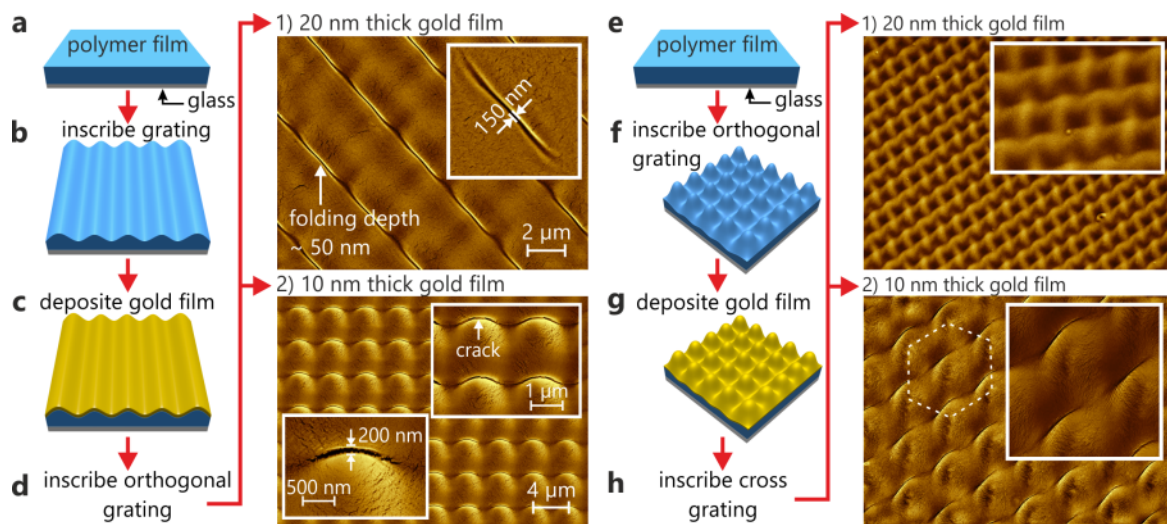
Fig. 8.25. Photo-patterning of metal film on photosensitive polymers. (a–c) SRG (primary grating) is induced in polymer film followed by deposition of thin gold film on developed grating. (d–1) Orthogonal grating (secondary grating) inscribed in 20 nm thin gold film on PAZO to obtain 150 nm wide and 50 nm deep metal film folding features. (d–2) Orthogonal grating induced in 10 nm thin gold film on PAZO to obtain 200 nm wide periodic cracks. (e–g) Orthogonal SRG (bell structures) are induced in only polymer film, followed by thin gold film deposition on developed bell structures. (h–1) Grating diagonal to bell structures inscribed in 20 nm thin gold film on PAZO to obtain complex thread weaved thread like features. (h–2) Diagonal grating is inscribed in 10 nm thin gold film on PAZO to obtain Hexagonal features.

8.10. Conductivity behaviour of Au films ruptured during the SRG formation[*]

Thin metallised polymers are very interesting for the applications in deformable electronics. In most of the cases, the failure of deformable electronics associated with the damage of conductive channels. In order to study the influence of controlled damage of the conductive channels on the conductivity of overall film, the deformation of Au/PAZO interface via inscription of SRG appears to be a suitable method. To achieve it, we have slightly modified our IIAFM as shown in Fig 8.26a. Here we have replaced the AFM with a nitrogen chamber modified to suit *in-situ* conductivity measurements (Fig 8.26b).

The sample was irradiated from the side of the glass substrate in such a way that the interfering beam spot on the sample surface was exactly at the center of the gold film cross as shown in Fig. 8.26b (blue spot). The diameter of the interference spot was set to 6 mm in order to achieve a regular and constant SRG growth throughout the gold-covered central part of the sample (junction of the cross). Standard experimental parameters were used such as ±45° interference pattern, 1 μm thick PAZO film, 10 nm thin Au film. In order to reduce the irradiation time, we used 400mW/cm², which requires around 6 hours of irradiation to achieve maximum possible SRG height.

After 6 hours of irradiation, we obtained a maximum grating height 'h' of 700 ± 30 nm with 10 nm thin metal film. The deposited gold film ruptured with periodic cracks as shown in Fig. 2.27b. The cracks which are 250 ± 20 nm in width are situated at the topography minima (Fig 8.27b) with a periodicity 'd' of 4 μm and extend along the whole area of irradiation. The cracks are continuous over several hundreds of micrometers but do not go all the way through the metal-film. We used scanning electron microscope to analyze the cracks along SRG from top to bottom for a width of 1 mm and found that above 75% of crack along the SRG is uniform except at the edges of 1 mm wide metal film

For *in-situ* measurements of the metal film resistance the sample was incorporated into a circuit with a known reference resistor in series with a voltage source (Fig 8.26b). By applying a voltage of 2V to the setup and measuring the voltage drop over the known resistance of 464 Ohm, we were able to calculate the resistance of the sample. The voltage-drop during the *in-situ* measurement was recorded automatically every 10 seconds by a self-written


"Profi-Lab" script (ProfiLab 4.0. by ABACOM). To understand the impact of cracks in metal film on overall resistance of sample, it is important to probe the voltage drop along both the perpendicular and parallel directions of emerging grating lines (along both legs of the cross). However, measuring the resistance of the sample parallel and perpendicular to the SRG *in-situ* at the same time would mean applying an additional voltage to the sample and consequently disturbing the measurement. To overcome this problem, we choose to perform *in-situ* measurement in any one direction of cross and an *ex-situ* measurement along other direction of cross during a period of every 30 min. During the *ex-situ* resistance measurement, the voltage across the *in-situ* measurement direction was switched off as the *ex-situ* measurement takes only a few seconds. To rule out any influence of moisture coming from the laboratory environment, the sample was kept in a chamber constantly flushed with nitrogen, so that the humidity near the sample surface always remained below 4%.
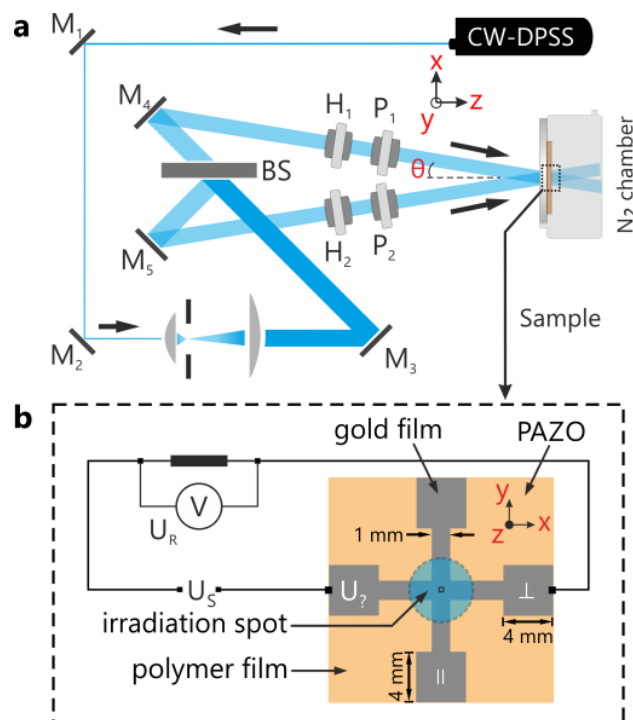
Fig. 8.26. (a) Scheme of the experimental set-up consisting of two-beam interferometry used to structure the sample surface and electronic part for measurements of conductivity. (b) Scheme of the geometry of the gold layer for the conductivity measurement. The film was deposited as a cross and irradiated at its center. The conductivity measurements were performed during irradiation with the grating vector perpendicular and parallel to the cracks formed.

Before the irradiation, the conductivity in both directions (perpendicular and parallel to the grating as shown in Fig. 8.26(b) was measured to be (175 ± 5) Ohm. The conductivity of the gold films perpendicular to the formed cracks is not changed significantly and remains constant during irradiation (Fig. 8.27c). Because of the low voltage applied, the voltage signal is noisy. Fitting the data points to a polynomial reveals that the resistance actually remained constant throughout. The electrical resistance of the sample parallel to the SRG was found not to fluctuate or change at all.
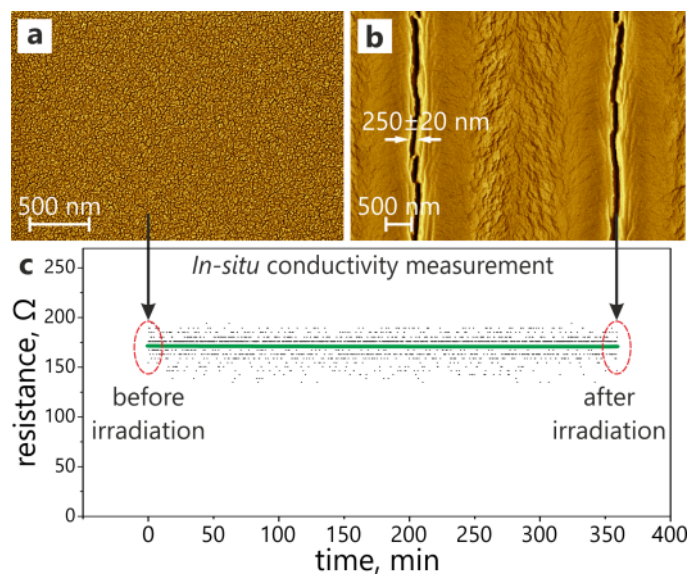
Fig. 8.27. (a) SEM micrograph of the gold covered sample surface after preparation. The gold layer of 10nm thickness does not form a completely smooth film but a well-interconnected, electrically conducting network. (b) SEM micrograph of the gold-covered sample surface after irradiation. The cracks run along the "valleys" of the sinusoidal shaped surface. (c) In-situ measured resistance during irradiation time (6 hrs). The (black) dots represent the single data points acquired every 10 seconds, the (green) line shows a polynomial fit to the data.

Although the gold surface undergoes deformation and clearly breaks up, no change in conductivity is observed. To confirm and understand our data in a better way, we applied AFM-tip lithography to produce cracks within the metal layer. A sample similar to the one used for the irradiation experiment is connected to an Ohm-meter and placed on the sample stage of an AFM. The cantilever is positioned at the edge of a metallic strip (see Fig. 8.28c) with the

help of an optical microscope. The AFM (NTEGRA, NT-MDT, Russia) is then set to contact mode. The force of 30 µN exerted on the cantilever (Si$_3$N$_4$ cantilever, non-rotated PointProbe Plus, Nanosensors) was chosen to be sufficient to penetrate the metal surface and a significant part of the underlying polymer layer.[118]

The final SEM analysis of the scratched groove (Fig. 8.28(c, d)) revealed that the metal film is clearly removed along the scratch on a width of 1.5 µm to 2 µm. Fig. 8.28d also clearly shows the removed metal being partially deposited at the edges of the scratched area. The strong contrast of the SEM image confirms the complete removal of metal from the polymer surface. The depth of the scratch was determined by AFM analysis to be 500 ± 50 nm.

While scratching the metallic strip the resistance is measured simultaneously. This allows relating the size of a micro-damage of the conductive layer to the electrical resistance of the whole sample. Fig. 8.28(d) (dotted black curve) shows the dependence of the resistivity on the length of the scratch. Scratching as far as 50% of the metal film cross-section does not result in any significant change in resistivity, i.e. the resistivity does not increase by a factor of 2, as it could be expected for halving a conductor's cross-sectional area. Only after "cutting" the metal film up to a width of 0.8 mm (80% of the full width of the layer) an increase in resistance was observed and after 0.9 mm, significant changes in the sample's resistance emerged.

To understand this phenomenon we modelled the sample by a series of three resistors (see Fig 8.29). One resistor represents the area of the metal film that will be removed by the AFM tip (or the cracks introduced by a grating formed), $R_{scratch}$, while the other two resistors, R_1 and R_2, represent the non-deformed metal film on both sides of scratch:

$$R_1 + R_2 = \frac{w - w_{scratch}}{w} R_{intital} \tag{8.7}$$

$$R_{scratch} = \left(\frac{w_{scratch}}{w}\right) \left(\frac{1}{1 - l_{scratch}/l}\right) R_{initial} \tag{8.8}$$
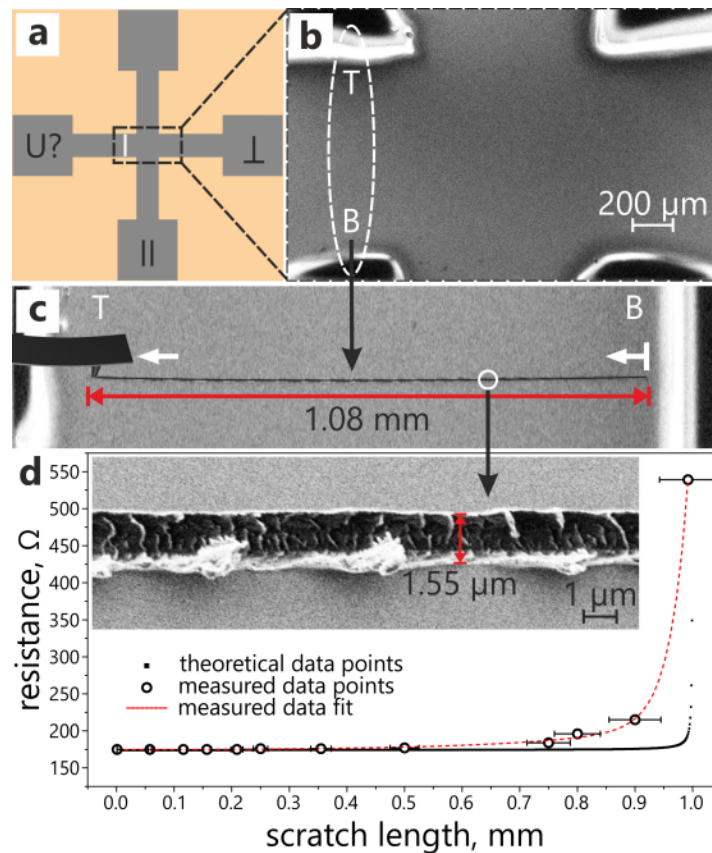
Fig. 8.28. (a) Sketch of the sample (top view). The grey cross represents the part of the polymer that is covered with gold. The vertical white line in the left leg of the cross shows the position of the scratch caused by an AFM tip. The resistance was measured in a direction perpendicular to the scratch. (b) SEM micrograph of the central sample area before scratching. The encircled area (white dashed line T and B) is where the scratch is about to be applied. (c) SEM micrograph of the final scratch running almost all the way through the conductive layer. (d) The dashed red curve is a fit to the resistance measured across the whole sample for different lengths of the scratch. The circles with x-error bars are the actual measured resistance data points. The dotted black curve shows theoretical data for the resistance of the whole sample for different lengths of the scratch, calculated from the width of the scratch, the geometry of the sample and the initial sample resistance. In the inset the magnified scratch area is shown.

Only the resistance of the gold area that deforms changes based on the change in the conductor's geometry. In our case, the initial resistance of such a small area is almost negligible compared to the resistance of the whole sample. To

compare the resistance of the two parts, we have to take their geometries into account. The scratched area is treated as a resistor with the same specific resistivity, film thickness and width as the rest of the metallic stripe. This means the resistance of the metal film that will be removed by the scratch is given by $\frac{w_{scratch}}{w} R_{initial}$ ($R_{initial}$ being the original resistance of the sample). The conducting parts of the sample have a length of 2 cm. For the length of the model resistor we used the average scratch width of 2 μm. This gives a ratio $R_{scratch}/R_{sample}= 10^{-4}$. This big difference in resistance between the modified parts of the sample and the ones not altered is the reason why a significant drop in conductivity across the whole sample was observed only after almost completely cutting the conducting layer. For any scratch length ($l_{scratch}$) and a given resistor length (l) the sample's resistance is given by

$$R_{sample} \approx R_{initial} \left(1 + 10^{-4} \frac{1}{1 - {l_{scratch}}/{l}} \right) \qquad (8.8)$$
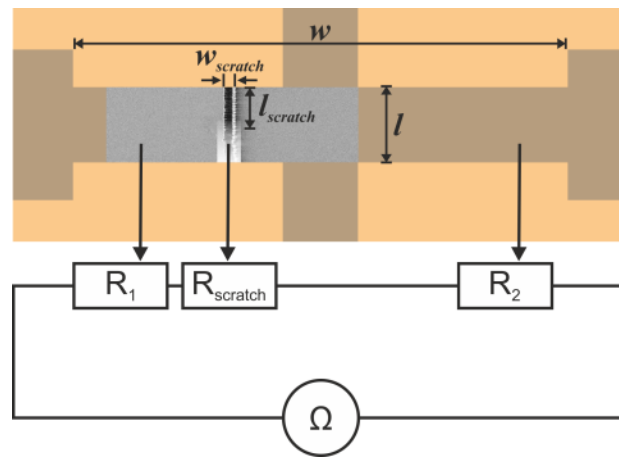
Fig. 8.29. The scheme of the crack sketched in the sample using AFM and a circuit to model the system resistance for different scratch length. R_1 and R_2 stay constant while $R_{scratch}$ depends on the length of the scratched groove.

Fig 8.28d shows a plot, comparing the experimental data to a theoretical curve. The basis for the theoretical model was described above, the initial resistance of the sample is 175 ± 5 Ω, and its dimensions derive from the scratch geometry. Although the curves do not correlate completely in Fig. 8.28d, the tendency for an agreement between experimental and theoretical results can qualitatively be

inferred. The model used for the theoretical curve is commonly used to calculate the resistance based on the geometry of macroscopic conductors. It neglects any effects due to the disturbance and deflection of the current density and the electric field within the sample. Furthermore we considered a film of uniform thickness, which is a rather rough assumption for 10 nm thick films.

Finally, the developed model was applied to the initial example where the formation of the SRG induced parallel cracks in the gold surface. For the irradiated samples we assume a constant crack-width of 250 ± 25 nm and a length 50% of that of the metal stripe's width. Furthermore it is reasonable to assume no more than 1500 parallel cracks as the beam diameter is 6 mm and the periodicity at which the cracks occur is 4 μm. This means that the area that could possibly be made non-conductive due to the rupture process has an initial resistance of 3.3 Ohm. Because the length of the cracks was estimated to be 0.5 mm this means an increase of the whole sample resistance of only 4%.

We would like to point out that the developed model is purely empirical and therefore could only be applied within the accuracy range of the equipment used for resistance measurements. It is also important that while the presented calculations are possible for thicker conductive layers, the model relies on a considerable electrical resistance of the whole sample. As the resistance scales inversely proportional to the conductor's cross-sectional area, the resistance of the whole sample would be too small to be measured with sufficient precision by the methods presented here, if the layer thickness exceeds 20nm.

8.11. Summary

In a short overview of this chapter, we have deposited a thin gold film (25 nm) on 1 μm thick PAZO film to probe the opto-mechanical stresses that may induce during the SRG formation using well studied ±45º interference pattern. Initial results demonstrate that a relative thick gold film (25 nm) is deformed considerably and even ruptured during the SRG formation. SEM analysis revealed that the cracks are positioned randomly throughout the irradiation area, parallel to the SRG lines (Fig 8.4). Though the cracks appear to be similar to a macroscopic mechanical tensile load test performed much thicker metallised polymers, SRG formation should rather involve localized opto-mechanical stresses due to mass transport of material from grating minima towards maxima. To verify this presumption, we have studied the influence of gold film thickness on the rupturing behaviour during the SRG formation. Interestingly, we have

observed a highly periodic rupturing behaviour with Au film thickness ≤ 15 nm (Fig 8.6 and 8.7). The observation of periodic and aperiodic cracks in Au films of different thickness posed an important question on the origin of stresses resulting in these cracks. To solve this riddle, we have irradiated the Au/PAZO films with RL interference pattern as an alternative to ±45° pattern. To our surprise the cracks resulted from RL pattern are very different from that of ±45° pattern (Fig 8.8), confirming the fact the diversity in rupturing behaviour is indeed represent the nature of localized stress patterns. These important observations lead us to further question on the adhesion between the Au/PAZO interfaces.

A good bonding or adhesion layer at the Au/PAZO interface should exit to translate the opto-mechanical stressed induced by different interference patterns to the Au layer, thereby leading to the crack formation. To study the possible existence of bonding layer at Au/PAZO interface experimentally, we have deal with the challenge in two phases. In first step, we have performed Neutron Reflectometry with 10 nm thin Au film deposited on a micrometre thick PAZO layer to probe for any diffused layer at the Au/PAZO interface. The "Scattering Length Density" profile shows that ~4.5 nm thick bonding layer exists at the Au/PAZO interface (Fig 8.13). In second phase, to check the impact of adhesion layer on the crack formation, we added an extra layer of multi-layered graphene (G-ML) at the Au/PAZO interface. Irradiation of Au/G-ML/PAZO samples with ±45° and RL interference patterns revealed the characteristic rupturing of Au film takes places only in the regions in direct contact with PAZO and the Au deposited on G-ML remains unaffected, confirming the presence of a very good bonding layer at the Au/PAZO interface. The results also indicate that the bonding layer acts as a transducer of local stress distribution in the polymer film to a metal layer.

Following these basic studies on the possibility to probe the opto-mechanical stresses that are induced during the SRG formation by placing thin Au film on top, we have extended the work to understand the influence of various experimental parameters on the nature of gold film rupturing behaviour, *viz.* Au film quality, irradiation intensity, interference pattern, temperature, and grating periodicity etc. Due to lack of clear understanding on the molecular level processes taking place during the SRG formation, estimating the stresses became a challenging task. However, we have applied some standard models on fast fracture used in the material science to study relatively thick metallised polymers and estimated a local stress of 100 MPa induced during the SRG formation in photosensitive polymer film. We presume that the stresses might be even larger and could be tuned by utilizing the vast number of photosensitive materials synthesized in the past decade.

In addition to probing the opto-mechanical stresses induced during the SRG formation, we have also put forward two possible applications of the ultra-thin metallised polymer system developed here. One of them is an easy photo-patterning of thin Au films on polymer substrate utilizing the advantage of reversible switching of topographic features in photosensitive polymer. Another application is on studying the electrical conductivity behaviour of ultra-thin gold films by applying controlled deformation and rupturing during the SRG formation. We believe that both these methods are valuable tools for deformable electronics industry.

Conclusions and Outlook

Conclusions

In this thesis we proposed for the first time an AFM connected two-beam interferometer (IIAFM) setup to study the correlation between surface relief topographies of photosensitive thin azobenzene polymer films and the distribution of $\vec{E}$-field vectors resulting from the polarization states of the two interfering beams (interference pattern). In chapters **4–6**, a comparative analysis is carried out for two photosensitive materials differing in molecular weight: an azobenzene-containing polymer (PAZO) and a molecular glass formed from a much smaller molecule consisting of three connected azobenzene units (trimer). In chapter **5**, we have showed that using our IIAFM it is possible to acquire local changes in topography of the polymer surface while at the same time switching between different types of interference patterns. The studies with all intensity interference patterns (IIPs) show that the position of intensity minima corresponds to topography maxima, whereas the positions of intensity maxima can be related to topography minima (for any photosensitive material mass transporting away from light intensity). This behavior is independent of polarization combinations (SS, PP, ‡45°, LL, and RR) of the interfering beams.

In chapter **6**, a detailed study on the correlation between SRG topography and different polarization interference patterns (PIPs) is presented (Table 6.1). In case of PIPs such as ±45°, SP and RL, it is only the orientation of the $\vec{E}$-field vector that varies while the intensity remains spatially uniform. Performing the *in-situ* AFM analysis of the changing topography due to subsequent irradiation with alternating intensity and polarization interference patterns, we are able to reveal the relations between the topographic maxima and minima, and the distribution of the $\vec{E}$-field vector within the polarization interference pattern. In particular, for the ±45° combination, the grating maxima are induced by a vertical $\vec{E}$-field vector (↕). By recording the topography response on irradiation in real time, we have also found a new feature in PAZO films, exclusively related to the ±45° combination: during the first few minutes of irradiation, the topography assumes a double grating arrangement with two maxima within one optical period. The maxima are situated at the positions of the horizontally (↔) and vertically oriented field vector (↕). The topography maxima due to horizontal vector (↔), however, disappear after 5 minutes of irradiation, while the second half of the

maxima grows continuously, finally reaching a height of up to 90% of the total thickness of polymer film. Similarly, in the case of the SP configuration, the formation of two maxima at one optical period is observed. Moreover, the double topography period is maintained over the whole irradiation time resulting in a SRG height of 25% of the total film thickness. With respect to SP interference patterns, the PAZO or trimer molecules tend to accumulate in regions where the field vector is linearly oriented (↘ and ↗). Since this orientation is encountered twice per period for the SP interference pattern, the "double grating" phenomenon arises.

We have also found that approaching the diffraction limit at D = 280 nm, we could produce SRG of 140 nm periodicity using SP pattern, which is more than three times smaller compared to incident wavelength (491 nm). Thus, we are able to fabricate surface relief structures below diffraction limit directly using far field irradiation. Moreover, we also produced an orthogonal grating with topographical features down to 175 nm in an area of 5 mm^2 (Chapter **7**).

In chapter **8**, we dealt with the question of complex stresses generated during SRG formation in photosensitive materials. To probe the photomechanical effects, we deposited a thin gold layer (5–30 nm) on the polymer and observed the deformation behaviour during the SRG formation with different interference patterns. Using neutron reflectivity, a 45 Å thick diffused metal layer into the polymer surface was found to form the bonding layer between the polymer and metal layers. The bonding or adhesion layer at the interface serves as transducer for opto-mechanical stresses that polymer material exerts on the metal layer during surface relief grating formation. The forces developed in the polymer layer under irradiation are quite strong and results in not only significant deformation in the glassy polymer material but also in a deformation and rupturing of the metal layer. When separated by the graphene multilayer the metal film still deforms due to the increase in the surface area, but no rupturing appears within the layer. We state here, that the periodic metallic cracks observed along (parallel) grating are to be the direct imprint of opto-mechanical stress developed in the skin of the polymer layer during SRG formation. Moreover, we have shown that the distribution of the electrical field vector within the interference pattern significantly change the local distribution of the opto-mechanical stress even when the kinetic and value of the surface area change is kept constant. The influence of different grating formation parameters on the behaviour of gold film deformation and rupturing is also presented. In addition, we have also studied the conductivity behaviour of metal films ruptured during the SRG formation. We have shown that periodic micro rupturing of thin metal films up to 80% of metal film width has no significant influence on the film's

electrical conductivity if the cracks make up only a small portion of the whole sample area and do not cut the metal film completely. Further experiments with AFM tip lithography have shown that this is even true for larger cracks of width in the micrometre range. This phenomenon has been explained and brought into agreement with standard theory. We have shown that our experimental values conclude with theoretical considerations for both the metal rupturing due to forces induced by SRG formation as well as for the "artificial" scratch created by an AFM-tip. The results presented here could be very useful for the production and quality control of micro-electronics as modern electronics are required to become more and more flexible and are applied in non-stationary conditions.

In chapter **8**, we have suggested that the response of a metal layer on top of photosensitive polymer upon deformation of the latter might constitute a test of the forces generated within the polymer film. In combination with suiTable simulations combining continuum mechanics with molecular dynamics, this might be developed into a method to probe and quantify forces developed during the mass transport of the photosensitive polymer films on molecular scales. In particular, we might ultimately address the question how a polymer film in its glassy state can deform so drastically without significant softening, at the same time doing significant work rupturing the adsorbed metal film.

Outlook

An interesting application awaiting in-depth study of Au/PAZO system presented in this work is the analysis of mechanical behaviour of metallised polymers during deformation, which are inseparable part of modern ever shrinking deformable electronics. In the recent years, the momentum in electronic industry to miniaturize and develop novel devices has created a huge interest on fabrication and understanding the various aspects of ultra-thin metal/polymer interfaces in variety of scientific disciplines such as in micro-fabrication processes to create photolithographic masks[119,120], conductive channels, capacitors in embedded microelectronics and deformable surfaces for paper like thin displays[121,122,123,124]; in optoelectronics to create optical waveguides, organic transistors and light emitting diodes (OLED)[125]; in bioengineering to create smart prostheses like sensitive skin[126,127] and sensors to monitor soft tissues[128]; in the field of renewable energy to create printable thin-film solar cells[129]; in electronic textiles[130] and many more.

We would like to propose a future study for developing a novel method to study the mechanical properties of ultra-thin novel hybrid materials using the

microscopic opto-mechanical tensile loads induced by RL interference pattern as presented in section 8.6.2.
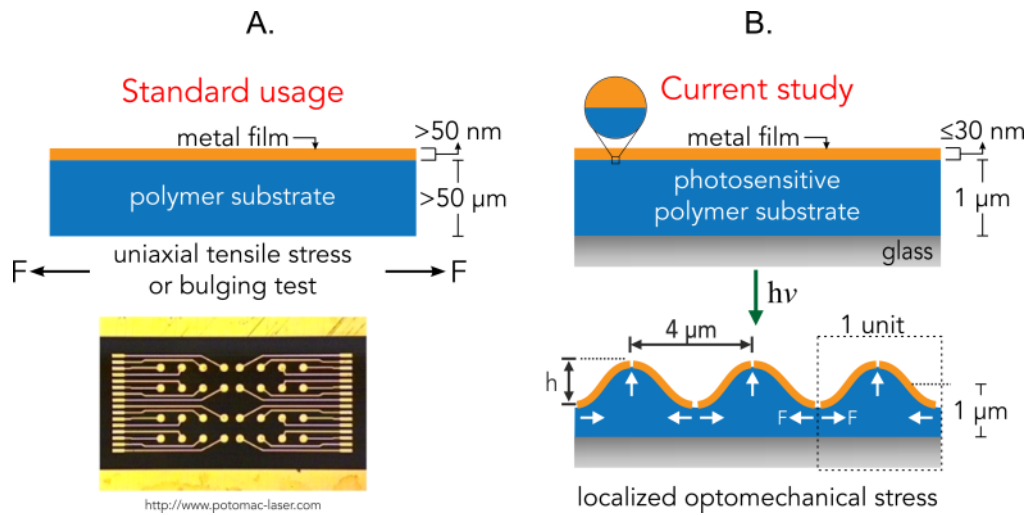
Fig. 8.1. Comparison of standard macroscopic tensile load test and the microscopic opto-mechanical tensile load test proposed in the current thesis

The major focus of scientific community in studying the ultra-thin metallised polymer films is to assess and control its mechanical and electrical properties in order to avoid failure of functional devices in variety of working environments. However, studying the mechanical properties of such thin metal films (< 30 nm) is a major challenge with conventional methods despite the advances in uniaxial tensile load test[131,132,133] in *in-situ* transmission electron microscope[134,135], tensile testing utilizing the surface tension of water[136] and dynamic bulge test[137,138,139,140] due to the inability of achieving free standing metal films. Further, ultra-thin metal films deposited on polymer substrates via physical deposition methods often consists of loosely connected metal islands or networks[141], thus becoming challenge to assess mechanical properties of metallised polymer system with conventional methods. For instance, a uniaxial mechanical tensile load test performed on ultra-thin metal/polymer system (Fig 8.1A) causes non-uniform distribution of stresses at local imperfections and results in the ambiguity of determined mechanical properties. In the recent years, several theoretical and experimental approaches are proposed to study the failure of metal films (> 50 nm) on thick polymer substrates based up on the elastic-plastic behaviour, necking and delamination of metal films under tensile loads[108,119,142,143,144]. However, in case of ultra-thin metallised polymers, considering the local

imperfections and larger film length-thickness ratios, characterizing the films at microscopic scale is more significant than whole system.

Using our metal on photosensitive polymer system presented in chapter **8**, it should be possible to address above discussed issues (Fig 8.1B). Despite incomplete nature of investigation in this work requiring many theoretical studies, we believe that our results will be good foundation to guide future research in the field of photo physics for credible understanding of light induced mass transport phenomena in photosensitive materials. We would like to highlight the fact that a wide variety of photosensitive materials are being researched with improved photo response properties under variety of light irradiation conditions, reversible switching property and availability of multitude light interference combinations makes the opto-mechanical tensile load test proposed here might be a very promising and flexible method to characterize ultra-thin metal films and interfaces at microscopic scale.

We also believe that the work presented in this thesis is a valuable asset to guide future endeavours in the field of photosensitive materials.

This page intentionally left blank

A.1. *In-situ* Atomic Force Microscope

In our *in-situ* AFM design, the AFM body is round in shape and easy to mount on supporting legs as shown in Fig A.1 (b). The cantilever scanning direction is set to 0° by default. The cantilever holder should orient perpendicular to the optical Table to achieve scanning of sample topography perpendicular to the grating lines.
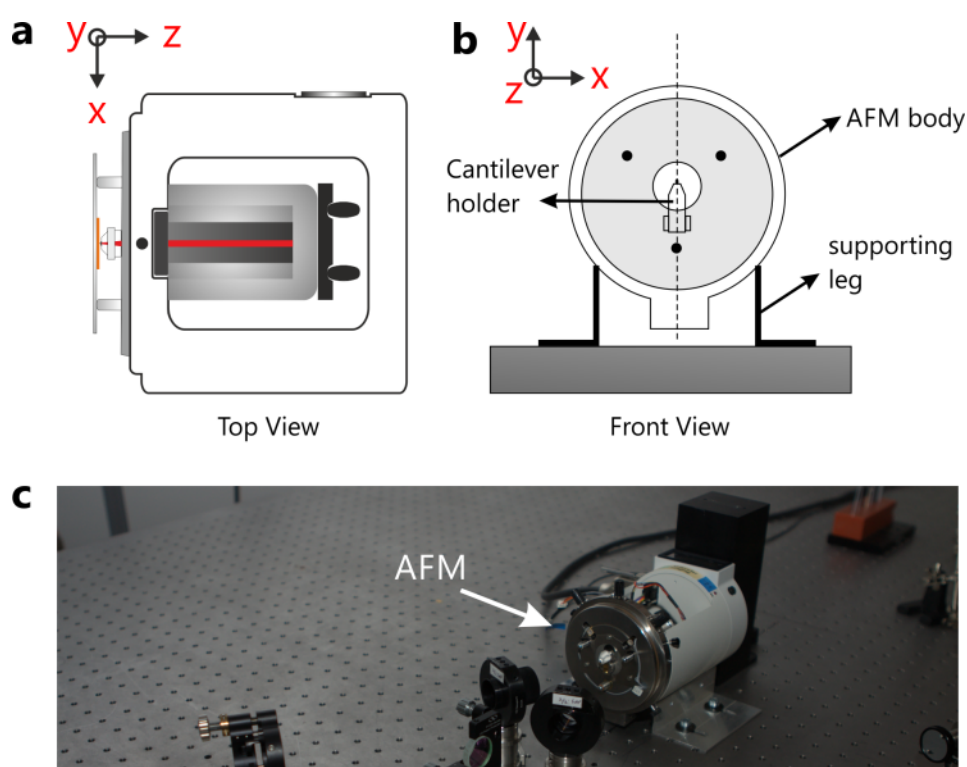
Fig. A.1. Scheme of atomic force microscope used to integrate with Mech-Zehnder interferometer to study the surface relief formation in *in-situ*. The scanning is performed in XY-plane. (c) AFM used in the current study for all *in situ* measurements

A.2. Comparison of SRG formation in Front and Back Irradiation conditions

In Fig A.2 we are comparing two different situations of light interfering from glass side (back side) and the polymer side (front side). As the light passing through different media, the wavelength modulates accordingly ($n_1\lambda_1 = n_2\lambda_2$). However, the actual periodicity [$d=\lambda/(2\sin\theta)$] of the polymer grating remains constant in both front and back irradiation conditions due to the change in angle of the refracted interfering beams. Further, the UV-Vis absorption spectra depends upon the frequency [$\Delta E=h\nu$] thus no real difference between the front and back irradiation situations.
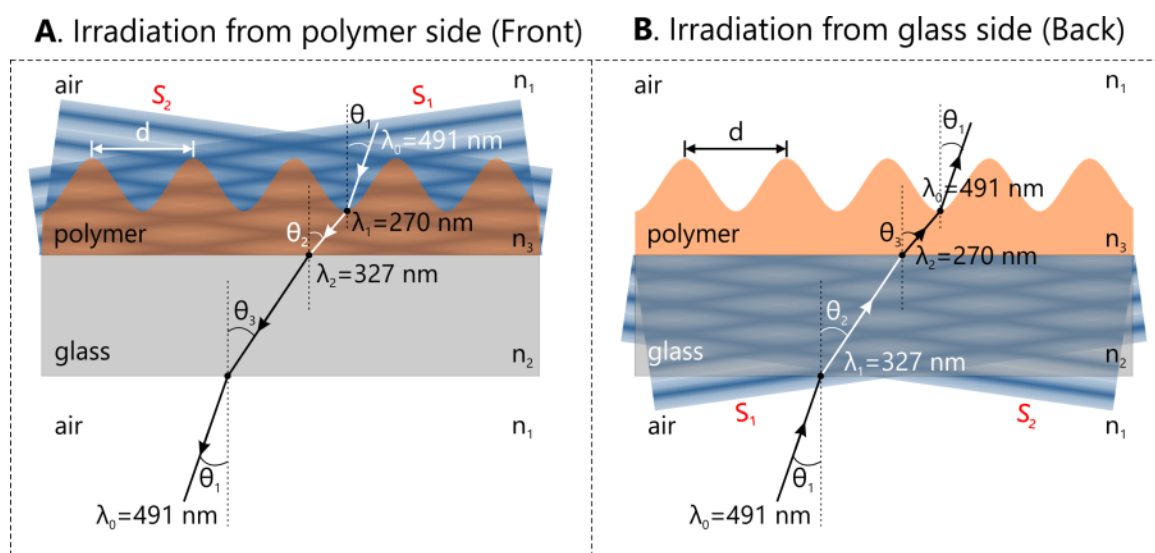
Fig. A.2. Comparison of SRG formation with front and back irradiation processes. (A) The air-polymer interface is exposed to a wavelength of 491 nm. (B) The glass polymer interface exposed to a wavelength of 327 nm.
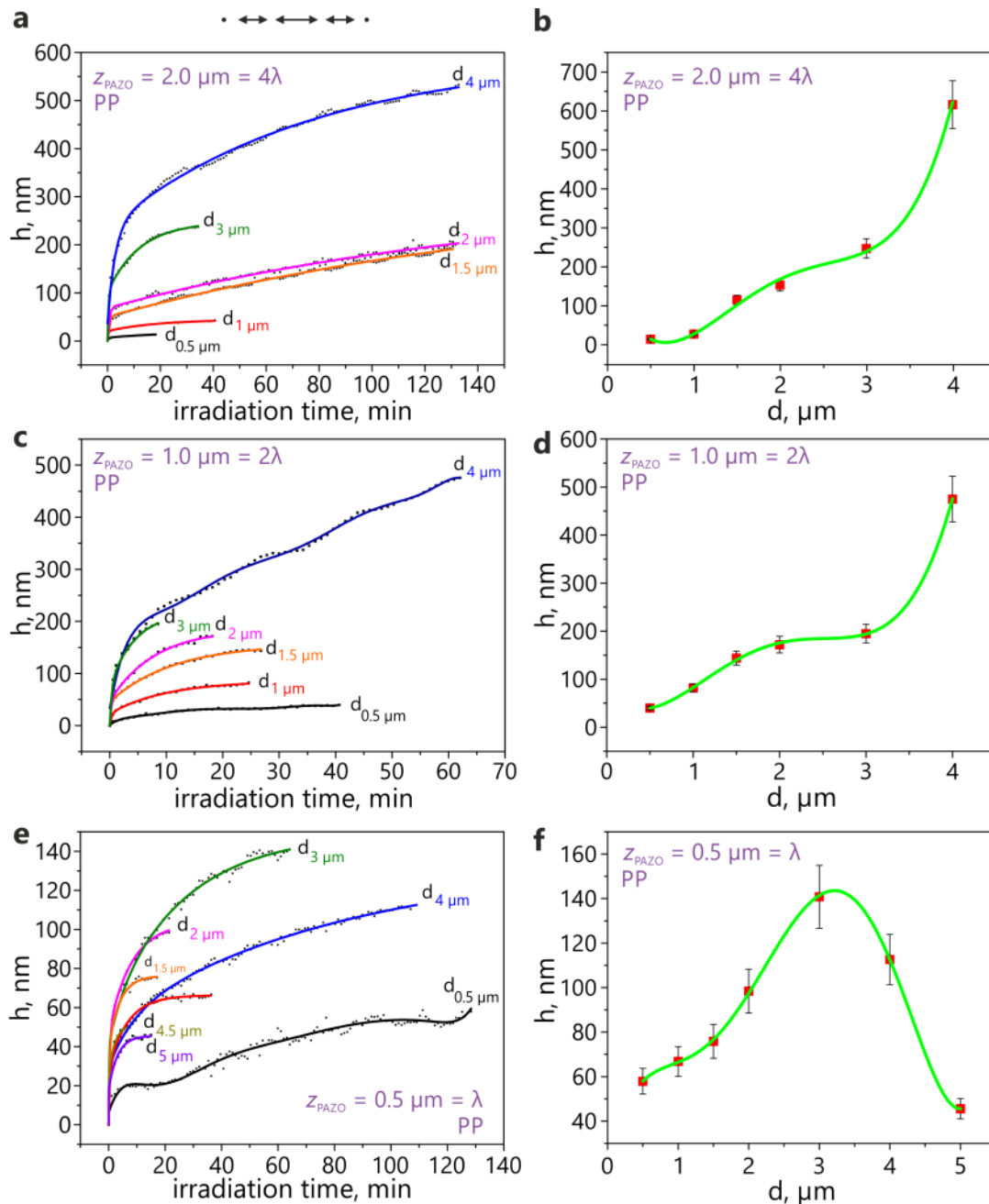
A.3. Influence of film thickness on SRG formation

The dependency of grating periodicity (d) on film thickness (z), grating height (h) and the interference patterns (‡45° and PP) is presented comprehensively in Fig A.3.1 and Fig A.3.2. Experimentally, a similar dependency is observed between d, h, and z for all different interference patterns. To understand this dependency, more experimental and theoretical understanding is required on molecular level azobenzene photo- dynamics during irradiation with different interference patterns.
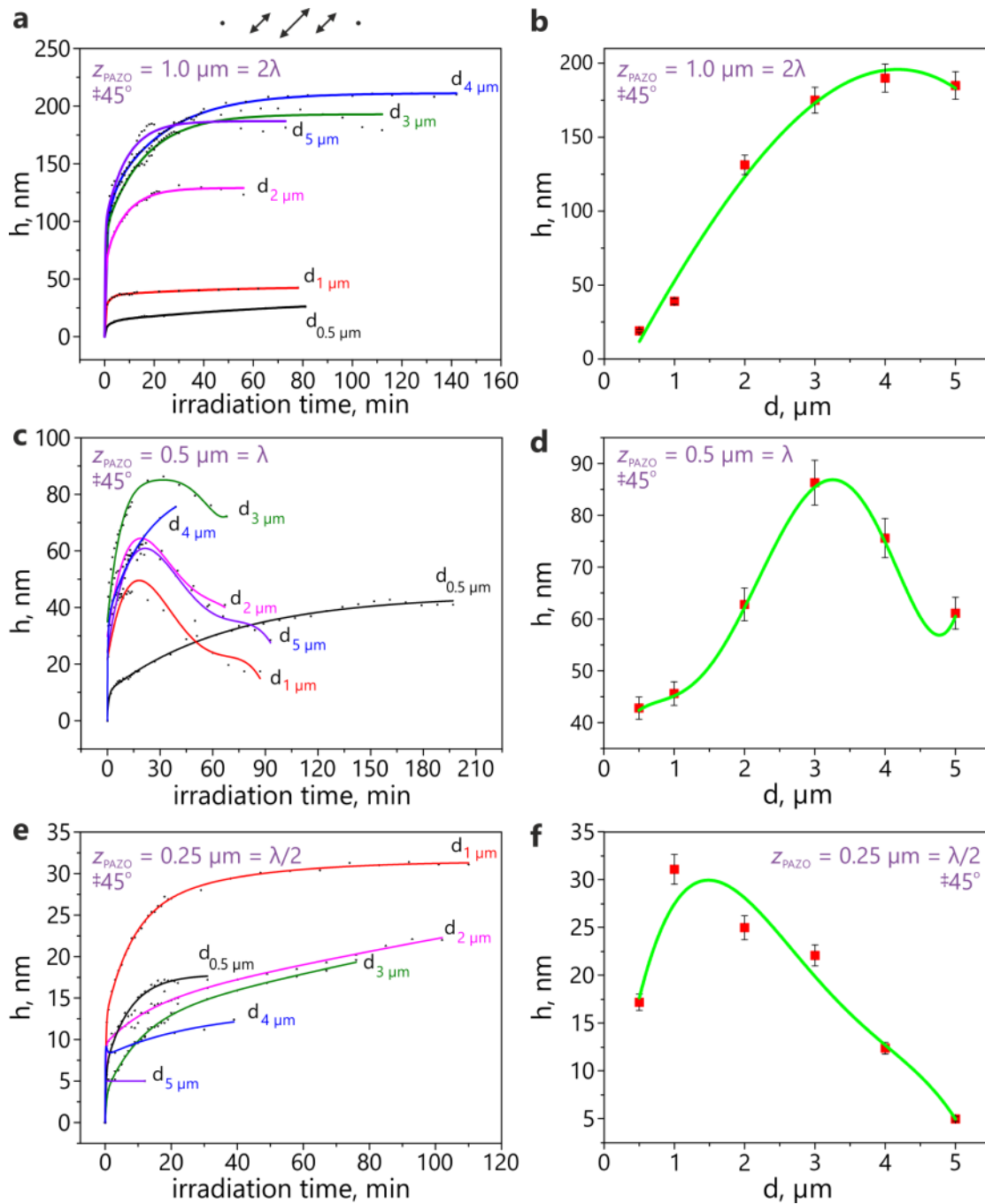
Fig. A.3.1. Dependence of SRG height on grating periodicity 'd' and film thickness 'z' for PAZO film using ‡45° interference pattern. (a) Grating growth kinetic for different periodicities using 1.0 μm thick PAZO film. (b) Relation between 'd' and 'h' for 1.0 μm thick PAZO film. (c) Grating growth kinetic for different periodicities using 0.5 μm thick PAZO film. (d) Relation between 'd' and 'h' for 0.5 μm thick PAZO film. (c) Grating growth kinetic for different periodicities using 0.25 μm thick PAZO film. (d) Relation between d and h for 0.25 μm thick PAZO film. Intensity (100 mW/cm²).

Fig. A.3.2. Dependence of SRG height on grating periodicity 'd' and film thickness 'z' for PAZO film using PP interference pattern. (a) Grating growth kinetic for different periodicities using 2.0 μm thick PAZO film. (b) Relation between 'd' and 'h' for 2.0 μm thick PAZO film. (c) Grating growth kinetic for different periodicities using 1.0 μm thick PAZO film. (d) Relation between d and 'h' for 1.0 μm thick PAZO film. (c) Grating growth kinetic for different periodicities using 0.5 μm thick PAZO film. (d) Relation between 'd' and 'h' for 0.5 μm thick PAZO film. Intensity (500 mW/cm²).

B.1. Mass transport response of trimer towards light intensity
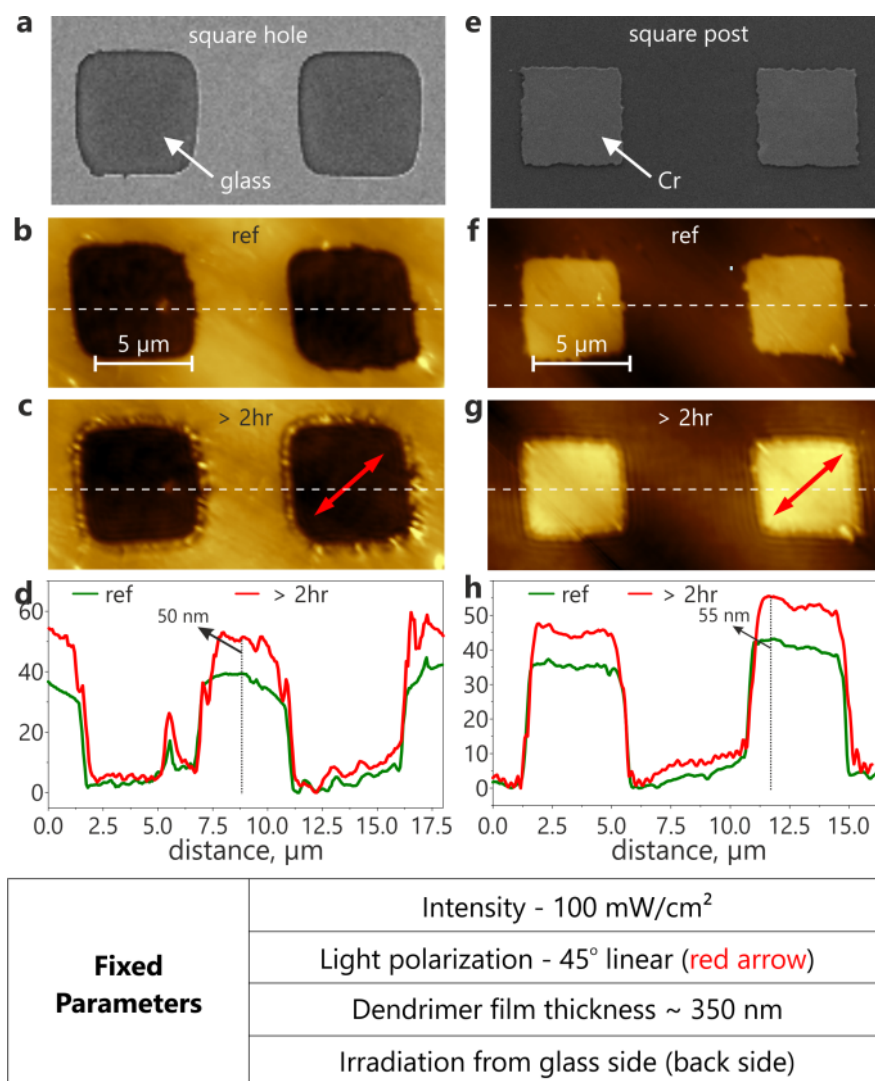
Fig. B.1. Chromium mask experiment to determine the response of trimer to the light intensity. a) Cr mask with square apertures. b) The AFM micrograph reveals the position of Cr apertures in a micrometre thick PAZO layer before irradiation. c) PAZO film after 2 hours of irradiation with homogenous light. d) Comparison of extracted profiles from AFM micrographs in figure 'b' and 'c'. Green colour profile represents the cross section of polymer topography before irradiation and the red colour profile represents the polymer surface after irradiation with homogenous light. e), f) g) and h) shows the Cr mask experiment with square posts.

## B.2. Multiple wave interference patterns through Cr apertures

When a monochromatic beam of light incident on a slit/aperture, the resultant diffraction patterns on the distant screen are well studied and understood. If the aperture dimensions are larger than the wavelength of the light passing through the sides or edges of the aperture, the edges acts as new sources for waves propagating along the sides of aperture with the wavelength in medium. When these waves interfere each other in phase condition one could expect interference patterns. However, these interference patterns are confined to several tens of nanometres distance at the aperture and the air interface.
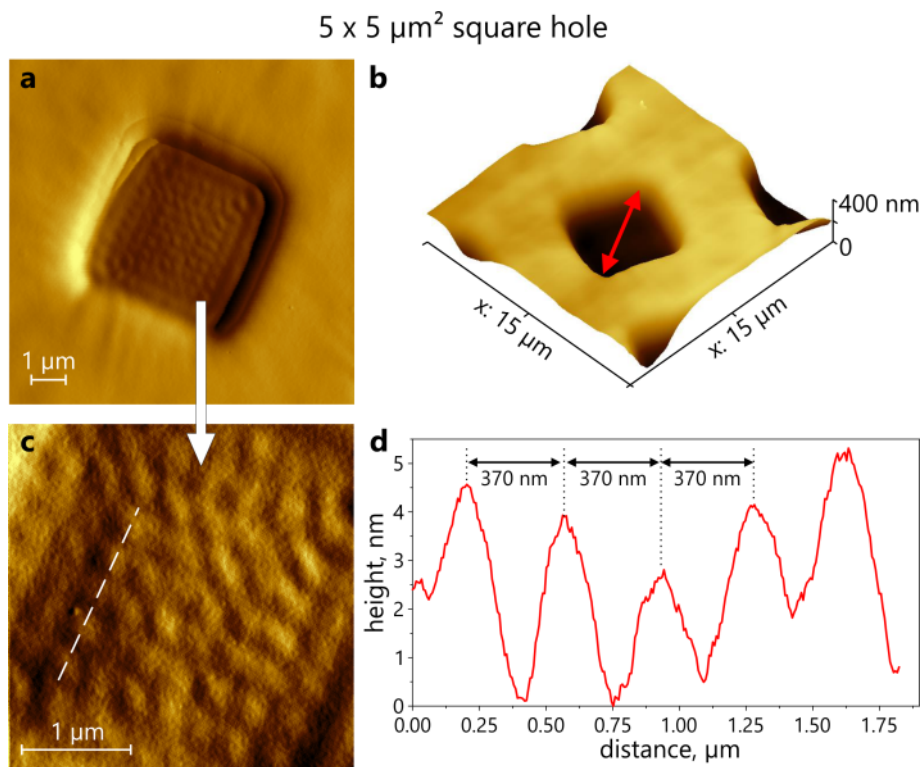
Fig. B.2.1. (a) AFM micrograph showing the multiple wave interference patterns recorded in a micrometre thick PAZO film as a result of Fresnel diffraction through Cr mask square aperture. (b) 3D view of square well with PAZO film after irradiation with homogenous light. The interference pattern is observed in the square aperture/hole. The red arrow represents the light polarization. (c) AFM micrograph of interference pattern in the square well. (d) Cross sectional profile of the dotted line shown in (c).

During the Cr mask experiments to probe the light intensity dependent response of PAZO as presented in section 5.1 (Ch. 5), we have also captured the multiple wave interference patterns as shown in Fig B.2.1.

In Fig B.2.1, we could see the four wave interference pattern recorded in PAZO film inside the square aperture/hole. The resultant pattern of four wave interference is less studied in past except few recent reports on effect of polarization on four beam laser interference. [145,146,147,148] The wave propagation from the edges of square hole could be observe in square posts mask as presented in Fig B.2.2.
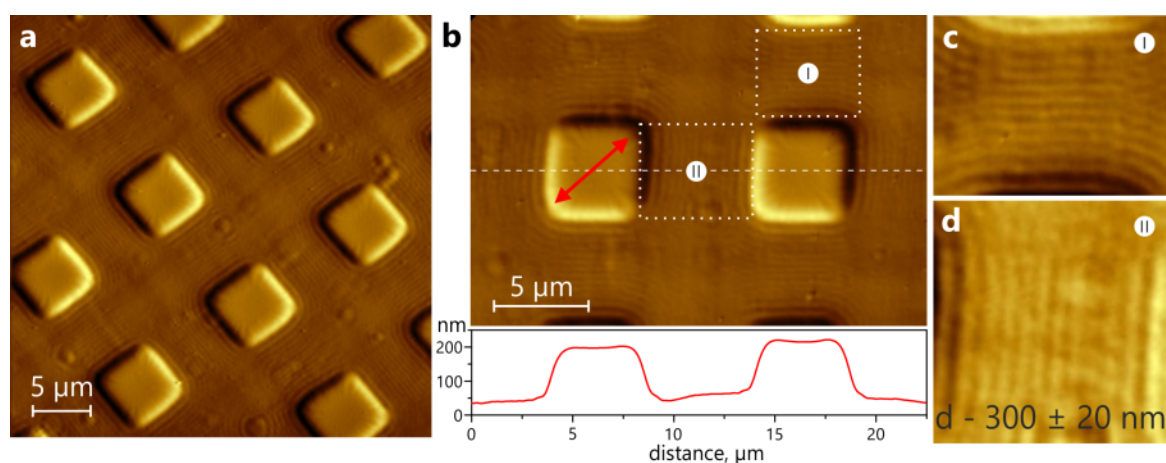
Fig. B.2.2. (a) AFM micrograph showing the wave interference between the propagating waves between two square posts. The patterns are recorded in a micrometre thick PAZO film as shown. (b) AFM micrograph focused on the interference patterns between two square posts. The associated profile corresponds to the dashed line in the AFM micrograph. The red arrow represents the polarization of homogenous light. (c), (d) Focus on the surface relief structures on the sides of square posts labelled as "I" and "II". 'd' represents the polymer grating periodicity.

In Fig B.2.2, we could see the mixing of two waves between every two square posts along each side. The resultant two wave interference pattern is recorded in polymer film with a grating periodicity of 300 ± 20 nm. The periodicity corresponds to the wavelength of light in glass. It is possible that in case of square holes, the interference pattern we see is due to the four wave interference originated from the four sides. To study this interference phenomenon, we have tested other Cr mask shapes such as circle and triangle as shown in Fig B.2.3. In

case of triangle hole or posts, the effect of three wave interference pattern is recorded in the PAZO film.

B.2.1. FDTD simulations

For the simulation of near fields, we have used the Finite-Difference-Time-Domain (FDTD) method. The commercial software from Lumerical Solutions is used for this purpose. This software enables the analysis of the intensity patterns of propagating near- and far fields at multiple interfaces.

We have designed the Cr mask features in the simulation area and different monitors are setup with mesh. The mesh is a collection of yee-cells. For every single cell (yee-cell) of the grid follows a time-dependence calculation of the field by solving the Maxwell equations. The smaller the yee-cell the higher is the resolution of information from the electromagnetic fields. This information will be collected by monitors, which can be adjusted individually as a point or a certain area. Several monitor types are available. We used a Frequency-Domain-Profile-monitor. It saves the components of pointing vector, power flow as a function of time at a certain place. Thus the field components at a certain place can be analysed after the simulation.

Following the simulation, we have compared the intensity distribution inside the corresponding wells at glass/air interface with the patterns observed in the PAZO film during experiments as shown in the Fig B.2.3. The periodicity of patterns in PAZO films correlated well with the simulations. We do not investigate several effects in detail as it is not the focus of the current investigation. Nevertheless we would like to mention that the photosensitive polymer film offers a unique possibility to visualize many near field optical phenomena experimentally. More detailed studies are necessary to further expand and prove our current understanding on the results presented in this section.
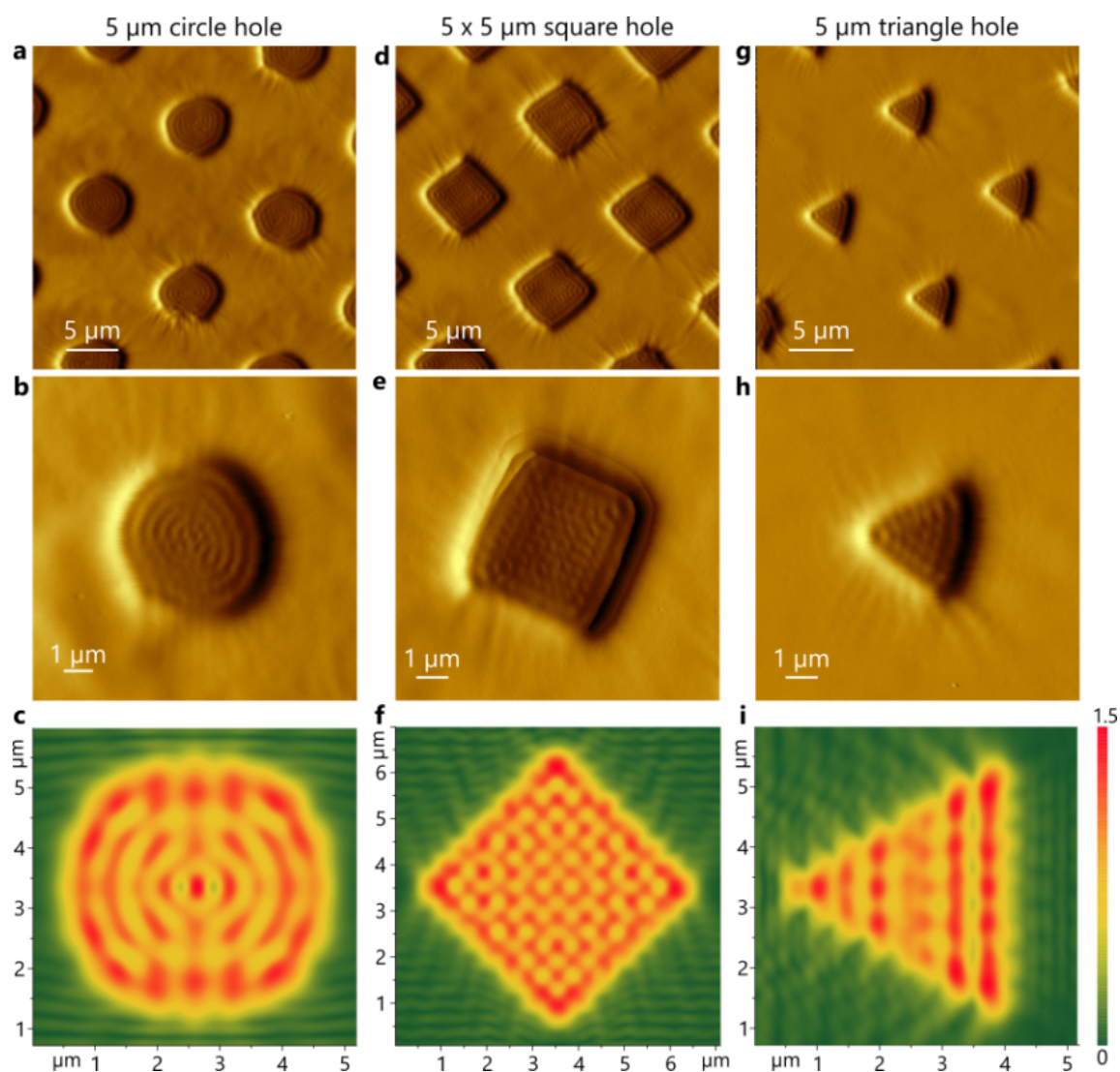
Fig. B.2.3. Comparison of multiple wave interference from experiments and FDTD simulations for different apertures (square, circle and triangle). (a), (b) diffraction pattern in the circle apertures. (c) FDTD simulation of plane wave passing through 5 μm diameter circle aperture without polymer. The pattern is at the Cr/air interface. (d), (b) Multiple wave interference patterns (mixing of 4 waves from the 4 sides as sources) recorded through 5x5 μm² square apertures. (f) FDTD simulation of plane wave passing through 5x5 μm² square apertures. (g), (h) Interference patterns recorded in PAZO film through a triangle aperture with 5 μm height. (i) FDTD simulation of plane wave passing through triangular aperture. All the simulations are performed at the Cr and air interface in the absence of photosensitive material. The periodicity in the intensity pattern of simulations correlated well with the experimental observations.
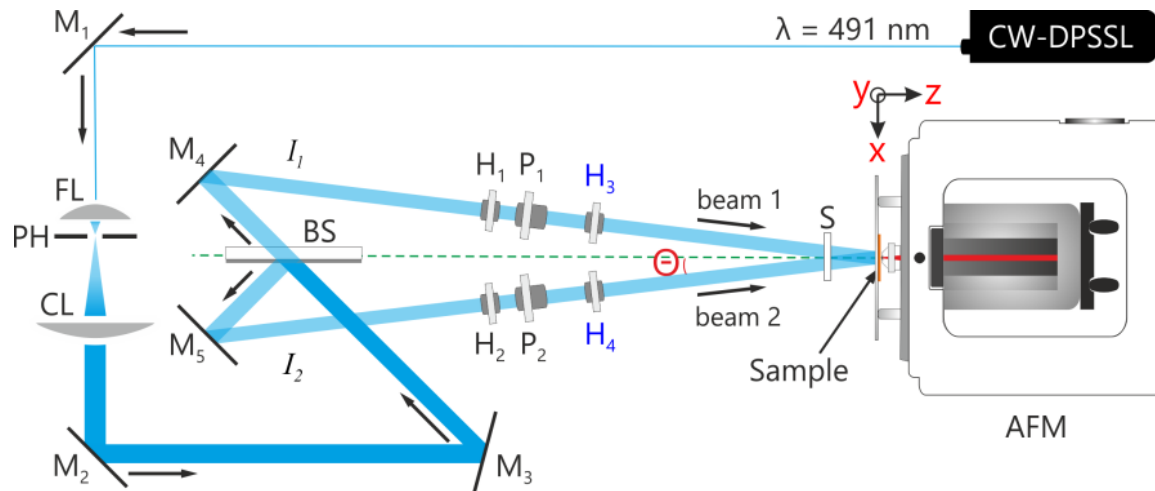
Fig. B.3. Experimental setup for recording SRG formation: (M_1, M_2, M_3, M_4 and M_5) – mirrors; BS - beam splitter; (H_1, H_2, H_3, and H_4) - half wave plates; (P_1 and P_2) –polarizer; (I_1, I_2) – intensities of beams; S – computer controlled shutter; FL – focusing lens; PH – pinhole; CL – collimating lens; and AFM – Atomic Force Microscope.
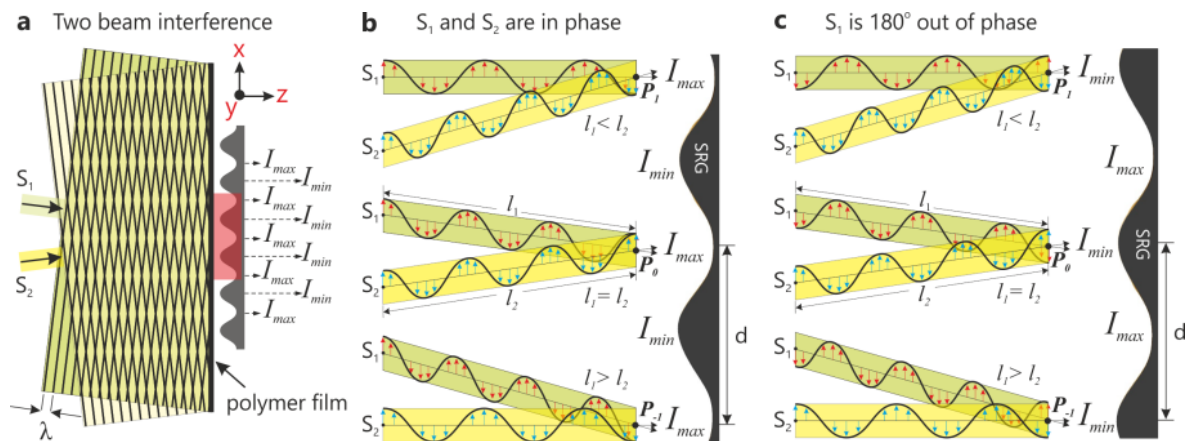
Fig. B.4. Effect of phase difference between two interfering waves on the SRG formation in PAZO polymer film. a) The surface relief formation in polymer film due to intensity modulation in the light interference pattern. The red shaded area is explained in detail further in 'b' and 'c'. b) S_1 and S_2 are waves from two beams from same source. When S_1 and S_2 are in phase with respect to an arbitrary point 'P_0' at the center of interfering beams, the surface relief formation as a function of intensity modulation is presented. c) Considering one of the breams (S_1) is 180° out of phase with respect to the point 'P_0', the resulting surface relief formation is shifted by half a period.
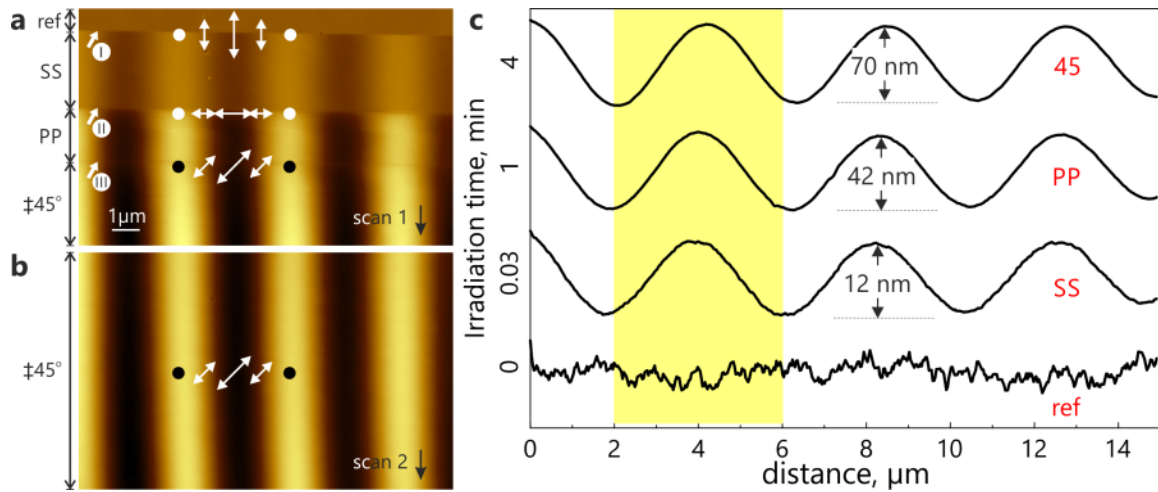
Fig. B.5. *In-situ* AFM measurement for all three combinations SS, PP and ‡45° in single measurement.

B.3. *In-situ* AFM alignment errors during manual positioning

Due to manual alignment procedure, sometimes the AFM body is rotated by few degrees, as a result the scan direction also tilt few degrees giving us an optical illusion that the topography features are phase shifting. However, it will not affect the *in-situ* AFM measurements.
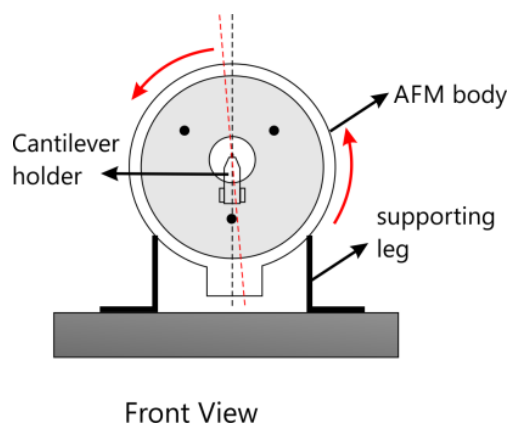

Fig. B.6. The cantilever scanning direction is set to 0° by default and the cantilever holder should orient perpendicular to the optical Table to achieve scanning of sample topography perpendicular to the grating lines.
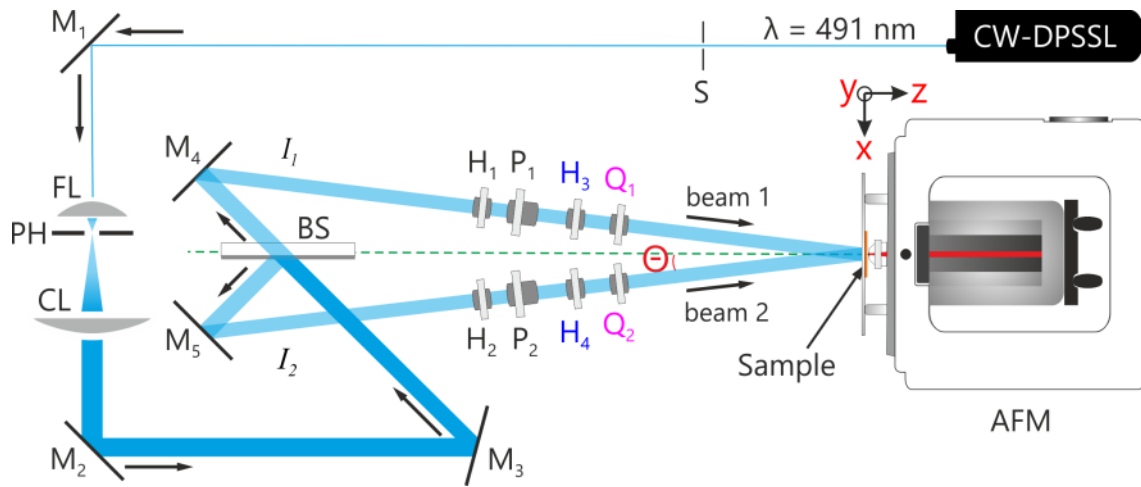
Fig. B.7. Experimental setup for recording SRG formation: (M_1, M_2, M_3, M_4 and M_5) – mirrors; BS - beam splitter; (H_1, H_2, H_3, and H_4) – $\lambda/2$ plates; (P_1 and P_2) – polarizer; (Q_1 and Q_2) – $\lambda/4$ plates; (I_1, I_2) – intensities of beams; S – computer controlled shutter; FL – focusing lens; PH – pinhole; CL – collimating lens; and AFM – Atomic Force Microscope.
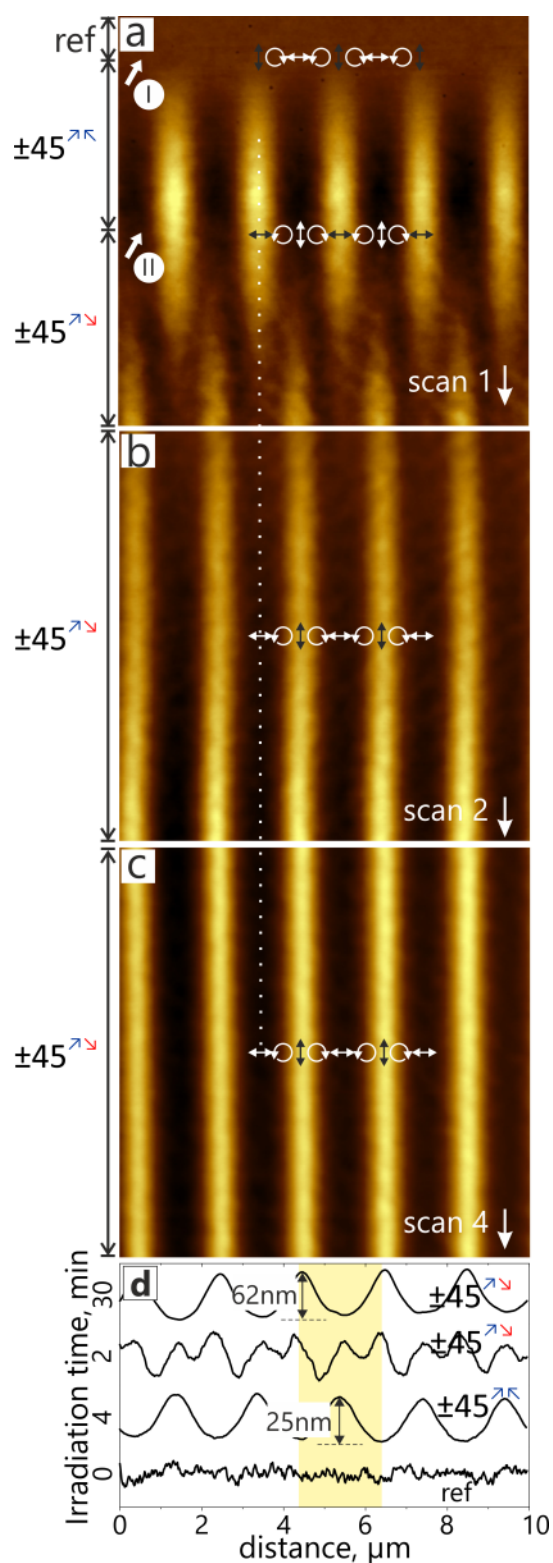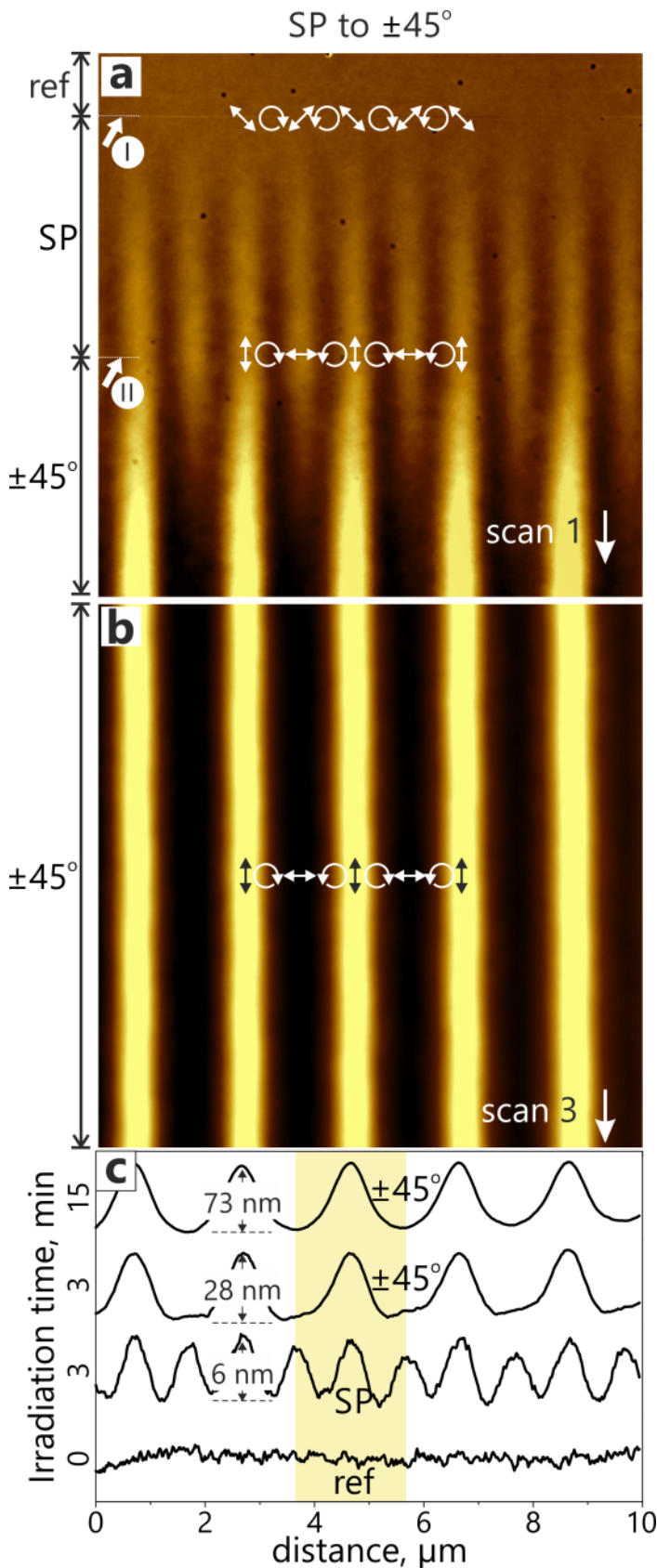
Fig C.1. AFM micrographs of the topography change recorded *in-situ* in trimer film (thickness ~350 nm) during switching the polarization combination of the interfering beams.

(a) The topography change induced by subsequent irradiation with only polarization modulated interference patterns (PIP) in reversible switching combinations: ±45↗↖ started at point "I" and ±45↗↘ marked by "II". The corresponding AFM cross sections are shown underneath.

The y-axis of (c) denotes the time of irradiation used for each combination before switching.

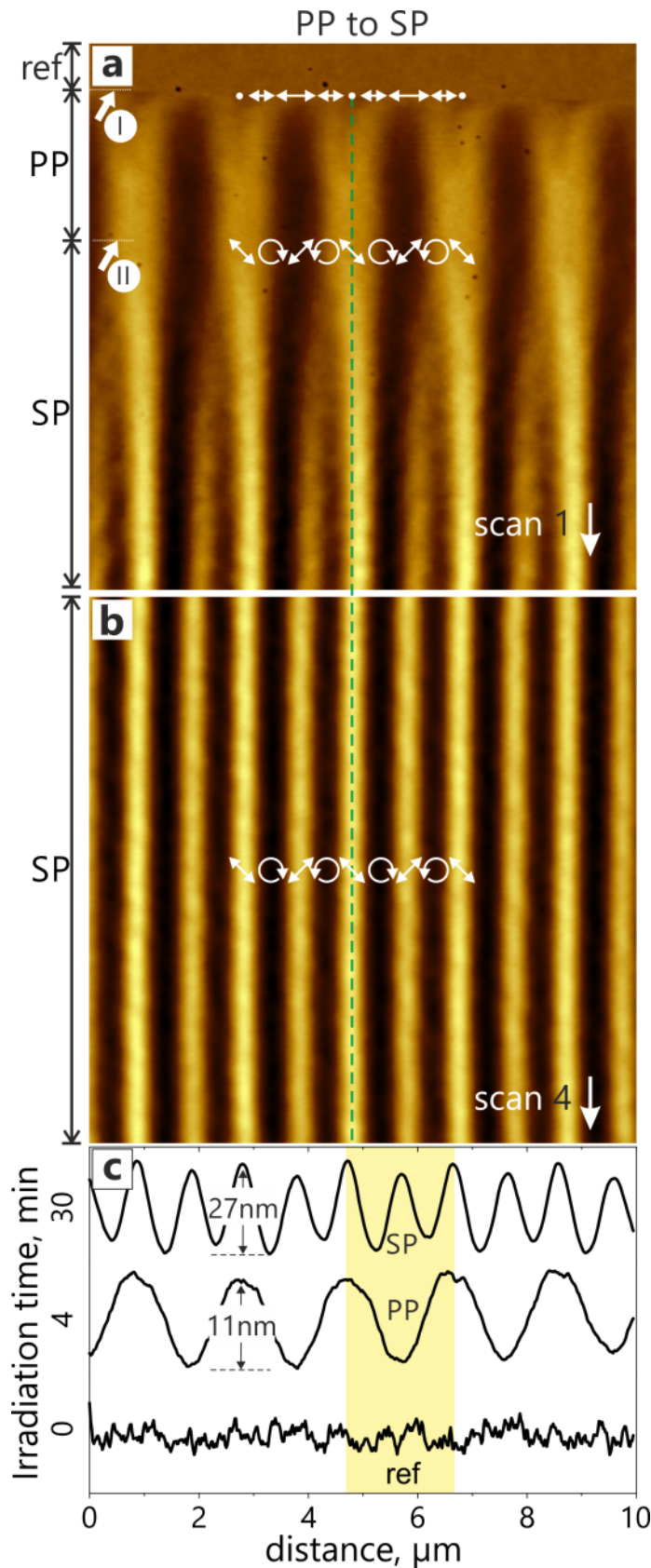Similar result is observed for switching experiment between ±45↗↘ to ±45↗↖ interference pattern (data not presented).

Fig C.2. AFM micrographs of the topography change recorded *in-situ* in trimer film (thickness ~350 nm) during switching the polarization combination of the interfering beams.

(a) The topography change induced by subsequent irradiation with only polarization modulated interference patterns (PIP) in reversible switching combinations: SP$^{\uparrow\leftarrow}$ started at point "I" and ±45$^{\nearrow\nwarrow}$ marked by "II". The corresponding AFM cross sections are shown underneath.

The y-axis of (c) denotes the time of irradiation used for each combination before switching.

Similar result is observed for switching experiment between ±45$^{\nearrow\nwarrow}$ to SP$^{\uparrow\leftarrow}$ interference pattern (data not presented).

Fig C.3. AFM micrographs of the topography change recorded *in-situ* in trimer film (thickness ~350 nm) during switching the polarization combination of the interfering beams.

(a) The topography change induced by subsequent irradiation with PP$^{\leftarrow}$ (IIP) and SP$^{\uparrow\leftarrow}$ (PIP) in reversible switching combinations: SP started at point "I" and $\pm45^o$ marked by "II". The corresponding AFM cross sections are shown underneath. The y-axis of (c) denotes the time of irradiation used for each combination before switching.
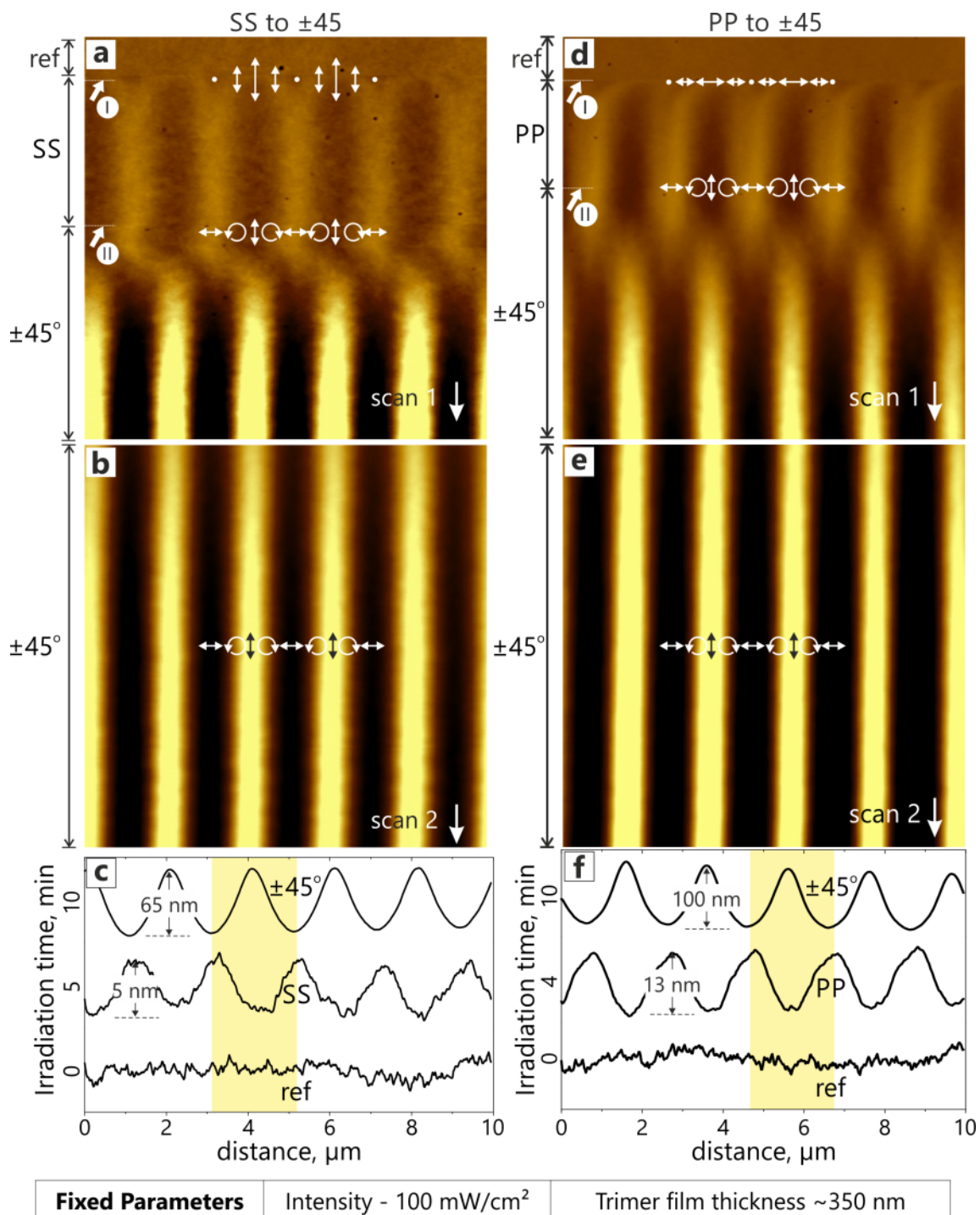
Similar results are observed for switching experiment between SS to SP and ‡45° to SP interference patterns (data not presented).

Fig. C.4. AFM micrographs of the trimer film topography change induced by switching the irradiation conditions. Irradiation is started at position "I" and the change in irradiation condition is marked by "II" in all experiments. (a) and (b) demonstrate the switching between SS to ±45°. (d) and (e) show the switching between PP to ±45° (c), (f) display the corresponding cross-sectional analysis of the topography change as a function of irradiation time and polarization combination.
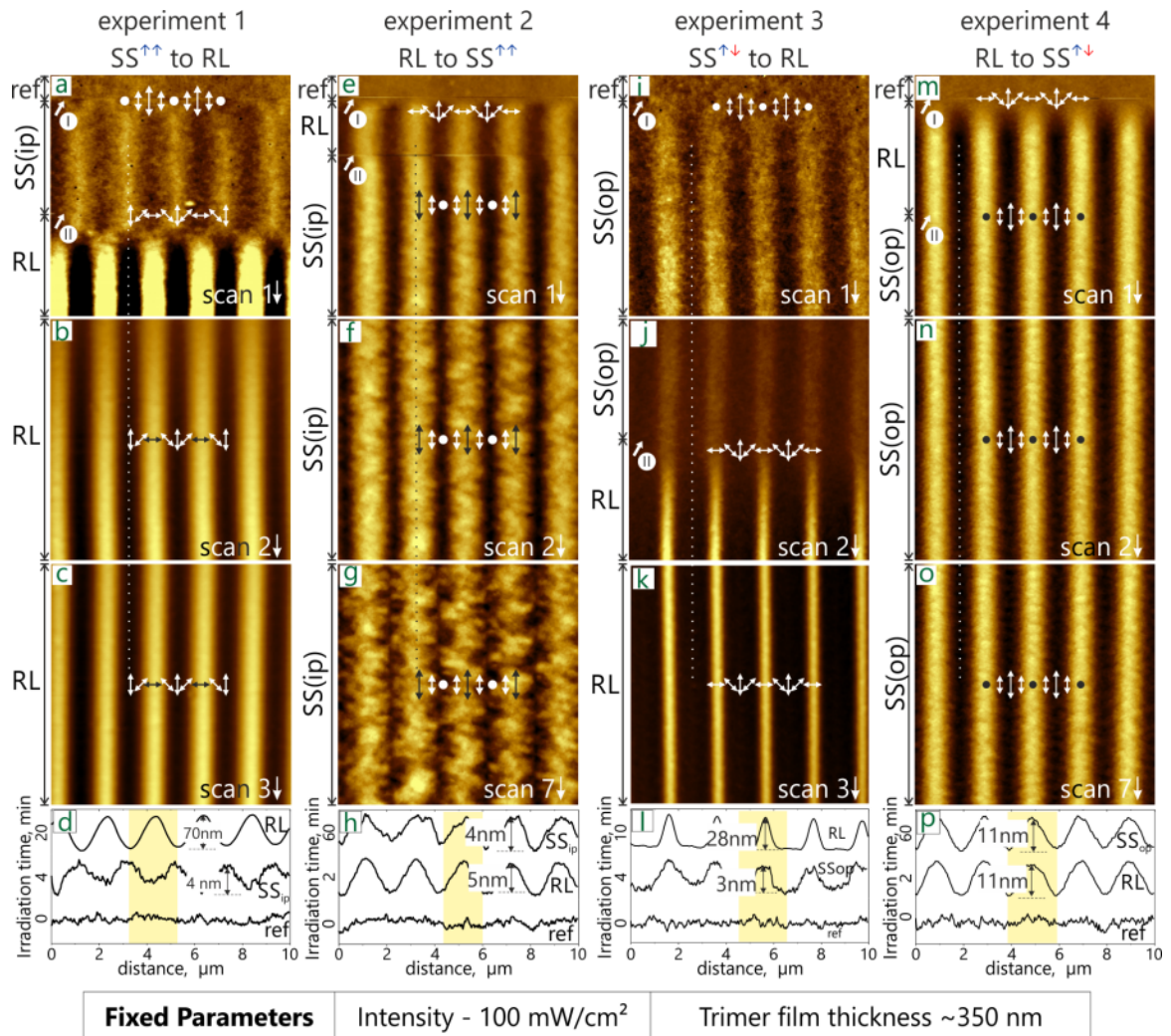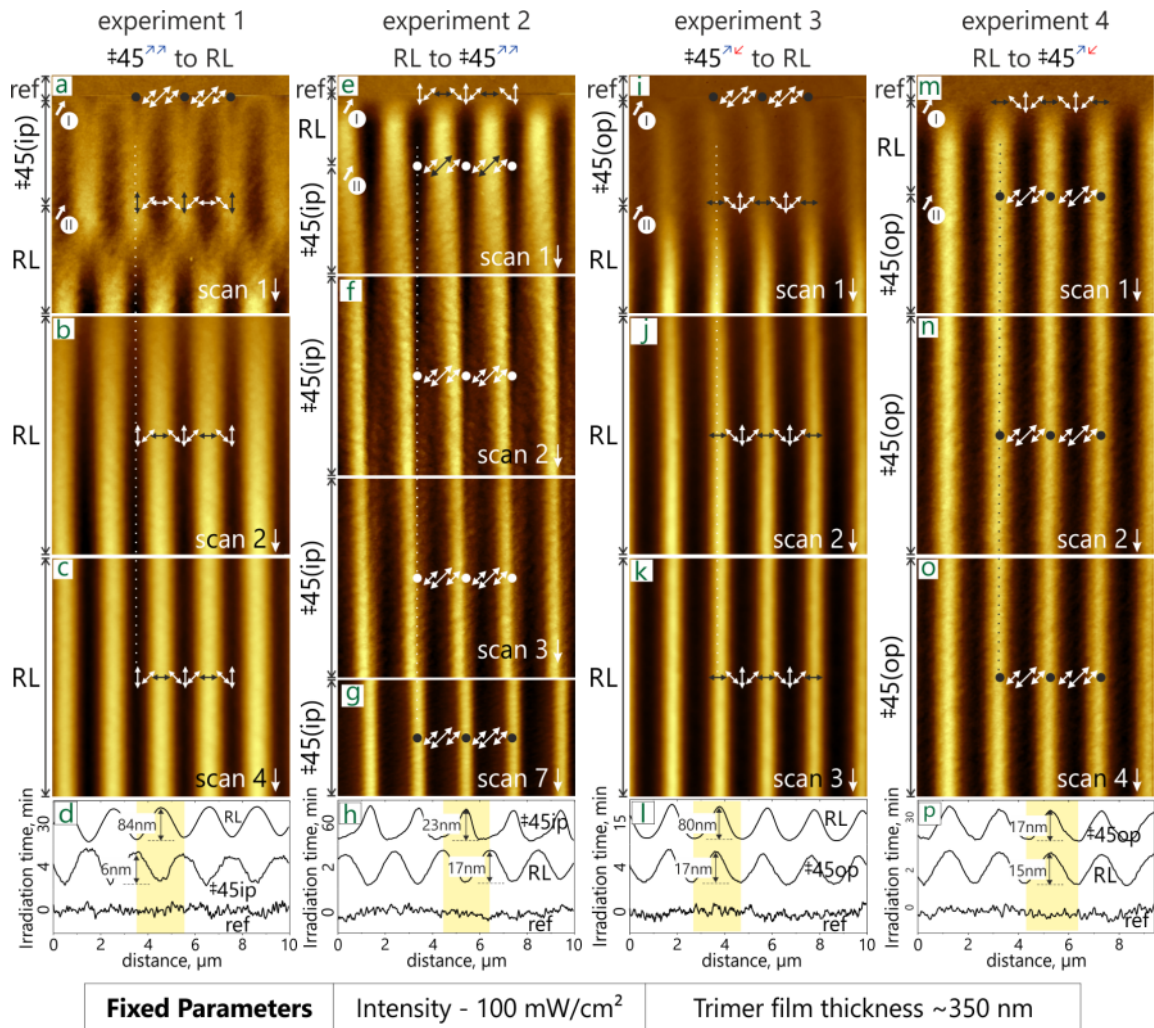
Fig. C.5. AFM micrographs of the trimer film topography recorded within a selected area. While the polymer topography is scanned, the polarization state of the interfering beams is changed in *in-situ*. **Experiment 1** (a, b, c): demonstrate the switching between SS$^{\uparrow\uparrow}$ to RL. (a) The first irradiation event lasts 5 min, followed by irradiation with RL (from position "II"). (b, c) Continuous scan during irradiation. (c) Comparison of AFM cross-sectional profiles. **Experiment 2** (d, e, f): demonstrate the switching between SS$^{\uparrow\uparrow}$ to RL. **Experiment 3** (i, j, k): The effect of 180º out of phase condition. (d) Switching between SS$^{\uparrow\downarrow}$ and RL marked by "I" and "II", respectively. **Experiment 4** (m, n, o): demonstrate the switching from RL to SS$^{\uparrow\downarrow}$. The black arrows besides the scan number at the bottom right side of each AFM micrograph represent the AFM scan direction. The y-axis of (d), (h), (l) and (p) denotes the time of irradiation used for each combination before switching. (**ip**): interfering beams in phase; (**op**): interfering beams out of phase by 180º to each other.
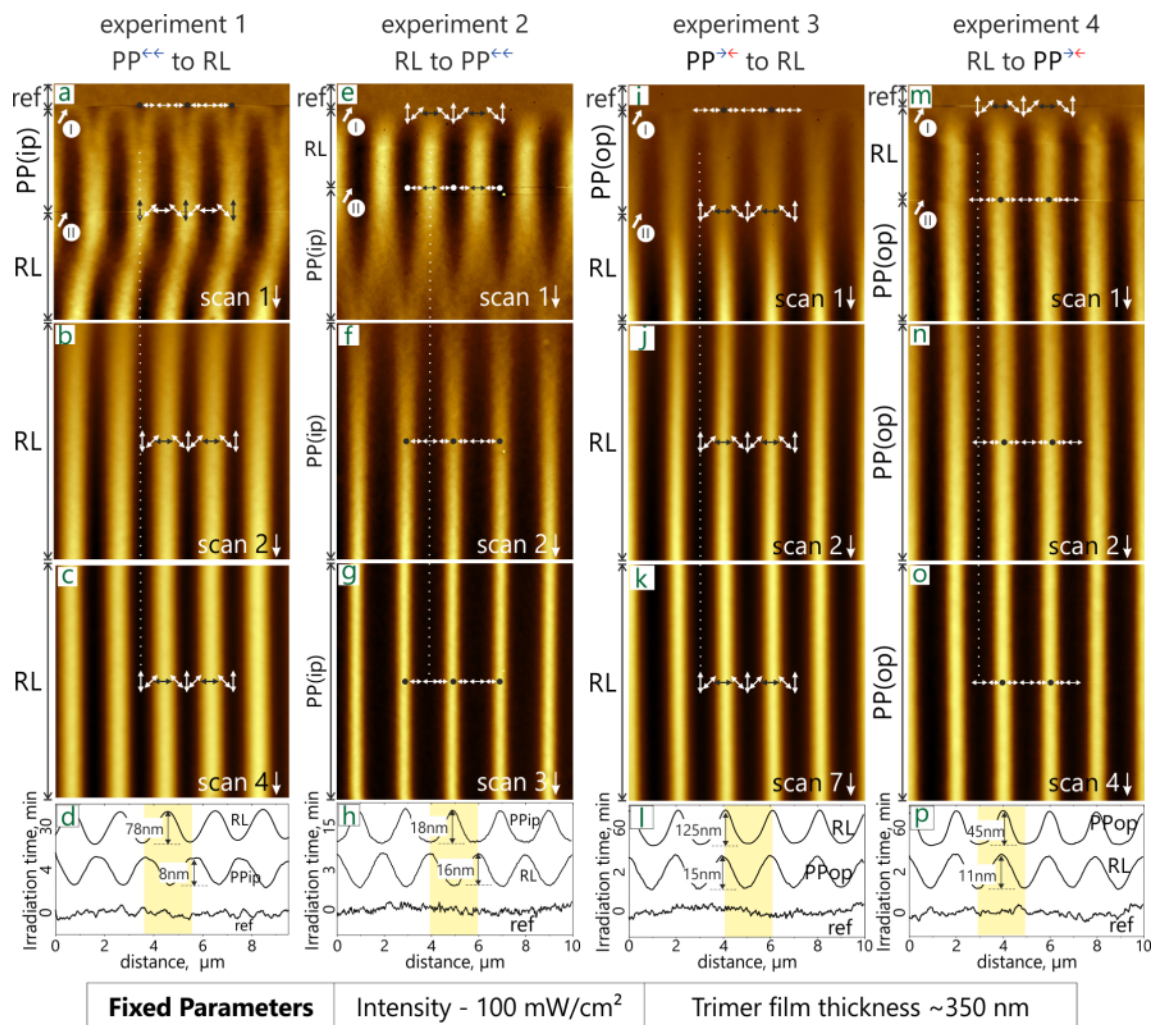
Fig. C.6. AFM micrographs of the trimer film topography recorded within a selected area. While the polymer topography is scanned, the polarization state of the interfering beams is changed in *in-situ*. **Experiment 1** (a, b, c): demonstrate the switching between PP$^{\leftarrow\leftarrow}$ to RL. (a) The first irradiation event lasts 5 min, followed by irradiation with RL (from position "II"). (b, c) Continuous scan during irradiation. (c) Comparison of AFM cross-sectional profiles. **Experiment 2** (d, e, f): demonstrate the switching between PP$^{\leftarrow\leftarrow}$ to RL. **Experiment 3** (i, j, k): The effect of 180° out of phase condition. (d) Switching between PP$^{\rightarrow\leftarrow}$ and RL marked by "I" and "II", respectively. **Experiment 4** (m, n, o): demonstrate the switching from RL to PP$^{\rightarrow\leftarrow}$. The black arrows besides the scan number at the bottom right side of each AFM micrograph represent the AFM scan direction. The y-axis of (d), (h), (l) and (p) denotes the time of irradiation used for each combination before switching. (**ip**): interfering beams in phase; (**op**): interfering beams out of phase by 180° to each other.
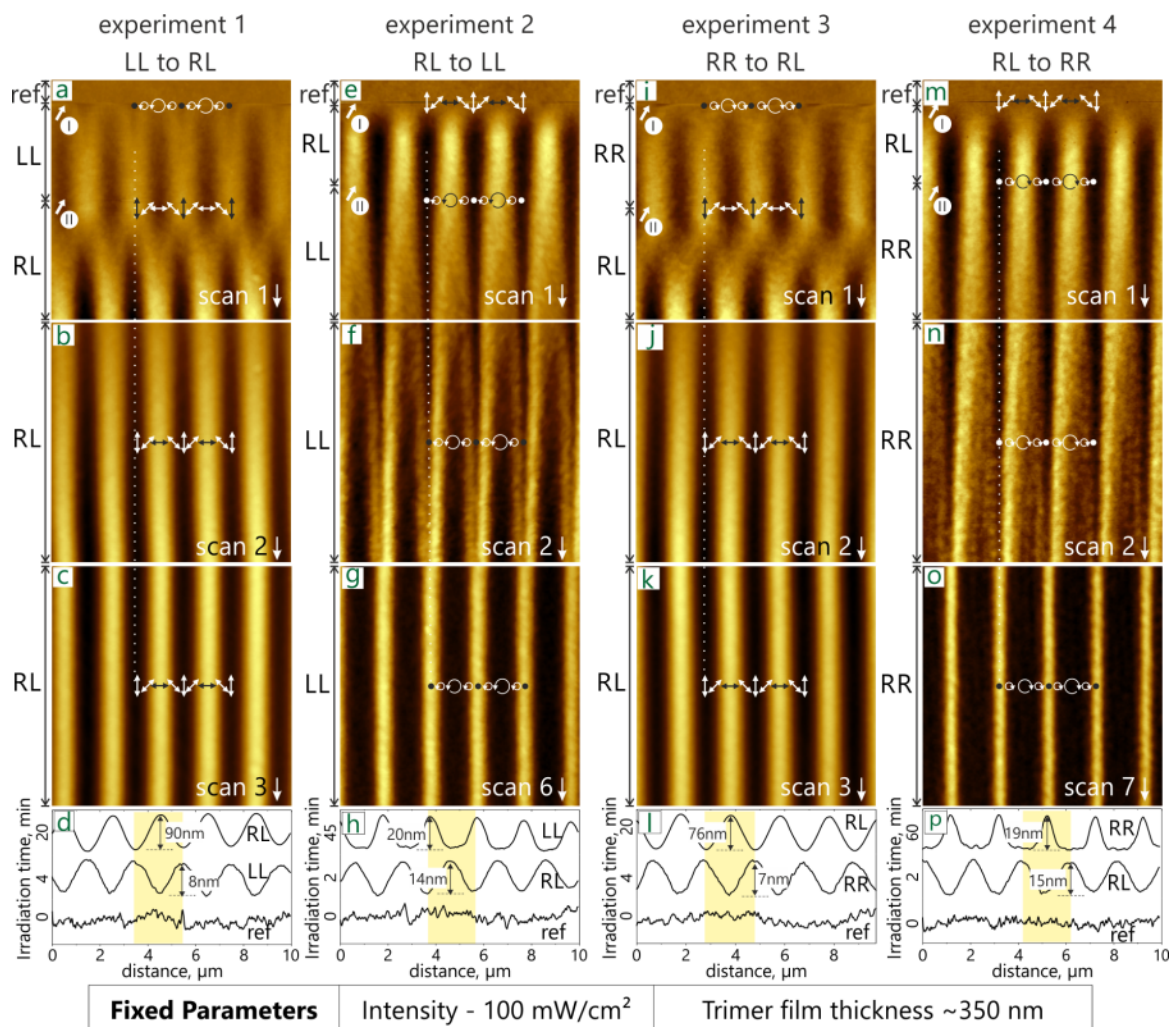
Fig. C.7. AFM micrographs of the trimer film topography recorded within a selected area. While the polymer topography is scanned, the polarization state of the interfering beams is changed in *in-situ*. **Experiment 1** (a, b, c): demonstrate the switching between ‡45↗↗ to RL. (a) The first irradiation event lasts 5 min, followed by irradiation with RL (from position "II"). (b, c) Continuous scan during irradiation. (c) Comparison of AFM cross-sectional profiles. **Experiment 2** (d, e, f): demonstrate the switching between RL to ‡45↗↗. **Experiment 3** (i, j, k): The effect of 180° out of phase condition. (i) Switching between ‡45↗↙ and RL marked by "I" and "II", respectively. **Experiment 4** (m, n, o): demonstrate the switching from RL to ‡45↗↙. The black arrows besides the scan number at the bottom right side of each AFM micrograph represent the AFM scan direction. The y-axis of (d), (h), (l) and (p) denotes the time of irradiation used for each combination before switching. (**ip**): interfering beams in phase; (**op**): interfering beams out of phase by 180° to each other.
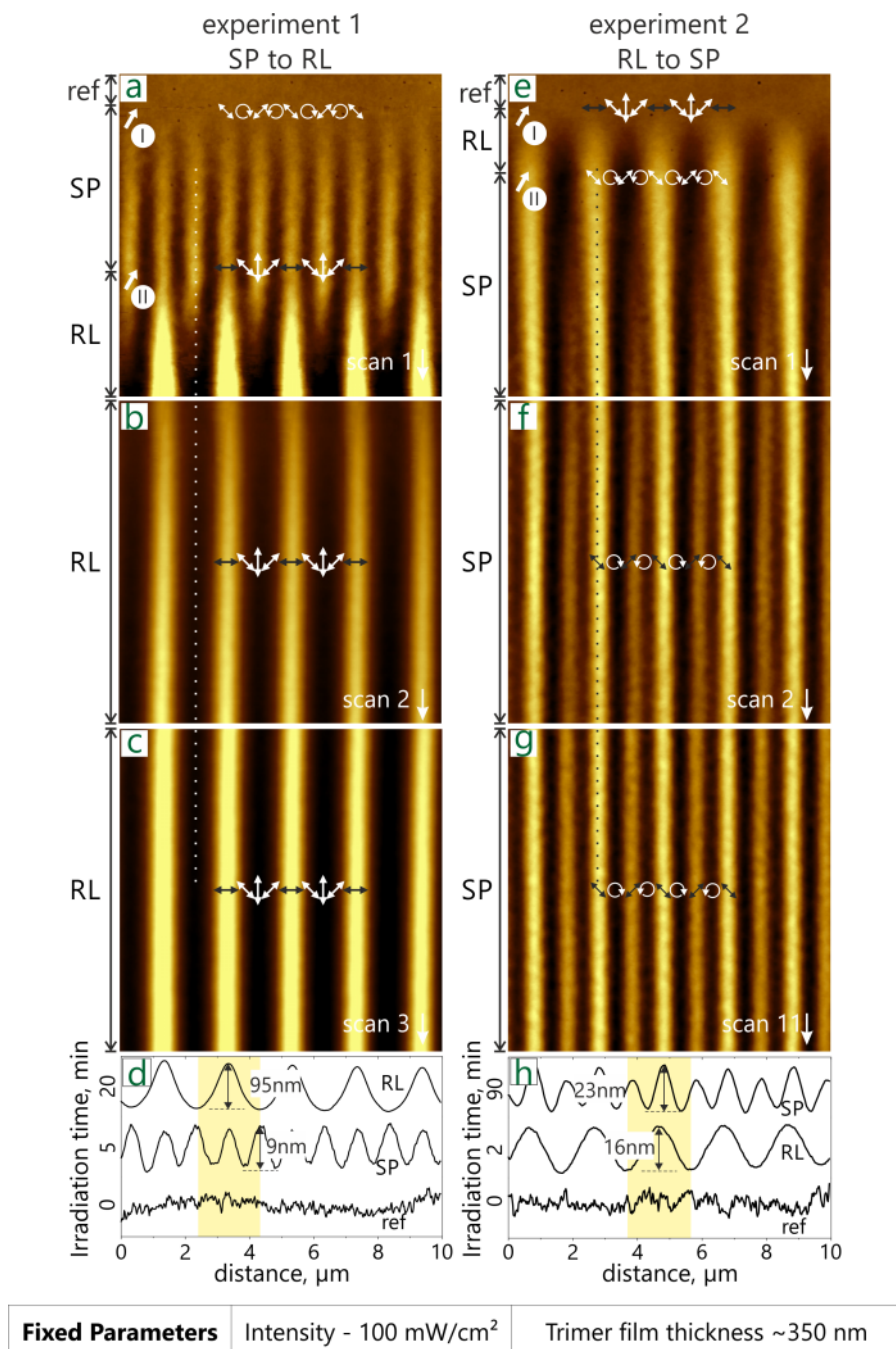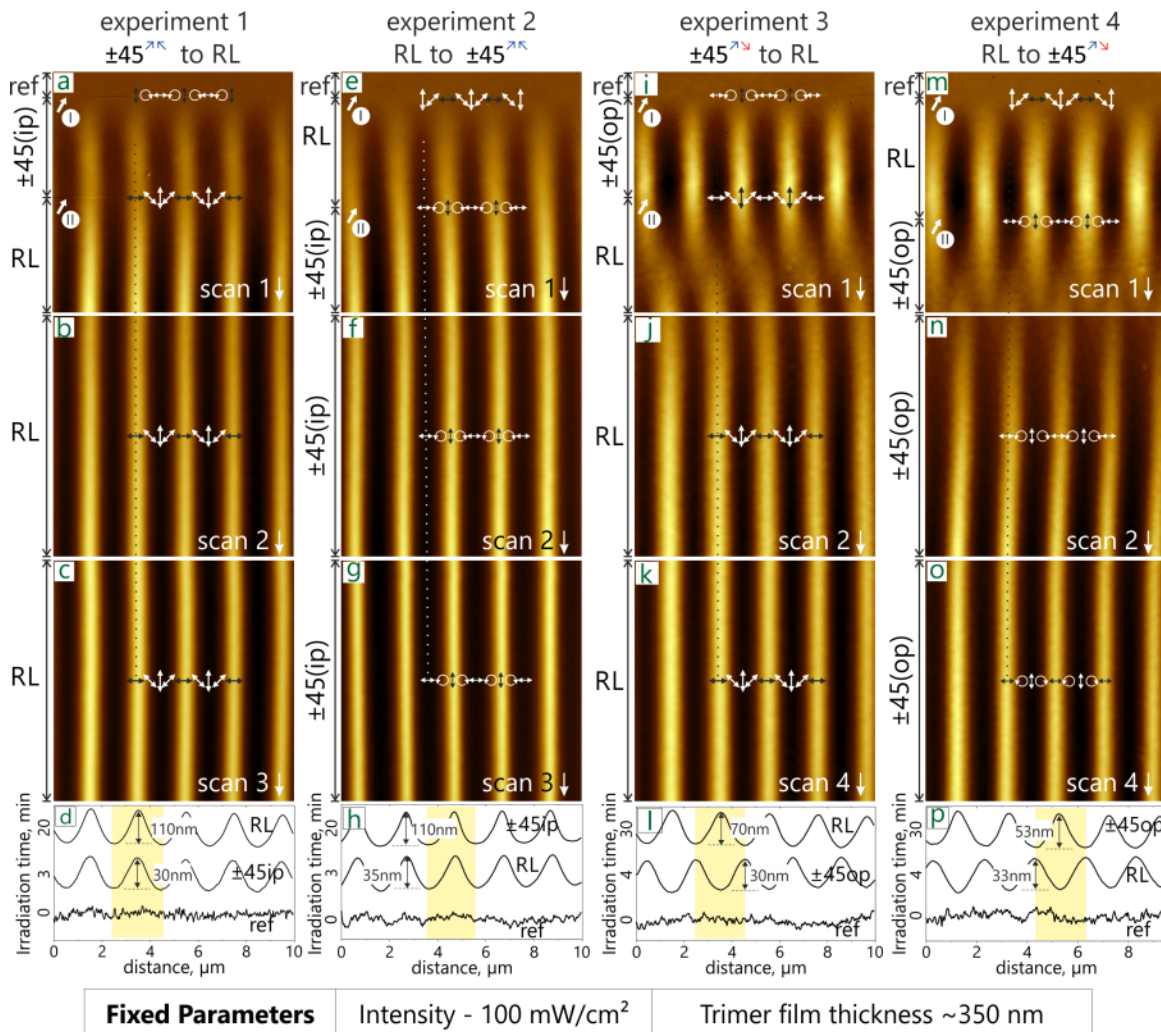
175

Fig. C.8. AFM micrographs of the trimer film topography recorded within a selected area. While the polymer topography is scanned, the polarization state of the interfering beams is changed in *in-situ*. **Experiment 1** (a, b, c): demonstrate the switching between LL to RL. (a) The first irradiation event lasts 5 min, followed by irradiation with RL (from position "II"). (b, c) Continuous scan during irradiation. (c) Comparison of AFM cross-sectional profiles. **Experiment 2** (d, e, f): demonstrate the switching between RL to LL. **Experiment 3** (i, j, k): Switching between RR and RL marked by "I" and "II", respectively. **Experiment 4** (m, n, o): switching from RL to RR. The white arrows besides the scan number at the bottom right side of each AFM micrograph represent the AFM scan direction. The y-axis of (d), (h), (l) and (p) denotes the time of irradiation used for each combination before switching.

Fig. C.9. AFM micrographs of the trimer film topography recorded within a selected area. While the polymer topography is scanned, the polarization state of the interfering beams is changed in *in-situ*. **Experiment 1** (a, b, c): demonstrate the switching between SP to RL. (a) The first irradiation event lasts 5 min, followed by irradiation with RL (from position "II"). (b, c) Continuous scan during irradiation. (c) Comparison of AFM cross-sectional profiles. **Experiment 2** (e, f, g): shows the switching between RL to SP. The y-axis of (d) and (h) denotes the time of irradiation used for each combination before switching.

Fig. C.10. AFM micrographs of the trimer film topography recorded within a selected area. While the polymer topography is scanned, the polarization state of the interfering beams is changed in *in-situ*. **Experiment 1** (a, b, c): demonstrate the switching between ±45↗↖ to RL. (a) The first irradiation event lasts 5 min, followed by irradiation with RL (from position "II"). (b, c) Continuous scan during irradiation. (c) Comparison of AFM cross-sectional profiles. **Experiment 2** (d, e, f): demonstrate the switching between RL to ±45↗↖. **Experiment 3** (i, j, k): Switching between ±45↗↘ and RL marked by "I" and "II", respectively. **Experiment 4** (m, n, o): switching from RL to ±45↗↘. The white arrows besides the scan number at the bottom right side of each AFM micrograph represent the AFM scan direction. The y-axis of (d), (h), (l) and (p) denotes the time of irradiation used for each combination before switching.
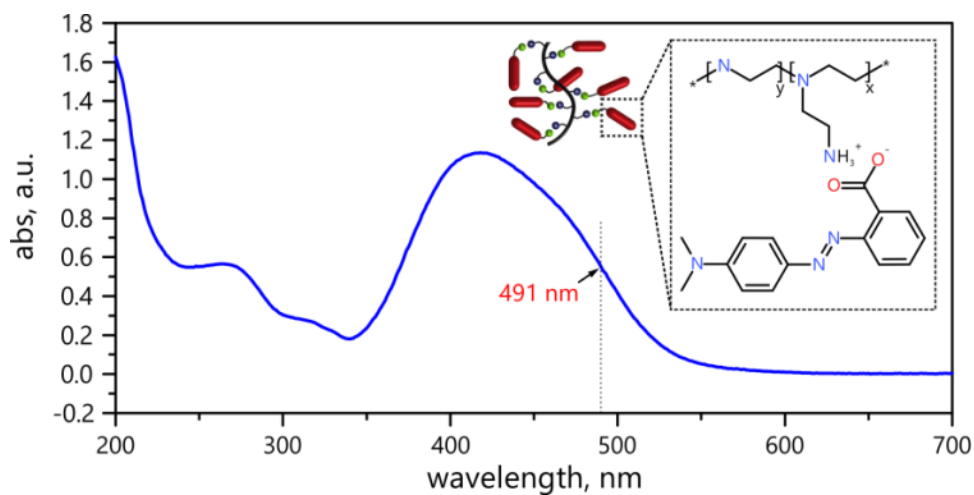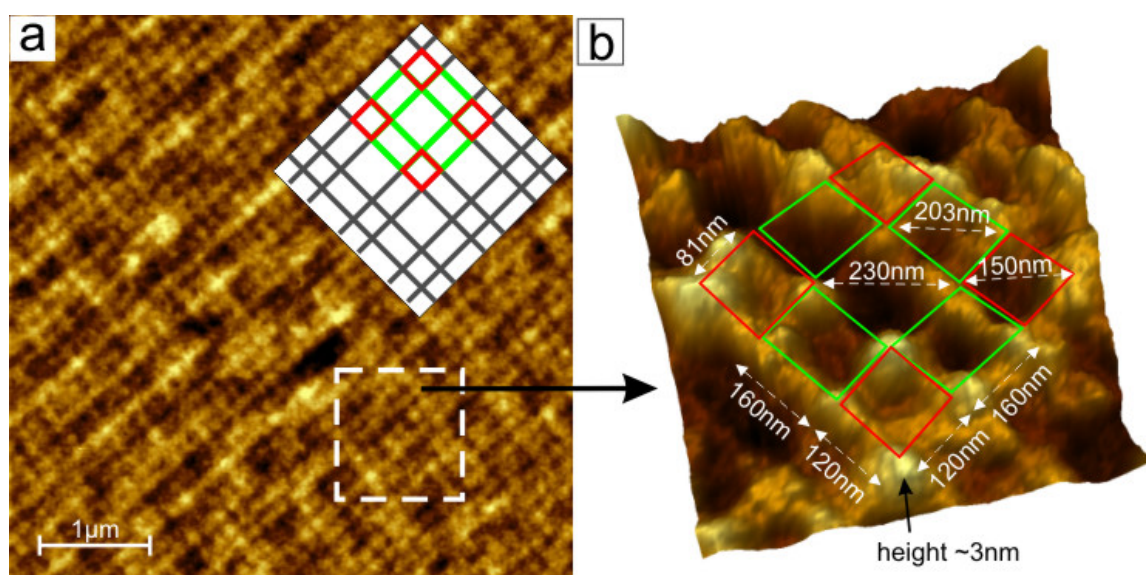
Fig. C.11. UV-Vis absorption spectra of poly(ethylene imine)-(Methyl red, Na salt). The inset shows the chemical structure of the polymer.

Fig. C.12. Asymmetric square arrays obtained by SP interference pattern. (a) The inset represents the expected square array pattern using asymmetric double grating. (b) 3D analysis of asymmetric pattern.
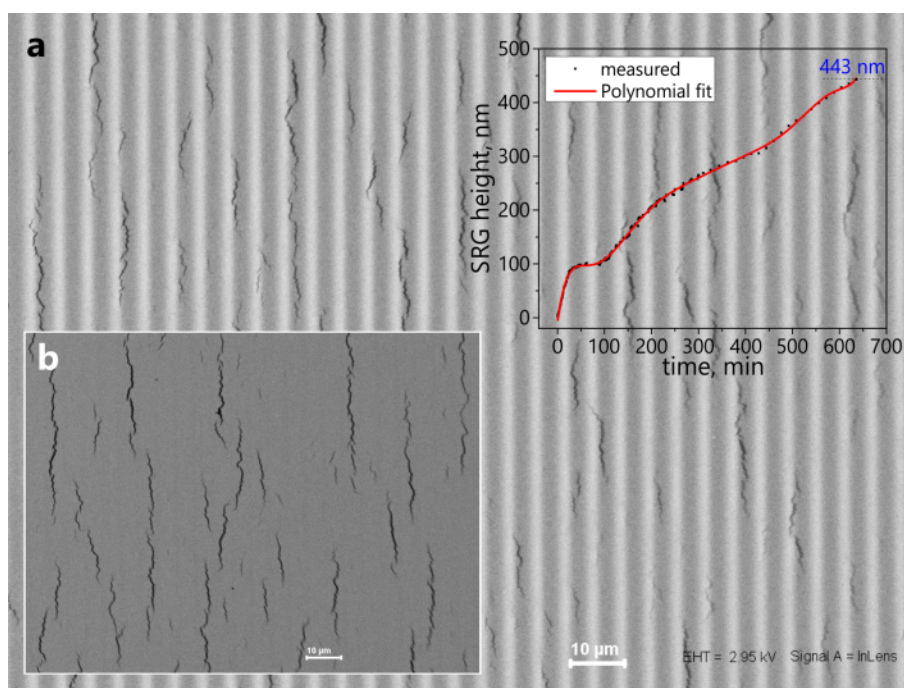
Fig. D.1. (a) SEM analysis of randomly ruptured 25 nm thin gold film during the SRG formation in PAZO film with 5 µm grating periodicity. (b) In-Lens image of focused only on cracks without grating. The grating growth kinetic is also presented.
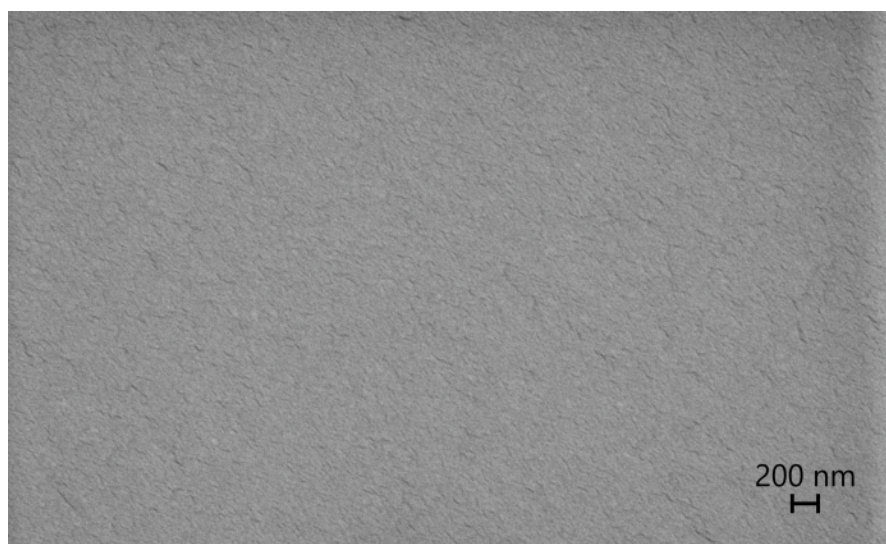
Fig. D.2. SEM image of topography of 15 nm thin gold layer deposited on PAZO film at 2.5 Å/sec.
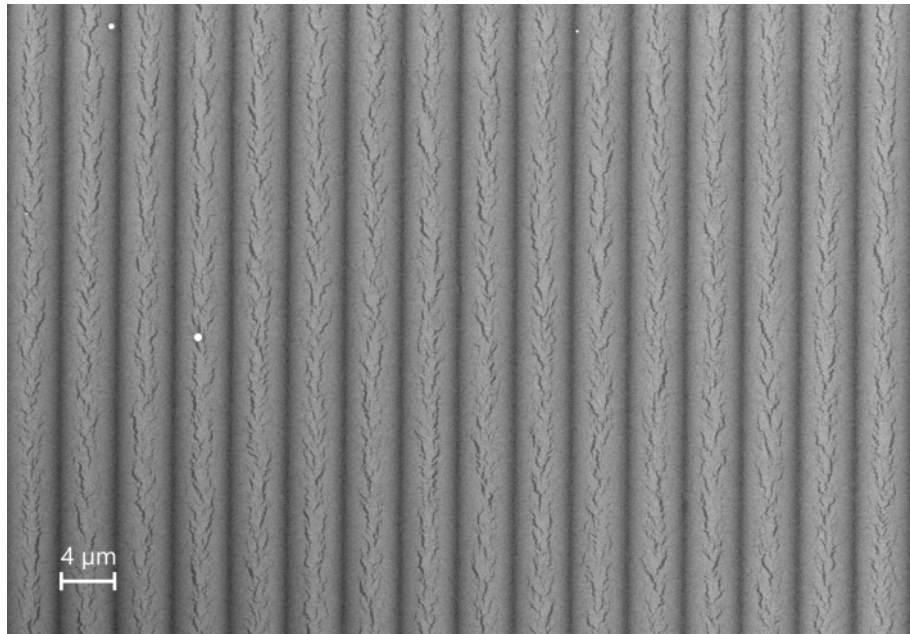
Fig. D.3. (a) SEM image of periodically ruptured 15 nm thin gold film on PAZO with 4 μm grating periodicity and ±45o interference pattern.
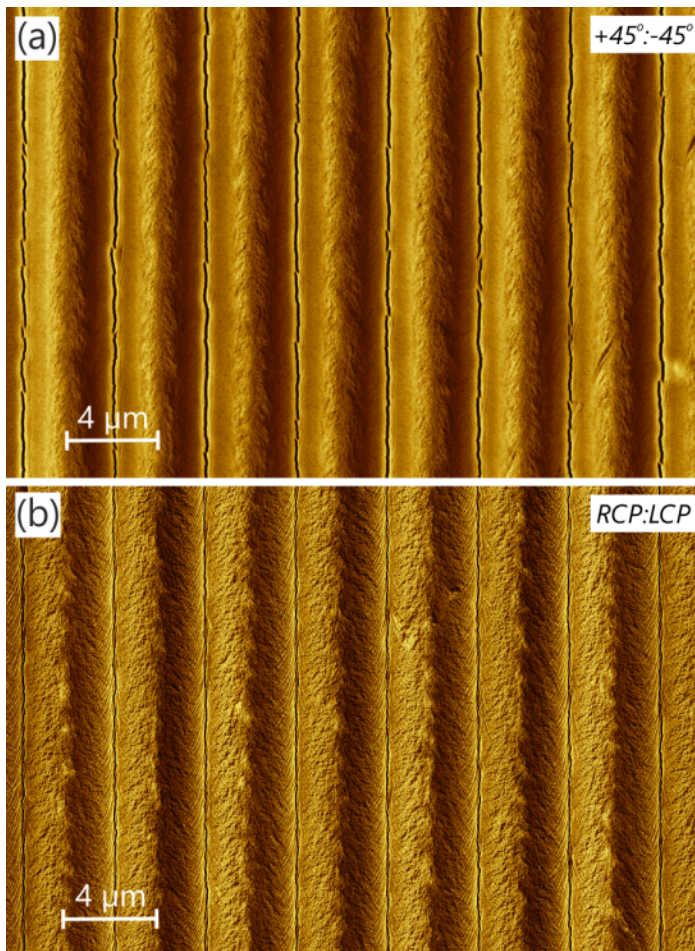
Fig. D.4. a) Periodically ruptured gold film on polymer during SRG formation using *±45°* interference pattern. b) Periodically ruptured gold film on polymer during SRG formation using RL interference pattern.
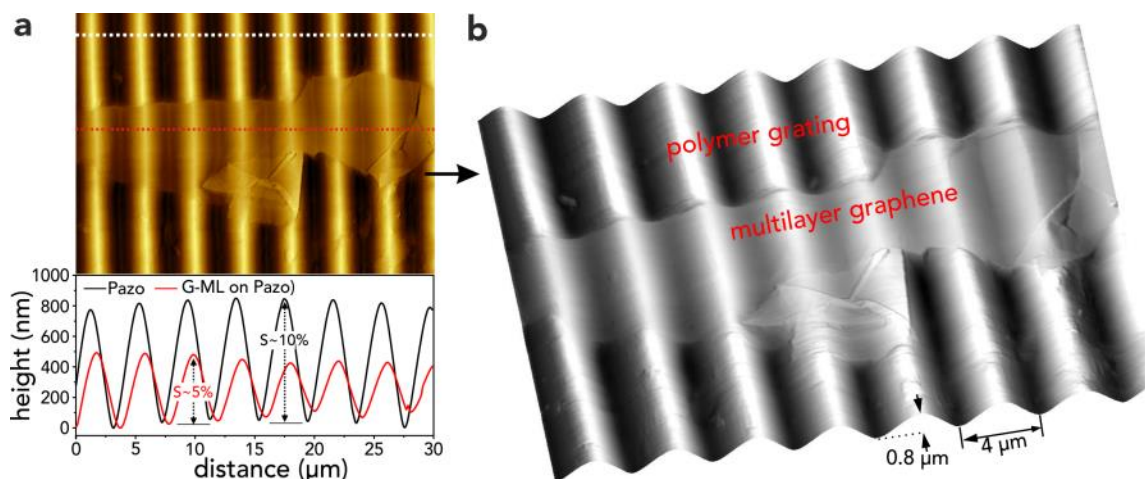
Fig. D.5. AFM micrograph of the graphene piece placed above the polymer layer after inscribing of the surface relief gratings. The AFM cross section profile of the naked polymer surface (black line) was recorded along the line marked by the white dotted line, while the profile along the polymer/graphene surface is marked in red. The change in the surface area is denoted by 's'. (b) 3D view of (a).
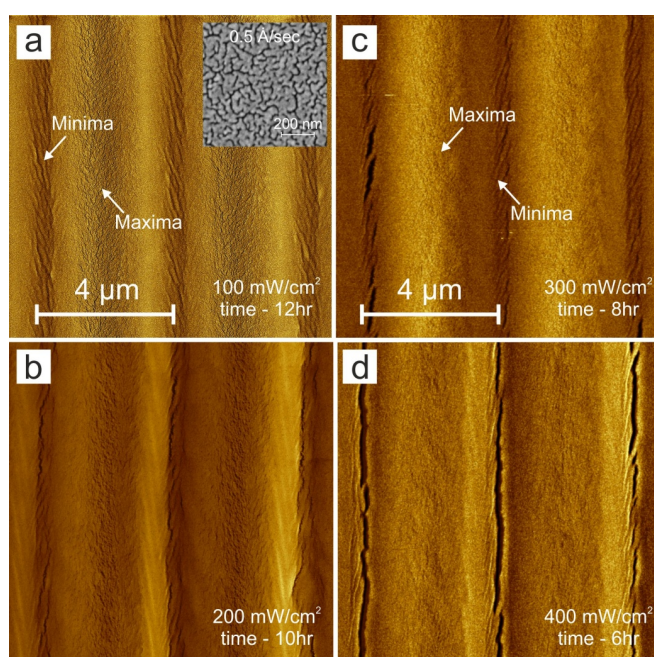
Fig. D.6. Visualization of opto-mechanical stress by controlling the rate of reaction through varying intensity. All the experiments are for 10±1 nm gold film with 0.5A/sec evaporation rate. a) Strong deformation only at the grating maxima with 100mW/cm². b) Weak rupturing at the valley and weak deformation at the maxima with 200mW/cm². c) Weak rupturing at the valleys and no deformation peaks with 300mW/cm². d) Strong rupturing at valleys and no deformation at the peaks with 400mW/cm².

Bibliography

1   S. Kawata and Y. Kawata. *Chem. Rev.* **100**, 1777 (2000).

2   J. A. Delaire, and K. Nakatani. *Chem. Rev.* **100**, 1817 (2000).

3   S. Lee, H. S. Kang, and J.-K. Park. *Adv. Funct. Mater.* **21**, 1770 (2011).

4   I. B. Divliansky, A. Shishido, I. C. Khoo, T. S. Mayar, D. Pena, S. Nishimura, C. D. Keating, and T. E. Mallouk, *Appl. Phys. Lett.* **79**, 3392 (2001).

5   T. König, N. S. Yadavalli, and S. Santer. *Plasmonics* **7**, 535 (2012).

6   T. König, V. V. Tsukruk, and S. Santer. *ACS Appl. Mater. Interfaces* **5**, 6009 (2013).

7   A. Emoto, E. Uchida and T. Fukuda. *Polymers* **4**, 150 (2012).

8   M. Yamada, M. Kondo, R. Miyasato, Y. Naka, J. Mamiya, M. Kinoshita, A. Shishido, Y. Yu, and C. J. Barrett. *J. Mater. Chem.* **19**, 60 (2009).

9   V. Ferri, M Elbing, G. Pace, M. D. Dickey, M. Zharnikov, P. Samori, M. Mayor, and M. A. Rampi. *Angew. Chem. Int. Ed.* **47**, 3407 (2008).

10 M. Yamada, M. Kondo, J. Mamiya, Y. Yu, M. Kinoshita, C. J. Barrett, and T. Ikeda. *Angew. Chem. Int. Ed.* **47**, 4986 (2008).

11 N. S. Yadavalli. *Master thesis*, CPI, IMTEK, Uni Freiburg (2010).

12 T. König, N. S. Yadavalli, and S. Santer. *J. Mater. Chem.* **22**, 5945 (2012).

13 S.-K. Oh, M. Nakagawa, K. Ichimura. *J. Mater. Chem.* **11**, 1563 (2001).

14 A. Kausar, H. Nagano, T. Ogata, T. Nonaka, and S. Kurihara. *Angew. Chem. Int. Ed.* **48**, 2144 (2009).

15 A. Kausar, H. Nagano, Y. Kuwahara, T. Ogata, and S. Kurihara. *Chem. Eur. J.* **17**, 508 (2011).

16 A. Diguet, R.-M. Guillermic, N. Magome, A. Saint-Jalmes, Y. Chen, K. Yoshikawa, and D. Baigl. *Angew. Chem. Int. Ed.* **48**, 9281 (2009).

17 Y. Zakrevsky, A. Kopyshev, N. Lomadze, E. Morozova, L. Lysyakova, N. Kasyanenko, and S. Santer. *Phys. Rev. E* **84**, 021909 (2001).

18 Y. Zakrevsky, P. Cywinski, M. Cywinska, J. Paasche, N. Lomadze, O. Reich, H.-G. Löhmannsröben, and S. Santer. *J. Chem. Phys.* **140**, 044907 (2014).

19 Y. Zakrevskyy, J. Roxlau, G. Brezesinski, N. Lomadze, and S. Santer. *J. Chem. Phys.* **140**, 044906 (2014).

20 R. B. Matthew, V. Matthew, and D. Trauner. *Biochemistry* **45**, 15129 (2006).

21 A. Goulet-Hanssens, and C. J. Barrett. *J. Polymer. Sci., Part A: Polymer Chem.* **51**, 3058 (2013).

22 C. Barrett, P. Rochon, and A. Natansohn, *J. Phys. Chem.* **100**, 8836 (1996).

23 P. Rochon, E. Batalla, and A. Natansohn. *Appl. Phys. Lett.* **66**, 136 (1995).

24 D. Y. Kim, L. Li, X. L. Jiang, V. Shivshankar, J. Kumar and S. K. Tripathy. *Macromolecules* **28**, 8835 (1995).

25 A. Natansohn, P. Rochon, M. S. Ho, and Battett, C. *Macromolecules* **28**, 4179 (1995).

26 D. K. Yi, E. M. Seo, and D. Y. Kim. *Appl. Phys. Lett*. **80**, 225 (2002).

27 K. V. Sreekanth, J. K. Chua, and V. M. Murukeshan *Appl. Opt*. **49**, 6710 (2010).

28 H. S. Kang, S. Lee, and J. Park. *Adv. Mater.* **24**, 2069 (2012).

29 D. Y. Kim, L. Li, J. Kumar, and S. K. Tripathy. *Appl. Phys. Lett*. **66**, 1166 (1995).

30 P. S. Ramanujam, N. C. R. Holme, and S. Hvilsted. *Appl. Phys. Lett*. **68**, 1329 (1996).

31 N. K. Viswanathan, D. Y. Kim, S. Bian, J. Williams, W. Liu, L. Li, L. Samuelson, J. Kumar, and S. K. Tripathy. *J. Mater. Chem*. **9**, 1941 (1999).

32 L. F. Johnson, G. W. Kammlott, and A. Ingersoll. *Appl. Opt*. **17**, 1165 (1978).

33 J. M. Carter, M. Farhoud, R. C. Fleming, T. A. Savas, M. Waslsh, M. L. Schattenburg, and H. I. Smith. Nanostructures Laboratory, MIT, USA. *http://nanoweb.mit.edu/annual-report01/07.html*.

34 M. J. Madou. Fundamentals of microfabrication: The science of miniaturization, 2nd edition, CRC press (2002.

35 H. Philips, D. Callahan, R. Sauerbrey, G. Szabo, and Z. Bor. *Appl. Phys. Lett*. **58**, 276 (1991).

36 S. Bian, L. Li, J. Kumar, D. Y. Kim, J. Williams and S. K. Tripathy. *Appl. Phys. Lett*. **73**, 1817 (1998).

37 J. Kumar, L. Li, X. L. Xiang, D. Y. Kim, T. S. Lee, and S. Tripathy. *Appl. Phys. Lett*. **73**, 2096 (1998).

38 X. L. Jiang, L. Li, J. Kumar, D. Y. Kim, S. K. Tripathy, *Appl. Phys. Lett*. **72**, 2502 (1998).

39 T. G. Pedersen, P. M. Johansen, N. C. R. Holme, P. S. Ramanujam, and S. Hvilsted. *Phys. Rev. Lett.* **80**, 89 (1998).

40 D. Bublitz, B. Fleck, and L. Wenke. *Appl. Phys. B* **72**, 931 (2001).

41 M. Saphiannikova, and D. Neher. *J. Phys. Chem. B* **109**, 19428 (2005).

42 V. Toshchevikov, M. Saphiannikova, and G. Heinrich. *J. Phys. Chem. B* **113**, 5032 (2009).

43 V. Toshchevikov, M. Saphiannikova, and G. Heinrich. *J. Phys. Chem. B* **116**, 913 (2012).

44   U. V. Padmanabh. *Investigation of the Surface Relief Grating formation on Amorphous Azobenzene Polymer Films*. PhD thesis, Department of Solid State Physics, University of Siegen, DE (2009).

45   A. Priimägi. *Polymer-azobenzene complexes: From supramolecular concepts to efficient photoresponsive polymers*. PhD thesis, Faculty of Information and Natural sciences, Department of Applied Physics, Helsinki University of Technology, ISBN 978-952-248-101-6 (2009).

46   M. Grenzer (Saphiannikova). *Photoinduced Material Transport in Amorphous Azobenzene Polymer Films.* PhD thesis, Faculty of Mathematics and Natural Sciences, University of Potsdam, DE (2007).

47   M. Saphiannikova, T. M. Geue, O. Henneberg, K. Morawetz, and U. Pietsch. *J. Chem. Phys*. **120**, 4039 (2004).

48   T. Matsui, S. Yamamoto, M. Ozaki, K. Yoshino, and F. Kajzar. *J. Appl. Phys.* **92**, 6959 (2002).

49   F. Lagugne-Labarthet, T. Buffeteau, and C. Sourisseau. *Phys. Chem. Chem. Phys.* **4**, 4020 (2002).

50   O. Kulikovska, K. Gharagozoloo-Hubmann, and J. Stumpe. *Proceedings of SPIE*. **85**, 4802 (2002).

51   U. J. Hwang, J. S. Kim, C. H. Oh, S. H. Song, B. Park, and P. S. Kim. *J. Korean Phys. Soc.* **43**, 629 (2003).

52   U. J. Hwang, J. S. Kim, C. H. Oh, G. J. Lee, Y. P. Lee, S. H. Song, P. S. K, and Y. K. Han. *J. Korean Phys. Soc.* **45**, 366 (2004).

53   F. Fabbri, D. Garrot, K. Lahlil, J. P. Boilot, Y. Lassailly, and J. Peretti. *J. Phys. Chem. B* **115**, 1363 (2011).

54   F. Lagugne Labarthet, and C. Sourisseau. *J. Phys. Chem. B* **108**, 17055 (2004).

55.   C. Barrett, A. Natansohn, and P. Rochon. *Chem. Mater.* **7**, 899 (1995).

56.   T. Seki, K. Fukuda, and K. Ichimura. *Langmuir* **15**, 5098 (1999).

57.   A. Ambrosio, L. Marrucci, F. Borbone, A. Roviello, and P. Maddalena. *Nat. Commun.* **3**, 989 (2012).

58   L. Nikolova, and P.S. Ramanujam, Polarization holography, Cambridge Academic Press, UK pp. 88 (2009).

59   D. François, A. Pineau, and A. Zaoui. *Mechanical Behaviour of Materials: Volume II: Viscoplasticity, Damage, Fracture and Contact Mechanics*; Springer: New York, (1998).

60   Veer, P. U.; Pietsch, U.; Rochon P.; Saphiannikova, M. *Mol. Cryst. Liq. Cryst.* **486**, 1108 (2008).

61   P. Karageorgiev, D. Neher, B. Schulz, B. Stiller, U. Pietsch, M. Giersig, L. Brehmer. *Nature Mater.* **4**, 699 (2005).

62   C. Schuh, N. Lomadze, A. Kopyshev, J. Ruhe, and S. Santer. *J. Phys. Chem. B* **115**, 10431 (2011).

63   N. Lomadze, A. Kopyshev, J. Ruhe, and S. Santer. *Macromolecules*, **44**, 7372 (2011).

64   Private discussion with Prof. Christopher. J. Barrett.

65   P. Hariharan. *Optical Interferometry* 2nd edition, Academic Press 2003.

66   N. K. Viswanathan, S. Balakrishnan, L. Li, S. K. Tripathy, and J. Kumar. *Jpn. J. Appl. Phys.* **38**, 5928 (1999).

67   L. Nikolova, and P. S. Ramanujam. *Polarization Holography*. Cambridge University Press. p:24–87 (2009).

68   L. M. Goldenberg, L. Kulikovsky, O. Kulikovska, J. Tomczyk, and J. Stumpe, *Langmuir* **26**, 2214 (2009).

69   http://www.tedpella.com/histo_html/coverslip-info.htm

70   M. Gohlke. *Documentation of APCSA Program.* Soft-matter group, University of Potsdam.

71   H. Rau. *Photoisomerization of azobenzenes Photochemistry and Photophysics* vol III ed J F Rabeck (Boca Raton, FL: CRC Press) p 119 (1990).

72   K. Ichimura, S. K. Oh, and M. Nakagawa. *Science* **288**, 1624 (2000).

73   T. Todorov, L. Nikolova, and N. Tomova. *Appl. Opt.* **23**, 4309 (1984).

74   C. Jones, and S. Day. *Nature* **15**, 351 (1991).

75   R. Loucif-Saibi, K. Nakatani, J. A. Delaire, M. Dumont, and Z. Sekkat. *Chem. Mater.* **5**, 229 (1993).

76   Z. Sekkat, and W. Knoll. *Photoreactive Organic Thin Films* Academic, New York, 2002.

77   M. Eich, and J. H. Wendorff. *Makromol. Chem. Rapid Commun.* **8**, 467 (1987).

78   (a) T. Todorov, L. Nikolova, and N. Tomova. *Appl. Opt.* **23**, 4588 (1984). (b) T. Todorov, L. Nikolova, K. Stoyanova, and N. Tomova. *Appl. Opt.* **24**, 785 (1985).

79   I. Naydenova, L. Nikolova, T. Todorov, N. C. R. Holme, P. S. Ramanujam, and S. Hvilsted. *J. Opt. Soc. Am. B* **15**, 1257 (1998).

80   A. Sobolewska, and A. Miniewicz, *J. Phys. Chem. B* **112**, 4526 (2008)

81   F. Lagugne Labarthet, T. Buffeteau, and C. Sourisseau, *J. Appl. Phys.* **90**, 3149 (2001).

82   L. M. Goldenberg, O. Kulikovska, and J. Stumpe. *Langmuir* **21**, 4794 (2005).

83   M. Saphiannikova, V. Toshchevikov, and J. Ilnytskyi. *Nonlinear Optics and Quantum Optics*, **41**, 27 (2010).

84   T. Geue, A. Ziegler, and J. Stumpe. *Macromolecules* **30**, 5729 (1997).

85   T König, L. M. Goldenberg, O. Kulikovska, L. Kulikovsky, J. Stumpe, S. Santer. *Soft Matter* **7**, 4174 (2011).

86   D. Elfström, B. Guilhabert, J. McKendry, S. Poland, Z. Gong, D. Massoubre, E. Richardson, B. R. Rae, G. Valentine, G. Blanco-Gomez, E. Gu, J.M. Cooper, R.K. Henderson, and M.D. Dawson. *Optics Express*. **17**, 23522 (2009).

87   N. Seok-In, K. Seok-Soon, J. Jang, O. Seung-Hwan, K. Juhwan, and K. Dong-Yu. *Adv. Funct. Mater*. **18**, 3956 (2008).

88   D. Sawaki and J. Amako. *Proc. of SPIE*. **7202**, 72020L-1 (2009).

89   G. D. Kubiak and D.R. Kania. *OSA Trends in Optics and Photonics*. 4 (1996). G. D. Kubiak and D. R. Kania, eds. (Optical Society of America, Washington, DC 1996), pp. 66-71.

90   D. K. Gramotnev and S. I. Bozhevolnyi. *Nature photonics* **4**, 83 (2010).

91   X. Luo and T. Ishihara. *Appl. Phy. Lett*. **84**, 4770 (2004).

92   T. König and S. Santer. *Nanotechnology* **23**, 485304 (2012).

93   T. König and S. Santer. *Nanotechnology* **23**, 155301 (2012).

94   A. Sundaramurthy, P. J. Schuck, N. R. Conley, D. P. Fromm, G. S. Kino, and W. E. Moerner. *Nano Lett*. **6**, 355 (2006).

95   Z. Sekkat, H. Ishitobi, M. Tanabe, S. Shoji, and S. Kawata. *M. J. Cond. Mater*. **11**, 111 (2009).

96   W. Srituravanich, N. Fang, C. Sun, Q. Luo, and X. Zhang. *Nano Lett*. **4**, 1085 (2004).

97   S. Lee, Y.-C. Jeong, and J.-K. Park. *Opt. Express* 15, 14550 (2007).

98   L. M. Goldenberg, Y. Gritsai, O. Sakhno, O. Kulikovska, and J. Stumpe. *J. Opt*. **12**, 015103 (2010).

99   M. Guo, Z. Xu, and X. Wang. *Langmuir* **24**, 2740 (2008).

100 Y. Gritsai, L. M. Goldenberg, O. Kulikovska, and J. Stumpe. *J. Opt. A: Pure Appl. Opt*. **10**, 125304 (2008).

101 P. Hariharan. *Optical Interferometry* 2nd edition, Academic Press 2003, Ch. 3 and pp. 28.

102 H. J. Eichler, P. Günter, D. W. Pohl, Laser-induced Dynamic Gratings, 1985, Springer-Verlag, pp. 13-21.

103 O. Kulikovska, L. M. Goldenberg, J. Stumpe. *Chem Mater* **19**, 3343 (2007).

104 Y. Xiang, T. Li, Z. Suo, and J. J. Vlassak. *Appl. Phys. Lett*. **87**, 161910 (2005).

105 K. Leosson, A. S. Ingason, B. Agnarsson, A. Kossoy, S. Olafsson, M. C. Gather. *Nanophotonics* **2**, 3–11 (2013).

106 F. Linde, N. S. Yadavalli, S. Santer. *Appl. Phys. Lett*. **103**, 253101 (2013).

107 http://www.mlz-garching.de/refsans

108. S. A. Stepanov, E. A. Kondrashkina, R. Koehler, D. V. Novikov, G. Materlik, S. M. Durbin. *Phys. Rev. B* **57**, 4829 (1998).

109. F. Abeles. *Ann. Phys. (Paris)* **5**, 596 (1950).

110 R. Zan, U. Bangert, Q. Ramasse, K. S. Novoseloc. *Small* **7**, 2868 (2011).

111 X. Liu, C-Z. Wang, M. Hupalo, H-Q. Lin, K-M. Ho, and M. C. Tringides. *Crystals* **3**, 79–111 (2013).

112 M. F. Ashby, and D. R. H. Jones. Engineering materials I: An introduction to properties, applications and design. Ch. 11, pp. 141–152. Oxford, Butterworth-Heinemann, (2005).

113 T. L. Anderson. Fracture Mechanics: Fundamentals and Applications. CRC Press: Boston (2005).

114 S. Olliges, P. A. Gruber, S. Orso, V. Auzelyte, Y. Ekinci, H. H. Solak, and R. Spolenak. *Scripta Materialia* **58**, 175 (2008).

115 T. Li, Z. Y. Huang, Z. C. Xi, S. P. Lacour, S. Wagner, and Z. Suo. *Mech. Mater*. **37**, 261 (2005).

116 T. Li, and Z. Suo. *Int. J. Sol. and Str*. **43**, 2351 (2006).

117 K. Ichimura. *Chem. Rev*. **100**, 1847 (2000).

118 T. König, T. Papke, A. Kopyshev, and S. Santer, *J. Mater. Sci*. **48**, 3863 (2013).

119 N. Maluf. *An introduction to microelectromechanical systems engineering*. Artech House, Boston (2000).

120 M. Madou. *Fundamentals of Microfabrication*. CRC Press, Boca Raton (1997).

121 S. Alborghetti, P. Stamenov. *ISRN Electronics* 652587 (2013).

122 R. Verplancke, F. Bossuyt, D. Cuypers, and J. Vanfleteren. *J. Micromech. Microeng*. **22**, 015002 (2012).

123 J. A. Rogers *et al*. *Proc. Natl. Acad. Sci*. **98**, 4835 (2001).

124 S. R. Forrest. *Nature*, **428**, 911 (2004).

125 K. Müllen, and U. Scherf. *Organic light emitting devices: Synthesis, Properties and Applications*. p.181–214 (Wiley, 2006).

126 V. J. Lumelsky, M. S. Shur, and S. Wagner. *IEEE Sens. J*. **1**, 41 (2001).

127 S. Wagner, S.P. Lacour, J. Jones, P.I. Hsu, J. C. Sturm, T. Li, and Z. Suo. *Physica E* **25**, 326 (2005).

128 D. S. Gray, J. Tien, and C. S. Chen. *Adv. Mater*. **16**, 393 (2004).

129 C. J. Brabec. *Sol. Energy Mater. Sol. Cells* **83**, 273 (2004).

130 E. Bonderover, and S. Wagner. *IEEE Electron Device Lett*. **25**, 295 (2004).

131. H. Huang, and F. Spaepen. *Acta mater*. **48**, 3261 (2000).

132. M. A. Haque, and M. T. A. Saif. *Scripta Materialia* **47**, 863 (2002).

133. S. Midturi, *ARPN J. Eng. Appl. Sci*. **5**, 72 (2010).

134. M. A. Haque, and M. T. A. Saif. *Natl. Acad. Sci. USA* **101**, 6335 (2004).

135. Y. Lu, J. Song, J. Y. Huang, and J. Lou. *Nano Res*. **4**, 1261 (2011).

136. J.-H. Kim *et al*. *Nat. Commun.* **4**, 2520 (2013).

137. M. P. Orthner, L. W. Rieth, and F. Solzbacher. *Rev. Sci. Instrum.* **81**, 055111 (2010).

138. J. J. Vlassak, and W. D. Nix. *J. Mater. Res*. **7**, 3242 (1992).

139. A. J. Kalkman, A. H. Verbruggen, and G. C. A. M. Janssen. *Appl. Phys. Lett*. **78**, 2673 (2001).

140. Y. Xiang, X. Chen, and J. J. Vlassak. *J. Mater. Res*. **20**, 2360 (2005).

141. A. Kossoy, D. Simakov, S. Olafsson, and K. Leosson. *Thin Solid Films* **536**, 50 (2013).

142. F. Aviles, L. Llanes, and A. I. Oliva. *J. Mater. Sci*. **44**, 2590 (2009).

143. T. Li, Z. Zhang, and B. Michaux. *Theor. Appl. Mech. Lett*. **1**, 041002 (2011).

144. S. Kim, S. Won, G.-D. Sim, I. Park, and S.-B. Lee. *Nanotechnology* **24**, 085701 (2013).

145 H. M. Su, Y. C. Zhong, X. Wang, X. G. Zheng, J. F. Xu, and H. Z. Wang. Phys. Rev. E 67, 056619 (2003).

146 J. H. Moon, J. Ford, and S. Yang. Polymers for Advanced Technologies 17, 83 (2006).

147 J. Huang, et al. Phys. Chem. Chem. Phys. 13, 16150 (2011).

148 D. Wang, Z. Wang, Z. Zhang, Y. Yue, and D. Li. Appl. Phys. Lett. 102, 081903 (2013).